

Core scale modelling of EOR transport mechanisms

by

Oddbjørn Mathias Nødland

Thesis submitted in fulfillment of
the requirements for degree of
PHILOSOPHIAE DOCTOR
(PhD)



University
of Stavanger

Faculty of Science and Technology
Department of Mathematics and Natural Sciences
2019

University of Stavanger
N-4036 Stavanger
NORWAY
www.uis.no

©2019 Oddbjørn Mathias Nødland

ISBN: 978-82-7644-811-5
ISSN: 1890-1387
PhD thesis UiS No. 430

Acknowledgements

The completion of this thesis would have been impossible without the continued support of many others.

First and foremost, I want to express my sincere gratitude to the two people who have helped me the most academically, namely Professor Aksel Hiorth (my main PhD advisor), and Arild Lohne (Senior Research Engineer at IRIS/NORCE). Thank you for always taking the time to answer my questions, and for attempting to steer me towards interesting and fruitful paths of inquiry. You have both contributed substantially to my publications. In particular, it was Arild Lohne's initial work on developing the IORCoreSim polymer model that spurred the writing of the first journal article, at a time when I felt rather stuck. Also, I am grateful to Aksel Hiorth for helpful and motivating conversations throughout my PhD period, and for providing very constructive comments to my writing.

I would like to acknowledge my co-author Arne Stavland, for providing relevant and succinct feedback whenever I asked. Also, thanks to fellow PhD student and co-author Irene Ringen; not only because of contributions to the thesis subject matter, but also for helping to establish a good social atmosphere at work. The same can be said for many other people, too many to list explicitly by name. However, I want to mention my office roommate and fellow PhD-student, Samuel Erzuah, who claims I live in the office, but who have spent far more time being locked up at work in the evenings than me.

I further want to thank Helmer André Friis, for several good conversations early on in my PhD period. Likewise, I appreciate the help I got from my co-supervisor Hans Kleppe during the first few years.

Thanks to Martin Helsø for allowing me to adapt his L^AT_EX template, and for giving such a prompt response when I asked him about this a short time before manuscript submission.

I acknowledge those who have supported my work financially: the Research Council of Norway, and The National IOR Centre of Norway and its industry partners: ConocoPhillips Skandinavia AS, Aker BP ASA, Eni Norge AS, Equinor ASA, Neptune Energy Norge AS, Lundin Norway AS, Halliburton AS, Schlumberger Norge AS, Wintershall Norge AS, and DEA Norge AS.

Last, but not least, I am greatly indebted to family, friends, and all others who have meant something important to me during the last four years. Unfortunately, I cannot mention all of you either, but if you should ever happen to read this, I trust you know who you are. An especially big thank you goes to my parents, for moral support, and for never letting me give up. On that note, I am very grateful to my father, for offering to discuss my work with him, and for patiently listening to all my frustrations. Finally, thanks to my brother Bernt Ivar, for helping with the final proofreading of the thesis, and for always being a good

Acknowledgements

friend.

Abstract

Reservoir simulators are frequently applied to interpret laboratory findings, and to assess the likely performance of various suggested injection strategies at the field. For example, when studying potential methods of enhanced oil recovery (EOR), a sensible working strategy seems to be this: first, any proposed working mechanism should be tested versus experimental data on smaller scales (usually, the core scale), before subsequently being investigated at field conditions. To improve the predictive accuracy of such endeavours, especially when attempting to upscale from the lab to the field, it is important to include sufficient granularity in the mathematical models that are used to describe the fluid flow.

The present thesis primarily intends to contribute towards the first part of the above stated workflow, though the second part is also tentatively addressed. To this end, the main objective has been to improve upon the mathematical modelling of polymer injection, i.e., to understand better how the addition of flexible polymer macromolecules to the brine can affect fluid transport inside porous rocks. A new simulation model for polymer flooding has recently been implemented into the IORCoreSim simulator. Several sets of laboratory (one phase) polymer floods, conducted under both transient and steady-state conditions, were history matched using the model.

An important fact to consider in all of the experiments was that the employed polymer solutions are non-Newtonian fluids. As a consequence, the apparent viscosity of the solutions could not be taken as a constant at a given temperature and pressure, at least not beyond a certain shear rate. Instead, it must be allowed to vary depending on the local rate, and it can be substantially influenced by both the rock and fluid properties (e.g., permeability and solvent ion composition). Two flow regimes could be identified as especially important for understanding the lab data, both occurring at elevated shear rates inside the porous medium: an apparent shear thickening flow resistance, and mechanical degradation (chain scission) of polymers. In the presented thesis work, a strong emphasis was placed on studying these two phenomena, because they both hold the potential to be real show stoppers when it comes to field implementation of polymer flooding. Also, mechanical degradation is presently not accounted for in most available reservoir simulation frameworks.

In addition to shedding light on multiple sets of coreflooding data, the IORCoreSim polymer model was applied to study degradation in synthetic sector models at the field scale. It was indicated that, absent fracturing conditions, shear thickening will significantly lower well injectivity, and that severe degradation is probable even when injecting into moderate to high permeability formations. However, as these effects are only expected in the near well bore area, field scale simulators only need to account for them in the well blocks. Further work should

Abstract

concentrate on developing effective well models for polymer flooding. Also, more research is required to fully understand the impact of factors such as temperature and salinity on the polymer behaviour.

List of Papers

Paper I

Nødland, Oddbjørn, Lohne, Arild, Stavland, Arne, Hiorth, Aksel. 'A Model for Non-Newtonian Flow in Porous Media at Different Flow Regimes'. In: *ECMOR XV-15th European Conference on the Mathematics of Oil Recovery* (2016).

Paper II

Ringen, Irene, Stiegler, Hjørdis, Nødland, Oddbjørn, Hiorth, Aksel, Stavland, Arne. 'Polymer flooding in sandpacs with a dual-porosity'. In: *Society of Core Analysts* (2016).

Paper III

Nødland, Oddbjørn, Lohne, Arild, Hiorth, Aksel. 'Mechanical Degradation of Polymers at the Field Scale-A Simulation Study'. In: *IOR 2017-19th European Symposium on Improved Oil Recovery* (2017).

Paper IV

Lohne, Arild, Nødland, Oddbjørn, Stavland, Arne, Hiorth, Aksel. 'A model for non-Newtonian flow in porous media at different flow regimes'. In: *Computational Geosciences*, **21:5-6** pp.1289-1312 (2017).

Paper V

Nødland, Oddbjørn, Lohne, Arild, Stavland, Arne, Hiorth, Aksel. 'Simulation of polymer mechanical degradation in radial well geometry'. Resubmitted, following major revision, to: *Transport in Porous Media* (2018).

Paper VI

Nødland, Oddbjørn, Ringen, Irene, Lohne, Arild, Stavland, Arne, Hiorth, Aksel. 'Flow of polymer fluids in a dual porosity sand pack: Experiments and simulations'. To be submitted (2018).

Contents

Acknowledgements	i
Abstract	iii
List of Papers	v
Contents	vii
List of Figures	ix
1 Introduction	1
1.1 Background and motivation	1
1.2 Research aims and objectives	4
1.3 Organization of thesis	4
2 Polymer flooding: Background and challenges	7
2.1 Proposed working mechanisms of polymer flooding	8
2.2 Description of EOR polymers	11
2.3 Practical challenges for field scale polymer flooding	12
3 Bulk rheology of polymer solutions	15
3.1 Newtonian fluids	15
3.2 Non-Newtonian fluids	16
3.3 Apparent shear thinning of EOR polymer solutions	16
4 Polymer rheology in porous media	19
4.1 Correlating bulk and in-situ polymer behaviour	21
4.2 Apparent shear thickening	23
4.3 Mechanical degradation in porous media	26
4.4 Inaccessible pore volume effects	27
4.5 Polymer retention in porous media	28
4.6 Salinity effects	29
5 Reservoir simulation background	31
5.1 Generic conservation law	32
5.2 Types of reservoir simulation models	32
5.3 Immiscible, two-phase flow equations	33
5.4 One-phase incompressible flow	35
5.5 IORCoreSim implementation approach	36

Contents

6	Summary of papers	47
6.1	Paper I	47
6.2	Paper II	48
6.3	Paper III	49
6.4	Paper IV	50
6.5	Paper V	50
6.6	Paper VI	51
7	Future prospects	53
	Bibliography	55
	Papers	68
I	A Model for Non-Newtonian Flow in Porous Media at Different Flow Regimes	71
II	Polymer flooding in sandpacks with a dual-porosity	99
III	Mechanical Degradation of Polymers at the Field Scale-A Simulation Study	115
IV	A model for non-Newtonian flow in porous media at different flow regimes	139
V	Simulation of polymer mechanical degradation in radial well geometry	167
VI	Flow of polymer fluids in a dual porosity sand pack: Experiments and simulations	199

List of Figures

- 2.1 Effect of mobility ratio on fractional flow (Buckley-Leverett) . . . 10
- 2.2 Structure of HPAM molecule 12

- 3.1 Example of HPAM bulk viscosity 17
- 3.2 Illustration of the end-over-end tumbling cycle for dumbbell polymers 17

- 4.1 Examples of non-linearity between pressure drop and flow rate for polymer solutions flooded through porous media 20
- 4.2 Example of core resistance factor versus flow rate, for both a synthetic and a biological polymer flooded through porous media 21
- 4.3 Visualization of flow lines inside a porous rock 22
- 4.4 Example of bulk vs in-situ rheology (HPAM) 23

- 5.1 Flowchart for an IORCoreSim simulation 45

Chapter 1

Introduction

1.1 Background and motivation

While in the long run fossil fuels are projected to give way to low carbon emission technologies, presently these alternate energy sources contribute in only a fairly limited way to the global energy supply (BP 2018). At the same time, the world population is expected to continue to increase until at least the end of the century (Gerland et al. 2014), fewer new oil reservoirs are discovered, and production from mature fields are declining. Worldwide, the average value of the oil recovery factor is in the range 20-40 % (Muggeridge et al. 2014). On the Norwegian Continental Shelf (NCS) the situation is better, with an average recovery factor of approximately 46 % (Åm et al. 2010), and similar numbers have been estimated for the UK Continental Shelf (UKCS) (Oil & Gas Authority 2016; Oil & Gas Authority 2017b). Even so, unless new and smart solutions are found, the majority of the remaining oil reserves on the NCS are projected to stay in the ground when production is eventually ceased (Norwegian Petroleum Directorate 2017).

To meet the world's demand for energy, while at the same time limiting the environmental impact, it is important to utilize the remaining petroleum resources as efficiently as possible. To this end, the use of Enhanced Oil Recovery (EOR) techniques could play a significant role in extending the lifetime of the fields. According to (Lake 1989, p.1), EOR can be defined as *oil recovery by the injection of materials not normally present in the reservoir*. This definition is broader than other definitions commonly seen in the literature, wherein EOR is introduced specifically as a tertiary oil recovery method. It covers thermal recovery methods, as well as the injection of various chemicals and/or gases into the reservoir, e.g.: CO₂ injection, low salinity water flooding, polymer flooding, and surfactant flooding. EOR is regarded as less general than the related concept of IOR (Improved Oil Recovery), which encompasses all practices that improve the oil production. However, the two terms have sometimes been used interchangeably (Stosur et al. 2003).

To estimate the potential for increased oil recovery of a proposed injection strategy, numerical simulation studies play a key part of the decision making process. Reservoir simulators were first developed during the 1950s and 1960s (Watts 1997). Since that time, they have become a cornerstone of the petroleum industry, and are used alongside simpler analytical and semi-analytical models as tools to forecast production performance. With the advent of more powerful computers, the mathematical complexity and capabilities of the models have greatly increased as a function of time, especially from the 1970s and onwards (Cao 2002; Watts 1997). Additionally, much work have gone into making the

1. Introduction

models less CPU intensive, which is clearly desirable from a user perspective. That said, concerns are often raised about the predictive accuracy of reservoir simulators. Just how accurate are they when it comes to depicting fluid flow in the reservoir?

One obvious problem is the lack of detailed knowledge about the subsurface, i.e., geological uncertainty. Real reservoirs are heterogeneous, and the nature of the heterogeneity can have a large impact on fluid flow. However, input parameters to simulation models are often derived by considering an extremely small sample of the reservoir, which need not be representative of the reservoir as a whole. One obvious source of error is the use of inaccurate values for parameters that can, at least in principle, be quantified. For instance, some data may simply be incorrectly measured. Another frequently encountered challenge is the issue of how to integrate data obtained using multiple experimental techniques. Because separate methods may be based on different assumptions, and may not probe the same scales of resolution, purported macroscopic parameter values do not always agree. Then, it can be hard to know how which value is the 'correct' one for a given application.

Yet another problem is that it can be very hard to decide whether increased oil recovery seen on the core scale can be extrapolated to the field. Some reasons for this can be mentioned. First, the geometric dimensions of laboratory core samples are on the order of centimetres, which means that molecular diffusion and capillary end effects (e.g., Fjelde et al. (2015)) can heavily influence the observed macroscopic flow behaviour. In contrast, at the field scale, transport tends to be dominated by advection. Second, while coreflooding experiments are typically conducted at a limited number of flow conditions, there is much greater variability at the field, where flow rates experienced by the reservoir fluids will change significantly as a function of space and time. Also, the injected water is usually colder than the resident formation water, which means that temperature gradients will be established within the reservoir. Since temperature affects chemical reaction rates, it could impact oil recovery in a non-negligible manner. Third, there is still considerable uncertainty as to the exact working mechanisms of several proposed EOR methods; even at the core scale. When this is the case, predictive accuracy is hampered not only by insufficient and/or inaccurate input data, but additionally by the fact that the underlying mathematical framework of the model is deficient. Fourth, for any given mathematical approach there will be numerical errors arising from the choice of algorithm used to approximately solve the governing equations of the model.

With regard to the third point raised above, there seems to be a clear need for improved mechanistic models that can explain reported laboratory findings. To achieve this, simulation models exploring interactions between porous media transport and aqueous geochemistry have received increasing attention during the last decade (see, e.g., Evje et al. (2010), Evje et al. (2009), Hiorth et al. (2013), Kazemi Nia Korrani et al. (2013), Kazemi Nia Korrani et al. (2016), Madland et al. (2011), and Omekeh et al. (2012)). The development of these models have been motivated by experimental work indicating that the ionic composition of the brine can greatly influence the oil production. In particular,

it has been observed that desalination of sea water before injection into the reservoir can have beneficial consequences (Al-Shalabi et al. 2016). Still, results have not always been consistent, and the precise mechanisms responsible for the observations are unclear.

Another important area of research concerns the use of non-Newtonian polymer solutions for oil recovery, so-called polymer flooding (Sorbie 1991). It was decided relatively early that the main focus of the thesis work should be on this particular technology. There are several reasons for focusing on polymer flooding at the present moment in time. First and foremost, the method has been investigated for a long time (Chang 1978; Sandiford 1964), and is therefore regarded as a mature technology with a well understood EOR mechanism (Lake 1989; Seright 2017; Sorbie 1991). Several successful field pilots have been performed, in different countries, and with promising results¹. Long term polymer injection has been initiated at multiple onshore fields, most notably at the Daqing oil field in China. Reports from this field have been positive, suggesting an amount of incremental oil due to polymer flooding in the range of 5-15 % (Dong et al. 2008; Wang et al. 2002; Wang et al. 2009; Wang et al. 2008). On the other hand, the method has been applied almost exclusively in onshore reservoirs (Saboorian-Jooybari et al. 2015; Sheng et al. 2015; Standnes et al. 2014). More work should be done to understand how it may potentially be applied in an offshore setting as well.

Despite the long term interest in applying polymers for EOR, there are still many unresolved scientific questions. The flow of polymers in porous media is extremely complex, and a variety of physical phenomena may need to be captured in the mathematical models used to explain experimental data. While the relevant mechanisms seen on the core scale have been explored to some extent by previous researchers (e.g. Bondor et al. (1972), Delshad et al. (2008), Masuda et al. (1992), Pope et al. (1978), Pope et al. (2000), and Sorbie et al. (1987)), not all of them have been adequately addressed. In particular, few models for polymer mechanical degradation have been reported in the literature.

During the last few years, there seems to have been a resurgence of interest in the method. As examples of this, one could mention the testing of polymer flooding offshore at the Dalia field in Angola (Morel et al. 2015), the planned polymer pilot at the Johan Sverdrup field (*Johan Sverdrup-Polymer* 2018), as well as the establishment of a task force to create a polymer EOR strategy for the British sector (Oil & Gas Authority 2017a). Polymer flooding has been selected as one of the main technologies to investigate in the National IOR Centre of Norway (NIORC). Recently, researchers from Imperial College (London) were commissioned by the Norwegian Petroleum Directorate (NPD) to evaluate the potential for application of EOR at 27 of the largest oil fields on the NCS. Of the 13 EOR methods that were considered, a combination of low salinity waterflooding and polymer flooding received the highest overall score for *technical* potential (Norwegian Petroleum Directorate 2017).

¹For some recent examples see, e.g., Chiotoroiu et al. (2017), Delamaide et al. (2016), Delamaide et al. (2014), and Al-saadi et al. (2012).

To evaluate the *practical* utility of polymer flooding offshore, it is paramount that improved simulation models be developed, and are compared with experimental data.

1.2 Research aims and objectives

The present thesis seeks to make a contribution towards better predictive modelling of polymer flooding. A first step in this regard is to improve upon models for single phase polymer flow at the core scale. A next step is to consider behaviour in a small sector model at the field scale.

Simulations have been performed using the software IORCoreSim (Lohne 2018). Recently, a comprehensive polymer model was implemented into this code (Lohne et al. 2017; Nødland et al. 2016), and the thesis work has largely revolved around the testing and further refinement of the IORCoreSim polymer model. Particular attention has been placed on understanding how the phenomena of apparent shear thickening and mechanical degradation may impact the flow resistance of polymer solutions flooded through porous rocks. However, to fully describe flow at the core scale, additional mechanisms have been found necessary to include as well.

1.3 Organization of thesis

The thesis consists of two parts. The second part includes six publications (ordered chronologically): three conference papers, one published journal article, one paper resubmitted to a journal following major revision, and one in preparation for journal submission.

The first part of the thesis is structured as follows:

- Chapter 2 presents basic background knowledge on polymers and reviews their possible working mechanisms as EOR agents. Challenges with respect to field implementation of polymer flooding are discussed.
- The topic of polymer (bulk) rheology is introduced, very briefly, in Chapter 3.
- Chapter 4 supplements the previous two chapters by providing more in-depth information about polymer behaviour in porous media. In particular, an attempt has been made to put the apparent shear thickening phenomenon in a broader context.
- Chapter 5 gives a taste for the kind of mathematics needed to develop reservoir simulators. Selected aspects of the theory are reviewed more fully than others, such as the classical fractional flow theory that are commonly found in textbooks on reservoir engineering. An overview of the particular simulation approach taken in IORCoreSim is given.

- Chapter 6 contains summaries of the individual articles presented in the second part of the thesis.
- The first part is rounded off in Chapter 7, by taking a step back and looking at the 'bigger picture'. Some possible avenues for future research are suggested.

Chapter 2

Polymer flooding: Background and challenges

Polymers are macromolecules, large molecules composed of many repeating subunits (monomers), which are often connected to each other by covalent chemical bonds (Colby et al. 2003). The name polymer stems from ancient Greek and literally means *many parts*. They are ubiquitous in nature, and examples that should be familiar to everyone are biological polymers found within the cell of every known living organism, such as DNA molecules and proteins. Synthetic polymers are also indispensable, being used in a vast number of products common to everyday life (e.g., plastics).

The number of monomers in a single polymer chain can be extremely large; a value on the order of 10^5 or beyond is not uncommon, even for man-made products (De Gennes 1979). Because of this fact, a large variety of conformational structures can be exhibited by these molecules when they are dissolved in an aqueous solution, and it gives rise to flow properties unlike those of fluids composed of smaller particles. Clearly, the flow behaviour will be influenced by the specific chemical structure of the polymer as well, through its impact on possible polymer-polymer and polymer-solvent interactions. Furthermore, when polymer solutions are flooded through a porous rock, the situation is made more complex still, because then the polymer can react with the rock in several interesting ways.

That said, after more than 50 years of studies (Saboorian-Jooybari et al. 2015; Standnes et al. 2014), the macroscopic effect most relevant for oil recovery seems well understood: Polymers work as *mobility control agents*. By adding large water-soluble polymer molecules to the injection brine, the flow resistance of the water is increased, thereby lowering the mobility ratio between the displacing aqueous phase and the displaced oil phase, which can result in an enhanced sweep of the reservoir. Water mobility reduction is achieved primarily through an increase in the *apparent viscosity* of the polymer solution (chapter 4). However, if polymer retention inside the rock is significant, associated permeability reduction will contribute in the same direction.

It is the goal of section 2.1 of this chapter to elaborate on how polymer flooding may enhance oil recovery. Only the big picture will be addressed, and in subsequent parts of the thesis the main focus will be on polymer behaviour in 1-phase flow ¹. In section 2.2, the most commonly applied EOR polymers are introduced, along with a short mention of some recent developments. Finally, in

¹For further details on multiphase polymer floods, several excellent textbooks are available, e.g., Lake (1989), Sheng (2010), and Sorbie (1991).

section 2.3, practical challenges associated with implementing a polymer flood at the field scale will be reviewed.

2.1 Proposed working mechanisms of polymer flooding

The ultimate goal of any EOR process is to increase the oil recovery factor, beyond that which could be obtained with conventional methods such as plain waterflooding. One way to achieve this is to mobilize oil that has been trapped by capillary forces, to lower the residual oil saturation S_{or} . The fluid flow in the reservoir is governed by a combination of viscous, capillary, and gravity forces. At the pore scale, capillary forces tend to dominate, and oil may be trapped in the form of, e.g., disconnected clusters (ganglia) surrounded by water (Blunt 2017; Dullien 1992). To mobilize immobile oil, the balance between viscous and capillary forces needs to be adjusted. This balance can be quantified by a dimensionless capillary number, often defined as (Blunt 2017)

$$N_c = \frac{u\mu}{\sigma}, \quad (2.1)$$

where u is the (Darcy) velocity of the injected phase, μ is fluid viscosity, and σ is the interfacial tension between the displacing and displaced phases. For standard waterflooding conditions, the value of N_c is very low, $N_c \sim 10^{-6}$ (Sorbie 1991). Although variations between different lithologies have been found, it is generally accepted that the capillary number must be increased by several orders of magnitude in order to mobilize previously trapped oil (Lenormand et al. 1988; Morrow et al. 1988). Accordingly, while adding polymers to the injection brine will enhance the magnitude of the viscous forces, the resulting increase is regarded as too small to lower S_{or} (Sorbie 1991).

Recently it has been argued that the elastic nature of certain synthetic polymer solutions can be used to mobilize previously immobile oil (e.g., Clarke et al. (2016), Qi et al. (2017), and Wang et al. (2000)). However, the precise mechanisms by which this is thought to occur are not well understood. It is also unclear whether such observations are relevant to consider at most practical field conditions (Vermolen et al. 2014).

Another possibility is to speed up the oil production. Frequently during water injection, substantial volumes of mobile oil are bypassed. This can be the consequence of large scale heterogeneities that are present in the formation, which may lead to stratification and channeling of the reservoir fluids (Sorbie 1991). Poor recovery may also occur when fractures are opened up near injectors (Dyes et al. 1958). Unstable displacements can be a problem even in relatively homogeneous reservoirs, because of the phenomenon known as *viscous fingering* (Homsy 1987). Viscous fingering refers to the formation and development of instabilities at the interface between two fluids, and it is known to happen when a low viscosity fluid is injected to displace a fluid of higher flow resistance. As such, it is a big concern when waterflooding very viscous oil reservoirs.

To summarize, the main challenge with waterflooding is that the oil recovery process quickly becomes very inefficient, because the water tends to move along

paths of 'least resistance' from injector to producer (Craig 1971). One way to accelerate production, and thus make the process more profitable, is to lower the mobility of the injected water phase (section 2.1.1). Traditionally, this has been the main rationale for considering polymer flooding as an EOR method (Sorbie 1991).

2.1.1 Oil recovery factor and the mobility ratio concept

To understand how the addition of polymers may improve reservoir sweep, a few more concepts need to be introduced. The total oil recovery factor E_O is here defined as the amount of oil recovered, divided by the original (estimated) amount of oil in place (OOIP). It is common to decompose the recovery factor into a product,

$$E_O = E_D \cdot E_V, \quad (2.2)$$

where E_D is the linear displacement efficiency, and E_V is the volumetric sweep efficiency (Craig 1971; Lake 1989). The former factor describes the fraction of oil produced from the pores invaded by the injection brine, while E_V is ratio of the contacted oil to OOIP. The volumetric sweep efficiency can be further decomposed into areal and vertical sweep efficiencies E_A and E_Z , so that

$$E_O = E_D \cdot E_A \cdot E_Z. \quad (2.3)$$

However, it should be remarked that these factors are interdependent, and can thus be hard to tease apart (Lake 1989). For a linear 1D core flood, in which all of the mobile oil comes into contact with the brine, the recovery factor is given by E_D . In such a situation, Buckley-Leverett theory (Buckley et al. 1942; Welge 1952) can be applied to gain a good understanding of how polymer flooding will affect recovery. In the classical case, the immiscible flow of water and oil is considered, and gravity and capillary pressure effects are neglected, which makes recovery a function of time and fluid mobilities only (see description provided in Chapter 5, e.g., Eq. (5.16)). The increased oil production induced by polymer flooding can then be interpreted as a consequence of a rightward shift in the fractional flow curve. That is, recovery is enhanced because of a higher water front saturation moving through the system, which results in a delayed onset of excessively high water cuts. In the theoretical limit of an infinite injection period, the final oil production would be the same during polymer flooding as for ordinary waterflooding, yet as a practical matter, the addition of polymers can make it economically feasible to extract more of the mobile oil within a realistic time window.

An illustration of this mechanism is provided in figure 2.1. In the figure, the endpoint mobility ratio ²

²In general when attempting to correlate mobility ratio and sweep efficiency, the endpoint values would not be used, see, e.g., discussions in Lake (1989) and Sheng (2010).

2. Polymer flooding: Background and challenges

$$M^* = \frac{\mu_o k_{rw}^*}{\mu_w k_{ro}^*}, \quad (2.4)$$

was varied by changing the viscosity ratio between water and oil. For a given choice of M^* , the red stars represent the front saturation and the average water saturation at time of breakthrough, as obtained from the Welge tangent method (Welge 1952). In this example case, it is clear that by increasing μ_w , significantly more oil will be produced during the first pore volume of injection. As is further seen from figure 2.1, for applications in which the mobility ratio is already low, the linear displacement efficiency can be quite high; it is not uncommon that E_D is in the range 50-80 % (Lake 1989). Nevertheless, because the total oil recovery is a product of both E_D and E_V , field scale recovery factors tend to be much lower than this (Muggeridge et al. 2014).

It should be remarked that for polymer flooding, the situation is somewhat more complicated than in the classical Buckley-Leverett theory, even when all simplifying assumptions are retained concerning no gravity, capillarity etc. During polymer flooding, a secondary shock front in the water saturation will tend to form, and the standard Buckley-Leverett analysis has to be slightly modified (Patton et al. 1971; Pope 1980). Furthermore, when adsorption is significant, consequent permeability reduction effects will lower the water mobility beyond the reduction caused by the viscosity change. If degradation is also occurring, the polymer properties might be spatially varying from inlet to outlet in a non-negligible manner ³ (Åsen et al. 2018).

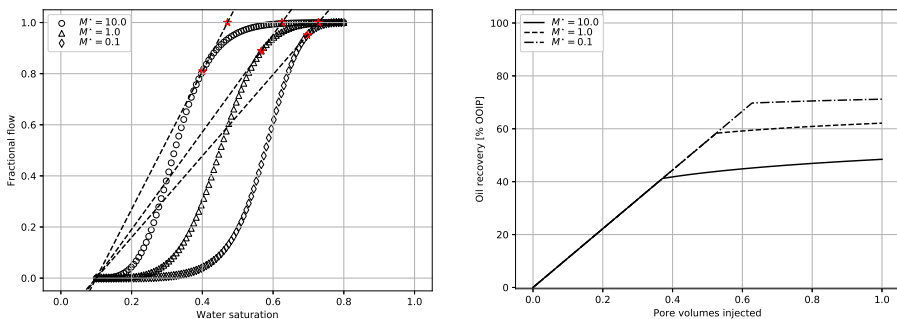


Figure 2.1: Left plot: Example of how increasing the viscosity ratio between water and oil can affect a fractional flow curve. Here, relative permeabilities were calculated using modified Brooks-Corey (power-law) functions, and the viscosities were chosen so as to obtain endpoint mobility ratios of respectively, $M^* = 10$, 1, and 0.1. Right plot: Corresponding oil recovery factors versus time.

Under ideal circumstances, polymer flooding can also be applied to combat poor volumetric sweep. For instance, lowering the mobility of the displacing water

³A short exploration of possible length effects of mechanical degradation is provided in Paper [V].

can help to increase areal sweep (Aronofsky 1952; Dyes et al. 1954; Sorbie 1991). This can happen both as a result of increasing the local displacement efficiency, by the same mechanism as described above, and by suppressing viscous fingering (Lake 1989). In terms of actual field implementation, continuous polymer injection is usually regarded as too expensive, and it is common to inject a finite amount of polymer into the reservoir, followed by a period of water injection. Then, it is vital that the injected polymer volume is sufficiently large, so that the chase water does not finger excessively into the polymer slug, and ends up ruining the economics of the project. For very heterogeneous formations, yet another way of increasing E_V can come about as a result of re-distributing the fluids between adjacent geological layers. Specifically, by lowering the mobility of the injection brine, more water can be diverted into low permeability zones, thus contacting more of the oil, and delaying water breakthrough (Seright et al. 2012).

It should be kept in mind that, compared with the linear displacement efficiency, E_V is much harder to quantify. In addition to the determinants of E_D , volumetric sweep is influenced by a myriad of factors, such as rock heterogeneity (areal and vertical), well pattern and well spacing, initial saturation distributions, and gravitational segregation of fluids (i.e., fluid densities) (Lake 1989). For polymer flooding in particular, effects of polymer degradation processes and the non-Newtonian fluid rheology will further complicate matters. Because of this, it is not straightforward to understand how a given polymer injection strategy will influence oil recovery at the field, which highlights the need for simulation studies to investigate different scenarios. For instance, injection of shear thinning fluids into very heterogeneous formations will exacerbate channeling tendencies already present, or might induce flow instabilities, and can thus in practice be detrimental for the oil recovery potential (Al-Sofi et al. 2009).

2.2 Description of EOR polymers

Historically speaking, the two most common polymer types considered for EOR are a) the biopolymer xanthan, produced through fermentation by microorganisms, and b) synthetic polymers based on the polyacrylamide (PAM) molecule, mostly partially hydrolyzed polyacrylamide (HPAM) (Sorbie 1991). Both xanthan and HPAM are polyelectrolytes, meaning that they contain ionizable groups along the polymer chain backbone. However, while biopolymers tend to exhibit a rigid rod conformation when dissolved in aqueous solutions, HPAM molecules are random coil polymers.

In recent years, a new class of polymers has started to attract the attention of researchers, the so-called *associative polymers* (Taylor et al. 1998). These polymers are hydrophilic long-chain molecules that contain a small number of hydrophobic groups randomly distributed along the polymer chain backbone. When dissolved in water, the hydrophobic groups will tend to aggregate and may form, e.g., three-dimensional networks, which results in a complex flow behaviour. However, this work considers synthetic polymers that are not of the

2. Polymer flooding: Background and challenges

associative type, mainly HPAM. The chemical structure of HPAM is depicted in figure 2.2.

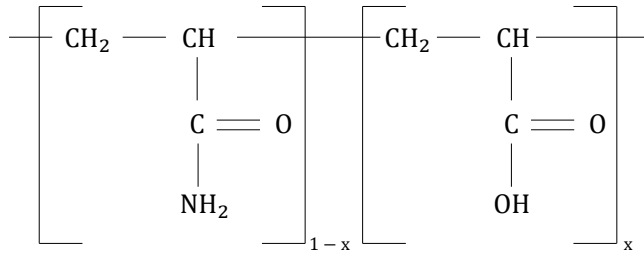


Figure 2.2: Structure of HPAM molecule. The fraction x of carboxyl acid groups is known as the degree of hydrolysis. When dissolved in water, protons may be released, giving carboxylate ions (COO^-).

In Paper [VI], a co-polymer of acrylamide and ATBS (Acrylamido Tertiary-Butyl Sulfonic acid) was employed to study polymer flow in a dual porosity medium. This type of polymer is known to be less prone to mechanical degradation than HPAM, as well as being more tolerant towards both temperature and reservoir salinity (Stavland et al. 2013; Thomas et al. 2012). However, it is also more costly to manufacture.

2.3 Practical challenges for field scale polymer flooding

As mentioned in the introduction, polymer flooding has rarely been implemented offshore. The reasons for this are multifactorial, but obviously heavily dependent on platform logistics (Delamaide et al. 2015). One significant hurdle can simply be the space requirements. For field scale polymer floods, huge volumes of polymer solution have to be injected into the reservoir to ensure an efficient displacement. This polymer has to be stored at, or near, the oil platform. To obtain the desired fluid properties, the polymer solutions need to be adequately handled and prepared before injection, which places even further demands on personnel and platform infrastructure. Commonly, synthetic polymers are supplied in powder form, but they can also be shipped in the liquid state as emulsions (Jouenne et al. 2016). Naturally, more prosaic economic concerns have to be factored into the equation as well, e.g., the cost of buying and transporting the chemicals, as well as the influence of general driving forces such as tax rates and crude oil prices on petroleum investment activities.

Environmental sustainability is a big concern when it comes to field implementation of polymer flooding, particularly the question of how to handle back-produced polymer. Currently, many EOR polymers are listed as red chemicals in Norwegian regulations, meaning that they are only to be used if they are deemed *necessary* for technical and safety reasons. This is because of the many uncertainties regarding their impact on the marine environment when discharged into the sea. In general, all chemicals used for petroleum production

have to be tested for ecotoxicological properties, such as their biodegradability or acute toxicity (Petroleum Safety Authority Norway 2018, Section 62). The conventional solution to the problem of back-produced polymer is to inject the polymer back into the reservoir, but this poses its own set of challenges, e.g., with regard to requirements for water treatment plants and surrounding technology. Clearly, such demands increase the cost of the operations and, in any event, it may not be practically possible to prevent some of the chemicals from leaking into the sea.

Yet another potential show stopper is the issue of well injectivity (Glasbergen et al. 2015). Injecting very viscous fluids may place undue restrictions on the well pressures needed to operate at economic injection rates, and for synthetic polymer types that exhibit dilatant behaviour in the near well zone (apparent shear thickening), this is an especially salient concern. Though a continuing worry, practical experience from both onshore and offshore fields have frequently revealed better injectivity than feared beforehand. In many cases, the explanation seems to be that polymer injection was performed under fracturing conditions (Clemens et al. 2013; Manichand et al. 2013; Seright et al. 2008).

An important difference from the case of onshore reservoirs has to do with the cost and placement of wells. First, offshore wells are much more expensive than their onshore counterparts. Second, well spacings are significantly larger in the offshore setting; often on the order of several hundred metres to a few kilometres. The residence time of the polymer in the reservoir will therefore increase substantially compared with the case of onshore polymer flooding, which impacts the project economics by requiring large capital investments a long time before results can be expected to be seen.

Large residence times also raise concerns about the stability of the polymer molecules in the reservoir. It is well documented that EOR polymers can be very susceptible to various forms of degradation (Sorbie 1991). For instance, at lower temperatures, biopolymers are particularly prone to molecular breakdown as a result of bacterial attacks (Bragg et al. 1983; Hou et al. 1986). To mitigate this, biocides may be added to the injection brine. On the other hand, synthetic polymer molecules seem to be much more resistant towards microbial degradation. The low biodegradability of HPAM molecules is a major reason why it has earned the status of a red chemical in Norwegian legislation.

The viscosifying potential of a polymer solution can also be impeded by chemical and thermal degradation processes. In the short term, the presence of contaminants may lead to rapid oxidative degradation of the polymer chain backbone. For example, studies have consistently revealed that even small amounts of dissolved oxygen present in the water can lead to significant reduction in polymer solution viscosity (e.g., (Levitt et al. 2011b; Yang et al. 1985)). The degradation is probably not caused by the oxygen itself, but by the presence of other agents, e.g., ferrous iron Fe^{2+} (Knight 1973). When oxygen is present, very low concentrations of iron may lead to rapid chain scission, even at low temperatures. The concentrations of alkaline species such as carbonate and bicarbonate have also been shown to influence the chemical stability of polymer solutions, although the precise mechanisms are unclear (Levitt et al. 2011b). The most important

2. Polymer flooding: Background and challenges

action to prevent oxidative degradation is to ensure low amounts of oxygen in the injection facilities, and near the injector as the polymer enters the formation (Seright et al. 2010). One way to do this is to add oxygen scavengers to the injected water. However, care has to be taken when preparing the solutions because certain combinations of chemicals (e.g., certain combinations of biocides and oxygen scavengers) may actually increase the chemical degradation (Shupe 1981).

On longer timescales, spontaneous hydrolysis reactions might become a major problem, particularly in brines where the divalent ion content is high, and at elevated temperatures (Levitt et al. 2011a; Ryles 1988). Several properties of the polymer solution may be affected by increased hydrolysis, e.g., polymer adsorption levels and tolerance to shear forces (Sorbie 1991). Some degree of hydrolysis seems beneficial (Stavland et al. 2010), but as the process continues, the net effect of continued hydrolysis is detrimental for the EOR potential. In extreme cases, a cloud point is reached, and the polymer molecules will precipitate out of solution (Davison et al. 1982; Moradi-Araghi et al. 1987). Studies have revealed the effect of various divalent ions to be different; for example, the presence of calcium ions has more of an adverse impact than magnesium ions (Ryles 1988). Although clearly important for field scale implementation of polymer floods, the issues of chemical and thermal degradation have not been investigated in the present work, and will not be mentioned further.

Another form of degradation, which mainly poses a threat when employing synthetic, high molecular weight polymer types, is mechanical degradation (Zaitoun et al. 2012). This term refers to the breakdown of covalent bonds along the polymer chain backbone as a consequence of large mechanical stresses being applied to the molecules. To limit the extent of mechanical degradation, it is critical to select the proper polymer injection facilities. Otherwise, severe degradation can occur during polymer solution mixing, and in inside equipment such as chokes and valves (Stavland et al. 2016). In the reservoir, it is primarily an issue in the near well regions, where the flow rates are highest. If mechanical degradation occurs, it will improve the well injectivity, albeit at the cost of a permanent reduction in the flow resistance of the polymer solution. This was exemplified by results from the recent polymer pilot at the Dalia field in offshore Angola (Morel et al. 2015). After polymer injection had been conducted for some time, sampling of fluids downstream of the injector revealed a severe loss in low shear bulk viscosity, which was attributed to degradation close to the sandface. The topic of mechanical degradation has been a major focus of the work done in this thesis.

Before closing the chapter it is noted that, though degradation is mostly regarded as negative, it could be envisaged to have some positive consequences as well. For instance, it could be argued that as long as the injected polymer achieves its designated purpose to enhance the displacement efficiency, some degradation within the reservoir could mitigate challenges associated with back produced polymer (Al Kalbani et al. 2014).

Chapter 3

Bulk rheology of polymer solutions

Rheology is the *study of flow and deformation* (Macosko et al. 1994). An important distinction is made between fluids that are Newtonian, and fluids that are not.

3.1 Newtonian fluids

Water and oil can be regarded as Newtonian fluids, which means that at a given pressure and temperature, there is a linear relationship between stress and rate-of-strain. This is expressed by Newton's law of viscosity, generally formulated as a tensor equation as ¹

$$\bar{\tau} = -\eta \cdot \bar{\dot{\gamma}}. \quad (3.1)$$

in which $\bar{\tau}$ is the stress tensor, $\bar{\dot{\gamma}}$ is the rate-of-strain tensor, and the constant of proportionality η is known as the viscosity. The rate-of-strain tensor can be written in terms of the velocity gradient tensor $\overline{\nabla \mathbf{v}}$ as

$$\bar{\dot{\gamma}} = \overline{\nabla \mathbf{v}} + \overline{\nabla \mathbf{v}^\dagger}, \quad (3.2)$$

with the magnitude of the tensor being known as the shear rate, $\dot{\gamma}$. In simple shear flow, the viscosity is related to shear stress $\tau = \tau_{xy}$ and shear rate via

$$\tau = \tau_{xy} = -\eta \cdot \frac{dv_x}{dy} = -\eta \cdot \dot{\gamma}. \quad (3.3)$$

Bulk flow of a Newtonian incompressible fluid can be described mathematically by the continuity equation (conservation of mass)

$$\nabla \cdot \mathbf{v} = 0, \quad (3.4)$$

together with the celebrated Navier-Stokes equations, derived from Newton's second law of motion by applying a momentum balance to an infinitesimal fluid element. In tensor notation, these equations can be written as (Bird et al. 1977)

$$\rho \frac{D\mathbf{v}}{Dt} \equiv \rho \frac{\partial \mathbf{v}}{\partial t} + \rho \mathbf{v} \cdot \nabla \mathbf{v} = -\nabla \cdot \bar{p}\bar{I} - \nabla \cdot \bar{\tau} + \rho \mathbf{f}, \quad (3.5)$$

in which ρ is the fluid density, \mathbf{f} is a body force acting on the fluid (e.g., gravity), \mathbf{v} is fluid velocity, $\bar{p}\bar{I}$ is pressure, and $\bar{\tau}$ is given by Eq. (3.1).

¹Here, the sign convention employed by Bird et al. (1977) is used.

3.2 Non-Newtonian fluids

In contrast with the case of water and oil, polymer solutions cannot usually be described by a single viscosity value (Bird et al. 1977). To account for this *non-Newtonian* behaviour, it is common to modify Eq. (3.1) by making the viscosity term shear dependent. If this approach is taken, a suitable functional relationship between η and $\dot{\gamma}$ needs to be established. Generally, a proposed mathematical relationship between stress and rate of deformation is referred to as a constitutive relation.

The flow properties of polymer solutions can be characterized mathematically through the measurement of various *material functions*. The most commonly reported such function is the steady shear viscosity, hereby referred to simply as the (bulk) viscosity of the solution. Two standard ways to measure this quantity are by using 1) a cone-and-plate rheometer, or 2) a capillary tube rheometer.

3.3 Apparent shear thinning of EOR polymer solutions

For EOR polymers, the most frequently observed deviation from Newton's law of viscosity is apparent shear thinning, i.e., the trend of a declining viscosity with increasing shear rate. This is the case for both synthetic and biological polymer types, though the magnitude of the effect is expected to be greater for polymers which exhibit a rigid rod structure (Sorbie 1991). An illustration of shear thinning is provided in figure 3.1, which shows cone-and-plate rheometer data for an HPAM polymer dissolved in a synthetic sea-water (SSW) brine, at two different polymer concentrations. The displayed viscosity curves are typical for these polymers: a relatively constant plateau is observed at low shear rates (Newtonian flow regime), followed by a marked decrease in viscosity with increasing levels of shear (shear thinning flow regime).

Physically, shear thinning is thought to arise as a consequence of the polymer molecules aligning in the direction of the flow field. As shear rates increase, the molecules are exposed to drag forces sufficiently large so as to overcome the entropic Brownian motion, which results in less frictional interaction between particles in the solution. Though it is by no means clear how to link microscopic behaviour to the measured macroscopic material functions, qualitatively this picture seems to be supported by recent experimental and theoretical developments within the field of polymer science. For instance, the behaviour of individual DNA polymers in steady shear flow has been probed by video fluorescence microscopy methods, as well as by Brownian dynamics simulations (Shaqfeh 2005; Smith et al. 1999). Several such studies have investigated the end-over-end tumbling motion of polymeric particles, which is the net result of advective processes in the flow direction, and diffusion in the gradient direction (Schroeder et al. 2005). Based on statistics of polymer conformation in shear flow it has been found that, on average, the polymer molecules spend most of the time being positively aligned with the velocity field, and that the degree of alignment increases at higher shear rates. However, due to the interplay

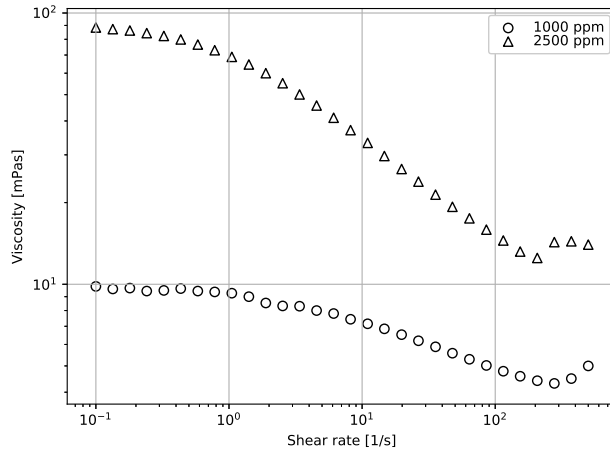


Figure 3.1: Example of polymer bulk viscosity measured in a rotational cone-and-plate rheometer (Anton Paar Physica MCR301). The polymer used was an HPAM 3630S, manufactured by SNF. The ionic composition of the SSW brine can be found in, e.g., Table 3 of Paper [IV].

between the rotational component of the flow field and thermal fluctuations, the molecules tend to flip over every now and then, and will possibly experience a sequence of intermediate states, before again becoming positively oriented along the flow field (figure 3.2).

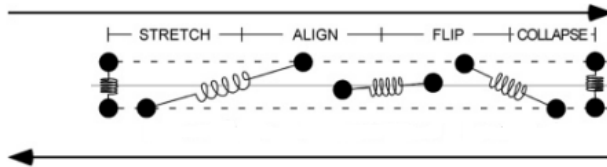


Figure 3.2: Illustration of the end-over-end tumbling of a model dumbbell polymer. According to Teixeira et al. (2005), this tumbling process can be summarized as a cycle consisting of four phases (ignoring possible re-coiling and re-stretching events): stretch, align, flip, and collapse. The figure is a slightly adapted version of Fig.13 from Teixeira et al. (2005).

Note that for the highest shear rates included in figure 3.1, there seems to be a sudden increase in viscosity. It is known that various experimental artifacts can lead to an erroneous characterization of the solution rheology, particularly at low and high shear rates (Ewoldt et al. 2015; Macosko et al. 1994; Walters 1980). For a cone-and-plate apparatus, the steady shear viscosity scales linearly with the torque \mathcal{T} on the stationary plate of the rheometer (Macosko et al. 1994). Thus,

3. Bulk rheology of polymer solutions

if the torque is overestimated, apparent shear thickening behaviour (section 4.2) will be falsely suggested.

Inaccuracies in rheometer data may be due to insufficient instrument resolution, e.g., when applying torques lower than the specified minimum value for a given instrument. Errors will also arise if inertial flow effects are significant, or in the presence of notable end or edge effects, because such occurrences violate the mathematical assumptions used to derive the viscosity. Recently, it has additionally been suggested that secondary flows may form in rheometers at high shear rates as a result of *elastic instabilities* (Howe et al. 2015).

Chapter 4

Polymer rheology in porous media

For water flowing through a porous rock sample, the equation most frequently used to relate volumetric flow rate Q and pressure drop ΔP is Darcy's law. When neglecting gravity, and assuming constant rock and fluid properties, it becomes

$$Q = \frac{kA}{\eta_s} \cdot \frac{\Delta P}{L}, \quad (4.1)$$

where L is the length of the sample, A is the cross-sectional area, η_s is the water (solvent) viscosity, and k is the absolute permeability of the rock. For non-Newtonian fluids, Eq. (4.1) does not apply, and the relation between Q and ΔP is non-linear. Two examples of this, based on data reported by Stavland et al. (2010), are provided in figure 4.1. The left plot shows experimental pressure drops ¹ for an HPAM polymer dissolved in SSW, while the right plot is for a biopolymer solution. Significant non-linearity is observed in both cases. Note that the recorded y -axis values shown in the figure are not directly comparable, because of varying permeability and polymer concentration in the two experiments. However, even when correcting for this, it seems clear that the magnitude of ΔP will be significantly larger for the HPAM polymer than for the biopolymer, at higher flow rates. Also, the left curve in figure 4.1 has an inflection point, which is not the case for the biopolymer solution curve (within experimental error).

As reservoir simulators are almost exclusively based on the the Darcean approach, it becomes necessary to operate with the concept of an *apparent*, or *in-situ*, viscosity (Sorbie 1991). For a given combination of flow rate and pressure drop ΔP , Eq. (4.1) is inverted to yield

$$\eta_{app} = \frac{k_p A}{L} \cdot \frac{\Delta P}{Q}, \quad (4.2)$$

in which k_p denotes the effective permeability for polymer flow. Because of possible polymer retention within the core, k_p may be lower than the permeability k estimated during waterflooding. Experimentally, it is found by performing a post-polymer waterflood and re-estimating the water permeability. Implicit in this procedure is the assumption that the permeability during polymer flooding is the same as the permeability to water after polymer flooding. The amount of permeability reduction after a polymer coreflood can be quantified with the residual resistance factor (Jennings et al. 1971):

$$RRF = \frac{k}{k_p}. \quad (4.3)$$

¹Both cylindrical cores had a length $L \approx 7$ cm, and the diameter was $d \approx 3.8$ cm.

4. Polymer rheology in porous media

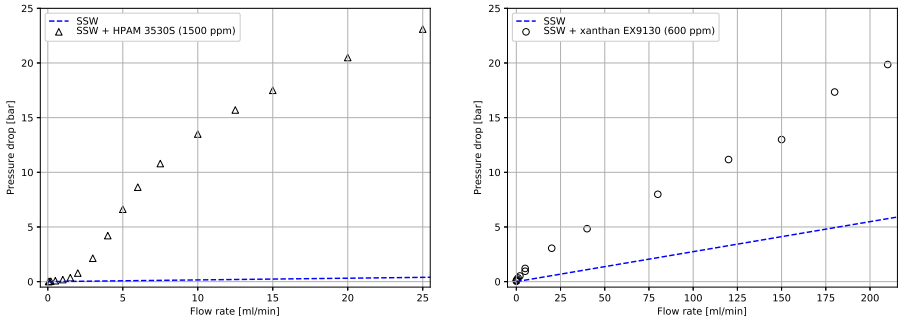


Figure 4.1: Left plot: Measured steady-state ΔP across a 721.7 mD Berea sandstone rock sample, when an HPAM polymer diluted in SSW was flooded through the core (scatter points). The blue dashed line shows theoretical values obtained from Darcy's law when no polymer is assumed present. Right plot: Steady-state ΔP measured across a 414.5 mD Berea sandstone core sample, for a xanthan biopolymer solution.

Another useful construct is the mobility reduction factor, or *resistance factor*. As the name implies, it is the ratio of mobility to water divided by the corresponding mobility to polymer. For polymer flooding and waterflooding conducted at the same flow rate, the steady-state resistance factor becomes

$$RF = \frac{\Delta P}{\Delta P_w}, \quad (4.4)$$

where $\Delta P = \Delta P_{pol}$ is the steady-state pressure drop during polymer flooding, and ΔP_w is the corresponding value for water. By combining the above definitions, it is seen that the mathematical relationship between RF and η_{app} is

$$RF = \frac{\eta_{app}}{\eta_s} \cdot RRF. \quad (4.5)$$

The data from figure 4.1 is replotted as resistance factor versus flow rate in figure 4.2. Now, the differences between the HPAM and the xanthan polymer become even clearer. The biopolymer seems to follow the same trend as it does in a lab rheometer, i.e., lower RF with increasing flow rate (apparent shear thinning). On the other hand, the data for the HPAM polymer is more complicated, and seems to evince a combination of (slightly) apparent shear thinning and apparent shear thickening behaviour. The latter term refers to the opposite trend to the one described previously, i.e., to a flow resistance that *increases* with increasing rate. Understandably, the large resistance factors seen in the left plot may lead to concerns about well injectivity if such fluids are to be injected into reservoirs offshore, because relatively large flow rates are required to sustain an economical operation at the field. However, as is also evident from figure 4.2, RF seems to reach a maximum point, after which there is a decline

with further increase in rate. This is attributed to mechanical degradation of the polymer molecules (section 4.3).

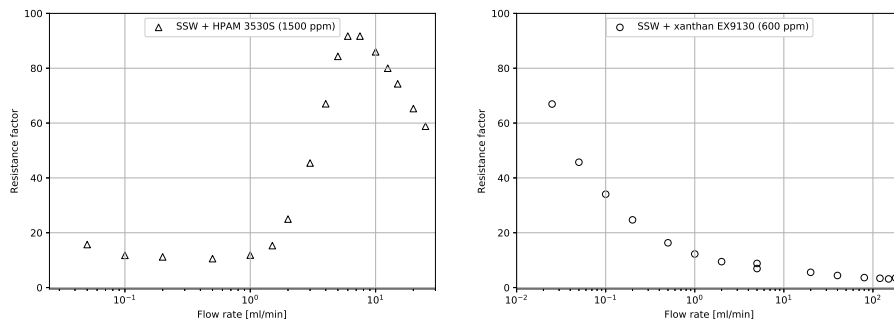


Figure 4.2: Left plot: Experimental resistance factors for an HPAM polymer solution flooded through a 721.7 mD Berea sandstone core sample. Right plot: Resistance factors for a xanthan biopolymer in a 414.5 mD Berea sandstone.

4.1 Correlating bulk and in-situ polymer behaviour

Inside a rock, the tortuous structure of the pore network leads to the establishment of a complicated flow pattern, characterized by different local flow regimes (figure 4.3). As a consequence, and in contrast with typical experiments conducted in much simpler geometries, this leads to a mixed flow field with both shearing and elongational components, that vary from point to point in space in a highly non-trivial manner. While shearing forces tend to dominate close to the walls of a mineral surface, conditions approximating pure extensional flow may occur elsewhere, e.g., near stagnation points in-between neighbouring grains. Nevertheless, as a practical matter when interpreting corefloods and simulating polymer flooding, it is standard procedure to operate with a phenomenological apparent viscosity η_{app} , as given by Eq. (4.2). Furthermore, it is common to correlate this term with a suitably defined *apparent shear rate in porous media* $\dot{\gamma}_{pm}$, as well as to compare the resulting η_{app} - $\dot{\gamma}_{pm}$ relationship with corresponding bulk shear viscosity curves measured in a rheometer.

In the literature, proposed expressions for $\dot{\gamma}_{pm}$ have almost invariably been based on the capillary bundle model of the porous medium, which makes the shear rate proportional to the Darcy velocity of the water phase, and inversely proportional to the square root of the product of permeability and porosity (e.g., Cannella et al. (1988), Christopher et al. (1965), Teeuw et al. (1980), and Wreath et al. (1990)). The capillary bundle approach has worked fairly well in many practical situations, despite its known shortcomings when it comes to accurately depicting flow in realistic porous media Sorbie (1991). This approach was also taken in the present work, and for 1-phase flow we define:

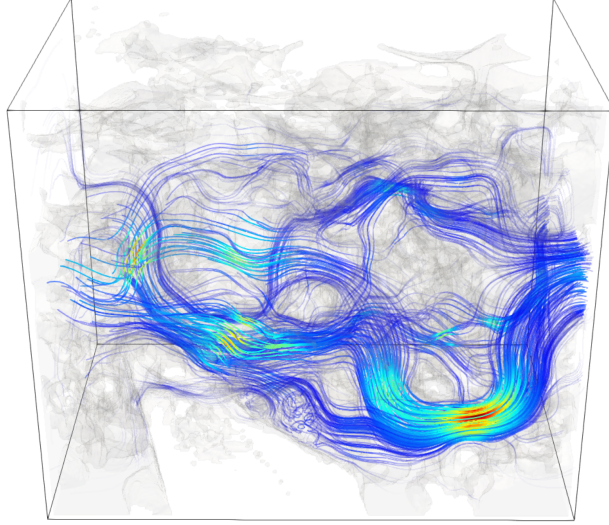


Figure 4.3: Visualization of flow lines in a pore scale representation of a porous rock sample. The figure has previously been printed in Okstad (2018) and NIORC (2018).

$$\hat{\gamma}_{pm} = \frac{4\alpha_c u_w}{\sqrt{8k\phi}} \cdot \sqrt{\frac{R_k}{1 - IPV_0}}. \quad (4.6)$$

Appendix A.2 of Paper [IV] contains more details on this expression. However, it is remarked here that α_c is a correction factor used to correlate the in-situ and bulk rheology curves (Fletcher et al. 1991; Wreath et al. 1990).

In general, there seems to be no clear consensus about the 'best way' to correlate bulk and in-situ polymer behaviour. The difficulty stems from the fact that, while η_{app} and $\hat{\gamma}_{pm}$ are effective quantities defined to capture the macroscopic flow behaviour in a particular type of geometry, the bulk shear viscosity describes a physical property of the polymer solution in any simple shearing flow. A priori it is not obvious why there should be a simple relationship between the two.

4.2 Apparent shear thickening

As already indicated by figure 4.2, large molecular weight flexible polymer types behave differently in porous media than their more rigid counterparts. This fact is well known in the literature, and studies have repeatedly revealed enhanced flow resistance, or *apparent shear thickening*, when such polymers are flooded through cores at high flow rates (Chauveteau 1986; Heemskerk et al. 1984; Magueur et al. 1985; Pye 1964; Smith 1970; Southwick et al. 1988; Stavland et al. 2010).

The typical situation is further illustrated in figure 4.4. The figure shows resistance factors versus in-situ shear rate (Eq. (4.6)) for four HPAM polymers, of different initial molecular weight, that was diluted in SSW and flooded through successive sandstone cores at a polymer concentration of 1500 ppm. The two portions of the total flow system are denoted by Core 1 and Core 2, respectively. As indicated, a different permeability was estimated for each experiment, and there was also some variation in porosity. Observe that the data points plotted using circular markers are for the same HPAM polymer as shown in figure 3.1. By comparing the two figures it is clear that the bulk and in-situ rheologies differ markedly for this polymer.

At low shear rates, both plots in figure 4.4 indicate that the core resistance factor may be approximately constant or, possibly exhibit shear thinning behaviour. However, as was the case in figure 4.2, there seems to be a critical rate beyond which the flow resistance increases dramatically, and hence also the apparent viscosity. Moreover, when plotting RF versus shear rate, the critical rate is lower for higher molecular weight polymers.

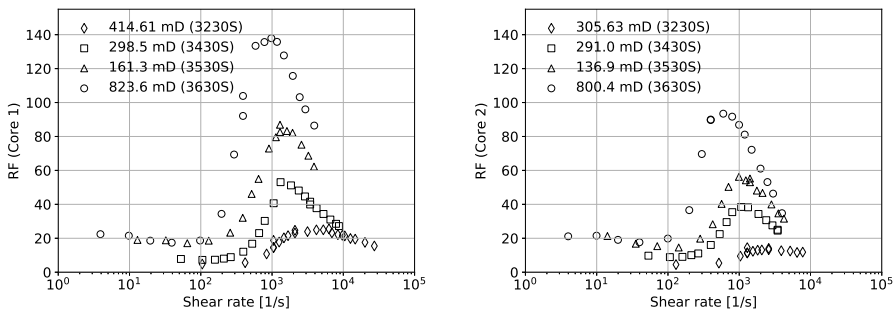


Figure 4.4: Resistance factors versus in-situ shear rate, for 4 different HPAM polymers, of differing initial molecular weight, flooded through successive sandstone cores (experimental data from Stavland et al. (2010); the figure shows the same data as in Fig. 6 of Paper [IV]). The stated initial molecular weights of the polymers were: 5 MDa (3230S), 10 MDa (3430S), 15 MDa (3530S), and 20 MDa (3630S).

The onset and duration of apparent shear thickening has been explained

4. Polymer rheology in porous media

by polymer solution elasticity. In the petroleum literature, it has traditionally been understood in terms of the notion of *elongational* or *extensional* viscosity (e.g., Chauveteau et al. (1981a), Chauveteau (1981), and Delshad et al. (2008)). The basic idea is that, as a flexible polymer molecule experiences high stretch rates inside a porous medium (e.g., near pore entrances), the molecule becomes elongated in the flow field. Given enough time, thermal motion will ensure that the molecule again reaches an approximate equilibrium coil conformation, but if the characteristic time scale of diffusion is longer than the time until another extension of the molecule occurs, it may experience a state of persistent elongation (Keller et al. 1985). The resulting build-up of stress has been thought to explain, at least a significant part of, the macroscopic apparent shear thickening effect. This conclusion has been bolstered by observations made in simpler geometries, e.g., systems of capillary tubes, or membranes connected in a series. Results from such studies have indicated a sharper dilatant effect for cases involving many successive contractions, than when only a single flow restriction is encountered by the polymer (Chauveteau et al. 1984a; Chauveteau 1981; Magueur et al. 1985).

In the polymer science literature, the initial elongation of a flexible polymer molecule in stretching flows is referred to as the *coil-stretch transition*. For idealized geometries, the transition is expected to occur when the product of stretch rate and a characteristic time scale (relaxation time) of the polymer is close to, or on the order of unity² (De Gennes 1974; Keller et al. 1985). This onset condition has often been phrased in terms of a critical value of a certain dimensionless number, such as the Deborah number or the Weissenberg number, though the precise usage of these numbers have often been conflated (Poole 2012). Originally, the Deborah number N_{De} was defined as (Reiner 1964)

$$N_{De} = \frac{\lambda}{t_{obs}}, \quad (4.7)$$

in which λ is the characteristic time scale of the polymer, and t_{obs} is a representative time scale of observation. For long observation times and/or small relaxation times, $N_{De} \approx 0$ and the solution behaves like a fluid. In the opposite extreme, $N_{De} \rightarrow \infty$ signifies solid-like behaviour. Essentially, it is a measure of how fast rheological conditions change. On the other hand, the Weissenberg number Wi quantifies the balance between elastic and viscous forces. For simple shear flow, it is defined according to (Poole 2012)

$$Wi = \lambda \cdot \dot{\gamma}. \quad (4.8)$$

For the case of porous media flow, researchers have attempted to link the onset of apparent shear thickening to a critical value of a suitably defined N_{De} (e.g., Haas et al. (1982)). However, it has not been easy to generalize findings across studies, which is probably a consequence of the complex structure of

²This is only believed to be a necessary criterion. In addition, the polymer has to experience strain for a sufficient duration of time.

the velocity field inside real rocks ³ (Gupta et al. 1985; Heemskerk et al. 1984). Another confounding factor could be polymer polydispersivity. Presumably, if the sizes of the individual molecules are very different, it would result in a spectrum of polymer relaxation times, with a corresponding spread in rates at which the molecules stretch. That said, it also seems likely that a relatively narrow fraction of the molecular weight distribution (i.e., the largest molecules) will have the most to say for the macroscopic observations.

A third complication could stem from variations in the dynamic behaviour of macromolecules. In recent decades, by using techniques such as video fluorescence microscopy, it has become possible to directly visualize the response of single long chain DNA molecules subjected to flow inside microfluidic devices (Shaqfeh 2005). The molecules in question are relatively uniform in size, which reduces difficulties in interpretation associated with polydispersivity. Although behaving like stiff rods at smaller scales, for sufficiently long chains these polymers act like flexible coils. As such, they could function as useful models for flexible polymer types in general ⁴. Typical experiments have been conducted in carefully constructed flow fields, wherein the polymer is exposed to an approximately constant stretch rate during the time of observation. Results from such studies have revealed the dynamics of polymer stretching to be highly variable among individual molecules, and very sensitive to the initial conditions (e.g., Perkins et al. (1997), Perkins et al. (1999), Smith et al. (1999), and Smith et al. (1998)) A diversity of polymer configuration types have been identified, including, but not limited to, 'dumbbells', 'half-dumbbells', 'kinks', 'folds' and 'coils'. It was observed that once a molecule gained a particular shape, it tended to persist in this configuration for a significant time period thereafter (Smith et al. 1998). Indeed, a substantial number of polymer chains did not reach steady-state conditions, even at the largest applied levels of strain, which seems to indicate that a gradual unravelling process is representative for the average behaviour (Perkins et al. 1999; Smith et al. 1998). On the other hand, when only considering the subset of molecules that did reach steady-state, it was possible to delineate a sharp coil-stretch transition, occurring at a critical Deborah number of 0.4 ± 0.1 (Perkins et al. 1997; Shaqfeh 2005; Smith et al. 1998). The wide variety of stretching behaviours seen in the above cited experiments was coined *molecular individualism* by De Gennes (1997). Similar results have been reproduced, at least qualitatively, in Brownian dynamics simulations using different theoretical models for the polymer chain, and are discussed at some length in a recent review by Shaqfeh (2005).

More recently, apparent shear thickening has been linked to various forms of elastic instabilities (Howe et al. 2015; Kawale et al. 2017), e.g., *elastic turbulence*. The term elastic turbulence was coined by Groisman and Sternberg, in analogy to the well known phenomenon of inertial turbulence, which occurs for Newtonian fluids at large Reynolds numbers, Re (Groisman et al. 2000). Inertial turbulence is characterized by chaotic fluctuations in pressure and velocity, which can

³For a more thorough discussion than what is presented here, see Chapter 6.4 of Sorbie (1991), as well as further references therein.

⁴It should be kept in mind that very large molecules are needed for the flow behaviour to be *universal*, i.e., independent of chemical structure (Tree et al. 2013).

4. Polymer rheology in porous media

result in the formation of phenomena such as eddies and vortices. Similar flow instabilities have been inferred to occur at very low Re , when studying viscoelastic polymer solutions in flows with curvilinear streamlines, such as inside specifically constructed microfluidic devices (Li et al. 2012). These instabilities are not well understood, but are thought to be produced by the accumulation of elastic stresses when polymer molecules are being stretched non-uniformly in the flow field (Pakdel et al. 1996). Mathematically, a non-linearity in the equations describing the fluid dynamics arises, because of the polymer contribution to the total stress tensor, i.e., because of the non-linear relation between stress and the rate-of-strain tensor.

As the above presentation should make clear, it is certainly not straightforward to predict how processes occurring at the molecular level will affect measurements performed at the macroscopic scale. This is especially the case for porous media flow, in which interactions between the polymer and the rock are important.

4.3 Mechanical degradation in porous media

When large molecular weight, flexible polymers are exposed to large stresses, polymer chain scission may occur. For example, in the vicinity of an injection well at the field scale, shear rates on the order of $1.0 \times 10^{-4} \text{ s}^{-1}$ and higher are not uncommon. Under such conditions, a significant subset of the covalent bonds along the polymer chain backbone may fracture, resulting in smaller molecules, and hence in an irreversible loss of apparent viscosity (Puls et al. 2016). This process, referred to as mechanical degradation⁵, has long been recognized in the petroleum literature (Maerker 1975; Martin 1986; Morris et al. 1978; Seright 1983; Southwick et al. 1988). A short review of work done within the more general field of polymer science, to elucidate mechanisms of chain cleavage in simple geometries, was provided in Paper [IV].

Signs of mechanical degradation were clearly present in the core flooding data reported by Stavland et al. (2010). This is exemplified by the right-most part of the left plot of figure 4.2. The figure reveals a significant reduction in the steady-state resistance factor at high shear rates, following a period of apparent shear thickening. Further evidence for degradation could be obtained by collecting effluent samples, and comparing bulk shear viscosity of the resulting samples with data from before polymer injection started. When this was done for the investigated HPAM polymers, a reduction in effluent viscosity was observed at high rates. Moreover, the viscosity decline correlated well with corresponding trends in the core resistance factor (see, e.g., fig. 5 of Stavland et al. (2010)).

The presently implemented simulation model for mechanical degradation was first presented in papers [I] and [IV], where it was applied to some of the experiments from Stavland et al. (2010). Subsequently, it was used to study polymer injection in radial flow at the metre scale (Papers [III] and [V]). The IORCoreSim degradation model is also briefly presented in section 5.5.4.

⁵Sometimes also described by the name *shear degradation*.

4.4 Inaccessible pore volume effects

When a polymer and a tracer is injected simultaneously into a core sample, the polymer sometimes arrives earlier at the effluent than the tracer. This can happen even in the presence of measurable polymer adsorption, which will retard the movement of the polymer front through the core (Shah et al. 1978). The behaviour has been understood as a consequence of polymer inaccessible pore volume (IPV) (Dawson et al. 1972; Shah et al. 1978), i.e., because of the large sizes of the polymer molecules in solution, which may be comparable to, or even larger than, typical pore sizes of the rock (Sorbie 1991).

One explanation for the velocity enhancement effect can be that a substantial fraction of the pore space is practically impenetrable to the polymer molecules, yet available for water and ions to flow in. Although discussed in the literature for decades, a recent series of experiments demonstrated this possibility especially clearly. The study in question, described in papers [II] and [VI], was conducted in glass columns packed with synthetic mesoporous silica sand that had significant amounts of pore volume inside the grains. The intragranular pores had an average pore size on the nanometre scale. Consequently, because the polymer was unable to enter the smallest pores, it travelled much faster through the medium than co-injected ions.

Another possibility is that there is an accumulation of polymer near the centre of the pores, where flow velocities are larger than close to the rock surface. At a fixed pressure gradient, this will cause the volumetric flux of polymer to increase, compared to when the molecules are evenly distributed within the pores. *Wall depletion* is a general phenomenon occurring in the flow of multi-phase liquids around solid boundaries; known to occur for suspensions of large particles in general, such as human blood (Fahraeus et al. 1931), and for emulsions with large droplet sizes (see Barnes (1995) for an overview). It refers to the establishment of a low viscosity layer close to the solid phase, which acts as a lubricating film for the fluid flowing there ('apparent slip effect').

An oft-repeated finding in reported polymer core floods, involving both biological and synthetic polymer types, is that the in-situ apparent viscosity in the low shear rate region may be lower than corresponding bulk viscosity values (Chauveteau et al. 1981b; Chauveteau 1982; Chauveteau et al. 1984b; Sorbie 1990; Sorbie et al. 1991). Such observations can also be rationalized by invoking the depletion layer concept. For example, Chauveteau (1982) proposed a simple two-fluid model for describing the flow of polymer solutions through a cylindrical pore. Near the walls of the pore, in an annular region of thickness δ , the effective polymer concentration was assumed lower than in the middle portion due to steric hindrance. That is, the probability that the centre of mass of a polymer molecule will be at a given position is lower close to the wall than in the centre of the pore, because of the lower degrees of freedom afforded to movement of the molecule when it is confined by the walls. By assuming constant fluid properties in each portion of the cylindrical model pore, Chauveteau (1982) derived an equation for relating the apparent viscosity of total flow through the tube to the viscosities in each region, and to the thickness of the depleted layer. The

4. Polymer rheology in porous media

equation seemed to be able to explain the trends seen in the experimental data.

Note that, depending on the situation, several potentially competing mechanisms may be responsible for wall depletion. Aside from steric hindrance, another possibility is shear-induced migration of polymers away from the walls of the pores (Agarwal et al. 1994). In IORCoreSim, only the former mechanism has been considered (section 5.5.5).

4.5 Polymer retention in porous media

Polymer retention, particularly adsorption, is yet another important factor to consider: If the movement of an injected polymer front is retarded, there will be a delay in the oil production, and more chemicals will be needed to obtain a desired target production. Though it is conceivable that polymer adsorption can have some positive consequences as well (e.g., by reducing the environmental impact), it is likely that the net outcome will be detrimental for the economics of a polymer flood, even with moderate adsorption values (Zhang et al. 2014).

The amount of polymer adsorption depends on the specific combination of polymer, solvent and rock type under investigation (Lakatos et al. 1981). The conformation of the polymers in solution seems to play a major role, since the larger the polymer molecules are, the less room there will be for them to occupy adsorption sites on the mineral surface. For polymers that are very sensitive to salt (section 4.6), varying the ionic composition of the brine could therefore have a big impact on adsorption levels, as could pH and degree of hydrolysis (Sorbie 1991). Indeed, a common finding has been that adsorption tends to increase with increasing ionic strength (e.g., Smith (1970)). Obviously, the nature of the rock will play a decisive role in determining the adsorption behaviour, such as the distribution of charged sites on mineral surfaces.

The kinetics of polymer adsorption in porous media has been described as a sequence of 1) effectively instantaneous adsorption, with the maximum level of adsorption reached at relatively low polymer concentrations, followed by 2) a much slower reorganization of adsorbed polymer molecules at the mineral surface, with larger molecular weight species being preferentially adsorbed at thermodynamic equilibrium (Chauveteau et al. 1988). As an illustration of the first point, Zhang et al. (2014) performed both static and dynamic adsorption experiments involving an HPAM polymer in porous media. The static experiments were conducted in sandpacks prepared with crushed and sieved Berea sandstone, whereas the dynamic tests were performed in both sandpacks and in Dundee sandstone cores. Though some desorption was inferred to occur, adsorption was largely found to be irreversible.

The apparent irreversibility of the adsorption process was interpreted by Zhang et al. (2014) as a consequence of the large, flexible structure of the HPAM polymer in solution. Specifically, because such a polymer molecule is expected to attach to the rock at multiple points of contact, it is improbable that it will ever fully detach from the surface. It was also observed that, if a low concentration of polymer solution was injected into a core at the beginning of an experiment,

subsequent injections at higher concentrations yielded little additional adsorption. This was taken to imply that following the first period of polymer injection, most adsorption sites were already occupied with polymer, leaving no room for additional molecules to adhere to the surface.

A detailed understanding of polymer adsorption has not been a focus of the present work. However, to properly match most laboratory corefloods, it is necessary to introduce some model for permeability reduction. In the present work, two such candidate models have been tested (section 5.5.6).

4.6 Salinity effects

The composition of the reservoir brine can have a profound impact on the rheological behaviour of polymer solutions. In particular, for a random coil polymer such as HPAM, the flexible structure of the molecule makes it very sensitive to the ion content of the solvent water. In the absence of salt, or at low salinity, Coulombic repulsion of the ionic groups distributed along the polymer chain backbone cause the volumetric extension of the polymer to expand. On the other hand, if ions of opposite charge are added to the solution, electrostatic screening will suppress the electrical double layers operating next to the polymer chain, which serves to lower the hydrodynamic size of the polymer in solution (Ward et al. 1981). The flow resistance is affected much more strongly by divalent ions than by monovalent ones (Mungan 1972; Stavland et al. 2013), which makes the choice of injection water an important factor to consider for field applications. On that note, it could be intriguing to explore possible synergy effects between polymer flooding and low salinity waterflooding.

The solution salinity can influence the apparent shear thickening and mechanical degradation behaviour as well. With regard to the former, the general trend seems to be one of enhanced thickening with increasing salinity; this has been observed for porous media flow (Maerker 1975), and for flow through systems of successive capillary tubes (Magueur et al. 1985). Conversely, in brines of low salinity apparent shear thickening is less pronounced. For instance, Seright et al. (2011) found that for a large molecular weight HPAM dissolved in distilled water, relatively little or no shear thickening was observed when the polymer was flooded through Berea sandstone cores. This was the case even at flow rates above 20 ml min^{-1} . In contrast, when the same polymer was dissolved in a 2.3 wt. % NaCl and 0.22 wt. % NaHCO_3 brine, marked dilatant behaviour was seen, and at substantially lower flow rates. The authors attributed this to the fact that in the distilled water, the difference between the relaxed and stretched-out polymer state was much smaller than in brines with higher salinity. As noted above, at low ionic strengths a relaxed polymer molecule will already be highly expanded, due to unshielded electrostatic repulsion between charged polymer sites. Consequently, less energy will be needed to stretch the polymer molecules in the flow field (Seright et al. 2011). The same explanation was forwarded in Paper [IV], to account for the less marked shear thickening effect found in experiments reported by Howe et al. (2015) (low salinity), compared with data

4. Polymer rheology in porous media

from Stavland et al. (2010) (synthetic sea water).

It should be remarked that, though the magnitude of the apparent shear thickening effect seems to decrease at lower ionic strengths, the onset of apparent shear thickening will tend to happen at lower shear rates (if it occurs at all). Again, this is because of the electrostatic repulsions, which increases the relaxation time of the polymer.

As for mechanical degradation, lowering the ionic strength seems to protect the polymer chains against chain scission (Maerker 1975; Martin 1986). For a recent demonstration of this, little evidence of degradation was detected in core flood experiments reported by Howe et al. (2015). These experiments, conducted in Bentheimer sandstone cores and involving multiple HPAM polymers dissolved in a 0.074 M NaCl brine, are briefly discussed in Paper [IV].

Chapter 5

Reservoir simulation background

Reservoir simulators are based on the premise that the solids and fluids inside the rock can be approximated by continuous, macroscopic quantities at each point in space and time. Central to this *continuum assumption* is the notion of a *representative elementary volume* (REV), i.e., a volume small relative to the total system under consideration, yet large enough that so that small scale statistical variations in a property may be captured by an average value (Bear 1988). This enables the use of differential calculus to describe relevant transport and reaction processes occurring in the medium. A similar approach is taken in fluid dynamics, to describe the bulk motion of fluids. The continuum approximation can then be justified by considering the vast number of molecules involved (Batchelor 2000). In contrast, because of the granular nature of rocks, flow in porous media is inherently discontinuous (Lichtner 1996). As such, additional modelling assumptions may sometimes be required to capture the average flow behaviour, e.g., if significant faults or fractures exist in the reservoir, or when studying media with clearly hierarchical porosity structures.

While detailed derivations of various forms of the macroscopic mass balance equations are beyond the scope of the present text ¹, for completeness, the general procedure will be outlined in this chapter:

- In section 5.1, the generic form of a conservation law is presented, in both integral and differential form.
- Next, a short description of the kind of approaches taken in reservoir simulation is provided, but without going into any mathematical details (section 5.2).
- Section 5.3 includes mathematical details for the specific case of immiscible, two-phase flow of oil and water. The classical fractional flow theory for Newtonian fluids is briefly reviewed. The extension of the theory to non-Newtonian fluids is not explicitly addressed.
- Section 5.4 further specializes to 1-phase flow, which has been the focus of this work. The standard way of modelling tracer transport in a reservoir is introduced.
- The topic of how to model polymer flooding in particular is addressed in the remaining sections of the chapter. Also, it is discussed at much greater length in the papers found in the second part of the thesis.

¹For further details see, e.g., Lichtner (1996).

5.1 Generic conservation law

Let $V \subset \mathbb{R}^3$ be a fixed volume with boundary A . For a conserved quantity Z , the net accumulation of Z within V must be balanced by the flux of material into or out of the volume, and by any sources or sinks present (Lichtner 1996):

$$\frac{d}{dt} \iiint_V Z dV = - \iint_A \mathbf{J}_Z \cdot \mathbf{n} dA + \iiint_V R_Z dV. \quad (5.1)$$

In Eq. (5.1), the vector \mathbf{J}_Z represents the flux of Z across the boundary. By convention, \mathbf{n} is the outward-pointing unit normal vector to a surface element dA , hence the negative sign on the right-hand side of the equation. The source term R_Z represents the amount of Z supplied to ($R_Z > 0$), or removed from ($R_Z < 0$), the volume V . By combining the Reynolds transport theorem and the Divergence Theorem, noting that the volume V was arbitrary and unchanging in time, equation (5.1) can be rewritten in differential form as:

$$\frac{\partial Z}{\partial t} + \nabla \cdot \mathbf{J}_Z - R_Z = 0. \quad (5.2)$$

Equations (5.1) and (5.2) are completely general, in that they can be used to describe any conserved quantity, such as mass, momentum, or energy. The exact form will therefore depend on the problem at hand.

5.2 Types of reservoir simulation models

The macroscopic flow of mass and heat in a permeable medium can be described by a coupled system of conservation laws, one for each conserved quantity under investigation. For reservoir simulation purposes, it is common to distinguish between models that are based on a *compositional* approach, and models based on the *Black Oil* formulation, though mathematically the latter is a specific instance of the former (Lake 1989).

In compositional reservoir simulators, the reservoir fluids are represented by, in principle, any number of components that can exist in any number of phases, yielding a potentially large system of coupled non-linear partial differential equations (PDEs) that need to be solved at each timestep during a numerical simulation (Trangenstein et al. 1989a). For this reason, compositional models tend to be very CPU intensive compared to simpler approaches. However, it is not only the sheer number of components that add to the computational complexity, but also the fact that more advanced phase equilibrium (flash) calculations are needed every time the phase flow fields are computed. Furthermore, one needs to account for the possibility of appearing and disappearing phases.

On the other hand, the Black Oil model represents the reservoir fluids by 3 flowing phases (aqueous, oleic, gaseous) and 3 (pseudo)components (water, oil, gas). In the classical case, the components are assumed to partition into phases as follows: the aqueous phase contains only water, the gaseous phase contains only gas, while the oleic phase may contain a mixture of oil and dissolved gas

(Lake 1989). Additionally, the possibility of vaporized oil may be taken into account. The resulting mass balance equations are typically reformulated as conservation of volumes at standard conditions, via the introduction of formation volume factors for each phase, and solubility factors for the partitioning of the hydrocarbon components. A presentation of the mathematical details can be found in, e.g., Trangenstein et al. (1989b).

For flows involving just 1 or 2 phases, and only a limited number of components, the equations simplify considerably. However, in addition to water and hydrocarbon components, it may be necessary to include the flow of other components as well, such as various tracers or ions. This is especially relevant when modelling EOR mechanisms. For most practical intents and purposes, these components can be treated as not occupying any volume, and thus the equations governing their transport need not be directly considered when updating the phase velocity fields. On the other hand, they may still influence the calculation of said fields via their effects on, e.g., fluid phase viscosities and rock wettability (saturation functions).

Interactions between the pore fluid and the rock will sometimes have to be incorporated more explicitly into the mathematical framework. For instance, this is the case when adsorption plays an important role, or if significant mineral precipitation and dissolution reactions occur in the medium.

5.3 Immiscible, two-phase flow equations

Consider the case of immiscible flow of a single oil and water component in porous media; in this situation, components and phases may be identified. Letting indices o and w denote, respectively, the oil and water phase, the mass flux terms become

$$\mathbf{J}_\alpha = \rho_\alpha \mathbf{u}_\alpha, \quad (5.3)$$

for $\alpha = o, w$, where ρ_α is the density of phase α , and \mathbf{u}_α is the velocity vector. As is common in petroleum science, phase velocities are obtained from Darcy's law. Originally derived for single phase flow (Hubbert 1956), it has since been generalized to multiple phases according to (Blunt 2017),

$$\mathbf{u}_\alpha = -\frac{k k_{r\alpha}}{\mu_\alpha} \cdot (\nabla P_\alpha - \rho_\alpha \mathbf{g}), \quad (5.4)$$

with the total driving force given as the sum of the pressure gradient, and the contribution due to gravity. The ratio of relative permeability $k_{r\alpha}$ to phase viscosity μ_α ² is the (relative) phase mobility, denoted by λ_α . With this setup, the mass of a given component/phase is

$$m_\alpha = \phi \rho_\alpha S_\alpha, \quad (5.5)$$

²In polymer science it is more common to employ the letter η for viscosity. This convention has been adopted most places in the thesis.

5. Reservoir simulation background

where S_α is the saturation of phase α , and ϕ is porosity. Thus, in the absence of source terms, equation (5.2) reduces to

$$\frac{\partial}{\partial t}(\phi\rho_w S_w) + \nabla \cdot (\rho_w \mathbf{u}_w) = 0 \quad (5.6)$$

for the water phase, and

$$\frac{\partial}{\partial t}(\phi\rho_o S_o) + \nabla \cdot (\rho_o \mathbf{u}_o) = 0 \quad (5.7)$$

for the oil phase. By adding the two phase velocities, and using the definition of the oil-water capillary pressure as the difference in phase pressures,

$$P_c = P_o - P_w, \quad (5.8)$$

an expression for the total Darcy velocity is obtained,

$$\mathbf{u}_T = -k\lambda_t \nabla P_w - k\lambda_o \nabla P_c + k\rho \mathbf{g}, \quad (5.9)$$

with $\rho = \lambda_w \rho_w + \lambda_o \rho_o$, and where $\lambda_t = \lambda_w + \lambda_o$ is the total mobility. Eq. (5.9) can be used to express the water velocity in terms of the total velocity as

$$\mathbf{u}_w = \frac{\lambda_w}{\lambda_t} \cdot (\mathbf{u}_T + k\lambda_o \Delta \rho \mathbf{g} + k\lambda_o \nabla P_c), \quad (5.10)$$

with $\Delta \rho = \rho_w - \rho_o$.

5.3.1 Fractional flow theory

In the classical theory developed by Buckley et al. (1942), Welge (1952) and several subsequent workers, the situation is as follows: Consider the immiscible flow of two phases in a homogeneous, isotropic, linear, 1-dimensional reservoir with constant cross-sectional area. Furthermore, assume that both the rock and the fluids are incompressible. For the flow of water and oil, Eqs. (5.6) and (5.7) then reduce to

$$\phi \frac{\partial S_w}{\partial t} + \frac{\partial u_w}{\partial x} = 0, \quad (5.11)$$

and

$$\phi \frac{\partial S_o}{\partial t} + \frac{\partial u_o}{\partial x} = 0. \quad (5.12)$$

Note that, since flow is unidimensional, the vector notation has been dropped. For incompressible flow, the total flow rate is constant in space, as can be verified by adding equations (5.11) and (5.12). The fractional flow of water, or water cut, is the relative flow rate of water:

$$f_w = \frac{u_w}{u_T}, \quad (5.13)$$

By rewriting Eq. (5.11) in terms of f_w and u_T , one obtains the Buckley-Leverett equation:

$$\phi \frac{\partial S_w}{\partial t} + u_T \cdot \frac{\partial f_w}{\partial x} = 0. \quad (5.14)$$

Using Eq. (5.10), the fractional flow of water is

$$f_w = \frac{\lambda_w}{\lambda_t} \cdot \left(1 + \frac{k\lambda_o}{u_T} \Delta\rho g_x + \frac{k\lambda_o}{u_T} \frac{\partial P_c}{\partial x} \right), \quad (5.15)$$

where g_x is the projection of the gravity vector along the direction of flow. Let $M = \lambda_w/\lambda_o$ be the mobility ratio between water and oil, evaluated at the local value of the water saturation. In the classical Buckley-Leverett theory, capillary and gravity forces are ignored, and Eq. (5.15) becomes

$$f_w = \frac{\lambda_w}{\lambda_t} = \frac{\lambda_w}{\lambda_w + \lambda_o} = \frac{1}{1 + \frac{1}{M}}. \quad (5.16)$$

The last equality in (5.16), valid for $\lambda_w > 0$, clearly shows that at a given value of the water saturation, the water cut will decrease with decreasing M .

If relative permeabilities are assumed to be functions of water saturation only, and fluid viscosities are regarded as constant, Eq. (5.14) can be further simplified to

$$\phi \frac{\partial S_w}{\partial t} + u_T \cdot f'_w(S_w) \cdot \frac{\partial S_w}{\partial x} = 0, \quad (5.17)$$

which is a non-linear, hyperbolic PDE. In most cases, Equation (5.17) cannot be solved in the conventional way using continuous functions. Mathematically, one requires the introduction of a sharp discontinuity (a 'shock') into the spatial saturation profile. The full details depend on the notion of a *weak solution* to the integral form of the conservation law, and it is of no concern here (LeVeque 1992). However, the classical Buckley-Leverett (Buckley et al. 1942) solution is recalled: it consists of a shock wave, immediately followed by a rarefaction wave. Specifically, a water front S_f moves through the system at characteristic velocity (wave speed) $f'_w(S_f)$, while higher saturations move at velocities $f'_w(S_w)$. At the location of the discontinuity, the saturation declines instantly from a value of S_f to the initial (connate) water saturation, S_{wc} . It can be shown that both S_f , as well as the average water saturation at the time of breakthrough $\langle S_w \rangle_{bt}$, can be derived geometrically from the fractional flow curve: By drawing a tangent to the f_w versus S_w curve passing through the point $(S_{wc}, 0)$, the front saturation is given as the x -intercept of the point of tangency, while $\langle S_w \rangle_{bt}$ can be read off from the intersection with the horizontal line $f_w = 1$ (Welge 1952). This was exemplified in figure 2.1.

5.4 One-phase incompressible flow

For 1-phase incompressible flow of water, the equation needed to be solved for pressure, and hence velocity, is

$$\nabla \cdot \mathbf{u}_w = 0, \quad (5.18)$$

with the expression for water velocity \mathbf{u}_w given by the 1-phase Darcy law.

5.4.1 Advection-dispersion equation (ADE)

The net flow of a tracer in the reservoir is a result of both advective and diffusive transport mechanisms. Advection refers to the passive transport of a substance by bulk motion; in the current context, to the movement of chemicals along the macroscopic velocity field established inside the rock. On the other hand, diffusive spreading of chemicals occurs even in the absence of an externally imposed flow, because of the random, thermal motion of ions and molecules (molecular diffusion). For pressure driven flows, additional mixing is induced at the macroscopic scale by a) mechanical dispersion, mixing due to the presence of local velocity gradients, and b) molecular diffusion across streamlines (Aris 1956; Taylor 1953). The combined effect is known by the name *hydrodynamic dispersion*. For flow through porous media additional complexities arise due to the solid obstacles encountered by the particles traversing the rock, which will serve to restrict diffusion. Mechanical mixing behaviour is in this case also affected by stream splitting, that is, by how the particles jump across junctions between adjacent pores inside the medium (Bear 1988; Jha et al. 2011).

Mathematically, hydrodynamic dispersion is often treated in the same way as the more fundamental process of molecular diffusion, i.e., as a statistically random process governed by the normal distribution. If this assumption is valid ³, both processes are described by Fick's first law, which states that the magnitude of the flux is proportional to the gradient in concentration ⁴. Then, by neglecting source terms and assuming no reactions with the rock, Eq. (5.2) for tracer transport becomes

$$\frac{\partial(\phi C)}{\partial t} + \nabla \cdot (\mathbf{u}_w C) - \nabla \cdot (\phi D^* \nabla C) = 0, \quad (5.19)$$

in which C is the mass concentration of the tracer in the fluid, and where the total flux is split into a sum of an advective and a diffusive term. Eq. (5.19) is the classical Advection-Dispersion-Equation (ADE). The quantity D^* is an effective diffusion-dispersion coefficient, given as the sum of two terms, one representing molecular diffusion, and one modelling the effects of hydrodynamic dispersion.

5.5 IORCoreSim implementation approach

In IORCoreSim, when solving for fluid phase pressures and saturations in a 2-phase simulation, a *sequential* approach is used, along the lines described by, e.g., Spillette et al. (1973) and Watts (1986). First, the total velocity field is

³See, e.g., Chapter 10 of Bear (1988) for a discussion of this issue

⁴More generally, the diffusive flux is driven by a gradient in chemical potential.

obtained by discretizing and solving an IMPES type pressure equation, after which effects of relative permeability and capillary pressure are corrected for in a separate step. This is done by solving a saturation equation, which is formulated in terms of the fractional flow of water ⁵. Numerically, the equation is solved 'semi-implicitly' with respect to the saturation-dependent variables, i.e., relative permeability and capillary pressure; essentially, by performing a single Newton-Raphson iteration on the discretized version of the equation. After finding the change in phase saturations, the individual phase velocities are updated, while keeping the total velocity fixed.

Component transport is handled using operator splitting, and can be treated with both an explicit and an implicit discretization in time. An example flowchart for the whole simulation process is displayed in figure 5.1.

It is remarked that the polymer is treated as a volumetric component in IORCoreSim, while tracers are regarded as occupying no volume. The mass of volumetric components are expressed as volumes at standard conditions, as in the Black-Oil approach. For all simulations presented in this work, zero compressibility was assumed for the polymer. While some effects of rock and water compressibility were included, this had negligible influence on the computed results, and only 1-phase flow was considered. Thus, effectively speaking, Eqs. (5.18) and (5.19) were used to model polymer flooding in porous media, with some modifications:

- The water phase viscosity used in Darcy's law, Eq. (5.4), is the *apparent viscosity* of the polymer solution, which is a complicated function of both fluid and rock properties. Note the non-linear coupling introduced between the apparent viscosity and velocity via the shear rate, Eq. (4.6).
- Whenever adsorption is to be modelled, an additional term must be added to the accumulation term of Eq. (5.19), to account for distribution of the total polymer mass between the rock and the aqueous phase.
- Polymer adsorption leads to a reduction in the effective pore size available for subsequent flow, and hence to a lower water permeability. If this mechanism is to be included, the denominator in Darcy's law (for the water phase) must be multiplied by the permeability reduction factor R_k , and a suitable model for computing R_k must be introduced.
- If effects of polymer inaccessible pore volume are to be modelled (including effects of layers depleted in polymer), mass balance considerations lead to the use of an effective transport concentration of polymer, which is larger than the injected concentration.

Below, the IORCoreSim polymer model is quickly reviewed. For more details, see Part II of the thesis.

⁵Derived by combining Eqs. (5.6) and (5.10).

5.5.1 Polymer molecular weight

A complicating factor when modelling polymer degradation is that synthetic polymer molecules are polydisperse. However, considering all the uncertainties, in both model and reservoir description, it seems like a formidable task to attempt to describe the molecular weight distribution explicitly. Even if it were possible, it would greatly increase the computational load of the simulations. Instead, the goal has been to match the correct viscosity behaviour of the degraded solutions. To achieve this goal, a single molecular weight parameter M_w has been introduced. It is calculated as the ratio between polymer mass concentration c_p , and a molar concentration c_m :

$$M_w = \frac{c_p}{c_m}. \quad (5.20)$$

That is, the polymer is actually represented by *two* components in the simulator, which both are transported through the reservoir. An additional reaction term is added to the equation for the molar concentration: While the total polymer mass is conserved, degradation is handled by increasing c_m .

5.5.2 Apparent shear thinning

Shear thinning behaviour is conventionally modelled by the Carreau-Yasuda equation, which is able to capture a Newtonian flow regime at low shear rates, as well as a stable viscosity when $\dot{\gamma} \rightarrow \infty$ (Bird et al. 1977):

$$\frac{\eta - \eta_\infty}{\eta_0 - \eta_\infty} = (1 + (\lambda_1 \dot{\gamma}_{pm})^x)^{-n/x}. \quad (5.21)$$

The Carreau-Yasuda model uses five parameters to describe the shear thinning viscosity η : η_0 is the plateau viscosity at zero shear rate, η_∞ is the limiting viscosity at high shear rates⁶, λ_1 is the polymer relaxation time, the inverse of which marks the transition from the Newtonian to the shear thinning flow regime, the parameter x governs the sharpness of the transition, and n essentially describes the slope of the viscosity decrease on a double logarithmic plot. Specifically, for $\dot{\gamma}_{pm} \gg 1$, (5.21) can be reformulated as

$$\log \eta_{sp} \approx \log \eta_{sp0} - n \cdot \log \lambda_1 - n \cdot \log \dot{\gamma}_{pm}, \quad (5.22)$$

in which η_{sp0} is the specific viscosity at zero shear rate. In general, the *specific viscosity* is defined as

$$\eta_{sp} = \frac{\eta}{\eta_\infty} - 1 = \eta_{rel} - 1, \quad (5.23)$$

where η_{rel} is the *relative viscosity*. A novel part of the IORCoreSim model is that expressions to compute λ_1 and n from the properties of the aqueous solution have been suggested. A crucial parameter in this regard is the *intrinsic viscosity*

⁶Often taken as equal to the solvent viscosity, $\eta_\infty = \eta_s$.

of the polymer solution, which is a measure of the additional flow resistance imparted by the polymer above that of the solvent, and related to the volumetric extension of the polymer chains. Formally, it is defined by (Hiemenz et al. 2007)

$$[\eta] = [\eta]_0 = \lim_{c_p \rightarrow 0} \frac{\eta_0 - \eta_s}{c_p \eta_s} = \lim_{c_p \rightarrow 0} \frac{\eta_{sp0}}{c_p}. \quad (5.24)$$

In this thesis, the zero shear specific viscosity is computed as a cubic polynomial in the product of intrinsic viscosity and polymer concentration,

$$\eta_{sp0} = [\eta]c_p + k'[\eta]^2 c_p^2 + k''[\eta]^3 c_p^3, \quad (5.25)$$

with the intrinsic viscosity obtained from M_w via the Mark-Houwink relationship:

$$[\eta] = K \cdot M_w^a \quad (5.26)$$

for constants K and a . The shear-thinning slope parameter is calculated from

$$n = 1 - \frac{1}{1 + (a_n K c_p M_w^a)^{b_n}}, \quad (5.27)$$

and the correlation used for the polymer relaxation time is

$$\lambda_1 = \lambda_a \cdot \frac{\eta_s \eta_{sp0} M_w}{c_p T}. \quad (5.28)$$

See Paper [IV] for the full meaning, and derivation, of these expressions.

5.5.3 Apparent shear thickening

In the absence of depletion layer effects, apparent shear thickening is included by multiplying the specific viscosity obtained from the Carreau-Yasuda model, η_{sp}^{sh} , by an elongational viscosity factor:

$$\eta_{sp} = \eta_{sp}^{sh} \cdot \eta_{elf}. \quad (5.29)$$

As outlined in section 3.3 of Paper [IV], this factor is given by the following expression:

$$\eta_{elf} = (1 + (\lambda_2 \dot{\gamma}_{pm})^{x_2})^{\frac{m+n}{x_2}}. \quad (5.30)$$

The crucial quantities here are:

- λ_2 , a characteristic time scale of the polymer in the flow field,
- m , the 'magnitude' of the shear-thickening effect, i.e., the slope of η_{sp} versus shear rate on a log-log plot,
- x_2 , a parameter governing the transition from shear thinning to shear thickening behaviour.

5. Reservoir simulation background

In turn, λ_2 is related to properties of the solution and the rock via

$$\lambda_2 = \frac{1}{N_{De}^*} \cdot \frac{3}{5R_g} \cdot \frac{\phi}{1-\phi} \cdot \frac{\eta_s K M_w^{a+1}}{T}. \quad (5.31)$$

Compared with the expression given in Paper [IV], Eq. (5.26) has been inserted to show more explicitly the dependence of λ_2 on M_w (this was also done for the parameter n).

5.5.4 Mechanical degradation in porous media

The combined transport and reaction (degradation) problem is handled by a standard sequential non-iterative operator splitting approach (figure 5.1). First, the polymer components are advected through the grid using a timestep Δt , yielding an intermediate solution M_w^0 for the molecular weight (Eq. (5.20)). Next, M_w is updated by solving the following initial value problem over the same timestep:

$$\frac{dM_w}{dt} = -f_{rup} \cdot M_w, M_w(0) = M_w^0. \quad (5.32)$$

In the present IORCoreSim implementation, Eq. (5.32) is discretized implicitly in time:

$$M_w = \frac{M_w^0}{1 + \Delta t \cdot f_{rup}(M_w)}. \quad (5.33)$$

The degradation rate has been chosen to be

$$f_{rup} = (r_{deg} \cdot \dot{\gamma}_{pm} \cdot \eta)^{\alpha_d} \cdot \frac{2M_w^{\beta_d}}{R_p}. \quad (5.34)$$

In this expression, R_p is the pore radius available for polymer flow, computed from a Kozeny-Carman type equation,

$$R_p = \sqrt{\frac{8kC}{\phi}} \cdot \frac{1}{\sqrt{R_k(1-IPV_0)}}, \quad (5.35)$$

in which C is a tortuosity factor. The rationale for using Eq. (5.34) to model mechanical degradation was discussed in Paper [IV] and summarized in Paper [V]. Those arguments are repeated here as well:

1. The probability for chain rupture seems to increase dramatically beyond a critical level of shear stress, while for smaller values, little or no degradation is expected. This behaviour is represented by the term $(r_{deg} \cdot \dot{\gamma} \cdot \eta)^{\alpha_d}$.
2. Inside a pore, the shear forces are largest close to the pore surface. It seems reasonable that a substantial amount of degradation will take place there, which is represented by including the term $2/R_p$ (i.e., specific surface area) in the degradation rate, where R_p denotes the effective pore radius available to polymer flow.

3. Longer polymer chains tend to rupture more easily than shorter ones, simply because they experience a higher shear force across the molecule. This is accounted for by the factor $M_w^{\beta_d}$.

5.5.5 Inaccessible pore volume effects

The total IPV factor is calculated as a sum of two parts:

$$IPV = IPV_0 + IPV_d \cdot (1 - IPV_0). \quad (5.36)$$

The first term IPV_0 is the fraction of the flowing aqueous phase that is completely inaccessible to polymer, and it is assumed constant. In contrast, the contribution from the depletion layer effect is taken as variable, and determined by the volume fraction of the depletion layer in the polymer accessible pore space, IPV_d .

In the thesis work, two models for incorporating the depletion layer mechanism have been suggested, both of which are based on the same two-fluid model as proposed by Chauveteau (1982). For completeness, some additional background for this model is included, beyond that which is already found in Appendix A of Papers [I] and [IV].

The situation can be viewed as an extension of the well known case of Hagen-Poiseuille flow (Sutera et al. 1993): Consider a cylindrical tube, in which two (Newtonian) fluids flow simulataneously. The fluid in the inner part of the tube has viscosity η_1 , while the fluid flowing close to the wall has viscosity η_2 . Place the origin along the symmetry axis in the middle of the tube, let R be the radius of the whole cylinder, and let $R_d \leq R$ be the radius delineating the interface between the two fluid regions. Then, an analytical solution can be derived for the steady-state laminar flow problem (Chauveteau 1982; Zaitoun et al. 1988):

$$v_1 = -\frac{\nabla P}{4\eta_2} \cdot \left(\frac{\eta_2}{\eta_1} (r^2 - R_d^2) + (R_d^2 - R^2) \right), \quad (5.37)$$

is the velocity for the inner part, and

$$v_2 = -\frac{\nabla P}{4\eta_2} \cdot (r^2 - R^2), \quad (5.38)$$

is the velocity in the region close to the wall. In the above expressions, ∇P is the pressure gradient. Let $M_\nu = \frac{\eta_1}{\eta_2}$ be the viscosity contrast between the two layers. By integrating Eqs. (5.37) and (5.38), expressions for the volumetric flow rates in the two regions are obtained:

$$Q_1 = \int_0^{R_d} 2\pi r \cdot v_1 dr = \frac{\pi \nabla P}{8\eta_1} \cdot (2M_\nu R_d^2 (R^2 - R_d^2) + R_d^4), \quad (5.39)$$

and

5. Reservoir simulation background

$$Q_2 = \int_{R_d}^R 2\pi r \cdot v_2 dr = \frac{\pi \nabla P}{8\eta_1} \cdot M_\nu \cdot (R^2 - R_d^2)^2. \quad (5.40)$$

The fluid flowing in the annular region closest to the wall represents the depletion layer, while the fluid flowing in the middle of the cylinder is the polymer rich phase. The thickness of the depleted layer is thus given by $\delta = R - R_d$, the viscosity in the polymer rich phase is $\eta_p = \eta_1$, and $\eta_{dw} = \eta_2$ is the viscosity in the depleted layer. The total volume in the cylinder represents the polymer accessible pore volume of the rock, i.e., the water phase volume after IPV_0 has been subtracted out.

The total flow rate is $Q_t = Q_1 + Q_2$. Let \widetilde{Q}_t be the corresponding flow rate in the case without any depletion layer, as given by the standard Hagen-Poiseuille equation with viscosity η_p . Then, by requiring the same pressure gradient for the two scenarios, the corrected effective viscosity η_{pa} must satisfy

$$\eta_{pa} \cdot Q_t = \eta_p \cdot \widetilde{Q}_t. \quad (5.41)$$

By inserting the above expressions for $Q_p = Q_1$ and $Q_{dw} = Q_2$, and performing some calculations, Eq. 45 of Paper [IV] is obtained:

$$\eta_{pa} = \frac{\eta_p}{M_\nu - (M_\nu - 1)E_{PVd}^2}. \quad (5.42)$$

Here, $E_{PVd} = 1 - IPV_d$ represents the fraction of the polymer rich phase in the tube, which amounts to

$$E_{PVd} = \frac{\pi R_d^2 L}{\pi R^2 L} = \left(\frac{R_d}{R}\right)^2 = \left(1 - \frac{\delta}{R}\right)^2, \quad (5.43)$$

for a cylinder of length L . Expression (5.42) is the same as, e.g., Eq. 9 in Chauveteau 1982. In IORCoreSim, this equation is used to update the apparent viscosity of the solution after including shear thinning (η_p), but before adding the contribution from apparent shear thickening.

As described in section 4.4, the fluid in the polymer rich phase will travel at a higher average transport velocity than the fluid in the depleted layer. Similarly, the presence of microporosity inaccessible to polymer will also increase the macroscopic velocity of the polymer compared to the solvent. To account for these effects, an effective transport concentration of polymer c_{pef} is defined. If c_p is the average polymer concentration in the rock, the concentration in the polymer accessible part (represented by the capillary tube) is

$$c_p^* = \frac{c_p}{E_{PV0}}, \quad (5.44)$$

for $E_{PV0} = 1 - IPV_0$. In the absence of depletion layer effects, $c_{pef} = c_p^*$. However, if the depletion layer mechanism is included, a further correction is made. At steady-state, mass balance considerations require that

$$c_{pef} \cdot q_t = c_{pp} \cdot q_p, \quad (5.45)$$

where c_{pp} is the polymer concentration in the polymer rich phase:

$$c_{pp} = \frac{c_p^*}{E_{PVd}} = \frac{c_p}{E_{PV0} \cdot E_{PVd}}. \quad (5.46)$$

Using Eqs. (5.39) and (5.40), one can show that the fractional flow of the polymer rich phase is

$$f_p = \frac{Q_1}{Q_1 + Q_2} = \frac{E_{PVd} \cdot (2M_\nu(1 - E_{PVd}) + E_{PVd})}{M_\nu - (M_\nu - 1)E_{PVd}^2}, \quad (5.47)$$

i.e., the denominator is the same as in Eq. (5.42) for the viscosity correction. By combining (5.45), (5.46) and (5.47),

$$c_{pef} = \frac{c_p}{E_{PV0}E_{PVd}} \cdot E_{PVd} \cdot \frac{2M_\nu(1 - E_{PVd}) + E_{PVd}}{M_\nu - (M_\nu - 1)E_{PVd}^2}. \quad (5.48)$$

Note that, in the above derivations, zero polymer concentration was assumed in the depleted layer, meaning that $\eta_{dw} = \eta_s$. Moreover, the thickness of the depleted layer was made independent of polymer concentration, $\delta \approx R_h$, where R_h is the hydrodynamic radius of the polymer in solution. In Paper [IV], a second model was also suggested, in which both of these assumptions were relaxed. This was found necessary to match core flooding data from low salinity polymer injection, in which the depletion layer effect was greatly exaggerated in the original model.

5.5.6 Polymer adsorption modelling

Adsorption can be modelled by extending the accumulation term of Eq. (5.19):

$$\frac{\partial(\phi C_i)}{\partial t} + \frac{\partial(\phi C_{ads,i})}{\partial t} + \nabla \cdot (\mathbf{u}_w C_i) - \nabla \cdot (\phi D^* \nabla C_i) = 0, \quad (5.49)$$

In Eq. (5.49), $C_{ads,i}$ is the mass of adsorbed material, expressed in terms of the pore volume. Note that in IORCoreSim, it is the total concentration $C_i + C_{ads,i}$ that is transported through the grid at each time step, after which component mass is distributed between the rock and fluid phases. For polymer flooding, a Langmuir equilibrium isotherm is used, possibly modified to describe irreversible adsorption.

Two tentative models for permeability reduction as a consequence of polymer adsorption have been tested, see section 3.7 and Appendix A.3 of Paper [IV].

5.5.7 Effective salinity model

As described in Appendix A.4 of Paper [IV], salinity effects on polymer behaviour are introduced into the simulator via the intrinsic viscosity term:

$$[\eta] = [\eta]_{ref} \cdot C_S^{\alpha_s}. \quad (5.50)$$

5. Reservoir simulation background

The parameter C_s is an effective salt concentration; for a pure NaCl brine, it is just the molar concentration. More generally, it is computed according to the relation

$$C_s = \sum_i C_i \beta_i, \quad (5.51)$$

in which C_i is the concentration of ion type i , and β_i is a constant that varies among different ions. Multivalent ions are assigned a larger weight than monovalent ones.

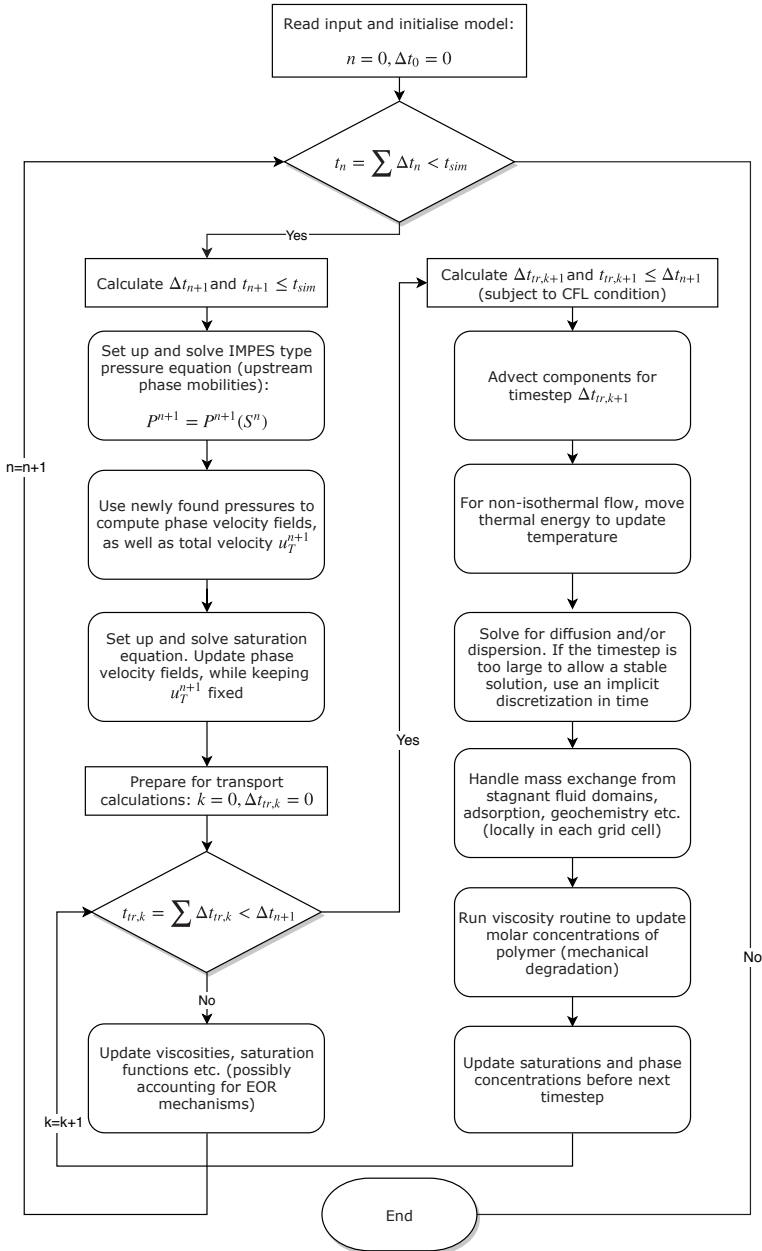


Figure 5.1: Flowchart for an IORCoreSim simulation (explicit transport scheme)

Chapter 6

Summary of papers

To be able to simulate polymer flooding at the field, it seems important to first reproduce behaviour seen at smaller scales. However, even at the core scale, a severe limitation with most presently available simulation codes is that it is difficult, or impossible, to accurately describe the in-situ polymer rheology across the full range of realistic flow conditions. One problem is that important physical mechanisms may sometimes be neglected, e.g., mechanical degradation. Another issue is that many models tend to require a large number of free input parameters, which makes translating from one set of conditions to another very challenging. For example, for field scenarios, a separate table of input data might be needed for each rock type in the reservoir, which greatly complicates the process of upscaling.

It is true that in order to history match linear core floods, relatively simple models may often suffice, at least if factors such as brine composition and temperature are being held fixed. This is because, for constant flow rate boundary conditions in 1D linear flow, the in-situ shear rate can be taken as spatially constant¹. In contrast, for flow near a well at the field scale, the apparent viscosity of an injected polymer solution will be a strong function of radial distance from the wellbore.

The main focus of the papers included in Part II of this thesis has been to improve upon the modelling of polymer rheology in porous media, at the core scale and beyond. The slight exception is Paper [II], which is primarily a report of experimental findings. Six papers are included, however note that the papers are not all independent:

- Paper [IV] is an improved version of Paper [I], and Paper [V] is an updated version of Paper [III]. Both revised versions contain substantial amounts of new material compared with the originals.
- Paper [VI] is an attempt to shed more light on the data from Paper [II] by means of numerical simulations.

6.1 Paper I

For large flexible molecules of the HPAM type, Newtonian behaviour is usually observed at low shear rates, followed by shear thinning, shear thickening and mechanical degradation at increasing rates. Moreover, the onset of these flow regimes, and their impact on the flowing aqueous phase pressure, depend upon not only the composition of the pore fluid, but also on properties of the formation

¹Unless significant core scale heterogeneities exist. Also, this assumption may need to be relaxed when permeability reduction effects are important.

(e.g., permeability). To meet some of these challenges, it was desired that a more comprehensive polymer model should be developed.

The purpose of Paper [I] was to introduce this model for the first time, and was done by history matching the model to a series of core floods conducted in sandstones. The main experimental variable with which the simulations were compared was the resistance (mobility reduction) factor. In the experiments, the flow rate was systematically varied, and there were also differences in both permeability and polymer molecular weight. Four HPAM polymers, with reported molecular weights in the range 5-20 MDa, were considered. The lowest permeability was approximately 150 mD, while the highest permeability was about 2 D. Considering that a single set of input parameters were used to describe apparent shear thickening and mechanical degradation across all experiments, as well as the many model and experimental uncertainties, a very satisfactory history match was achieved.

A novel feature of the proposed model was the inclusion of an equation to describe polymer mechanical degradation in porous media. The polymer degradation rate was linked to pore radius, and thus permeability, via a Kozeny-Carman type equation: For a given shear rate, more degradation was predicted at lower permeability, in line with experimental observations. The degradation rate was further linked to wall shear stress, computed as the product of in-situ shear rate and apparent viscosity, and to polymer molecular weight M_w .

The work done in Paper [I], originally presented as a poster presentation at EAGE ECMOR XV 2016, was subsequently developed into a journal publication, Paper [IV].

6.2 Paper II

Paper [II] is a presentation of experimental work performed by Irene Ringen and Hjørdis Stiegler during their master's degree at the University of Stavanger. A small contribution was made to this work in terms of numerical simulations of the experiments.

In the experiments, an acrylate-ATBS polymer (Flopaam 5115SH, SNF Floerger) was injected into glass columns packed with mesoporous silica sand. The polymer was mixed in a brine with lower salinity than that of the water already residing inside the core. Resistivity measurements provided information about the salinity fronts moving through the system, while a capillary rheometer connected to the effluent was used to track the polymer front.

In this work it was clearly demonstrated that:

1. Synthetic polymers can be very sensitive to the ionic composition of the brine, with an additional flow resistance observed at low salinities.
2. In the presence of microporosity, the polymer can move significantly faster through the porous medium than co-injected ions (IPV effect).

6.3 Paper III

In Paper [III], steady-state polymer behaviour in homogeneous formations at the field scale was explored. Several hundred simulations were carried out, in a radial sector model with dimensions $\Delta r \sim 20$ m. A single polymer type was considered, HPAM 3630S (SNF Floerger), with model input parameters chosen based on history matched parameters from Papers [I] and [IV]. The polymer was injected into the reservoir via a single vertical injector, which was placed in the middle of the radial grid. A constant pressure was required at the exterior boundary $r = r_e$, and the properties of the solution at this point was used as a proxy for the polymer deep within the reservoir.

The main motivation for the study was to understand the model predicted degradation behaviour in terms of variations in enforced flow rate Q , and the formation permeability k . For the particular polymer tested, a substantial amount of degradation was estimated when operating at realistically large flow rates, even at moderate to relatively high permeabilities. On the other hand, little or no degradation was predicted when the effective shear rate at the sand face, $\dot{\gamma}_w$, was kept below a certain level (approximately 1000 s^{-1} , but with significant scatter in the results). This indicates that in the presence of open fractures near the well, the amount of degradation should be small. Though degradation in the model essentially terminated very close to the injection point, the simulated polymer molecular weight at $r = r_e$ showed an additional dependence on permeability, beyond that already captured in the scaling $\dot{\gamma}_w \propto 1/k$ (Eq. (4.6)). An empirical (non-unique) correlation was found able to reduce the scatter in degradation versus Q and k .

Paper [III] revealed the estimated amount of mechanical degradation to be very sensitive to grid dimensions; in fact, grid cells on the order of millimetres had to be employed near the wellbore. Obviously, it is not feasible to use such low resolution in a realistic field case, which stresses the need for some sort of effective or up-scaled model to be implemented.

In the paper, the importance of including not only shear thinning, but also shear thickening, was pointed out. The results further suggested that injecting a polymer with the highest possible molecular weight may not always be the most economical option. Instead, if a certain level of degradation is tolerated and expected to occur anyway, injecting a slightly lower molecular weight polymer could lead to more or less the same improved sweep efficiency, while demanding a lower injection pressure.

To investigate effects of reservoir heterogeneity, preliminary simulations were conducted in a two-layered reservoir (assuming no crossflow). However, due to time limitations these tests were considered rather superficially, and no firm conclusions were drawn.

6.4 Paper IV

Paper [IV] is a heavily revised version of Paper [I]. Compared with the initial paper, the main new additions are:

- The incorporation of a brief literature review on previously reported simulation models. It was concluded that good reservoir simulation models that include mechanical degradation are lacking.
- An expanded literature review for the various physical mechanisms modelled.
- Testing of the simulator implementation, for the case without any assumed degradation, by directly solving the steady-state flow problem (i.e., without any iteration).
- The inclusion of a new series of experiments, this time using data from the literature (Howe et al. 2015). The experiments in question were conducted in Bentheimer sandstones with synthetic HPAM polymers dissolved in a 0.074 M brine. Because of the low salinity, and relatively large polymer concentrations, viscosities were significantly higher than in the previously considered dataset. It was concluded that the IORCoreSim model could fit both datasets reasonably well, but that modifications needed to be made when brines of differing ion composition were used: Both apparent shear thickening and mechanical degradation appeared 'slower' in the low salinity case.

6.5 Paper V

Paper [V] is a direct follow-up article to Paper [III]. It is currently undergoing peer review for the second time, having been resubmitted following major revision.

As was the case with Paper [IV], the updated version of the article includes much material not present in the original one, e.g.:

- The testing of the simulator implementation by numerically integrating the governing degradation equation for steady-state flow (using an independent Python implementation).
- Derivations of approximate analytical solutions, in explicit form. While these expressions were not sufficiently accurate so as to quantitatively match the full analytical solution, they could be used to gain a better understanding of how various model parameters affect the degradation rate in homogeneous radial flow.
- The analytical approach was also applied to the case of linear core floods. It was commented that a power-law decline of M_w with distance can often be expected. This is in contrast with the case of radial flow at the field, where degradation effectively stops a very small distance from the injector.

Some parts of the original work were also removed, e.g., no study of flow in heterogeneous formations was attempted.

6.6 Paper VI

Paper VI gives a more detailed account of some of the experiments that were presented in Paper II. However, in this work the emphasis was on using IORCoreSim to interpret the observations. A somewhat different modelling approach was taken compared to previously, in that the component transport equations were solved by assuming more than one macroscopic fluid continuum: a distinction was made between the pore volume that existed in-between the silica grains (i.e., the 'macropores'), and the volume that was inside the grains. The polymer size exclusion (IPV) effect was then represented by only allowing the polymer to flow in the macropore continuum, while ions could additionally diffuse in and out of the intragranular pore space.

By incorporating the IPV effect, and by assuming a salinity-dependent polymer solution viscosity, the experimentally observed trends were recreated in the IORCoreSim model. The simulations clearly revealed that the polymer front moved faster through the medium than the co-injected ions.

It was pointed out that the observations made in this study could have ramifications when considering simultaneous injection of polymer and low salinity water into certain types of reservoirs, e.g., fractured rocks. For such systems, combining the two EOR methods could be made more challenging by the fact that the injected polymer would mix primarily with the water already present in the formation, which typically has a high salinity, instead of with the injected water.

Chapter 7

Future prospects

To make large scale reservoir simulation computationally efficient, it is common to employ grid blocks with sizes on the order of tens to several hundred metres. When using such a coarse description of the reservoir, important aspects concerning fluid flow at smaller scales may be lost. For instance, heterogeneities in relative permeability and capillary pressure at the centimetre scale can have considerable impact on fluid flow at the field scale, and thus may need to be captured with an upscaling method (Lohne et al. 2006). The same is true for one phase flow: subgrid heterogeneity in absolute permeability and porosity can cause predictions made from a coarse reservoir model to be markedly different than from a more finely gridded one (Christie 1996). Even if a reservoir could be assumed to be perfectly homogeneous, the way in which the governing fluid flow equations are solved numerically may lead to inaccurate forecasts. For instance, the predicted flow pattern may in some cases be very sensitive to the orientation of the underlying geometric grid (Brand et al. 1991; Todd et al. 1972). Also, it is generally very hard to characterize the spreading of chemical concentration fronts accurately. This is the well known problem of *numerical dispersion* (Fanchi 1983; Lantz 1971).

Another challenge is the issue of how to handle wells in a reservoir simulator. Because of large differences in scale between the dimensions of a well and the size of a typical well block ¹, and as a consequence of the non-linear flow pattern that tends to be established near the wellbore, there will be considerable variations in pressure within the area of the reservoir represented by a well block. One solution to this problem is to discretize the well itself. Though such models are becoming more commonplace (e.g., (Jiang 2008)), the conventional approach is to relate the wellbore pressure to the well block pressure via a simplified well model, such as the Peaceman model, or some modification thereof (Ding 1996; Peaceman 1978; Peaceman 1983).

When simulating polymer flooding, several of the above mentioned issues become especially salient. As mentioned previously, a very important factor to consider is the amount of chemicals needed to secure an efficient displacement, which means that realistic estimates for the extent of polymer adsorption need to be made. However, simulated adsorption levels are greatly affected by numerical dispersion (Lee 2013). Similarly, numerical errors in concentrations of mobile polymer can lead to wrong predictions for the EOR potential of a planned polymer flood (Al-Sofi et al. 2010). The use of higher order discretization methods could be worthwhile to explore in this regard (Mykkeltvedt et al. 2017).

As discussed at length in this thesis, the non-Newtonian flow behaviour of polymer solutions can have a profound influence on the macroscopic flow

¹The well radius is typically on the order of 10 cm.

7. Future prospects

resistance of the water phase; and hence on the predicted oil recovery. It is important to quantify how observations made in the laboratory scale up to the field. To make further headway in this direction, the newly implemented IORCoreSim model can hopefully become a useful tool. A particular strength of this model is that it already includes proposed correlations for how the in-situ polymer rheology depends on changing reservoir conditions. However, more effort should be put into understanding the impact of varying temperature and salinity. Chemical degradation processes should also be considered.

Note that some of the flow regimes seen at the core scale may play less of a role at the field. For example, apparent shear thickening and mechanical degradation will only occur in a very limited region close to the wells. This is because fluid velocities in the bulk of the reservoir are too low to trigger the onset of these flow regimes. A simplified rheology model can therefore be used to describe flow in the vast majority of grid cells. Still, it is crucial to consider spatial variations in polymer solution rheology within the well blocks; after all, it is the polymer solutions leaving an injection well block that will propagate throughout the reservoir. Moreover, accounting for polymer elasticity and degradation near the well is clearly important when making well injectivity forecasts.

To reproduce effects of the fine scale polymer rheology in realistic field models, some sort of effective model seems to be needed. This is true even in the case of a purely shear thinning polymer, for which smearing of the fluid front near the wells is known to lead to overtly pessimistic forecasts of well injectivity. In an early work, Bondor et al. (1972) attempted to correct for this by introducing a rate-dependent, negative skin factor for each injection well. The researchers calculated the skin factor by integrating their chosen non-Newtonian fluid model around the wellbore, assuming radial flow. The same approach has also been pursued by other workers. Recently, Li et al. (2017) used the concept of an apparent skin factor to investigate multiple rheology models for polymer flow in porous media, including the UTCHEM Unified Viscosity Model (UVM) (Delshad et al. 2008), which incorporates both apparent shear thinning and shear thickening behaviour. They concluded that for a shear thinning polymer, it seemed possible to produce relatively accurate simulation results when using a constant skin factor as input, at least for the cases considered. On the other hand, when shear thickening effects were included, similar results were not achieved.

None of the above workers considered degradation processes as part of the equation. In particular, mechanical degradation in regions of high shear can dramatically lower the apparent viscosity of a polymer solution, and a fully satisfactory well model for polymer flooding should include this mechanism as well. To do so properly is a challenging task, not least if significant heterogeneities are present near the wellbore. However, one possible starting point was sketched out in Paper [V], based on analytical formulas for the steady-state degradation problem in a homogeneous formation.

At the end of the day, the practical usefulness of a proposed model can only be ascertained by comparing it with experimental data. To this end, it is hoped that a real field case can be investigated some time in the near future.

Bibliography

- Agarwal, U., Dutta, A., and Mashelkar, R. (1994). "Migration of macromolecules under flow: the physical origin and engineering implications". In: *Chemical Engineering Science* 49.11, pp. 1693–1717.
- Al Kalbani, H., Mandhari, M., Al-Hadhrami, H., Philip, G., Nesbit, J., Gil, L., and Gaillard, N. (2014). "Treating back produced polymer to enable use of conventional water treatment technologies". In: *SPE EOR Conference at Oil and Gas West Asia*. Society of Petroleum Engineers.
- Åm, K., Al-Kasim, F., Bjerkedal, N., Gjerdseth, A., Kindem, S., Skauge, A., Skjærpe, T., Sund, B., Sætre, J., and Wiborg, R. (2010). "Økt utvinning på norsk kontinentalsokkel". In: *Ministry of Petroleum and Energy of Norway, Oslo, Norway*.
- Aris, R. (1956). "On the dispersion of a solute in a fluid flowing through a tube". In: *Proc. R. Soc. Lond. A* 235.1200, pp. 67–77.
- Aronofsky, J. (1952). "Mobility ratio-its influence on flood patterns during water encroachment". In: *Journal of Petroleum Technology* 4.1, pp. 15–24.
- Åsen, S. M., Stavland, A., Strand, D., and Hiorth, A. (2018). "An Experimental Investigation of Polymer Mechanical Degradation at cm and m Scale". In: *SPE Improved Oil Recovery Conference*. Society of Petroleum Engineers.
- Barnes, H. A. (1995). "A review of the slip (wall depletion) of polymer solutions, emulsions and particle suspensions in viscometers: its cause, character, and cure". In: *Journal of Non-Newtonian Fluid Mechanics* 56.3, pp. 221–251.
- Batchelor, G. K. (2000). *An introduction to fluid dynamics*. Cambridge University Press.
- Bear, J. (1988). *Dynamics of fluids in porous media*. Dover Publications.
- Bird, R. B., Armstrong, R. C., Hassager, O., and Curtiss, C. F. (1977). *Dynamics of polymeric liquids*. Vol. 1. Wiley, New York.
- Blunt, M. J. (2017). *Multiphase flow in permeable media: a pore-scale perspective*. Cambridge University Press.
- Bondor, P., Hirasaki, G., and Tham, M. (1972). "Mathematical simulation of polymer flooding in complex reservoirs". In: *Society of Petroleum Engineers Journal* 12.5, pp. 369–382.
- BP (2018). *BP Statistical Review of World Energy - June 2018*. URL: <https://www.bp.com/content/dam/bp/en/corporate/pdf/energy-economics/statistical-review/bp-stats-review-2018-full-report.pdf> (visited on 07/23/2018).
- Bragg, J., Maruca, S., Gale, W., Gall, L., Wernau, W., Beck, D., Goldman, I., Laskin, A., and Naslund, L. (1983). "Control of xanthan-degrading organisms in the Loudon pilot: approach, methodology, and results". In: *SPE Annual Technical Conference and Exhibition*. Society of Petroleum Engineers.

- Brand, C., Heinemann, J., and Aziz, K. (1991). "The grid orientation effect in reservoir simulation". In: *SPE Symposium on Reservoir Simulation*. Society of Petroleum Engineers.
- Buckley, S. and Leverett, M. (1942). "Mechanism of fluid displacement in sands". In: *Transactions of the AIME* 146.01, pp. 107–116.
- Cannella, W., Huh, C., and Seright, R. (1988). "Prediction of xanthan rheology in porous media". In: *SPE annual technical conference and exhibition*. Society of Petroleum Engineers.
- Cao, H. (2002). "Development of techniques for general purpose simulators". PhD thesis. Stanford University.
- Chang, H. L. (1978). "Polymer flooding technology yesterday, today, and tomorrow". In: *Journal of Petroleum Technology* 30.8, pp. 1–113.
- Chauveteau, G. (1986). "Fundamental Criteria in Polymer Flow Through Porous Media and Their Relative Importance in the Performance Differences of Mobility Control Buffers". In: *Water-Soluble Polymers*. Ed. by Glass, J. Vol. 213. Advances in Chemistry Series of the American Chemical Society, pp. 227–268.
- Chauveteau, G. and Lecourtier, J. (1988). "Propagation of polymer slugs through adsorbent porous media". In: *Water-Soluble Polymers for Petroleum Recovery*. Springer, pp. 53–68.
- Chauveteau, G. and Moan, M. (1981a). "The onset of dilatant behaviour in non-inertial flow of dilute polymer solutions through channels with varying cross-sections". In: *Journal de Physique Lettres* 42.10, pp. 201–204.
- Chauveteau, G., Moan, M., and Magueur, A. (1984a). "Thickening behaviour of dilute polymer solutions in non-inertial elongational flows". In: *Journal of Non-Newtonian Fluid Mechanics* 16.3, pp. 315–327.
- Chauveteau, G. and Zaitoun, A. (1981b). "Basic rheological behavior of xanthan polysaccharide solutions in porous media: effects of pore size and polymer concentration". In: *Proceedings of the First European Symposium on Enhanced Oil Recovery, Bournemouth, England*, pp. 197–212.
- Chauveteau, G. (1981). "Molecular interpretation of several different properties of flow of coiled polymer solutions through porous media in oil recovery conditions". In: *SPE Annual Technical Conference and Exhibition, SPE-10060-MS*. Society of Petroleum Engineers.
- (1982). "Rodlike polymer solution flow through fine pores: influence of pore size on rheological behavior". In: *Journal of Rheology* 26.2, pp. 111–142.
- Chauveteau, G., Tirrell, M., and Omari, A. (1984b). "Concentration dependence of the effective viscosity of polymer solutions in small pores with repulsive or attractive walls". In: *Journal of colloid and interface science* 100.1, pp. 41–54.
- Chiotoroiu, M.-M., Peisker, J., Clemens, T., and Thiele, M. (2017). "Forecasting Incremental Oil Production of a Polymer-Pilot Extension in the Matzen Field Including Quantitative Uncertainty Assessment". In: *SPE Reservoir Evaluation & Engineering*.
- Christie, M. A. (1996). "Upscaling for reservoir simulation". In: *Journal of Petroleum Technology* 48.11, pp. 1004–1010.

- Christopher, R. H. and Middleman, S. (1965). "Power-law flow through a packed tube". In: *Industrial & Engineering Chemistry Fundamentals* 4.4, pp. 422–426.
- Clarke, A., Howe, A. M., Mitchell, J., Staniland, J., Hawkes, L. A., et al. (2016). "How viscoelastic-polymer flooding enhances displacement efficiency". In: *SPE Journal* 21.3, pp. 675–687.
- Clemens, T., Deckers, M., Kornberger, M., Gumpenberger, T., and Zechner, M. (2013). "Polymer Solution Injection-Near Wellbore Dynamics and Displacement Efficiency, Pilot Test Results, Matzen Field, Austria." In: *EAGE Annual Conference & Exhibition incorporating SPE Europec*. Society of Petroleum Engineers.
- Colby, R. and Rubinstein, M. (2003). *Polymer physics*. New-York: Oxford University.
- Craig, F. F. (1971). *The reservoir engineering aspects of waterflooding*. Vol. 3. HL Doherty Memorial Fund of AIME New York.
- Davison, P. and Mentzer, E. (1982). "Polymer flooding in North Sea reservoirs". In: *Society of Petroleum Engineers Journal* 22.03, pp. 353–362.
- Dawson, R. and Lantz, R. B. (1972). "Inaccessible pore volume in polymer flooding". In: *Society of Petroleum Engineers Journal* 12.05, pp. 448–452.
- De Gennes, P.-G. (1974). "Coil-stretch transition of dilute flexible polymers under ultrahigh velocity gradients". In: *The Journal of Chemical Physics* 60.12, pp. 5030–5042.
- (1979). *Scaling concepts in polymer physics*. Cornell University Press.
- (1997). "Molecular individualism". In: *Science* 276.5321, pp. 1999–2000.
- Delamaide, E., Let, K., Bhoendie, K., Paidin, W., and Jong-A-Pin, S. (2016). "Interpretation of the Performance Results of a Polymer Flood Pilot in the Tambaredjo Oil Field, Suriname". In: *SPE Annual Technical Conference and Exhibition*. Society of Petroleum Engineers.
- Delamaide, E., Moreau, P., and Tabary, R. (2015). "A New Approach for Offshore Chemical Enhanced Oil Recovery". In: *Offshore technology conference*. Offshore Technology Conference.
- Delamaide, E., Zaitoun, A., Renard, G., and Tabary, R. (2014). "Pelican Lake field: first successful application of polymer flooding in a heavy-oil reservoir". In: *SPE Reservoir Evaluation & Engineering* 17.3, pp. 340–354.
- Delshad, M., Kim, D. H., Magbagbeola, O. A., Huh, C., Pope, G. A., and Tarahhom, F. (2008). "Mechanistic interpretation and utilization of viscoelastic behavior of polymer solutions for improved polymer-flood efficiency". In: *SPE Symposium on Improved Oil Recovery*. Society of Petroleum Engineers.
- Ding, Y. (1996). "A generalized 3D well model for reservoir simulation". In: *SPE Journal* 1.04, pp. 437–450.
- Dong, H., Fang, S., Wang, D., Wang, J., Liu, Z. L., and Hou, W. (2008). "Review of practical experience & management by polymer flooding at Daqing". In: *SPE Symposium on Improved Oil Recovery*. Society of Petroleum Engineers.
- Dullien, F. A. (1992). *Porous media: fluid transport and pore structure*. 2nd. Academic Press.

- Dyes, A., Caudle, B., and Erickson, R. (1954). "Oil production after breakthrough as influenced by mobility ratio". In: *Journal of Petroleum Technology* 6.4, pp. 27–32.
- Dyes, A., Kemp, C., and Caudle, B. (1958). "Effect of fractures on sweep-out pattern". In: *Trans., AIME*, pp. 245–249.
- Evje, S. and Hiorth, A. (2010). "A mathematical model for dynamic wettability alteration controlled by water-rock chemistry." In: *NHM* 5.2, pp. 217–256.
- Evje, S., Hiorth, A., Madland, M. V., and Korsnes, R. I. (2009). "A mathematical model relevant for weakening of chalk reservoirs due to chemical reactions." In: *NHM* 4.4, pp. 755–788.
- Ewoldt, R. H., Johnston, M. T., and Caretta, L. M. (2015). "Experimental challenges of shear rheology: how to avoid bad data". In: *Complex Fluids in Biological Systems*. Springer, pp. 207–241.
- Fahraeus, R. and Lindqvist, T. (1931). "The viscosity of the blood in narrow capillary tubes". In: *American Journal of Physiology* 96.3, pp. 562–568.
- Fanchi, J. R. (1983). "Multidimensional numerical dispersion". In: *Society of Petroleum Engineers Journal* 23.1, pp. 143–151.
- Fjelde, I., Lohne, A., and Abeysinghe, K. P. (2015). "Critical Aspects in Surfactant Flooding Procedure at Mixed-wet Conditions". In: *EUROPEC 2015*. Society of Petroleum Engineers.
- Fletcher, A., Flew, S., Lamb, S., Lund, T., Bjornestad, E., Stavland, A., and Gjovikli, N. (1991). "Measurements of polysaccharide polymer properties in porous media". In: *SPE International Symposium on Oilfield Chemistry*. Society of Petroleum Engineers.
- Gerland, P., Raftery, A. E., Ševčíková, H., Li, N., Gu, D., Spoorenberg, T., Alkema, L., Fosdick, B. K., Chunn, J., and Lalic, N. (2014). "World population stabilization unlikely this century". In: *Science* 346.6206, pp. 234–237.
- Glasbergen, G., Wever, D., Keijzer, E., and Farajzadeh, R. (2015). "Injectivity loss in polymer floods: causes, preventions and mitigations". In: *SPE Kuwait Oil and Gas Show and Conference*. Society of Petroleum Engineers.
- Groisman, A. and Steinberg, V. (2000). "Elastic turbulence in a polymer solution flow". In: *Nature* 405.6782, p. 53.
- Gupta, R. and Sridhar, T. (1985). "Viscoelastic effects in non-Newtonian flows through porous media". In: *Rheologica acta* 24.2, pp. 148–151.
- Haas, R. and Durst, F. (1982). "Viscoelastic flow of dilute polymer solutions in regularly packed beds". In: *Progress and Trends in Rheology*. Springer, pp. 212–217.
- Heemskerk, J., Rosmalen, R., Janssen-van, R., Holtslag, R., and Teeuw, D. (1984). "Quantification of viscoelastic effects of polyacrylamide solutions". In: *SPE Enhanced Oil Recovery Symposium*. Society of Petroleum Engineers.
- Hiemenz, P. C. and Lodge, T. P. (2007). *Polymer chemistry*. 2nd. CRC Press.
- Hiorth, A., Jettestuen, E., Cathles, L. M., and Madland, M. V. (2013). "Precipitation, dissolution, and ion exchange processes coupled with a lattice Boltzmann advection diffusion solver". In: *Geochimica et Cosmochimica Acta* 104, pp. 99–110.

- Homsy, G. M. (1987). “Viscous fingering in porous media”. In: *Annual review of fluid mechanics* 19.1, pp. 271–311.
- Hou, C. T., Barnabe, N., and Greaney, K. (1986). “Biodegradation of xanthan by salt-tolerant aerobic microorganisms”. In: *Journal of Industrial Microbiology & Biotechnology* 1.1, pp. 31–37.
- Howe, A. M., Clarke, A., and Giernalczyk, D. (2015). “Flow of concentrated viscoelastic polymer solutions in porous media: effect of MW and concentration on elastic turbulence onset in various geometries”. In: *Soft Matter* 11.32, pp. 6419–6431.
- Hubbert, M. K. (1956). “Darcy’s law and the field equations of the flow of underground fluids”. In: *Transactions of the American Institute of Mining and Metallurgical Engineers* 207, pp. 222–239.
- Jennings, R., Rogers, J., and West, T. (1971). “Factors influencing mobility control by polymer solutions”. In: *Journal of Petroleum Technology* 23.03, pp. 391–401.
- Jha, R. K., Bryant, S., and Lake, L. W. (2011). “Effect of diffusion on dispersion”. In: *SPE Journal* 16.01, pp. 65–77.
- Jiang, Y. (2008). “Techniques for modeling complex reservoirs and advanced wells”. PhD thesis. Stanford University.
- Johan Sverdrup-Polymer (2018). URL: http://www.force.org/Global/Seminars/2016/2016_04_05%20Polymer%20Flooding/Statoil%20presentation.pdf (visited on 03/23/2018).
- Jouenne, S., Klimenko, A., and Levitt, D. (2016). “Tradeoffs Between Emulsion and Powder Polymers for EOR”. In: *SPE Improved Oil Recovery Conference*. Society of Petroleum Engineers.
- Kawale, D., Marques, E., Zitha, P. L., Kreutzer, M. T., Rossen, W. R., and Boukany, P. E. (2017). “Elastic instabilities during the flow of hydrolyzed polyacrylamide solution in porous media: effect of pore-shape and salt”. In: *Soft Matter* 13.4, pp. 765–775.
- Kazemi Nia Korrani, A., Sepehrnoori, K., and Delshad, M. (2013). “A novel mechanistic approach for modeling low salinity water injection”. In: *SPE Annual Technical Conference and Exhibition*. Society of Petroleum Engineers.
- (2016). “A Mechanistic Integrated Geochemical and Chemical-Flooding Tool for Alkaline/Surfactant/Polymer Floods”. In: *SPE Journal* 21.01, pp. 32–54.
- Keller, A. and Odell, J. (1985). “The extensibility of macromolecules in solution; a new focus for macromolecular science”. In: *Colloid and Polymer Science* 263.3, pp. 181–201.
- Knight, B. L. (1973). “Reservoir stability of polymer solutions”. In: *Journal of Petroleum Technology* 25.05, pp. 618–626.
- Lakatos, I., Lakatos-Szabo, J., and Toth, J. (1981). “Factors influencing polyacrylamide adsorption in porous media and their effect on flow behavior”. In: *Surface Phenomena in Enhanced Oil Recovery*. Springer, pp. 821–842.
- Lake, L. W. (1989). *Enhanced oil recovery*. Prentice Hall Inc., Old Tappan, NJ.
- Lantz, R. (1971). “Quantitative evaluation of numerical diffusion (truncation error)”. In: *Society of Petroleum Engineers Journal* 11.03, pp. 315–320.

- Lee, J. (2013). “Upscaling polymer flooding in heterogeneous reservoirs”. PhD thesis.
- Lenormand, R. and Zacone, C. (1988). “Physics of blob displacement in a two-dimensional porous medium”. In: *SPE Formation Evaluation* 3.01, pp. 271–275.
- LeVeque Randall, J. (1992). “Numerical methods for conservation laws”. In: *Lectures in Mathematics ETH Zürich*.
- Levitt, D. B., Pope, G. A., and Jouenne, S. (2011a). “Chemical degradation of polyacrylamide polymers under alkaline conditions”. In: *SPE Reservoir Evaluation & Engineering* 14.03, pp. 281–286.
- Levitt, D. B., Slaughter, W., Pope, G., and Jouenne, S. (2011b). “The effect of redox potential and metal solubility on oxidative polymer degradation”. In: *SPE Reservoir Evaluation & Engineering* 14.03, pp. 287–298.
- Li, X.-B., Li, F.-C., Cai, W.-H., Zhang, H.-N., and Yang, J.-C. (2012). “Very-low-Re chaotic motions of viscoelastic fluid and its unique applications in microfluidic devices: a review”. In: *Experimental thermal and fluid science* 39, pp. 1–16.
- Li, Z., Fortenberry, R., Luo, H., and Delshad, M. (2017). “An examination of the concept of apparent skin factor in modeling injectivity of non-Newtonian polymer solutions”. In: *Journal of Petroleum Science and Engineering* 158, pp. 160–174.
- Lichtner, P. C. (1996). “Continuum formulation of multicomponent-multiphase reactive transport”. In: *Reviews in Mineralogy and Geochemistry* 34.1, pp. 1–81.
- Lohne, A. (2018). *User’s manual for IORCoreSim - combined EOR and SCAL simulator*.
- Lohne, A., Nødland, O., Stavland, A., and Hiorth, A. (2017). “A model for non-Newtonian flow in porous media at different flow regimes”. In: *Computational Geosciences* 21.5-6, pp. 1289–1312.
- Lohne, A., Virnovsky, G. A., and Durlofsky, L. J. (2006). “Two-stage upscaling of two-phase flow: from core to simulation scale”. In: *Spe Journal* 11.03, pp. 304–316.
- Macosko, C. W. and Larson, R. G. (1994). *Rheology: principles, measurements, and applications*. VCH New York.
- Madland, M., Hiorth, A., Omdal, E., Megawati, M., Hildebrand-Habel, T., Korsnes, R., Evje, S., and Cathles, L. (2011). “Chemical alterations induced by rock–fluid interactions when injecting brines in high porosity chalks”. In: *Transport in porous media* 87.3, pp. 679–702.
- Maerker, J. (1975). “Shear degradation of partially hydrolyzed polyacrylamide solutions”. In: *Society of Petroleum Engineers Journal* 15.04, pp. 311–322.
- Magueur, A., Moan, M., and Chauveteau, G. (1985). “Effect of successive contractions and expansions on the apparent viscosity of dilute polymer solutions”. In: *Chemical engineering communications* 36.1-6, pp. 351–366.
- Manichand, R. N., Let, M. S., Kathleen, P., Gil, L., Quillien, B., and Seright, R. S. (2013). “Effective propagation of HPAM solutions through the Tambaredjo

- reservoir during a polymer flood”. In: *SPE Production & Operations* 28.04, pp. 358–368.
- Martin, F. (1986). “Mechanical degradation of polyacrylamide solutions in core plugs from several carbonate reservoirs”. In: *SPE Formation Evaluation* 1.02, pp. 139–150.
- Masuda, Y., Tang, K.-C., Miyazawa, M., and Tanaka, S. (1992). “1D simulation of polymer flooding including the viscoelastic effect of polymer solution”. In: *SPE reservoir engineering* 7.02, pp. 247–252.
- Moradi-Araghi, A. and Doe, P. H. (1987). “Hydrolysis and precipitation of polyacrylamides in hard brines at elevated temperatures”. In: *SPE reservoir Engineering* 2.02, pp. 189–198.
- Morel, D., Zaugg, E., Jouenne, S., Danquigny, J., and Cordelier, P. (2015). “Dalia/Camelia Polymer Injection in Deep Offshore Field Angola Learnings and in Situ Polymer Sampling Results”. In: *SPE Asia Pacific Enhanced Oil Recovery Conference*. Society of Petroleum Engineers.
- Morris, C. and Jackson, K. (1978). “Mechanical degradation of polyacrylamide solutions in porous media”. In: *SPE Symposium on Improved Methods of Oil Recovery*. Society of Petroleum Engineers.
- Morrow, N., Chatzis, I., and Taber, J. (1988). “Entrapment and mobilization of residual oil in bead packs”. In: *SPE Reservoir Engineering* 3.03, pp. 927–934.
- Muggeridge, A., Cockin, A., Webb, K., Frampton, H., Collins, I., Moulds, T., and Salino, P. (2014). “Recovery rates, enhanced oil recovery and technological limits”. In: *Phil. Trans. R. Soc. A* 372.2006, p. 20120320.
- Mungan, N. (1972). “Shear viscosities of ionic polyacrylamide solutions”. In: *Society of Petroleum Engineers Journal* 12.06, pp. 469–473.
- Mykkeltvedt, T. S., Raynaud, X., and Lie, K.-A. (2017). “Fully implicit higher-order schemes applied to polymer flooding”. In: *Computational Geosciences* 21.5-6, pp. 1245–1266.
- NIORC (2018). *The National IOR Centre of Norway, Annual Report 2017*. URL: https://www.uis.no/getfile.php/13428558/IOR-senter/Vedlegg/Annual_Report_2017_net.pdf (visited on 08/06/2018).
- Nødland, O., Lohne, A., Stavland, A., and Hiorth, A. (2016). “A Model for Non-Newtonian Flow in Porous Media at Different Flow Regimes”. In: *ECMOR XV-15th European Conference on the Mathematics of Oil Recovery*.
- Norwegian Petroleum Directorate (2017). *Resource Report 2017*. URL: <http://ressursrapport2017.npd.no/en/> (visited on 03/23/2018).
- Oil & Gas Authority (2016). *Enhanced Oil Recovery (EOR) Strategy*. URL: https://www.gov.uk/government/uploads/system/uploads/attachment_data/file/540028/OGA_EOR_Strategy.pdf (visited on 03/23/2018).
- (2017a). *Polymer Enhanced Oil Recovery - Industry lessons learned*. URL: <https://www.ogauthority.co.uk/media/4283/polymer-eor-industry-starter-pack-ver3.pdf> (visited on 03/23/2018).
- (2017b). *Recovery Factor Benchmarking*. URL: <https://www.ogauthority.co.uk/media/4155/recovery-factor-report-7-september.pdf> (visited on 07/23/2018).

- Okstad, K. A. (2018). *Slik kan oljeteknologi hjelpe hjertepasienter*. URL: <https://forskning.no/bransje-petroleum-fysikk-hjertet/slik-kan-oljeteknologi-hjelpe-hjertepasienter/298144> (visited on 08/06/2018).
- Omekeh, A. V., Friis, H. A., Fjelde, I., and Evje, S. (2012). “Modeling of ion-exchange and solubility in low salinity water flooding”. In: *SPE improved oil recovery symposium*. Society of Petroleum Engineers.
- Pakdel, P. and McKinley, G. H. (1996). “Elastic instability and curved streamlines”. In: *Physical Review Letters* 77.12, p. 2459.
- Patton, J., Coats, K., and Colegrove, G. (1971). “Prediction of polymer flood performance”. In: *Society of Petroleum Engineers Journal* 11.01, pp. 72–84.
- Peaceman, D. W. (1978). “Interpretation of well-block pressures in numerical reservoir simulation”. In: *Society of Petroleum Engineers Journal* 18.3, pp. 183–194.
- (1983). “Interpretation of well-block pressures in numerical reservoir simulation with nonsquare grid blocks and anisotropic permeability”. In: *Society of Petroleum Engineers Journal* 23.03, pp. 531–543.
- Perkins, T. T., Smith, D. E., and Chu, S. (1997). “Single polymer dynamics in an elongational flow”. In: *Science* 276.5321, pp. 2016–2021.
- Perkins, T., Smith, D., and Chu, S. (1999). “Single polymers in elongational flows: Dynamic, steady-state, and population-averaged properties”. In: *Flexible Polymer Chains in Elongational Flow*. Springer, pp. 283–334.
- Poole, R. (2012). “The Deborah and Weissenberg numbers”. In: *British Soc. Rheol. Rheol. Bull* 53, pp. 32–39.
- Pope, G. and Nelson, R. (1978). “A chemical flooding compositional simulator”. In: *Society of Petroleum Engineers Journal* 18.05, pp. 339–354.
- Pope, G. A. (1980). “The application of fractional flow theory to enhanced oil recovery”. In: *Society of Petroleum Engineers Journal* 20.03, pp. 191–205.
- Pope, G. A., Sepehrnoori, K., and Delshad, M. (2000). *Development of an Improved Simulator for Chemical and Microbial EOR Methods*. Tech. rep. National Petroleum Technology Office, Tulsa, OK (US).
- Petroleum Safety Authority Norway (2018). *Regulations relating to conducting petroleum activities (The Activities Regulations)*. URL: <http://www.ptil.no/activities/category399.html/> (visited on 01/02/2018).
- Puls, C., Clemens, T., Sledz, C., Kadnar, R., and Gumpenberger, T. (2016). “Mechanical Degradation of Polymers During Injection, Reservoir Propagation and Production-Field Test Results 8 TH Reservoir, Austria”. In: *SPE Europec featured at 78th EAGE Conference and Exhibition*. Society of Petroleum Engineers.
- Pye, D. J. (1964). “Improved secondary recovery by control of water mobility”. In: *Journal of Petroleum technology* 16.8, pp. 911–916.
- Qi, P., Ehrenfried, D. H., Koh, H., and Balhoff, M. T. (2017). “Reduction of Residual Oil Saturation in Sandstone Cores by Use of Viscoelastic Polymers”. In: *SPE Journal* 22.02, pp. 447–458.
- Reiner, M. (1964). “The Deborah number”. In: *Physics today* 17.1, p. 62.
- Ryles, R. (1988). “Chemical stability limits of water-soluble polymers used in oil recovery processes”. In: *SPE Reservoir Engineering* 3.1, pp. 23–34.

- Al-saadi, F. S., Al-amri, B. A., Nofli, A., Mubarak, S., Van Wunnik, J. N., Jaspers, H. F., Al Harthi, S., Shuaili, K., Cherukupalli, P. K., and Chakravarthi, R. (2012). "Polymer Flooding in a Large Field in South Oman-Initial Results and Future Plans". In: *SPE EOR Conference at Oil and Gas West Asia*. Society of Petroleum Engineers.
- Saboorian-Jooybari, H., Dejam, M., and Chen, Z. (2015). "Half-Century of Heavy Oil Polymer Flooding from Laboratory Core Floods to Pilot Tests and Field Applications". In: *SPE Canada Heavy Oil Technical Conference*. Society of Petroleum Engineers.
- Sandiford, B. (1964). "Laboratory and field studies of water floods using polymer solutions to increase oil recoveries". In: *Journal of Petroleum Technology* 16.08, pp. 917–922.
- Schroeder, C. M., Teixeira, R. E., Shaqfeh, E. S., and Chu, S. (2005). "Characteristic periodic motion of polymers in shear flow". In: *Physical review letters* 95.1, p. 018301.
- Seright, R. S. (1983). "The effects of mechanical degradation and viscoelastic behavior on injectivity of polyacrylamide solutions". In: *Society of Petroleum Engineers Journal* 23.03, pp. 475–485.
- (2017). "How Much Polymer Should Be Injected During a Polymer Flood? Review of Previous and Current Practices". In: *IOR 2017-19th European Symposium on Improved Oil Recovery*.
- Seright, R. S., Campbell, A., Mozley, P., and Han, P. (2010). "Stability of partially hydrolyzed polyacrylamides at elevated temperatures in the absence of divalent cations". In: *Spe Journal* 15.02, pp. 341–348.
- Seright, R. S., Fan, T., Wavrik, K., and Balaban, R. d. C. (2011). "New insights into polymer rheology in porous media". In: *SPE Journal* 16.01, pp. 35–42.
- Seright, R. S., Seheult, J. M., and Talashek, T. (2008). "Injectivity characteristics of EOR polymers". In: *SPE annual technical conference and exhibition*. Society of Petroleum Engineers.
- Seright, R., Zhang, G., Akanni, O., and Wang, D. (2012). "A comparison of polymer flooding with in-depth profile modification". In: *Journal of Canadian Petroleum Technology* 51.05, pp. 393–402.
- Shah, B. N., Lawrence, G., Willhite, P., and Green, D. W. (1978). "The effect of inaccessible pore volume on the flow of polymer and solvent through porous media". In: *SPE Annual Fall Technical Conference and Exhibition*. Society of Petroleum Engineers.
- Al-Shalabi, E. W. and Sepehrnoori, K. (2016). "A comprehensive review of low salinity/engineered water injections and their applications in sandstone and carbonate rocks". In: *Journal of Petroleum Science and Engineering* 139, pp. 137–161.
- Shaqfeh, E. S. (2005). "The dynamics of single-molecule DNA in flow". In: *Journal of Non-Newtonian Fluid Mechanics* 130.1, pp. 1–28.
- Sheng, J. (2010). *Modern chemical enhanced oil recovery: theory and practice*. Gulf Professional Publishing.

- Sheng, J. J., Leonhardt, B., and Azri, N. (2015). "Status of polymer-flooding technology". In: *Journal of Canadian Petroleum Technology* 54.02, pp. 116–126.
- Shupe, R. D. (1981). "Chemical stability of polyacrylamide polymers". In: *Journal of Petroleum Technology* 33.08, pp. 1513–1529.
- Smith, D. E., Babcock, H. P., and Chu, S. (1999). "Single-polymer dynamics in steady shear flow". In: *Science* 283.5408, pp. 1724–1727.
- Smith, D. E. and Chu, S. (1998). "Response of flexible polymers to a sudden elongational flow". In: *Science* 281.5381, pp. 1335–1340.
- Smith, F. W. (1970). "The behavior of partially hydrolyzed polyacrylamide solutions in porous media". In: *Journal of Petroleum Technology* 22.02, pp. 148–156.
- Al-Sofi, A. M. and Blunt, M. J. (2010). "Control of numerical dispersion in simulations of augmented waterflooding". In: *SPE Improved Oil Recovery Symposium*. Society of Petroleum Engineers.
- Al-Sofi, A. M., La Force, T., and Blunt, M. J. (2009). "Sweep impairment due to polymers shear thinning". In: *SPE Middle East Oil and Gas Show and Conference*. Society of Petroleum Engineers.
- Sorbie, K. S. (1991). *Polymer-improved oil recovery*. Springer Science & Business Media.
- Sorbie, K. (1990). "Depleted layer effects in polymer flow through porous media: I. Single capillary calculations". In: *Journal of colloid and interface science* 139.2, pp. 299–314.
- Sorbie, K. and Huang, Y. (1991). "Rheological and transport effects in the flow of low-concentration xanthan solution through porous media". In: *Journal of Colloid and Interface Science* 145.1, pp. 74–89.
- Sorbie, K., Parker, A., and Clifford, P. (1987). "Experimental and theoretical study of polymer flow in porous media". In: *SPE Reservoir Engineering* 2.03, pp. 281–304.
- Southwick, J. and Manke, C. (1988). "Molecular degradation, injectivity, and elastic properties of polymer solutions". In: *SPE reservoir engineering* 3.04, pp. 1193–1201.
- Spillette, A., Hillestad, J., and Stone, H. (1973). "A high-stability sequential solution approach to reservoir simulation". In: *Fall Meeting of the Society of Petroleum Engineers of AIME*. Society of Petroleum Engineers.
- Standnes, D. C. and Skjevrak, I. (2014). "Literature review of implemented polymer field projects". In: *Journal of Petroleum Science and Engineering* 122, pp. 761–775.
- Stavland, A., Asen, S., Mebratu, A., and Gathier, F. (2016). "Impact of Choke Valves on the IOR Polymer Flooding: Lessons Learned from Large Scale Tests". In: *37th Annual Workshop & Symposium IEA-EOR, Rueil-Malmaison*, pp. 18–22.
- Stavland, A., Jonsbrotten, H., Lohne, A., Moen, A., and Giske, N. (2010). "Polymer Flooding–Flow Properties in Porous Media Versus Rheological Parameters". In: *Presented at the 72nd EAGE Conference and Exhibition incorporating SPE EUROPEC, SPE-131103-MS*.

- Stavland, A., Jonsbrotten, H., and Strand, D. (2013). “When will polymer viscosity be a design criterion for EOR polymer flooding?” In: *IEA-EOR 34th Annual Symposium, Stavanger, Norway*.
- Stosur, G. J., Hite, J. R., Carnahan, N. F., and Miller, K. (2003). “The alphabet soup of IOR, EOR and AOR: effective communication requires a definition of terms”. In: *SPE International Improved Oil Recovery Conference in Asia Pacific*. Society of Petroleum Engineers.
- Sutera, S. P. and Skalak, R. (1993). “The history of Poiseuille’s law”. In: *Annual Review of Fluid Mechanics* 25.1, pp. 1–20.
- Taylor, G. I. (1953). “Dispersion of soluble matter in solvent flowing slowly through a tube”. In: *Proc. R. Soc. Lond. A* 219.1137, pp. 186–203.
- Taylor, K. C. and Nasr-El-Din, H. A. (1998). “Water-soluble hydrophobically associating polymers for improved oil recovery: A literature review”. In: *Journal of Petroleum Science and Engineering* 19.3-4, pp. 265–280.
- Teeuw, D. and Hesselink, F. T. (1980). “Power-law flow and hydrodynamic behaviour of biopolymer solutions in porous media”. In: *SPE Oilfield and Geothermal Chemistry Symposium*. Society of Petroleum Engineers.
- Teixeira, R. E., Babcock, H. P., Shaqfeh, E. S., and Chu, S. (2005). “Shear thinning and tumbling dynamics of single polymers in the flow-gradient plane”. In: *Macromolecules* 38.2, pp. 581–592.
- Thomas, A., Gaillard, N., and Favero, C. (2012). “Some key features to consider when studying acrylamide-based polymers for chemical enhanced oil recovery”. In: *Oil & Gas Science and Technology—Revue d’IFP Energies nouvelles* 67.6, pp. 887–902.
- Todd, M., O’dell, P., and Hirasaki, G. (1972). “Methods for increased accuracy in numerical reservoir simulators”. In: *Society of Petroleum Engineers Journal* 12.06, pp. 515–530.
- Trangenstein, J. A. and Bell, J. B. (1989a). “Mathematical structure of compositional reservoir simulation”. In: *SIAM journal on scientific and statistical computing* 10.5, pp. 817–845.
- (1989b). “Mathematical structure of the black-oil model for petroleum reservoir simulation”. In: *SIAM Journal on Applied Mathematics* 49.3, pp. 749–783.
- Tree, D. R., Muralidhar, A., Doyle, P. S., and Dorfman, K. D. (2013). “Is DNA a good model polymer?” In: *Macromolecules* 46.20, pp. 8369–8382.
- Vermolen, E., Van Haasterecht, M., and Masalmeh, S. (2014). “A systematic study of the polymer visco-elastic effect on residual oil saturation by core flooding”. In: *SPE EOR Conference at Oil and Gas West Asia*. Society of Petroleum Engineers.
- Walters, K. (1980). *Rheometry, industrial applications*. Vol. 1. Research Studies Press.
- Wang, D., Cheng, J., Wu, J., and Wang, G. (2002). “Experiences learned after production of more than 300 million barrels of oil by polymer flooding in Daqing oil field”. In: *SPE Annual Technical Conference and Exhibition*. Society of Petroleum Engineers.

- Wang, D., Cheng, J., Yang, Q., Wenchao, G., Qun, L., and Chen, F. (2000). “Viscous-elastic polymer can increase microscale displacement efficiency in cores”. In: *SPE annual technical conference and exhibition*. Society of Petroleum Engineers.
- Wang, D., Dong, H., Lv, C., Fu, X., and Nie, J. (2009). “Review of practical experience by polymer flooding at Daqing”. In: *SPE Reservoir Evaluation & Engineering* 12.03, pp. 470–476.
- Wang, D., Han, P., Shao, Z., Hou, W., and Seright, R. S. (2008). “Sweep-improvement options for the Daqing oil field”. In: *SPE Reservoir Evaluation & Engineering* 11.01, pp. 18–26.
- Ward, J. and Martin, F. D. (1981). “Prediction of viscosity for partially hydrolyzed polyacrylamide solutions in the presence of calcium and magnesium ions”. In: *Society of Petroleum Engineers Journal* 21.05, pp. 623–631.
- Watts, J. (1986). “A Compositional formulation of the pressure and saturation equations”. In: *SPE Reservoir Engineering* 1.03, pp. 243–252.
- (1997). “Reservoir simulation: Past, present, and future”. In: *SPE Computer Applications* 9.06, pp. 171–176.
- Welge, H. J. (1952). “A simplified method for computing oil recovery by gas or water drive”. In: *Journal of Petroleum Technology* 4.04, pp. 91–98.
- Wreath, D., Pope, G., and Sepehrnoori, K. (1990). “Dependence of polymer apparent viscosity on the permeable media and flow conditions”. In: *In Situ* 14.3, pp. 263–283.
- Yang, S. and Treiber, L. (1985). “Chemical stability of polyacrylamide under simulated field conditions”. In: *SPE Annual Technical Conference and Exhibition*. Society of Petroleum Engineers.
- Zaitoun, A. and Kohler, N. (1988). “Two-phase flow through porous media: effect of an adsorbed polymer layer”. In: *SPE Annual Technical Conference and Exhibition*. Society of Petroleum Engineers.
- Zaitoun, A., Makakou, P., Blin, N., Al-Maamari, R. S., Al-Hashmi, A.-A. R., and Abdel-Goad, M. (2012). “Shear stability of EOR polymers”. In: *SPE Journal* 17.02, pp. 335–339.
- Zhang, G. and Seright, R. (2014). “Effect of concentration on HPAM retention in porous media”. In: *SPE Journal* 19.03, pp. 373–380.

Papers

Paper I

A Model for Non-Newtonian Flow in Porous Media at Different Flow Regimes

By:

Nødland, Oddbjørn

Lohne, Arild

Stavland, Arne

Hiorth, Aksel

Presented as a poster at:

ECMOR XV - 15th European Conference on the Mathematics of Oil
Recovery (2016).

Summary

The EOR potential of polymer flooding is well documented in the scientific literature. However, it has remained a challenge to create good simulation tools that can be used for predictive purposes. A main limitation with the current models is the insufficient description of the transition between the different flow regimes that characterize the polymer rheology. Typically, Newtonian behaviour is observed at low shear rates, followed by shear-thinning, shear-thickening and shear-degradation regimes at increasing shear rates. Furthermore this is complicated by the fact that the apparent viscosity of the polymer is influenced by a combination of factors, such as adsorption, brine salinity, polymer concentration and molecular weight.

In this work we present a core scale simulation model that is capable of describing all the aforementioned flow regimes. The novel feature of the proposed model is the inclusion of an equation to describe polymer (mechanical) degradation. The polymer degradation rate is linked to the effective pore radius (via permeability through a Kozeny-Carman type equation), wall shear stress, and polymer molecular weight, M_w . The degradation results in a lower M_w , while the polymer volumetric concentration is unaffected. The change in M_w over a time step is found using an implicit chord method at the end of each transport time step, and the solution is then used to update the effective polymer properties. The main flow field is computed using a standard sequential algorithm, where a linear pressure equation is solved first, followed by an implicit saturation equation formulated in a fractional flow approach.

The model is applied to a series of laboratory experiments. Our model explains the core data very well, taking into account that several experimental factors have been varied such as synthetic polymer types, core length and permeability.

Introduction

Polymers added to the injection brine increase the aqueous phase viscosity, which leads to a reduction in the mobility ratio between water and oil, $M = \lambda_w/\lambda_o$. This results in better sweep and hence, in faster production of oil. However, many factors must be considered for the proper evaluation of a polymer flooding project. Aside from more practical issues, such as economic viability and environmental concerns, there are still many theoretical challenges remaining when it comes to predicting polymer behaviour inside a reservoir. In particular, we need to improve our understanding of the different rheological flow regimes of the polymer, and how they depend upon local variations in the reservoir parameters, such as porosity, permeability, temperature, and brine salinity. This is crucial if we are to obtain higher predictive accuracy for simulation of polymer flooding at the field scale.

One critical factor to consider is polymer mechanical degradation in porous media. It is well documented that when sufficient extensional forces are applied, the chemical bonds of a polymer molecule will rupture (Maerker, 1975; Seright, 1983). This can result in a dramatic decrease in the effective polymer molecular weight and viscosity, which will lower the EOR potential of the polymer flood. The issue of mechanical degradation is especially critical in regions of high flow rates and in turbulent flow, such as in the injection facilities and near the wellbore, and it has been found that the amount of polymer that gets degraded is greatly affected by the type of high shear equipment used, such as the choice of pumps, chokes and valves (Thomas et al., 2012). To this end, use of proper equipment can help minimize the viscosity loss caused by polymer chain scission near the injector. However, it is important to establish whether significant degradation can occur deeper within the formation as well, and if so, to what extent.

In order to better quantify the uncertainties surrounding a polymer flooding project, we therefore need to include all of the relevant physics into our simulation tools. To the best of our knowledge, the commercial simulators available on the market today do not provide an adequate description of polymer degradation in porous media. In this paper, we present a core scale simulation model that covers all the experimentally observed flow regimes, including shear thinning, shear thickening, and shear degrading flow. A challenge with models for polymers in a porous medium is that they contain a large number of parameters that needs to be determined experimentally. A novel feature of our model is that that we are able to reduce the number of free parameters greatly by applying pore scale models. Thus we can simulate the behaviour of different polymers with the same set of input parameters.

Mathematical model description and preliminary discussion

The traditional way of modeling fluid flow in reservoir simulators is to employ Darcy's law, which for a 1-phase fluid in the absence of gravity takes the form

$$q = -\frac{k}{\eta}\nabla p, \quad (1)$$

where q is the average fluid (Darcy) velocity, k is the permeability, η is the viscosity, and p is the pressure. However, this equation is strictly speaking only valid for Newtonian fluids, which are characterized by a direct proportionality between stress and strain rate (shear rate). In contrast, the relationship between stress and strain can for non-Newtonian fluids be very complex, with both the geometry and the history of the flow greatly affecting the fluid behaviour (Sochi, 2010). This is clearly the situation for EOR polymers in porous media, which have been seen to display both pseudoplastic (shear thinning) and dilatant (shear thickening) behaviour, depending on the conditions. In order to properly model polymer flooding at the core scale and the field scale, it is therefore necessary to operate with an effective viscosity, η , which will have to be a function of the local reservoir parameters, and that takes into account both shearing and extensional contributions to the flow resistance. Complicating matters even further, a polymer subjected to excessive amounts of stress can break, leading to irreversible damage to the molecular structure, and thus to a permanent change in the fluid properties.

In this work we propose the following model for the effective (apparent) viscosity, η :

$$\eta = \eta_s + (\eta_{sh} - \eta_s) \cdot \eta_{el}. \quad (2)$$

That is, we calculate the total apparent viscosity as consisting of a viscous, shear thinning part, η_{sh} , and an elongational/extensional part, η_{el} , where the latter will satisfy $\eta_{el} \approx 1.0$ at low shear rates. Moreover, each of the two viscosities will be related to the local rock and fluid properties. In expression (2), η_s is the solvent viscosity.

In addition to the effects of the different flow regimes, it is important to consider the fact that polymers can adsorb on the rock, and that large polymer molecules may be physically hindered from flowing in all parts of the pore space. The latter effect will increase the transport velocity of the polymer through the reservoir, and can also modify the viscosity. Furthermore, when polymers adsorb the permeability might change, and this must be taken into account. Finally, in a field case there will, in addition to spatial variation in permeability and porosity, be (possibly large) gradients in temperature and salinity, stemming from differences between the injection and formation brines. Temperatures deep within the reservoir are typically much hotter than the injected water, and the ion concentrations that are injected are usually lower than those already present in the formation.

The rest of this article is organized as follows. First, we give a thorough account of the mathematical model used to describe the polymer rheology in porous media, i.e., we derive expressions for η_{sh} and η_{el} . We start by describing the shear thinning model, which we subsequently test by comparing it to bulk rheology data from Stavland et al. (2010). Next, we present models that can be used to simulate the shear thickening and degradation flow regimes, before we shortly discuss how polymer adsorption can influence the permeability of the rock. Then, we summarize the entire viscosity model with focus on numerical implementation. Finally, we apply the model to experimental core flooding data, also from Stavland et al. (2010), and we discuss the applicability of the model. Other important factors that are needed in the model, such as excluded volume effects and the roles of temperature and salinity, are relegated to an Appendix at the back.

Shear thinning model and rotational relaxation time

The shear thinning behaviour of EOR polymers can normally be well matched with a Carreau-Yasuda model (Bird et al., 1977; Yasuda et al., 1981):

$$\frac{\eta_{sh} - \eta_s}{\eta_{sh0} - \eta_s} = (1 + (\lambda_1 \dot{\gamma})^x)^{-n/x}. \quad (3)$$

Here η_{sh} is the shear thinning viscosity at a given shear rate, $\dot{\gamma}$, and η_{sh0} is the shear thinning viscosity at zero shear rate (Newtonian regime). The parameter λ_1 is a time constant that determines the onset of shear thinning (rotational relaxation time), and x and $n > 0$ are dimensionless tuning parameters, with x determining the sharpness of the transition from the Newtonian to the shear thinning regime. Higher values of x indicate a sharper transition. The Carreau-Yasuda equation can be rewritten in terms of the specific viscosity as

$$\eta_{sp} = \eta_{sp0} \cdot (1 + (\lambda_1 \dot{\gamma})^x)^{-n/x}. \quad (4)$$

The specific viscosity, η_{sp} , provides a measure of the incremental amount of viscosity added by the polymer relative to the pure solvent:

$$\eta_{sp} = \eta_{sh}/\eta_s - 1. \quad (5)$$

In the limit of high shear rates, equation (4) becomes a power-law model in the specific viscosity with slope equal to $-n$. The parameter n is known as the shear thinning index. The values of the parameters λ_1 and n will in general be valid only for a specific polymer-solvent combination at a specific temperature, and at a given polymer concentration. Therefore, in order to reduce the amount of free parameters, it would be of great interest to be able to relate λ_1 and n to other, known parameters in the model. In the rest of this subsection, we will propose a way to do this. Before we start, we need to introduce the fundamental notion of the polymer *intrinsic viscosity*, which is a measure of the effective hydrodynamic volume of the polymer in solution (Hiemenz and Lodge, 2007). It is defined as

$$[\eta] = \lim_{c_p \rightarrow 0} \frac{\eta_{sh} - \eta_s}{c_p \eta_s}, \quad (6)$$

where c_p is the mass concentration of polymer. It is clear that $[\eta]$ has units of inverse concentration. The polymer intrinsic viscosity is typically estimated from lab measurements by plotting the the reduced (specific) viscosity, $\eta_{red} := \eta_{sp}/c_p$, versus dilute polymer concentration, and then extrapolating to $c_p = 0$. It is common to calculate the intrinsic viscosity from the molecular weight, M_w , by means of the Mark-Houwink equation:

$$[\eta] = K \cdot M_w^a. \quad (7)$$

In equation (7), K and a are constants, which in general will depend upon the given polymer-solvent pair, and the solution temperature. For random chain polymers in good solvents, typical values of a lie in the range 0.5-0.8 (Hiemenz and Lodge, 2007). It should be mentioned that due to the inherent polydispersivity of many polymers, an estimate of the molecular weight based on equation (7) gives a viscosity-averaged value of the molecular weight.

In this work we calculate the specific viscosity at zero shear rate, η_{sp0} , as a cubic polynomial in the intrinsic viscosity (a modified Huggins equation):

$$\eta_{sp0} = [\eta]c_p + k'[\eta]^2 c_p^2 + k''[\eta]^3 c_p^3 = X + k'X^2 + k''X^3. \quad (8)$$

The parameters k' and k'' are constants, and $X = c_p \cdot [\eta]$ will be used to denote the product of polymer concentration and polymer intrinsic viscosity. Equation (8) captures the (main) effect of polymer concentration on the effective viscosity. The equation can further account for the viscosity altering effect of changing the ionic concentrations, by making $[\eta]$ salinity dependent (see the Appendix).

In order to calculate the shear thinning viscosity at a given, local shear rate in the reservoir, equation (8) is combined with the Carreau-Yasuda model introduced previously. The shear thinning index in the Carreau-Yasuda expression depends on polymer concentration and the intrinsic viscosity and can be formulated as a function of X (Stavland et al., 2010). We have chosen a formulation that binds n between its physical limits, $n \in [0, 1]$:

$$n = 1 - \frac{1}{1 + (a_n[\eta]c_p)^{b_n}} = 1 - \frac{1}{1 + (a_n \cdot X)^{b_n}}. \quad (9)$$

Here a_n and b_n are tuning parameters.

Next, we wish to obtain an expression for the rotational relaxation time, λ_1 . It can be calculated as $\lambda_1 = 1/2D_{rot}$, where D_{rot} is a rotational diffusion coefficient. This diffusion coefficient can be determined from the Stokes-Einstein-Debye equation as

$$D_{rot} = \frac{kT}{8\pi\eta_s R_h^3}. \quad (10)$$

In the above expression, the polymer in solution is treated as a rigid sphere with an equivalent hydrodynamic radius, R_h . Also, $k = 1.38 \cdot 10^{-23} \text{ J K}^{-1}$ is the Boltzmann constant, and T is the temperature. Inserting equation (10) into the expression for λ_1 yields

$$\lambda_1 = \frac{4\pi\eta_s R_h^3}{kT}. \quad (11)$$

Next, we show that the hydrodynamic diameter, $D_h = 2R_h$, can be related to the intrinsic viscosity and the polymer molecular weight by

$$D_h = \left(\frac{6}{2.5\pi N_A}\right)^{1/3} \cdot ([\eta]M_w)^{1/3} \quad (12)$$

where N_A is Avogadro's number. Expression (12) is based on introducing an equivalent hydrodynamic concentration of the polymer:

$$\Phi_h = \Phi_{sw} \cdot \frac{c_p}{\rho_p}. \quad (13)$$

That is, Φ_h is the effective volumetric (spherical) concentration of the polymer in solution. In equation (13), ρ_p is the polymer density, and the factor $\Phi_{sw} = (D_h/D_{sph})^3$ is a 'swelling parameter', defined as the ratio between the effective hydrodynamic volume occupied by the polymer, and the dense spherical volume calculated from the polymer molecular weight and the polymer density. The dense spherical radius, R_{sph} , therefore satisfies

$$\rho_p = \frac{M_w/N_A}{4\pi R_{sph}^3/3}, \quad (14)$$

which leads to:

$$D_{sph} = \left(\frac{6}{\pi N_A}\right)^{1/3} \cdot \left(\frac{M_w}{\rho_p}\right)^{1/3}. \quad (15)$$

The swelling parameter can be calculated from the Stokes-Einstein equation for the viscosity of a diluted suspension of solid spheres (Rajagopalan and Hiemenz, 1997):

$$\frac{\eta}{\eta_s} = \frac{1 + \Phi_h/2}{(1 - \Phi_h)^2} \approx (1 + 2.5\Phi_h). \quad (16)$$

We get:

$$\rho_p \frac{\eta - \eta_s}{\eta_s c_p} = 2.5 \cdot \Phi_{sw}. \quad (17)$$

Taking the limit $c_p \rightarrow 0$, we obtain an expression for the swelling parameter:

$$\Phi_{sw} = \frac{[\eta] \rho_p}{2.5}. \quad (18)$$

By inserting the obtained expression (15) for D_{sph} into the relation (17), we finally end up with equation (12). We note that expression (12) compares well with the one given in (Hirasaki and Pope, 1974), when making the proper unit conversions.

Combining equations (11) and (12), the rotational relaxation time can now be calculated as

$$\lambda_1 = \frac{6}{5R} \cdot \frac{\eta_s [\eta] M_w}{T}, \quad (19)$$

where $R = k/N_A$ is the ideal gas constant. Equation (19) suggests that λ_1 should be independent of polymer concentration. However, this is in contrast to experimental data found in the literature, which indicate sensitivity of λ_1 to c_p (Chauveteau, 1986). To account for increased relaxation time caused by interaction forces between polymer molecules at higher concentrations, we replace $[\eta]$ with the first order approximation:

$$[\eta] \approx \frac{\eta_{sp0}}{c_p}. \quad (20)$$

Thus, the final expression used in the simulation model becomes

$$\lambda_1 = \lambda_a \cdot \frac{\eta_s \eta_{sp0} M_w}{c_p T}, \quad (21)$$

where we use the prefactor λ_a as a tuning parameter. The theoretical value is $\lambda_a = 6/5R = 0.144$ in SI units. From equation (21), the rotational relaxation time can be predicted for any temperature and polymer concentration. Moreover, the formula accounts for changes in the polymer molecular weight as a result of degradation. The remaining input parameters required to calculate λ_1 — k' , k'' , K , and a —may be varied among different polymers, but they should be known from bulk rheology measurements.

Shear thinning model versus bulk rheology data

The shear thinning model was matched with bulk rheology data for the different hydrolyzed polyacrylamide (HPAM) polymers investigated in Stavland et al. (2010). The polymers are listed in table 1 using a four digit name indicating their molecular weight (two first digits) and hydrolysis degree (two last digits), e.g., 2030 indicates an average molecular weight of 20MDa, with 30% degree of hydrolysis. For most polymer types the data were recorded at 7 different concentrations in the range from 250 ppm to 5000 ppm, and at shear rates from 0.1 s^{-1} to 500 s^{-1} .

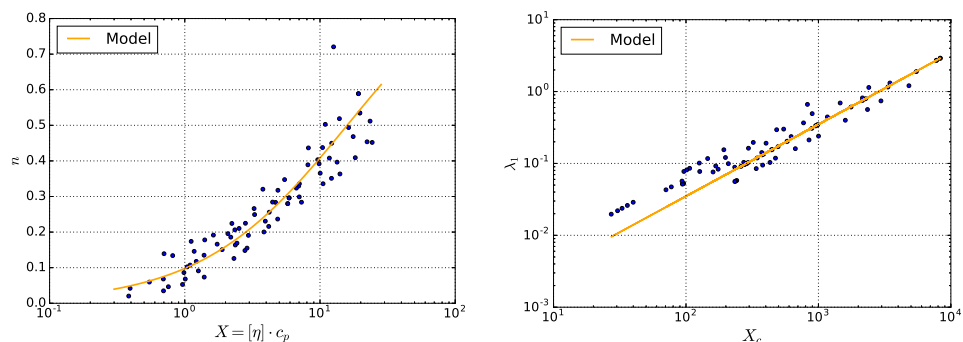


Figure 1 Left: Shear index n obtained for the dataset fitted with $a_n = 0.063$ and $b_n = 0.804$. Right: λ_1 from the second match. The line represents the model with $\lambda_a = 0.350 \text{ K mol}^{-1} \text{ J}^{-1}$.

The model parameters were estimated, for one polymer at the time, by minimizing the sum of squared relative error between calculated and measured η_{sp} for all datapoints covering variation in concentration and shear rate. The minimization was first done with a minimum of constraints. The expression for the shear thinning index, equation (9), was fitted to the result in the left plot of figure 1. Then, the minimization was repeated with fixed shear thinning index parameters.

In the right plot of figure 1 we see the matched values of λ_1 versus the scaling group $X_c = \eta_s \eta_{sp0} M_w / c_p T$ on a log-log plot, see equation (21). The line in the figure indicates a constant λ_a parameter that matches the higher λ_1 -values. Attempts to fix the λ_a parameter among all polymer types resulted in somewhat poorer match to the simulated coreflood experiments presented later.

Shear thickening model

Although polymers tend to display shear thinning behaviour in capillary tubes, the apparent viscosity in porous media has frequently been seen to *increase* with increasing shear rate. This flow behaviour, which has become known as *shear thickening* in the literature, can be explained as an elastic effect due to elongation and contraction of the polymer molecule as it moves through the medium. When the polymer passes through a narrow pore throat, its shape in solution will be deformed, and it will take some time for it to regain its original conformation. If the time scale of deformation is comparable to the residence time inside a typical pore, shear thickening behaviour will occur. This effect has also been observed in capillary tubes with an abrupt contraction and in channels with varying cross-sections (Chauveteau and Moan, 1981; Chauveteau, 1986; Buchholz et al., 2004). For the case of capillary tubes, it is believed that the increased flow resistance is caused mainly by the sharp acceleration at the entry point of the tube, due to the abrupt change in the diameter at the capillary entrance (Chauveteau, 1986; Al Hashmi et al., 2013).

As with shear thinning flow, there seems to be a critical shear rate at which shear thickening flow occurs. This shear rate can be given as the inverse of λ_2 , where λ_2 is a relaxation time that determines the time for the onset of elongation. The elongational viscosity is in this paper calculated according to

$$\eta_{el} = (1 + (\lambda_2 \dot{\gamma})^{x_2})^{\frac{m+n}{x_2}}, \quad (22)$$

where x_2 is a tuning parameter for the transition to the new flow regime, and m is an exponent fitting parameter. The motivation for the model can be seen from figure 2. In this figure we have plotted the logarithm of the apparent specific viscosity of a polymer solution versus the logarithm of the in-situ porous media shear rate, using data from one of the dual core experiments in Stavland et al. (2010). From

the figure, the graph looks approximately linear for shear rates following the onset of shear thickening. A combination of the formulas (2), (3), and (22) yields

$$\eta_{sp} = \eta_{sp0} \cdot \frac{(1 + (\lambda_2 \dot{\gamma})^{x_2})^{(m+n)/x_2}}{(1 + (\lambda_1 \dot{\gamma})^x)^{n/x}}, \quad (23)$$

which for $\lambda_2 \dot{\gamma} \gg 1$ predicts that $\eta_{sp} \propto \dot{\gamma}^m$, i.e., that $\log \eta_{sp}$ is a linear function of $\log \dot{\gamma}$ with slope m . The plot in figure 2 was typical for all experiments investigated, and the estimated maximum slope m in the shear thickening region was found to be fairly constant among the different cases, with values lying in the range $m = 1.5 \pm 0.2$. (11 samples). The maximum slope of the declining part (purple line in figure 2) was 0.49 ± 0.09 . Note that the results in the figure represents average properties integrated over the length of the core plug. Since all investigated core plugs were of the same length (7 cm), some interesting observations can be made from the intersection point between the two curves shown in figure 2. The average shear rate at this point (9 samples, two outliers removed) was $1480 \pm 550 \text{ s}^{-1}$, while average shear stress, calculated as $F_s = \dot{\gamma} \cdot \eta$, was $54 \pm 5 \text{ Pa}$. This strongly indicates that shear stress at the pore surface rather than shear rate governs the degradation. The tests compared here are all from the first core in the dual core experimental setup. Results for the second core essentially overlap the results for the first core in the elongation region, while the declining part shows a parallel shift downwards.

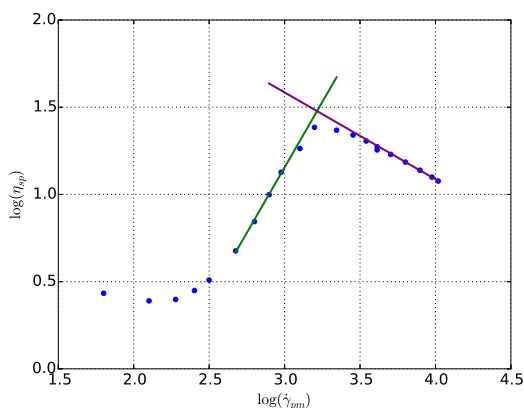


Figure 2 In-situ rheology of the 1030 polymer in a 0.299 D Berea sandstone core. The slope of the green line, which represents the maximum slope in the shear thickening region, was found to be $m = 1.5$. Note that this plot represents averaged parameters, i.e., it is based on measured pressure drops across a full column of length $L \approx 7.0 \text{ cm}$. The effective shear rate in porous media, $\dot{\gamma}_{pm}$, was calculated according to equation (47).

Similarly as for the rotational relaxation time, we wish to derive an expression for λ_2 in terms of more fundamental quantities. The ideal situation would be if we could find a general expression that would apply to a wide class of polymers, and that could be used at varying reservoir conditions, e.g. at different permeabilities and temperatures.

We take as our starting point a simplified picture of the pore scale geometry, see figure 3. In the figure we consider a situation where a polymer encounters a restriction inside the porous medium, i.e., a sharp reduction in the pore radius. When the polymer molecule enters the narrow pore throat, it is believed that it will undergo a sharp coil-stretch transition at the entry point, whereby the conformation of the polymer molecule will change from a coiled state to a more elongated one (De Gennes, 1974). This will increase the flow resistance, and hence the measured pressure drop, over the constriction. Once the polymer molecule enters back into a larger pore body, thermal forces will push it back towards its

equilibrium coil conformation. Whether this is achieved depends upon the residence time inside the pore body.

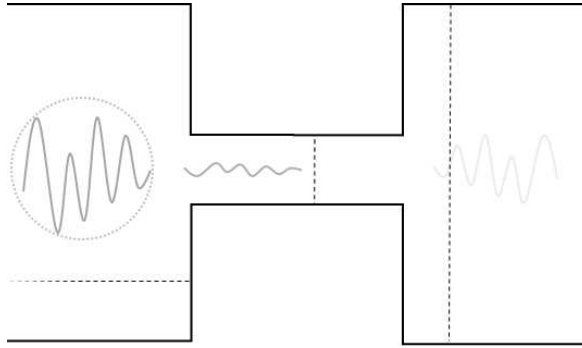


Figure 3 A narrow pore throat surrounded by two larger pore bodies. As the polymer enters the constriction, it will be deformed.

To compute the pore residence time, we assume a pore length L_p equal to the characteristic grain size D_g of the medium obtained by a Kozeny Carman equation. The Kozeny Carman approach consists in converting from a capillary tube representation of the porous medium to a medium of spherical grains by preserving the medium surface area, S_A . The relation between the effective pore radius R_p and effective grain size is $S_A = 2\phi/R_p = 6(1 - \phi)/D_g$ (Lake, 1989). Then we can write

$$\frac{L_p}{R_p} = 3 \cdot \frac{1 - \phi}{\phi}, \quad (24)$$

where ϕ is the porosity. The residence time can therefore be computed as

$$\tau_r = \frac{L_p}{v_p} = 12 \cdot \frac{1 - \phi}{\phi \dot{\gamma}_c}, \quad (25)$$

where $\dot{\gamma}_c = 4v_p/R_p = 1/\lambda_2$ is the critical shear rate, and v_p is the average pore velocity. The critical shear rate is obtained when the elongational relaxation time of the polymer, τ_{el} , is of the same order of magnitude as τ_r (Chauveteau and Moan, 1981; Chauveteau, 1986). The elongational relaxation time is the time it takes for the polymer molecule to regain its original shape after deformation, and it can be related to a translational diffusion coefficient, D_t , by

$$\tau_{el} = \frac{2R_h^2}{D_t}, \quad (26)$$

where R_h is the hydrodynamic radius introduced earlier. In other words, τ_{el} is the time it takes for the polymer to diffuse a length equal to its effective size in solution. The translational diffusion coefficient can further be calculated from the Stokes-Einstein equation (Chauveteau, 1986):

$$D_t = \frac{kT}{6\pi\eta_s R_h}. \quad (27)$$

The ratio between the two time scales can be quantified by introducing a Deborah number:

$$N_{De} = \frac{\tau_{el}}{\tau_r}. \quad (28)$$

In the literature the critical Deborah number for the onset of shear thickening has been estimated from theoretical models to be 0.5 (Haas and Durst, 1982). Combining equations (12), (24), (25), (26), (27), and (28), we end up with the following expression for the time constant, λ_2 :

$$\lambda_2 = C_{el} \cdot \frac{3}{10R} \cdot \frac{\phi}{1-\phi} \cdot \frac{\eta_s[\eta]M_w}{T}, \quad (29)$$

where $C_{el} = 1/N_{De}$. In the simulation model, C_{el} is used as a model tuning parameter, and we found that $C_{el} = 4$ gave a good match. With the definition of the Deborah number given here, this corresponds to $N_{De} = 0.25$. As with λ_1 , the formula for λ_2 can be used to predict the onset of shear thickening at various conditions, and for different polymer types.

Shear degradation model

As the flow rate is increased further beyond the critical rate for onset of shear thickening, experiments indicate that the viscosity reaches a 'maximum level', after which there is a sharp decline in viscosity at yet higher rates, see figure 2. This is because of polymer mechanical degradation in porous media. At sufficiently high stresses, the chemical bonds of a polymer molecule will break, causing a reduction in the effective molecular weight and apparent viscosity. It has been observed that this chain scission happens more rapidly for polymers with higher molecular weights. Indeed, multiple investigators have reported a critical strain rate for the onset of chain scission (fracture), $\dot{\epsilon}_f$, that scales as a power-law with the weight-average polymer molecular weight (Keller and Odell, 1985; Odell et al., 1988; Nguyen and Kausch, 1991; Buchholz et al., 2004; Vanapalli et al., 2006; Dupas et al., 2012):

$$\dot{\epsilon}_f \propto M_w^{-k}. \quad (30)$$

This power-law dependence has been seen for both turbulent and laminar flows, although the numerical value of the scaling exponent can vary depending on the flow pattern, as well on differences in solvent quality (Vanapalli et al., 2005). The strain rate used by e.g. (Dupas et al., 2012) is proportional to our porous media effective shear rate, $\dot{\epsilon} \propto \dot{\gamma}_{pm}$. We would therefore expect the onset of shear degradation to occur at a critical shear rate, $\dot{\gamma}_f$, as indeed seems to be the case, based on the intersection point found in figure 2 and others like it. However, as we have already seen, $\dot{\gamma}_f$ is a system dependent parameter whose value can vary greatly from case to case. On the other hand, based on our data we saw that the onset of degradation happened at relatively constant values of stress, F_s .

In order to develop a mathematical model for polymer chain rupture, we assume that most of the degradation takes place close to the rock surface, where the shear force is large, and that it decreases away from the surface where F_s is lower. The degradation rate is taken to be proportional to the rock specific surface area, which is $S_0 = \text{rock surface/pore volume} = 2/R_p$ for a capillary tube. The implication of this term is that at a given shear stress, $F_s = \nabla p \cdot R/2$, the polymer will degrade faster in a low permeable rock with smaller R_p (∇p is the pressure gradient along the direction of the tube).

In the simulator we model the mechanical shear degradation by introducing a parameter f_{rup} , which is the fraction of polymer molecules that rupture per time unit. It is calculated as

$$f_{rup} = (r_{deg} \cdot F_s)^{\alpha_d} \cdot \frac{2M_w^{\beta_d}}{R_p}, \quad (31)$$

where r_{deg} is a rate constant, that together with F_s characterizes the onset and magnitude of degradation. The parameters α_d and β_d are used to scale the dependence of chain scission kinetics on, respectively, the applied force and polymer molecular weight. In the absence of data to suggest otherwise, we set $\beta_d = 1.0$. In the simulations we used a value of $r_{deg} = 0.0015$ for the rate constant, assuming that F_s in equation (31) were in units of Pa, R_p in μm , and M_w in MDA. The molecular weight is now updated according to the differential equation

$$\frac{dM_w}{dt} = -M_w \cdot f_{rup}. \quad (32)$$

A novel feature of the proposed approach is that the polymer is represented by two components in the simulator:

1. A volumetric polymer concentration, c_p/ρ_p (recall that c_p is the mass concentration), and
2. A molar polymer concentration, c_{mol} (e.g. mol l^{-1}).

Equations (31) and (32) establish a mathematical relation between the porous medium effective shear rate, and the molecule rupturing rate. The result is an increased molar concentration and a corresponding reduction in molecular weight since the volumetric concentration is unchanged:

$$c_{mol} = \frac{c_p}{M_w}. \quad (33)$$

Once a new value for M_w has been found, the polymer intrinsic viscosity is updated using the Mark-Houwink equation (7).

Polymer adsorption and residual resistance factor

We model polymer adsorption as an irreversible process given by a Langmuir isotherm:

$$A_p = \frac{bc_p Q_m}{1 + bc_p}. \quad (34)$$

In equation (34), A_p is the polymer concentration adsorbed on the rock and Q_m is the maximum adsorption capacity, both expressed as a fraction of the total pore volume. The parameter b determines how fast the adsorption occurs, i.e., at which polymer concentration the plateau, $A_p = Q_m$, is reached. Polymer adsorption can lead to permeability reduction, which is typically quantified in core floods by introducing the residual resistance factor, RRF . It is calculated as

$$RRF = \frac{k_w}{k_{w2}}, \quad (35)$$

where $k = k_w$ is the initial permeability to water before polymer injection, and k_{w2} is the post-flush water permeability. However, for simulation purposes we need to be able to have a spatially varying permeability reduction. We have tested two models for relating RRF to the adsorbed amount of polymer, which we introduce shortly here (see Appendix for more details). Let A_{pt} denote the effective volume fraction of the total pore space that is occupied with polymer. We then compute RRF according to

$$RRF = \frac{1}{(1 - A_{pt})^2}. \quad (36)$$

In model I, which is independent of shear rate, we compute A_{pt} as

$$A_{pt}^I = f_{rkf} \cdot \frac{A_p \Phi_{sw}}{(1 - IPV_0)}, \quad (37)$$

where Φ_{sw} is the swelling factor defined in equation (18) computed from the molecular weight of adsorbed polymer, which can differ significantly from M_w in solution. Equation (37) models the extension of adsorbed polymer molecules into the solution. The term IPV_0 is the fraction of the pore volume that is totally inaccessible to the polymer (see Appendix), and f_{rkf} is included as a tuning parameter. The investigated dataset provides no information about adsorbed polymer, so in the simulations we used $f_{rkf} = 1$ and adjusted Q_m to approximate experimental RRF .

Model II should be regarded as a test of one possible method which can improve the match of experimental effluent viscosity (see the section on simulation results). In this model, A_{pt} is made a function of shear rate. We have tested the following expression:

$$A_{pt}^{II} = f_{rkf} \cdot \frac{A_p}{(1 - IPV_0)} \cdot ((\Phi_{sw} - 1)f_{sh} + 1). \quad (38)$$

For simplicity, we relate f_{sh} to a time constant in the same way as for the shear thinning and shear thickening viscosities:

$$f_{sh} = (1 + (\lambda_3 \dot{\gamma})^{x_3})^{-n_3/x_3}. \quad (39)$$

That is, at low flow rates we will have $f_{sh} \approx 1.0$, and polymer molecules adsorbed at the pore wall extend fully into the solution. On the other hand, as the flow rate increases, more and more of the polymer will be forced closer towards the surface, resulting in less pore blocking. In formula (39), x_3 and n_3 are constants, and we take λ_3 to be proportional to λ_2 . Moreover, we assume that the onset of this effect happens at a higher shear rate than the critical shear rate for the onset of shear thickening, i.e., that $\lambda_2 > \lambda_3$. For the simulations presented in this paper, we have used $\lambda_2/\lambda_3 = 8$.

Numerical solution of the polymer model

We have implemented the polymer viscosity model in an in-house simulator at IRIS, IorCoreSim. This simulator, which is written in C++, has the capability to simulate a variety of EOR processes for two-phase flow in porous media. The main flow field is obtained from a finite-difference discretization, using a sequential solution method for pressures and saturations (Watts, 1986). First the pressure fields are calculated using a linear pressure equation, keeping the saturation-dependent variables fixed at their values from the previous timestep. Next, the phase velocities computed in the first step are updated by solving an additional saturation equation for the water saturation. The saturation equation is formulated in terms of the fractional flow of water, and it is solved implicitly with respect to the saturation dependent variables k_r (relative permeability) and p_c (capillary pressure), whilst keeping the oil pressure and total flowrate from the pressure solution fixed.

Once the flow field has been obtained for a global timestep, the transport of the individual species, in this case the brine and polymer components, is performed explicitly using operator splitting. First, the total

concentration of polymer is updated in each grid cell. Next, polymer adsorption is computed, followed by an update of the solution viscosity and the *RRF* factor. The viscosity algorithm used for a grid block during a transport timestep, Δt , can be roughly summarized as follows:

1. Compute in-situ shear rate using current flowrate and *RRF* from the previous timestep.
2. Compute the intrinsic viscosity in terms of the effective salinity of the brine (see Appendix).
3. Calculate an initial value for the viscosity-averaged polymer molecular weight, M_w^0 , based on the newly updated molar and volumetric concentrations, see equation (33).
4. Find the polymer concentration to be used in the viscosity calculations (correct for inaccessible pore volume and/or depletion layer, see Appendix), and calculate polymer apparent viscosity as a function of polymer concentration, shear rate, and depletion layer. Next, add the effect of elongation. The degradation is solved implicit in time with respect to M_w , by employing an iterative algorithm where in each iteration the full viscosity model is calculated. The initial value for M_w estimated in step 3 is used as a starting point.
5. If adsorption is included, calculate *RRF*.

The crucial step that necessitates an iteration loop is the solution of equation (32). This is because most of the parameters in the model are functions of M_w . We discretize (32) as

$$M_w = \frac{M_w^0}{1 + \Delta t \cdot f_{rup}(M_w)}, \quad (40)$$

where M_w^0 is the molecular weight before degradation is included, and M_w represent the unknown value when degradation over the last time step is included. We solve (40) using a modified false position ('regula falsi') chord method, also known as an 'Illinois-type' method (Ford, 1995).

Simulation results and final discussion

We applied the model to some of the experiments performed in Stavland et al. (2010). The selected experiments cover variations in molecular weight from 5 to 20MDa, and in permeability from 130 to 2000 mD. The hydrolysis degree was the same, 30 %, for all the polymers. The experiments were designed to investigate the elongation and degradation flow regimes. For the shear thinning model, individual input parameters were used, see table 1. The adsorption capacities were adjusted to obtain *RRF* factors close to the experimental values, but the values listed (table 5) are consistent with what would be expected from variation in permeability. The rest of the model parameters describing elongation and degradation were kept fixed among all cases (table 2). For all simulations, we compared predicted resistance factors, *RF*, to the ones obtained from the experimental data. The resistance factor, or mobility reduction factor, is defined by

$$RF = \frac{\lambda_w}{\lambda_p} = \frac{\Delta p}{\Delta p_w}. \quad (41)$$

That is, *RF* is the ratio of the water mobility prior to polymer injection, $\lambda_w = k_w/\eta_s$, to the polymer mobility at the same rate, $\lambda_p = k_p/\eta$. If the residual resistance factor, equation (35), can be considered a constant for a given medium, we obtain the following relation between *RRF* and *RF*:

$$RF = \frac{\eta}{\eta_s} \cdot RRF = \eta_{rel} \cdot RRF. \quad (42)$$

All the investigated polymers were mixed with synthetic sea water (SSW), with ionic concentrations reported in table 3. As a result, we could represent the brine by a single component, using a constant viscosity of $\eta_s = 1.07$ mPa s at room temperature, $T = 20^\circ\text{C}$. The polymer-brine solutions were injected into different serial mounted sandstone cores, with properties given in table 4. All of the cores were cylindrical, with a length of approximately 7 cm, a diameter of 3.8 cm, and a porosity close to 20%. The solutions were flooded at a variety of rates, and steady-state differential pressures were recorded over both cores, which we will denote by Core 1 and Core 2, respectively. The polymer solutions were injected at a polymer concentration of 1500 ppm.

We simulate the experiments starting with the experimental initial rate because, in some of the experiments, initial rate seemed to be in the lower end of the degradation regime, which affects molecular weight of adsorbed polymer, and consequently RRF . After that, the injection rate was stepwise increased from low to high value, and finally a post-polymer water injection was simulated. Simulated values of in particular RF , but also shear rate and RRF , showed decreasing trends from inlet to outlet of the core. Thus, to compare with experimental results, these properties are computed in the same way as used for the experiments, from total pressure drop over the core and the flowrate. RRF is first computed from the final water flood data, then, for each flowrate, RF and η can be computed using the equations (41) and (42), while the shear rate is computed from equation (47).

In addition to estimating RF and RRF factors, polymer samples were collected at the effluent, at different injection rates. These samples were subsequently analyzed in a rheometer at low shear rate, to characterize the extent of degradation. Initially we matched the experimental RF profiles by tuning the degradation model and assuming constant RRF , model I (equation (37)). Although good reproduction of RF were obtained at all flow rates, computed viscosities using simulated effluent M_w were substantially lower than the experimental values, as can be seen from figure 4. Since RF is a product of viscosity and RRF , equation (42), the intuitive idea is that if viscosity is higher, RRF must be reduced to obtain the same RF value. This was the motivation for introducing model II with rate dependent RRF , equation (38). The difference between the two models is illustrated in figure 4, where we have compared the experimentally determined effluent viscosities with values predicted from the simulator for the 1530 polymer.

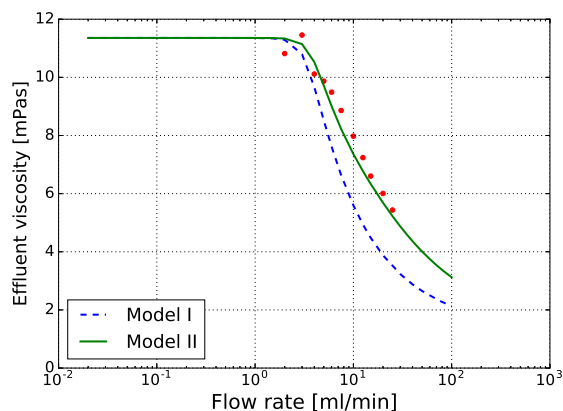


Figure 4 Effluent viscosities for the 1530 polymer, measured from bulk samples collected at the effluent. The data are taken for the case where Core 1 and Core 2 had permeabilities of 721.7 mD and 612.8 mD, respectively. The red dots are experimental datapoints, whilst the solid line was obtained from the match with the model for shear dependent permeability, model II. The stippled lines represent the shear independent model, model I.

Based on figure 4, the shear rate dependent model (model II) is able to reproduce both effluent polymer

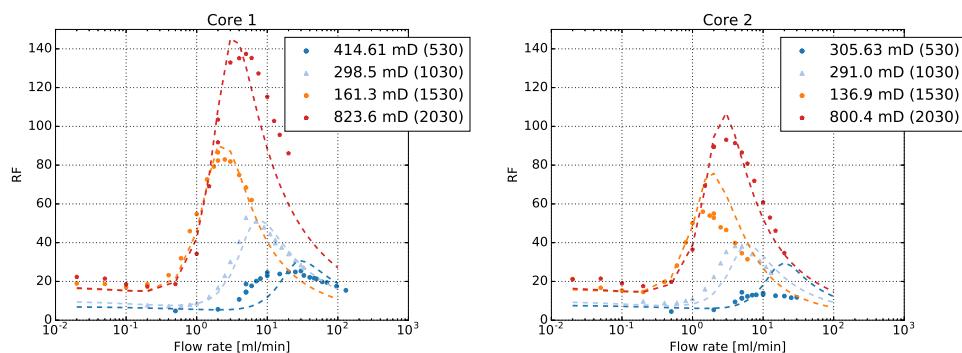


Figure 5 Resistance factors plotted versus flow rate for 4 different polymer types, with M_w varied from 5 to 20 MDa. Stippled lines are from the simulator, whereas the points are derived from experimentally measured Δp and Q .

properties and RF satisfactory (shown later). We conclude that rate dependent RRF is a good candidate for explaining what goes on inside the core, but it is not the only possible mechanism. Another possible explanation, which remains to be tested, is the choice of the Mark-Houwink exponent, a , from equation (7). Since this exponent is expected to vary depending on the polydispersivity of the polymer sample, or more precisely on the shape of the molecular weight distribution, it implies that the standard values found in the literature may not apply once a polymer has been significantly degraded, especially if the shape of the distribution has been heavily altered. By decreasing a , the polymer will lose less of its viscosity when degraded. The polymer will be degraded more (to a lower M_w), but may still result in an increased effluent viscosity.

It should be remarked that there are several experimental uncertainties that can make a proper estimation of the residual resistance factor difficult, such as excess pressure drops being measured during the post-polymer phase (Seright et al., 2011). Another issue, which may potentially be misleading, is that the RRF factor may not be a constant at all, but may rather depend on the applied flow rate. This is what we have explored with our model II. However, we remark that a predictive simulator needs to take the permeability reduction effect into account, as it would otherwise be impossible to match the observed pressure drops. The same applies to the other mechanisms modeled in the simulator, i.e., although there are considerable uncertainties in the precise values used for many of the input parameters in the model, they all need to be included if predictive capabilities are to be achieved. What is important for us here, in order to properly compare theory with experiment, is that the RRF factors obtained from the final water injections are reasonably close to the experimentally recorded values. A comparison between experimental and simulated RRF factors is given in table 5.

In figure 5, we have compared model versus experimental RF values for 4 different polymer types, all with a hydrolysis degree of 30%, but with varying molecular weight. We observe that the model is able to capture the main trends of the different experiments, although the result for the 530 polymer is not as good as the others. The resistance factors are slightly over- or underestimated, depending on the case, but overall the match is remarkably good when we take into account that the input parameters used in the shear thickening and shear degradation models were kept constant for *all* polymer types.

In order to look more closely at the effect of permeability, we have studied three of the experiments in more detail. In figure 6, we have plotted the simulated and experimental RF values for the synthetic 1530 HPAM polymer. We obtain a good match for Core 1, but the simulator overpredicts RF in the second core. About half of the decrease in RF , going from Core 1 to Core 2, is captured. One may also observe that the increasing part of RF is well matched for both cores in all three experiments, and that the horizontal shift of the curves due to different permeability is very well captured. Overall, considering

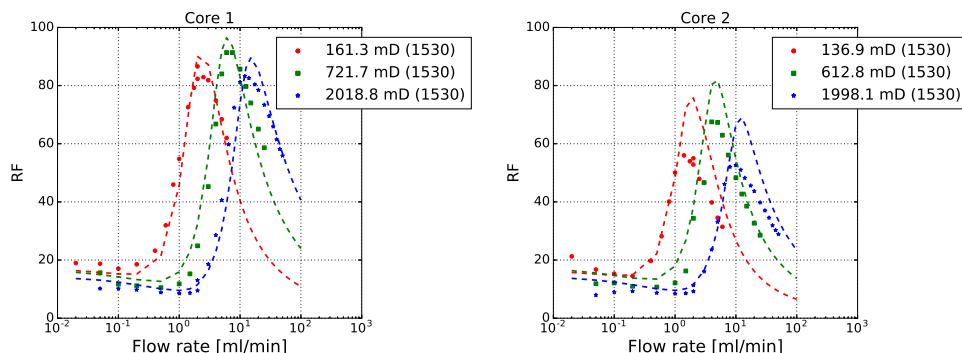


Figure 6 Resistance factors for experiments performed with the 1530 HPAM polymer in 3 different serial core systems. The permeability varied from 136 mD to 2000 mD.

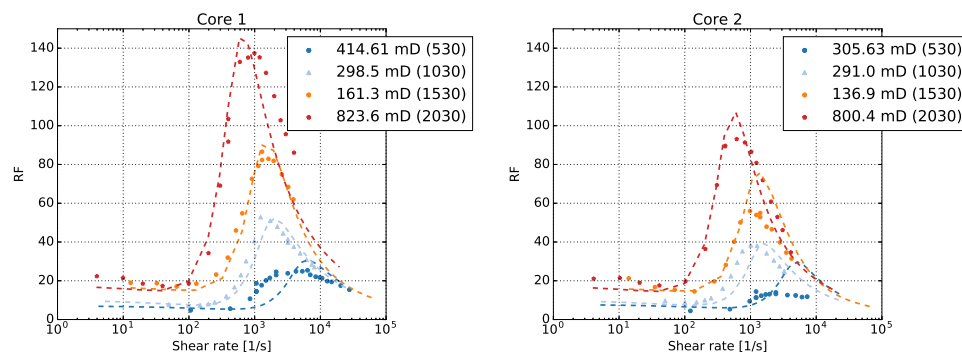


Figure 7 Resistance factors plotted versus shear rate for 4 different polymer types. Stippled lines are from the simulator, whereas the points are derived from experimentally measured Δp and Q .

experimental and model uncertainties, we find the result to be acceptable, as the trends are captured very well for all 3 permeabilities, and for both cores.

In figures 7 and 8 we replot some of the results from figures 5 and 6, respectively, but this time by using shear rate on the x-axis. Compared with figure 5, the profiles in figure 7 have a more even distribution of the onset of elongation, which is essentially a function of the polymer M_w and $[\eta]$, while the declining part of the curves come closer together. For the case of variable permeability, figure 8, we observe that the curves fall more on or less in line when plotted versus shear rate. This is as expected from the model, where the onset of elongation is not affected by permeability. There is a difference in RF level at low shear rate, which can be explained by permeability dependent effects of a depletion layer (see Appendix) and by differences in RRF , see table 5.

As remarked previously, the molecular weight for the adsorbed polymer can be very different from the corresponding value of the flowing polymer. Since polymer adsorption is modeled as irreversible, it is the polymer from the first round of injection that sticks to the wall. This means that the RRF factor in our model becomes a function of the initial flow rate. The difference between bulk and adsorbed polymer molecular weight is illustrated in figure 9, where we plot M_w versus distance along the core for one of the experiments. From the figure, we see that the polymer in bulk solution is quickly degraded near the inlet of the first core plug, with progressive degradation at increasing flow rates. Figure 9 also shows that the degradation continues well into the second core. In contrast, the adsorbed polymer retains a very

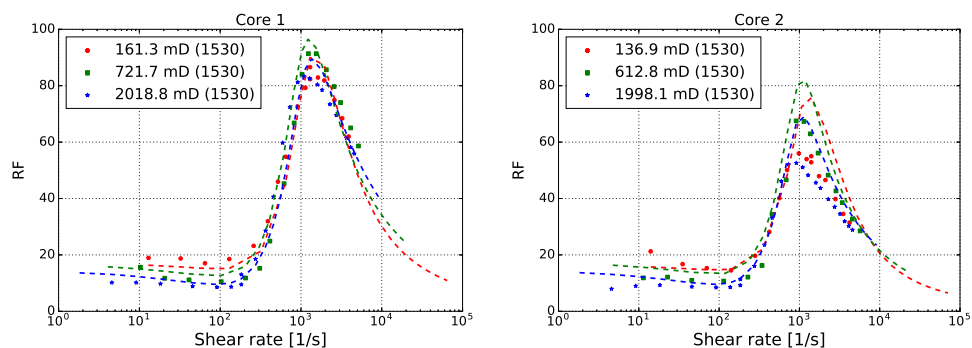


Figure 8 Resistance factors plotted versus shear rate for experiments performed with the 1530 HPAM polymer in 3 different serial core systems. Stippled lines are from the simulator, whereas the points are derived from experimentally measured Δp and Q .

high molecular weight throughout the core, as the adsorption happened at a lower rate when not much polymer was degraded.

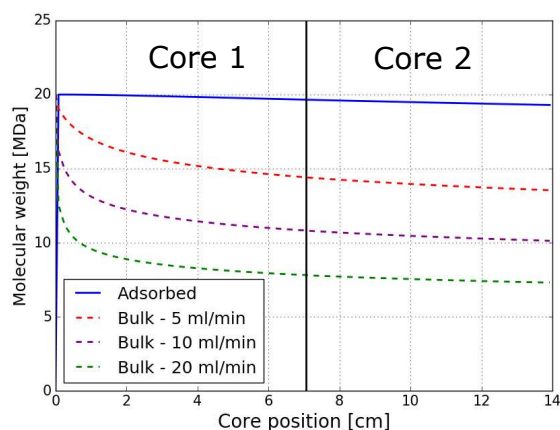


Figure 9 Molecular weight as a function of distance for the case of the 2030 HPAM polymer in the 823.6 mD and 800.4 mD dual core system. The spatial profile of the adsorbed polymer molecular weight is represented by the blue, solid line. The three stippled lines show spatial profiles of M_w at 3 different rates, all higher than the initial rate at which the adsorption occurred.

Finally, we show an example of what can happen at low shear rates. In figure 10, we clearly see that the predicted RF factors are larger than the bulk viscosity for the low permeable core, whereas the predicted apparent viscosity curves lie well below the bulk viscosity curves (figure 11). The reason for the large difference between RF and η for this core is the high $RRF = 6.3$. And, we see that the bulk viscosity is closer to both RF and the apparent viscosity in the high permeability case, as expected due to the lower $RRF = 2$, and since the effect of a depletion layer become smaller at higher permeability. These plots illustrate nicely how the effects of permeability reduction and depletion layers of polymer can alter the in-situ rheology of the polymer. However, we should point out that the experimental data at the lowest shear rates were of rather poor quality. Therefore, the clear differences shown in figures 10 and 11 may not be as large in reality.

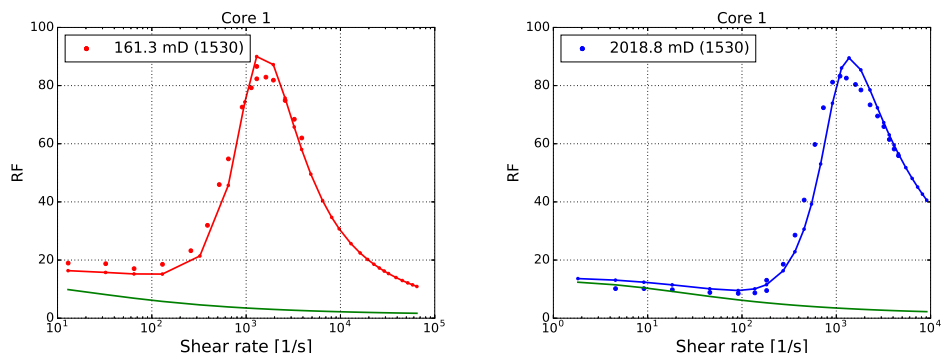


Figure 10 Resistance factors versus shear rate for experiments performed with the 1530 HPAM polymer in high and low permeability cores. The green solid lines represents the predicted bulk viscosity of undegraded polymer at the same shear rates.

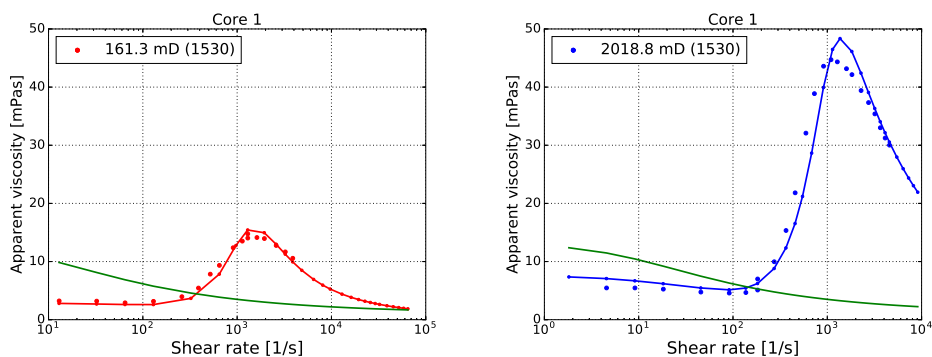


Figure 11 Polymer apparent viscosity, η , versus shear rate for experiments performed with the 1530 HPAM polymer in high and low permeability cores. The green solid lines represents the predicted bulk viscosity of undegraded polymer at the same shear rates.

Final remarks

We have introduced a mathematical model for simulating polymer flooding at the core scale. The model covers all the commonly observed flow regimes, such as shear thinning, shear thickening, and shear degrading flow. We have suggested possible equations for describing how the onset and duration of these flow regimes depend upon the reservoir parameters, which is needed for upscaling the results to the field.

By employing the model, we were able to obtain reasonable matches for a wide range of experiments, using different polymer types and core samples with varying permeability. It is worth pointing out the decent predictions that were obtained for two consecutive cores in the tested serial core systems. Even more important is the fact that so many of the input parameters were kept constant. As shown in table 2, the simulation model for the shear thickening and shear degradation flow regimes were based on a *single set of input parameters* for all polymer types tested. Thus, for polymers of the type investigated here at least, the model can be a useful tool to investigate the EOR potential of polymer flooding projects under varying reservoir conditions.

Our model predicts noticeable degradation in both cores. However, as we used a linear 1D geometry,

the results are not directly transferable to the field. Near a well, the flow is approximately radial, which means that the flow rate, and hence the shear stress, will rapidly decrease away from the injector. As a consequence, less polymer will be predicted to degrade in a real field case when this is taken into account.

In future work, it might be interesting to apply the model to larger geometries, i.e. to model a pilot project and/or a field case. Furthermore, the effect of changing the solution salinity should be tested, as most EOR polymers are very sensitive to the ions present in the water, particularly divalent ions. To this end, a possible avenue for research could be to combine the model with a code for simulating aqueous geochemistry, for example in order to investigate a combined low salinity and polymer flood.

Acknowledgements

The authors acknowledge the Research Council of Norway and the industry partners; ConocoPhillips Skandinavia AS, BP Norge AS, Det Norske Oljeselskap AS, Eni Norge AS, Maersk Oil Norway AS, DONG Energy A/S, Denmark, Statoil Petroleum AS, ENGIE E&P NORGE AS, Lundin Norway AS, Halliburton AS, Schlumberger Norge AS, Wintershall Norge AS of The National IOR Centre of Norway for support.

Appendix

Excluded volume effects

A common observation in polymer flooding experiments is that polymer travels a higher flow rate than its solvent (water). This has been attributed to the large molecular size of the polymer molecules (Dawson and Lantz, 1972). If a rock contains a significant amount of small pores, not all of them will be available for polymer flow. As a result, the effective porosity to the polymer will be smaller than that of the solvent. This can be modelled by introducing an inaccessible pore volume, IPV_0 .

It has also been noticed that at low shear rates, the effective viscosity in a core sample can lie below the corresponding value measured in bulk solution (Chauveteau, 1981; Omari et al., 1989; Chauveteau, 1986). This behaviour indicates a parallel flow of water depleted on polymer beside a flow of polymer rich solution. The flow of water may take place inside the micropores (IPV) and/or in a polymer depleted layer at the pore surface. The idea here is that due to entropic considerations, large polymer molecules will be sterically excluded from layers of fluid close to the rock surface, preferring to flow near the centre of the flow channels in the pores. Both types of inaccessible pore volume will tend to accelerate the velocity of the polymer compared to the velocity of the solvent.

In our model we consider both types, i.e., we calculate

$$IPV = IPV_0 + IPV_d \cdot (1 - IPV_0), \quad (43)$$

where IPV_0 denotes the fraction of micropores that are inaccessible to polymer, and IPV_d denotes the volume fraction of the depletion layer in the pores accessible for polymer. Next we assume negligible flow of water in the micropores, so the handling of IPV_0 is straightforward. The handling of IPV_d is more involved, and we only sketch the method here.

The flow in a capillary tube, representing a fraction $1 - IPV_0$ of the total volume, is divided in a pure water phase and a polymer rich phase, with fractional flows of f_{ws} and f_{ps} respectively. The water flows in a layer at the tube surface with thickness δ . The fractional flows are obtained by integrating the Hagen-Poiseuille equation over the capillary tube using constant properties (viscosity) for the polymer. These results are combined with a single fluid solution for the capillary tube, and the apparent polymer viscosity in the tube, η_{pa} , is obtained by requiring the same pressure gradient along the tube. We can then show that

$$\eta_{pa} = \frac{\eta_p}{M_v - (M_v - 1)E_{PVd}^2} \quad (44)$$

where $M_v = \eta_p/\eta_s$, and $E_{PVd} = 1 - IPV_d = (R - \delta)/R)^2$, with R being the tube radius.

We also need to handle the polymer concentration. Injected concentration is split into a polymer rich phase with concentration c_{pp} and a water rich depleted layer at the pore surface where we assume zero polymer concentration. The average concentration in the rock is c_p , and c_p^* denotes the concentration after excluding the constant part of the inaccessible pore volume. The relations between the different concentrations are given by

$$c_p^* = \frac{c_p}{E_{PV0}} = c_{pp} \cdot E_{PVd} \quad (45)$$

Note that the polymer concentration used in all viscosity calculations is c_{pp} , which will be higher than the injected concentration when the depletion layer model is activated. Using the capillary tube model, the interior polymer rich part in the capillary tube travels at a higher velocity due to the depleted layer. To capture this we define an effective polymer concentration, c_{pef} , to be used in the transport equation for polymer. Mass balance considerations require the effective concentration (at steady state) to be equal to the injected concentration, c_p^{inj} . Applying the mass balance, and combining with equation (45) and expressions for f_{vs} and f_{ps} (not shown here), yields the following expression for the effective polymer concentration:

$$c_{pef} = c_p \cdot \frac{1}{E_{PV0}} \cdot \frac{2M_v(1 - E_{PVd}) + E_{PVd}}{M_v - (M_v - 1)E_{PVd}^2} \quad (46)$$

The thickness of the depletion layer is computed as $\delta = f_{dpl} \cdot R_h$, where R_h is half the hydrodynamic diameter given in equation (12), and f_{dpl} is a tuning parameter set equal to 1 in all the simulations.

Calculation of effective pore radius and in-situ shear rate

The shear rates experienced by the polymer molecules will vary drastically depending on the local conditions in the reservoir. In this paper we have used the following correlation to calculate an average (effective) shear rate in porous media:

$$\dot{\gamma} = \dot{\gamma}_{pm} = \frac{4\alpha_c Q}{A\sqrt{8k\phi}} \cdot \sqrt{\frac{RRF}{1 - IPV_0}} \quad (47)$$

Equation (47) is based on a model of the porous media as a bundle of capillary tubes, and the parameter α_c is a tuning parameter to account for variations in the pore geometry, whereas Q is the Darcy flow rate, A is the cross-sectional area, and k is the permeability. We have explicitly included the fraction of pore volume that is totally inaccessible to the polymer, IPV_0 , into the calculation of $\dot{\gamma}_{pm}$, as well as the permeability reduction factor (equation (36)).

The effective pore radius for the flowing polymer, R_p , is calculated accordingly:

$$R_p = \sqrt{\frac{8k\tau^2}{\phi}} \cdot \frac{1}{\sqrt{RRF(1 - IPV_0)}} \quad (48)$$

We should stress that we have no measurements of the *IPV* factor in our experiments. For convenience we have simply set it to a value of 0.1, i.e. we assume that 10 % of the pores are too small for the polymer to enter. Small variations in α_c and IPV_0 do not greatly affect the results. However, there was a significant variation in the RRF factors estimated from the different experiments. In order to properly match the post-polymer flood pressure drops, we therefore needed to explicitly model the permeability reduction.

More on polymer adsorption and the permeability reduction model

By looking at the expression for the effective pore radius, equation (48), we see that the permeability scales linearly with R_p^2/ϕ . Both of these factors are reduced by a factor $1 - A_{pt}$ when adsorbed polymer is introduced, and this justifies the use of equation (36). Moreover, it is not enough to simply take $A_{pt} \approx A_p$, because this does not consider the swelling (volumetric extension) of the adsorbed polymer inside the pores. Had we used $A_{pt} \approx A_p$, we would have to model unrealistically high levels of adsorption in order to match the experimentally determined RRF factors.

A more realistic model might also allow for desorption and re-adsorption of polymer molecules, in line with experimental data from the literature that suggests continuous exchange of lighter molecular weight species at the wall with higher molecular weight species from the solution (Chauveteau and Lecourtier, 1988). However, in this work we were only able to estimate the adsorption indirectly. We have therefore not considered such an extension to the model, as more data would be needed to properly test it.

We should also mention that in the model the adsorption capacity, Q_m , is scaled with $\sqrt{\phi/k}$, since a smaller effective pore size results in a larger available surface area for adsorption, see equation (48). A value of Q_m is specified at reference values k_{ref} and ϕ_{ref} , and Q_m at arbitrary k and ϕ becomes

$$Q_m = Q_m(k, \phi) = Q_m^{ref} \cdot \sqrt{\frac{k_{ref}}{k}} \cdot \sqrt{\frac{\phi}{\phi_{ref}}}. \quad (49)$$

The ability to vary Q_m is important for upscaling to the field, since there are large variations in permeability and porosity in the reservoir.

Effective salinity model

The effect of solution salinity is included in the simulator by making $[\eta]$ in equation (8) salinity dependent. For the present purposes, we calculate $[\eta]$ as a power-law of an effective salinity parameter, C_s :

$$[\eta] = [\eta]_{ref} \cdot C_s^{\alpha_s}. \quad (50)$$

The parameter $[\eta]_{ref}$ is a reference intrinsic viscosity, calculated from the polymer molecular weight, and α_s is a fitting parameter which can be obtained as the slope of the intrinsic viscosity versus effective salinity on a log-log plot. The effective salinity is calculated as a weighted sum of the ionic concentrations in the solution:

$$C_s = \sum_i C_i \beta_i. \quad (51)$$

Here β_i is a constant that varies according to the valence of ion i , and C_i is the molar concentration. NaCl is used as a reference salt with $\beta_{Na} = \beta_{Cl} = 0.5$ so that C_s for a pure NaCl electrolyte becomes equal to the molar concentration. Other ions have β_i expressing their relative strength to either Na^+ or Cl^- . A common method is to set C_s equal to the ionic strength

$$I = \frac{1}{2} \sum_i C_i z_i^2, \quad (52)$$

which would put more weight on divalent ions and in our notation have $\beta_{Ca} = 2$. Investigation on interaction forces between ions and charged surfaces like clay or charged molecules like surfactant have shown that not only the valence, but also the hydrated sizes of the ions are important (Puerto and Reed, 1990). The ionic strength expression may severely underestimate the effect of divalent ions and Stavland et al. (2010) used a 'modified ionic strength' where the power of the valence term was allowed to be higher than 2 for divalent ions. The presented data indicated an order of magnitude higher effect from Ca^{2+} on the polymer viscosity, i.e., $\beta_{Ca} \approx 20$.

Temperature effects

In the current model, it is assumed that the main temperature dependence of the effective viscosity is through the viscosity of the solvent, which is computed according to an (exponential) Arrhenius equation. Additionally, we have seen that both relaxation time constants, λ_1 and λ_2 , are inverse functions of temperature, as they are related to diffusion. However, as we have only considered experiments performed at room temperature (20 °C), more experimental data is needed in order to test this part of the model.

Tables

Table 1 Matched parameters for the bulk shear thinning model. All the simulated HPAM polymers had a hydrolysis degree of 30 %, and the Mark-Houwink exponent was set to $a = 0.6$ for all four polymers.

Polymer	M_w [MDa]	$[\eta]$ [ml g ⁻¹]	k'	k''	λ_a [K mol ⁻¹ J ⁻¹]	a_n	b_n	x
530	5	1467	0.01	0.12	0.722	0.063	0.804	1
1030	10	2275	0.22	0.049	0.803	0.063	0.804	2
1530	15	2424	0.247	0.091	0.306	0.0782	0.56	1
2030	20	3750	0.01	0.077	0.350	0.063	0.804	1

Table 2 Model input parameters that were kept fixed in all cases. Note that the value for the rate constant, r_{deg} , listed here is based on equation (31) with F_s in units of Pa, R_p in μm , and M_w in MDa.

Parameter	Value	Explanation
IPV_0	0.1	Inaccessible pore volume (constant part)
f_{dpt}	1.0	Tuning parameter used in depletion layer model
f_{rkf}	1.0	Tuning parameter for size of adsorbed layer
$\tau^2 = (L_t/L)^2$	3.0	Tortuosity factor
α_c	2.0	Tuning parameter used in the shear rate calculation
C_{el}	4.0	Tuning parameter for calculating λ_2
m_2	1.5	Slope parameter for the shear thickening model
x_2	3.0	Governs the sharpness of the transition to the shear thickening regime
r_{deg}	0.0015	Rate constant used in degradation model
α_d	3.0	Degradation dependency on shear stress
β_d	1.0	Degradation dependency on molecular weight
λ_3	$8.0 \cdot \lambda_2$	Determines the onset of reduced swelling of adsorbed polymer
n_3	1.0	Exponent used in the shear dependent permeability reduction model
x_3	4.0	Parameter used in the shear dependent permeability reduction model

Table 3 Make-up of the synthetic sea water, SSW.

Salt	Concentration [g l ⁻¹]
NaCl	23.495
KCl	0.746
MgCl ₂ · 6H ₂ O	9.149
CaCl ₂ · 2H ₂ O	1.911
Na ₂ SO ₄	3.408
NaHCO ₃	0.168

Table 4 Properties for the various dual core systems. The diameter was in all cases $d = 3.8$ cm, while the lengths, permeabilities and porosities are denoted by L_i , k_i , and ϕ_i , for cores with indices $i = 1, 2$.

System id	Rock type	L_1 [cm]	L_2 [cm]	k_1 [mD]	k_2 [mD]	ϕ_1	ϕ_2
1	Berea	7.2	7.1	414.61	305.63	0.21	0.22
2	Berea	7.1	7.1	298.5	291	0.218	0.216
3	Berea	7	7	721.7	612.8	0.223	0.213
4	Berea	7.2	7.2	161.3	136.9	0.177	0.176
5	Berea	7.0	7.0	823.6	800.4	0.223	0.213
6	Bentheim	7.1	7.1	2018.8	1998.1	0.235	0.235

Table 5 Langmuir adsorption parameters used in the simulations. In all cases a value of $b = 1000000$ was used, and the maximum adsorption capacities are denoted by Q_m^1 and Q_m^2 for core 1 and core 2, respectively. The last five columns show comparisons between simulated and experimental RRF values.

System id	Rock type	Q_m^1	Q_m^2	Polymer	RRF ₁ model	RRF ₂ model	RRF ₁	RRF ₂
1	Berea	0.00044	0.00052	530	1.95	2.28	2	2
2	Berea	0.00034	0.00034	1030	2.28	2.24	2	2
3	Berea	0.00042	0.00045	1530	3.33	3.68	3.4	3.4
4	Berea	0.00058	0.00063	1530	6.26	6.39	6.3	6.3
5	Berea	0.00028	0.00028	2030	3.50	3.38	3.6	3.6
6	Bentheim	0.00027	0.00027	1530	1.99	2.00	2	2

References

- Al Hashmi, A., Al Maamari, R., Al Shabibi, I., Mansoor, A., Zaitoun, A. and Al Sharji, H. [2013] Rheology and mechanical degradation of high-molecular-weight partially hydrolyzed polyacrylamide during flow through capillaries. *Journal of Petroleum Science and Engineering*, **105**, 100–106.
- Bird, R.B., Armstrong, R.C., Hassager, O. and Curtiss, C.F. [1977] *Dynamics of polymeric liquids*, 1. Wiley, New York.
- Buchholz, B.A., Zahn, J.M., Kenward, M., Slater, G.W. and Barron, A.E. [2004] Flow-induced chain scission as a physical route to narrowly distributed, high molar mass polymers. *Polymer*, **45**(4), 1223–1234.
- Chauveteau, G. [1981] Molecular interpretation of several different properties of flow of coiled polymer solutions through porous media in oil recovery conditions. In: *SPE Annual Technical Conference and Exhibition, SPE-10060-MS*. Society of Petroleum Engineers.
- Chauveteau, G. [1986] Fundamental Criteria in Polymer Flow Through Porous Media and Their Relative Importance in the Performance Differences of Mobility Control Buffers. In: Glass, J. (Ed.) *Water-Soluble Polymers*, 213, Advances in Chemistry Series of the American Chemical Society, 227–268.
- Chauveteau, G. and Lecourtier, J. [1988] Propagation of polymer slugs through adsorbent porous media. In: *Water-Soluble Polymers for Petroleum Recovery*, Springer, 53–68.
- Chauveteau, G. and Moan, M. [1981] The onset of dilatant behaviour in non-inertial flow of dilute polymer solutions through channels with varying cross-sections. *Journal de Physique Lettres*, **42**(10), 201–204.
- Dawson, R. and Lantz, R.B. [1972] Inaccessible pore volume in polymer flooding. *Society of Petroleum Engineers Journal*, **12**(05), 448–452.
- De Gennes, P. [1974] Coil-stretch transition of dilute flexible polymers under ultrahigh velocity gradients. *The Journal of Chemical Physics*, **60**(12), 5030–5042.
- Dupas, A., Hénaut, I., Argillier, J.F. and Aubry, T. [2012] Mechanical degradation onset of polyethylene oxide used as a hydrosoluble model polymer for enhanced oil recovery. *Oil & Gas Science and Technology—Revue d'IFP Energies nouvelles*, **67**(6), 931–940.
- Ford, J. [1995] Improved algorithms of illinois-type for the numerical solution of nonlinear equations. *Tech. Rep. CSM-257, University of Essex*.

- Haas, R. and Durst, F. [1982] Viscoelastic flow of dilute polymer solutions in regularly packed beds. In: *Progress and Trends in Rheology*, Springer, 212–217.
- Hiemenz, P.C. and Lodge, T.P. [2007] *Polymer chemistry*. CRC press, 2nd edn.
- Hirasaki, G. and Pope, G. [1974] Analysis of factors influencing mobility and adsorption in the flow of polymer solution through porous media. *Society of Petroleum Engineers Journal*, **14**(04), 337–346.
- Keller, A. and Odell, J. [1985] The extensibility of macromolecules in solution; a new focus for macromolecular science. *Colloid and Polymer Science*, **263**(3), 181–201.
- Lake, L.W. [1989] *Enhanced oil recovery*. Prentice Hall Inc., Old Tappan, NJ.
- Maerker, J. [1975] Shear degradation of partially hydrolyzed polyacrylamide solutions. *Society of Petroleum Engineers Journal*, **15**(04), 311–322.
- Nguyen, T. and Kausch, H.H. [1991] Influence of nozzle geometry on polystyrene degradation in convergent flow. *Colloid and Polymer Science*, **269**(11), 1099–1110.
- Odell, J., Keller, A. and Rabin, Y. [1988] Flow-induced scission of isolated macromolecules. *The Journal of chemical physics*, **88**(6), 4022–4028.
- Omari, A., Moan, M. and Chauveteau, G. [1989] Wall effects in the flow of flexible polymer solutions through small pores. *Rheologica Acta*, **28**(6), 520–526.
- Puerto, M.C. and Reed, R.L. [1990] Surfactant selection with the three-parameter diagram. *SPE Reservoir Engineering*, **5**(02), 198–204.
- Rajagopalan, R. and Hiemenz, P.C. [1997] *Principles of colloid and surface chemistry*. CRC press, 3rd edn.
- Seright, R. [1983] The effects of mechanical degradation and viscoelastic behavior on injectivity of polyacrylamide solutions. *Society of Petroleum Engineers Journal*, **23**(03), 475–485.
- Seright, R.S., Fan, T., Wavrik, K. and Balaban, R.d.C. [2011] New insights into polymer rheology in porous media. *SPE Journal*, **16**(01), 35–42.
- Sochi, T. [2010] Flow of non-newtonian fluids in porous media. *Journal of Polymer Science Part B: Polymer Physics*, **48**(23), 2437–2767.
- Stavland, A., Jonsbrotten, H., Lohne, A., Moen, A. and Giske, N. [2010] Polymer Flooding–Flow Properties in Porous Media Versus Rheological Parameters. In: *Presented at the 72nd EAGE Conference and Exhibition incorporating SPE EUROPEC, SPE-131103-MS*.
- Thomas, A., Gaillard, N. and Favero, C. [2012] Some key features to consider when studying acrylamide-based polymers for chemical enhanced oil recovery. *Oil & Gas Science and Technology–Revue d'IFP Energies nouvelles*, **67**(6), 887–902.
- Vanapalli, S.A., Ceccio, S.L. and Solomon, M.J. [2006] Universal scaling for polymer chain scission in turbulence. *Proceedings of the National Academy of Sciences*, **103**(45), 16660–16665.
- Vanapalli, S.A., Islam, M.T. and Solomon, M.J. [2005] Scission-induced bounds on maximum polymer drag reduction in turbulent flow. *Physics of Fluids*, **17**(9), 095108.
- Watts, J. [1986] A compositional formulation of the pressure and saturation equations. *SPE Reservoir Engineering*, **1**(03), 243–252.
- Yasuda, K., Armstrong, R. and Cohen, R. [1981] Shear flow properties of concentrated solutions of linear and star branched polystyrenes. *Rheologica Acta*, **20**(2), 163–178.

Paper II

Polymer flooding in sandpacks with a dual-porosity

By:

Ringen, Irene

Stiegler, Hjørdis

Nødland, Oddbjørn

Hiorth, Aksel

Stavland, Arne

Printed in:

Society of Core Analysts (2016).

POLYMER FLOODING IN SANDPACKS WITH A DUAL-POROSITY

I. Ringen^{1,2,3}, H. Stiegler¹, O. Nødland^{1,2,3}, A. Hiorth^{1,2,3} and A. Stavland^{2,3}

⁽¹⁾University of Stavanger, Norway, ⁽²⁾The National IOR Center of Norway, ⁽³⁾IRIS AS – International Research Institute of Stavanger, Norway

This paper was prepared for presentation at the International Symposium of the Society of Core Analysts held in Snowmass, Colorado, USA, 21-26 August 2016

ABSTRACT

Polymer and low salinity water flooding are methods to improve oil recovery from both sandstone and carbonate reservoirs. Combining these two methods is of interest for at least two reasons. Firstly, this improves both the macroscopic and microscopic sweep efficiency at the same time, and secondly less polymer is needed when it is mixed with a low salinity brine. The last point is important since it reduces the amount of produced chemicals, which has both financial and environmental benefits. However, polymer molecules are large compared to the ions in the brine, and even large compared to the typical pore sizes. The polymer molecules may therefore flow at a completely different speed than the ions. This could be of particular importance in fractured carbonate systems.

In this paper we investigate the rheological behavior of a polymer solution in a system where the full pore system is accessible for ionic transport, while not for the polymer molecules. We have designed a novel experimental setup that allows for electric resistance measurements along the porous media. From the resistivity measurements, information about the porosity and ionic concentrations within the sandpack was gained. A low salinity polymer solution was injected into a dual porosity sandpack saturated with a higher salinity brine. The viscosity of the effluent fluid was monitored with a capillary tube rheometer, and the apparent viscosity in the porous medium was derived from the differential pressure across the column. The flooding experiments showed viscoelastic behavior, i.e. by increasing shear rates, the apparent viscosity increased dramatically due to elongation of the polymers molecules. Most importantly, the experimental results clearly show that the polymer front moves at a higher speed than the salinity front. As a result, the polymer solution mixes with the high salinity brine and the viscosity decreases. These effects are important to take into account when designing polymer floods in dual-porosity systems.

INTRODUCTION

In order to increase the oil recovery, waterflooding has been a successful recovery technique for many oil reservoirs during the last decades. However, in some reservoirs,

waterflooding may lead to early water breakthrough and low oil production rates. Polymer flooding is considered as a very promising technology in enhanced oil recovery (EOR) processes. If polymers are added to the injection water they increase the water viscosity. This can lead to a favorable mobility ratio between oil and water. Depending on the heterogeneities in the reservoir, the change in mobility ratio could greatly impact the macroscopic sweep efficiency and enhance oil recovery. However, polymer solutions are non-Newtonian fluids and hence, the rheological properties are sensitive to shear forces.

In field operations, hydrolyzed polyacrylamides (HPAM) are the most common EOR polymers [1]. These synthetic polymers show viscoelastic properties when flowing through a porous media [1-9]. At low fluid velocities, a Newtonian or near-Newtonian behavior is reported by Seright et.al. [9], while Heemskerk et al. [8] and Delshad et al. [10] reports shear thinning behavior. Both Chauveteau et al. [11] and Stavland et al. [1] demonstrate that the polymer solutions tested exhibit shear thinning behavior with lower viscosities than bulk viscosity because the polymer does not flow through the entire pore volume. At increasing shear rates, the polymer molecules get elongated and contracted due to the pore structures of the porous media. Consequently, the apparent viscosity of the polymer solution increases dramatically (usually named a shear thickening behavior). If the polymer solution is exposed to very high stresses, the molecules may rupture and degrade [1]. This could easily happen when the polymer is injected, if care is not taken.

The properties of polymer solutions are affected by the molecular weight, polymer concentration and salinity. Polymers are polyelectrolytes, i.e. the molecules have multiple charges distributed along the chain, hence, in low salinity brines the molecules expand due to mutual repulsion of charges along the molecule chain [12]. This repulsion increases the viscosity of the solution, and consequently less chemicals are needed to obtain the targeted viscosity. In recent years, it has been observed that the salinity of the injected fluid in itself can increase the microscopic sweep efficiency of oil reservoirs [13]. By mixing polymers in low salinity brines, it is possible to obtain an increase in both macroscopic and microscopic sweep efficiency. However, the polymer molecules and ions move with different speeds in the porous media, mainly because the polymer molecules are larger than the ions. This could have the effect that the polymer molecules leave the low salinity brine behind and consequently mixes with the formation water, and part of the benefit with injecting polymers in low salinity water is lost.

To shed some more light on this phenomenon, we have flooded polymer solutions with different salinities through a sandpack column. This column consisted of silica grain, where the grains themselves are porous. This system has to our knowledge not been used to study the flow of polymer flow before. Every individual grain consists of consolidated micro silica, thus there is a macro porosity between the grains and a micro porosity within the grains. As a consequence of the macro and micro porosity the full pore volume was accessible for ionic transport but not for the polymer molecules. Electric resistance was measured along the column to track ionic concentrations during the flooding

experiments. The effective polymer rheology was measured in the sandpack, and a capillary tube rheometer, at the outlet of the sandpack, monitored the effluent polymer rheology.

THEORY

In bulk, the polymers have a shear thinning behavior. The viscosity, η , decreases with increasing shear rate, $\dot{\gamma}$, and the behavior is well described by a Carreau model [14],

$$\eta(\dot{\gamma}) = \eta_{\infty} + (\eta_0 - \eta_{\infty}) \cdot [1 + (\lambda_1 \dot{\gamma})^x]^{(n-1)/x}, \quad (1)$$

where η_0 and η_{∞} is the polymer viscosity at zero and infinite shear rate, respectively, λ_1 is a time constant representing the critical shear rate at which the fluid deviates from Newtonian behavior, and n is the flow behavior index. For a shear thinning fluid, $n < 1$ and n typically ranges from 0.4 to 0.7 [15]. The tuning parameter, x , is used to improve the viscosity match.

Viscous flow in capillary tubes

A capillary tube was used to measure the effluent viscosity. In order to allow for a simple interpretation of the measured pressure drop across the capillary tube and the imposed flow rate, it is important to choose a tube with a diameter much larger than the polymer molecules to ignore wall effects, and a long tube to avoid entrance and exit effects. If an appropriate tube is chosen, the flow is well described by the Hagen-Poiseuille equation. In such a flow, the shear stress, τ , is given as

$$\tau = \frac{\Delta P r'}{2L}, \quad (2)$$

where ΔP is the differential pressure, r' is the radius, and L is the tube length. For a Newtonian fluid, the shear stress is related to the shear rate through $\tau = \eta \dot{\gamma}$. Here, the shear rate, $\dot{\gamma}$, is defined as

$$\dot{\gamma} = \frac{dv(r')}{dr'}, \quad (3)$$

where v is the flow velocity along the tube. Assuming a power-law shear rate, i.e. ignoring η_{∞} and assuming $\lambda_1 \dot{\gamma} \gg 1$, the viscosity of the polymer solution in the capillary tube follows a simple power law, $\eta = \eta_0 (\lambda_1 \dot{\gamma})^{n-1}$. Combining the two equations above, solving for $v(r')$, and then integrating over the cross section of the tube with radius R , we get the flow rate, q . We can then express the apparent shear rate, $\dot{\gamma}_A$, in the tube and apparent viscosity, η_A , as

$$\dot{\gamma}_A = \frac{3 + 1/n}{4} \cdot \frac{4q}{\pi R^3} \quad \text{and} \quad \eta_A = \frac{4}{3 + 1/n} \cdot \frac{\pi R^4 \Delta P}{8qL}, \quad (4)$$

respectively. The $(3 + 1/n)/4$ term is known as the Mooney-Rabinoswitch-Weissenberg correction factor that takes into account the effect of the change of shape of the velocity profile when non-Newtonian fluids flow through capillaries under laminar conditions. For Newtonian fluids ($n = 1$), equation (4) reverts to the usual Hagen-Poiseuille equation.

Apparent viscosity in porous media

The viscosity of the polymer solution cannot be measured directly in flooding experiments. Due to the complex network of pores and channels in the porous medium, the shear rate and thus the viscosity will vary within the medium. In this work we will extend the formulation developed in the previous section by introducing an average radius defined by the Kozeny-Carman relationship $k = \phi \frac{r^2}{8\tau_c}$ (τ_c is the tortuosity):

$$\dot{\gamma} = \alpha \cdot \frac{4q}{A\sqrt{8k\phi}} \quad (5)$$

Here A is the cross-sectional area, k is the permeability, ϕ is the porosity of the porous medium, and α is an empirical parameter used to match viscosity measured in bulk and porous medium, normally set equal to 2.5 [1]. The arguments for $\alpha > 1$ are that the permeability to the polymer is lower than to water and that the polymer velocity is higher than to water. The advantages of using this model is its simplicity and clarity, but clearly it has its limitations due to the dual-porosity of the system. We have therefore used the macro porosity ($\phi = \phi_{\text{mac}}$), since the polymer molecules are too large to flow in the narrow micro pores.

The apparent viscosity is estimated from the Darcy equation,

$$\eta_A = \frac{Ak \Delta P}{q \Delta L}. \quad (6)$$

Since the effective shear rate is proportional to the flow velocity, several models have been suggested for the viscosity as a function of flow rate and properties of the porous medium. Based on the Carreau model, Stavland et.al. derived a model for the apparent viscosity of polymers in porous media where the apparent viscosity is the sum of the shear viscosity and elongation viscosity multiplied by a degradation term [1]:

$$\eta_{\text{app}} = \eta_{\infty} + [(\eta_0 - \eta_{\infty}) \cdot (1 + (\lambda_1 \dot{\gamma})^n) + (\lambda_2 \dot{\gamma})^{\xi}] \cdot [1 + (\lambda_3 \dot{\gamma})^x]^{\frac{\xi-1/2}{x}}. \quad (7)$$

The first part of equation (7) represent the bulk viscosity matched with the Carreau model (1). The next term, $(\lambda_2 \dot{\gamma})^{\xi}$, represents the elongation viscosity, which increases dramatically by increasing the shear rate. The elongation exponent, $\xi > 0$, depends on molecular weight of the polymer. As we see from the expression, this elongation term is increasing for shear rates higher than $1/\lambda_2$, and the onset of elongation depends on the porous medium,

$$\frac{1}{\lambda_2} = N_{\text{De}} \left(\frac{1 - \phi}{\phi} \right) \frac{6\alpha\sqrt{\tau_c}}{\lambda_1}, \quad (8)$$

where N_{De} is the Deborah number describing the liquid-like behavior of the polymer. The last term in equation (7) represents the degradation of polymers, where the time constant λ_3 represents the onset of shear degradation and x is a tuning parameter used to improve viscosity match.

Chemical concentrations and resistivity

In this work we use resistance measurements to track concentration fronts in the sandpack. The resistivity, ρ , is the inverse of the conductivity, σ , and the relationship between resistivity and resistance is

$$r = \rho \frac{L}{A}, \quad (9)$$

where r is the resistance, L is the length and A is cross-sectional area of the porous media. The total resistance of a fluid-filled porous media, r_T , can be represented by the parallel resistance relationship, and since most rocks are non-conductive, the total resistance of a fluid-filled porous medium is related to the brine resistance ($r_T \approx r_w$). A fluid's ability to conduct electric current depends strongly on its ionic concentration. The most common approach to link resistance to concentration is to use Archie's law [16],

$$\sigma_o = \frac{1}{F} \sigma_w. \quad (10)$$

Here, σ_w is the conductivity of the brine, σ_o is the conductivity to the fluid-filled porous medium, and F is the formation factor, $F = \phi^{-m}$, which is related to the total porosity via the cementation exponent m . The total porosity, ϕ_T , of the sandpack is

$$\phi_T = \phi_{\text{mac}} + \phi_{\text{mic}}, \quad (11)$$

where ϕ_{mac} is the macro porosity and ϕ_{mic} is the micro porosity. Here we use the following generalization of Archie's law for a dual porosity medium [17]:

$$\sigma_o = \phi^{m-1} (\phi_{\text{mac}} \sigma_{w,\text{mac}} + \phi_{\text{mic}} \sigma_{w,\text{mic}}). \quad (12)$$

In the case where the conductivity of the two domains are equal, $\sigma_{w,\text{mac}} = \sigma_{w,\text{mic}} = \sigma_w$, equation (12) reduces to (10). From our experiments, conductivity versus salinity is,

$$\sigma_w = a c_{\text{NaCl}} + b, \quad (13)$$

where c_{NaCl} is the salinity of the brine in $[\text{g}/\text{cm}^3]$. From our experiments, $a = 1463 \text{ mS}\cdot\text{cm}^2/\text{g}$ and $b = 2.03 \text{ mS}/\text{cm}$.

MATERIALS AND METHODS

In the experiments, two brines were used, 35 g/L NaCl (B35) and 10 g/L NaCl (B10), where the latter was the polymer make up brine. The brines were filtered using a 0.45 μm HAWP-filter from Millipore. The polymer was Flopaam 5115SH, a synthetic acrylate-ATBS polymer with medium anionicity and high molecular weight, delivered by SNF. A 5000 ppm mother solution was prepared by gently adding the polymer in the brine under high rate mechanical mixing, thereafter overnight low rate mixing. Dilution to 1000 ppm was performed using a magnetic stirrer. Bulk viscosity was measured using an Anton Paar Physica MCR 301 rheometer at 20 °C and variable shear rates from 0.1 s^{-1} to 500 s^{-1} using a cone and plate geometry. Viscosities were measured at both increasing and decreasing shear rates. Due to better accuracy in the measurements, the viscosities

obtained at decreasing shear rates were used. In Table 1 and Table 2, the fluid properties and the conductivity of the NaCl brines is shown.

For the sandpack column, Silica Gel 63-200 μm was used as sand. In Figure 1, Scanning Electron Microscope (SEM) images of the grain structure are shown. The micro structure is clearly visible; each individual sand grain is porous as the grains are consolidations of multiple micro silica grains. The size of a micro grain is approximately 80 nm with a pore size of 6 nm. The density of Silica is 2.65 g/cm^3 . From the supplier, Sigma-Aldrich, the pore volume of the macro grains was reported to be $0.8 \text{ cm}^3/\text{g}$ rock, thus the micro porosity was estimated to 38 % (36.3-41.3 %) and the macro porosity to 44 % (39.2-46.6 %), based on 12 sandpacks. The properties of the column sandpack are shown in Table 3.

The column used was an 80 cm long construction of 6 glass cylinders and metal joints as illustrated in Figure 2. The dimensions of the glass cylinder were $D = 1.6 \text{ cm}$ and $L = 10 \text{ cm}$. This construction allows for measurements of electric current along the sandpack during flooding. An automatic RCL meter was connected to the column by 7 electrodes on the metal joints, which measured the 6 sections (Z1–Z6).

Experimental procedure

A schematic drawing of the experimental set-up is shown in Figure 2. Several sandpack columns were flooded with P10 during this work. All experiments were performed at ambient temperature. To control the pressure in the system, a backpressure regulator, set to 3 bars, was set up at the end of the system. To measure the viscosity of the effluent during flooding, a capillary tubing acting as a rheometer was connected to the outlet of the column. The capillary tube rheometer was 100 cm long with an inner diameter of 0.0762 cm. The flooding process was as follows:

1. Assemble the column. Successful packing was achieved by filling sand from the top of the column while the outlet was connected to a vacuum pump. Vibration during packing was not an option due to the glass construction.
2. Saturate the sandpack with brine B35 at the injection rate 1 ml/min.
3. Measure the porosity from the sandpack saturation (pore volume injected), and from mass measurements of the sand grains.
4. The effective brine permeability was determined by varying the injection rates and using the corresponding differential pressures across the column in equation (6).
5. In one separate sandpack/experiment, B10 was injected for evaluating ion dispersion in a brine-brine displacement experiment. The effluent ionic concentration was estimated by measuring Cl^- content.
6. In the following experiment, the polymer solution P10 was injected at a constant rate of 0.3 ml/min. This injection rate corresponds to the shear rate of $\sim 60 \text{ s}^{-1}$ in the sandpack and $\sim 115 \text{ s}^{-1}$ in the capillary tube rheometer.
7. Measure the pressure drop across the sandpack at different injection rates for estimating the apparent viscosity of the polymer solution within the sandpack.

8. Measure fluid effluent viscosity by measuring the pressure drop across the capillary tube rheometer connected to the outlet of the column. The injection rate was altered and effluent viscosity was recorded at stable differential pressure.
9. During all flooding experiments, the electrical resistance over 6 section (Z1–Z6) was continuously measured to track chemical concentration profiles.

RESULTS AND DISCUSSION

As the sandpacks comprises of porous silica grains, the total porosity is high, approximately 80 %. The total porosity, ϕ_T , includes the macro porosity, ϕ_{mac} , and the micro porosity, ϕ_{mic} , see equation (11). We clearly see the effect of the micro and macro porosity in Figure 3. In Figure 3, the effluent concentration is shown from one experiment where B35 was displaced by B10 at the injection rate of 2 ml/min. Effluent samples were collected to determine the ion concentration, where the Cl concentration was determined by titration with $AgNO_3$. Injection of at least 2.5 pore volumes of B10 was required to displace all initial ions, which we interpret as being caused by the dual-porosity structure. A possible explanation could be that the time it takes to flow through the macro pores is shorter than the time it takes to exchange ions from the micro pores. Consequently, a long concentration tail is observed. The electrical resistance measurements along the sandpack also support this, as can be seen in Figure 4. In this figure, the measured resistance has been calculated to NaCl concentration by the relation in equation (13). When the initial high salinity brine B35 is displaced by either the low salinity brine B10 or the polymer solution P10, the electrical resistance increases for every section as the front propagates through the sandpack. In Figure 5, the measured resistances for the 6 sections are plotted versus pore volume injected of P10, along with simulated values. As the front propagates there is an increasing lag before the resistivity reaches the expected plateau value.

In our view, the most interesting results is when the polymer solution was injected in the system. In Figure 6, the bulk properties of the polymer solutions are shown. There is a clear effect of the salinity of the make up brine. As seen, the measured viscosity for P10 and P35 are well matched with a Carreau model, where the shear thinning exponent n is 0.72 and 0.83 for P10 and P35, respectively. In Figure 7, the results from the capillary tube rheometer in 3 different sandpacks is shown and we see that there is a good match between the bulk measurements and the capillary tube rheometer. The viscosity of the low salinity P10 solution was higher than the viscosity of P35. At low salinities, the polymer molecules can expand due to electrostatic repulsion between the anionic groups along the polymer chain [15]. This results in a higher viscosity for the low salinity polymer solution. When the salinity is increased, the repulsive forces are reduced. This decreases the polymer chain and hence, the viscosity is decreased.

In Figure 8, the pressure drop across the capillary tube rheometer and the corresponding resistance measurements are shown when the low salinity polymer solution, P10, displaced the high salinity brine, B35. At PV = 0.58, the polymer breaks through, as seen by the increased differential pressure across the capillary tube rheometer. The apparent

viscosity of effluent between 0.58 and 1.0 pore volume injected is ~ 4.5 cp at the shear rate 115 s^{-1} . This apparent viscosity is close to the P35 bulk viscosity of 5.5 cp at 115 s^{-1} . The resistance measurements along the sandpack show that the salinity front lags behind, and from the resistance measurements in the last section (Z6) of the column, the salinity is high when the polymer leaves the sandpack. At approximately 1 PV injected, the low salinity water breaks through. When this happens, we see an increase in the resistance, and more importantly a second increased pressure drop occurs across the capillary tube. The apparent viscosity of the effluent after 1 PV injected is ~ 6.2 cp, which is close to the bulk viscosity of 7.0 cp at 115 s^{-1} for P10. This clearly demonstrates the different flow paths taken by the ions and the polymers through the column. The fraction of the macro pore volume to the total pore volume is 0.58, and because of this, $u_{\text{polymer}}/u_{\text{NaCl}} \approx 1.72$. A second run in the same column was performed to determine if there was any effect of polymer retention, see Figure 9. In Figure 9, the pressure drop across the sandpack is shown together with the pressure drop across the capillary tube rheometer at the outlet of the column. Within the experimental limits we could not observe any retention.

In Figure 10, the apparent viscosity in the column given by equation (6), is shown together with the estimated viscosity from the capillary tube rheometer when the polymer solution P10 was injected through the sandpack at various flow rates. All the experiments/sandpacks show the same trends: By increasing the shear rates, shear thickening behavior was observed and the apparent viscosity increased from a shear rate of 100 s^{-1} . This behavior is caused by elongation of the polymer molecules in the pore structure of the sandpacks. This elongation effect is well-known and well documented in the literature [1, 8, 9]. A further increase in shear rates could have ruptured the molecules, but shear degradation was not observed due to pressure limitations in the system. The results were well matched with the Carreau-based apparent viscosity model given in equation (7), by adjusting the shear elongation term. We were also able to match the experiments at $S_w = 1 - S_{or}$, see Figure 11.

CONCLUSION

The rheology behavior of the synthetic acrylate-ATBS polymer solution is affected by ionic concentration and shear. In bulk measurements, the polymer solution shows shear thinning behavior, while in the sandpack both shear thinning and shear thickening was observed. As the shear rates increases, the apparent viscosity increases dramatically due to elongation of the polymer molecule. The apparent viscosity is dependent on the effective porosity and permeability of the porous medium.

In a dual porosity system, the polymer molecules flow with higher velocity than the salinity front, i.e. the polymers flow in the macro pores, while the ions are transported (mainly by diffusion) in the entire pore volume. The polymer front mixes with the initial brine, hence the viscosity of the front decreases. When the initial ions are fully displaced, the viscosity of the polymer solution increases.

The difference in flow velocity is important to consider when evaluating the EOR potential of polymer flooding on field scale, e.g. in highly inhomogeneous reservoirs. The reservoir formation water is typically more saline than the injected water, which usually is seawater (on the Norwegian Continental Shelf). Thus, if the flow velocity of polymers is higher than the velocity of the salinity front, the polymer will mix with formation water and consequently the viscosity will be decreased. This does not mean that there is not a potential benefit by combining polymer and low salinity flooding. We have not at all considered the effect of low salinity water on the microscopic sweep efficiency which can be substantial.

ACKNOWLEDGEMENTS

The authors acknowledge the Research Council of Norway and the industry partners; ConocoPhillips Skandinavia AS, BP Norge AS, Det Norske Oljeselskap AS, Eni Norge AS, Maersk Oil Norway AS, DONG Energy A/S, Denmark, Statoil Petroleum AS, ENGIE E&P NORGE AS, Lundin Norway AS, Halliburton AS, Schlumberger Norge AS, Wintershall Norge AS of The National IOR Centre of Norway for support.

REFERENCES

1. Stavland, A., H. Jonsbraten, A. Lohne, A. Moen, and N.H. Giske. Polymer Flooding - Flow Properties in Porous Media versus Rheological Parameters. *Society of Petroleum Engineers*. 2010. DOI: 10.2118/131103-ms.
2. Pye, D.J., *Improved Secondary Recovery by Control of Water Mobility*. 1964.
3. Smith, F.W., *The Behavior of Partially Hydrolyzed Polyacrylamide Solutions in Porous Media*. 1970.
4. Jennings, R.R., J.H. Rogers, and T.J. West, *Factors Influencing Mobility Control By Polymer Solutions*. 1971.
5. Hirasaki, G.J. and G.A. Pope, *Analysis of Factors Influencing Mobility and Adsorption in the Flow of Polymer Solution Through Porous Media*. 1974.
6. Seright, R.S., *The Effects of Mechanical Degradation and Viscoelastic Behavior on Injectivity of Polyacrylamide Solutions*. 1983.
7. Masuda, Y., K.-C. Tang, M. Miyazawa, and S. Tanaka, *1D Simulation of Polymer Flooding Including the Viscoelastic Effect of Polymer Solution*. 1992.
8. Heemskerck, J., R. Rosmalen, R. Janssen-van, R.J. Holtslag, and D. Teeuw. Quantification of Viscoelastic Effects of Polyacrylamide Solutions. *Society of Petroleum Engineers*. 1984. DOI: 10.2118/12652-ms.
9. Seright, R.S., J.M. Seheult, and T. Talashek, *Injectivity Characteristics of EOR Polymers*. 2009.
10. Delshad, M., D.H. Kim, O.A. Magbagbeola, C. Huh, G.A. Pope, and F. Tarahhom. Mechanistic Interpretation and Utilization of Viscoelastic Behavior of Polymer Solutions for Improved Polymer-Flood Efficiency. *Society of Petroleum Engineers*. 2008. DOI: 10.2118/113620-ms.
11. Chauveteau, G., M. Tirrell, and A. Omari, *Concentration dependence of the effective viscosity of polymer solutions in small pores with repulsive or attractive walls*. *Journal of Colloid and Interface Science*, 1984. **100**(1): p. 41-54.

12. Sorbie, K.S., *Polymer - improved oil recovery* 1991: Springer Science & Business Media.
13. Tang, G.-Q. and N.R. Morrow, *Influence of brine composition and fines migration on crude oil/brine/rock interactions and oil recovery*. Journal of Petroleum Science and Engineering, 1999. **24**(2–4): p. 99-111.
14. Green, D.W. and G.P. Willhite, *Enhanced oil recovery*. SPE textbook series. Vol. vol. 6. 1998, Richardson, Tex: Henry L. Doherty Memorial Fund of AIME, Society of Petroleum Engineers.
15. Sheng, J., *Modern chemical enhanced oil recovery: theory and practice* 2010: Gulf Professional Publishing.
16. Archie, G.E., *The Electrical Resistivity Log as an Aid in Determining Some Reservoir Characteristics*. 1942.
17. Singha, K., F.D. Day - Lewis, and J. Lane, *Geoelectrical evidence of bicontinuum transport in groundwater*. Geophysical Research Letters, 2007. **34**(12).

Table 1 Overview of fluids

Brine	B10	10 g/L NaCl
	B35	35 g/L NaCl
Polymer solution	P10	1000 ppm, 10 g/L NaCl
	P35	1000 ppm, 35 g/L NaCl

Table 2 Conductivity of NaCl brines at 22.5 °C

Concentration [g/L]	Conductivity [mS/cm]
10	16.84
15	22.79
20	31.90
25	39.50
30	45.60
35	53.60

Table 3 Average properties of the sandpack. The values are estimated from 12 sandpacks.

Properties of sandpack column		
Length	L	80 cm
Diameter	D	1.5 cm
Grain size	d_{macro}	63-200 μm
Micro grain size	d_{micro}	80 nm
Pore size		6 nm
Surface area		500 m^2/g
Total porosity	ϕ_{total}	82 %
Macro porosity	ϕ_{macro}	44 %
Micro porosity	ϕ_{micro}	38 %
Permeability	k	6.835 D
Formation resistivity factor	F	1.8626
Tortuosity	τ	1.529
Cementation factor	m	1.0

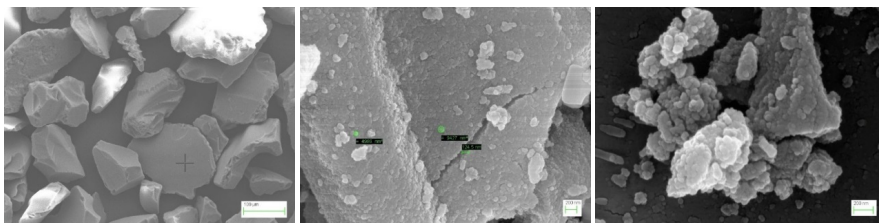


Figure 1 The Silica Gel grains. a) Overview of the sand grains, b) the surface of one grain, the size of the micro grains is 80 nm and the fracture measures 126 – 200 nm, c) the micro structure close-up, every grain is a rigid network of silica grains consolidated together. The pictures are taken with SEM at UiS.

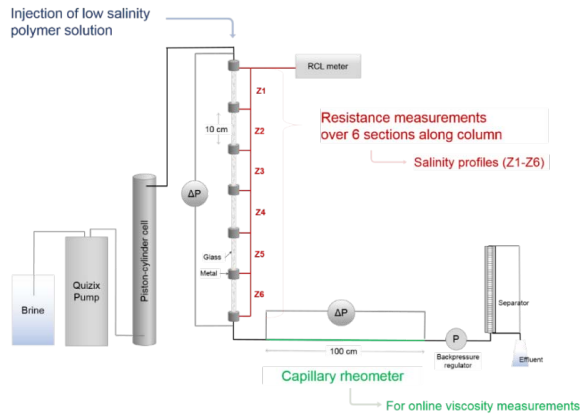


Figure 2 The experimental set-up, the sandpack was flooded from the top. The electric resistance was measured over 6 glass sections, and a capillary tube rheometer connected at the outlet of the column was used to measure the viscosity of effluent fluid.

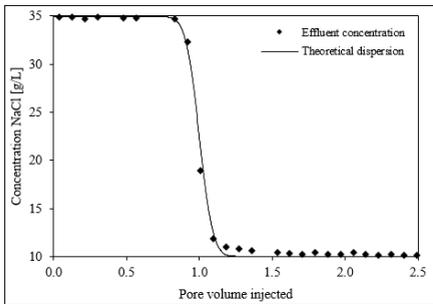


Figure 3 Displacing B35 by B10. Effluent salinity concentration profile.

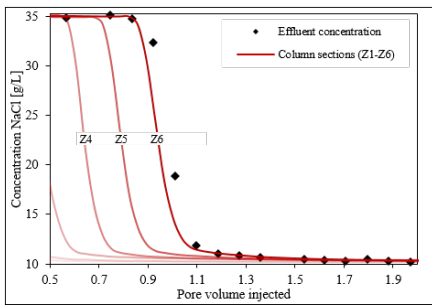


Figure 4 Effluent and calculated concentrations from resistance measurements

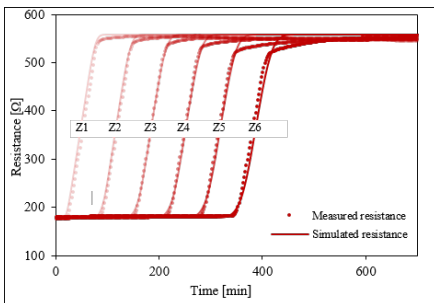


Figure 5 The electric resistance in the 6 sections along the sandpack during P10 injection at 0.3 ml/min. The circles are experimental data and the solid lines represents simulated data.

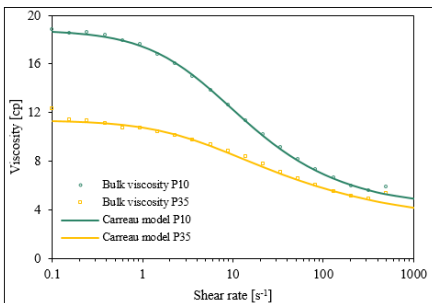


Figure 6 Bulk rheology of polymer solution P10 and P35 in rheometer (plate and cone).

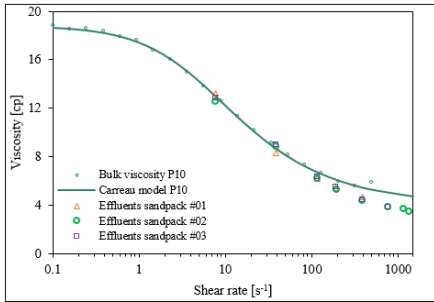


Figure 7 Bulk measurements and effluent viscosity from capillary tube rheometer of P10 at various injection rates in 3 different experiments.

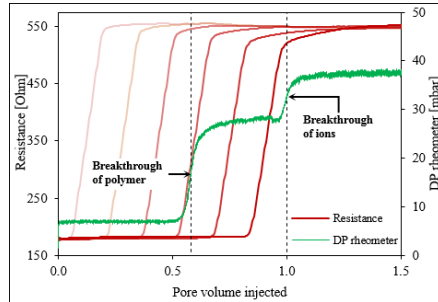


Figure 8 The pressure difference over the capillary tube rheometer and the corresponding resistance measurements along the sandpack column during P10 injection at 0.3 ml/min.

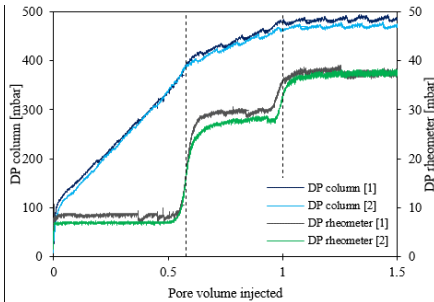


Figure 9 The pressure difference across the sandpack and across the capillary tube rheometer during P10 injection at 0.3 ml/min. [1] and [2] represent the first and the second injection.

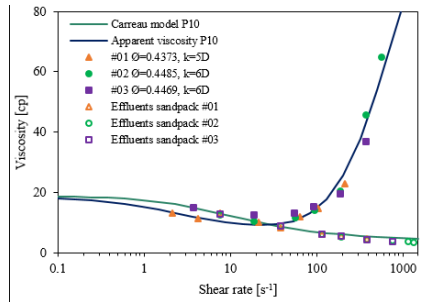


Figure 10 The apparent viscosity of P10 in-situ and in the capillary tube rheometer versus shear rates. The apparent viscosity in-situ is shear thickening, while the effluent is shear thinning.

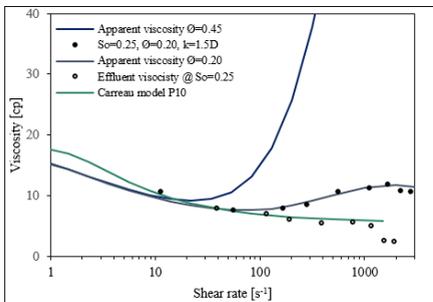


Figure 11 The apparent viscosity of P10 in-situ and in the capillary tube rheometer versus shear rates when oil was present in pores ($S_w \approx 75\%$).

Paper III

Mechanical Degradation of Polymers at the Field Scale-A Simulation Study

By:

Nødland, Oddbjørn

Lohne, Arild

Hiorth, Aksel

Presented at:

IOR 2017-19th European Symposium on Improved Oil Recovery (2017).

III. Mechanical Degradation of Polymers at the Field Scale-A Simulation Study

Abstract

Flexible polymer molecules display a variety of macroscopic flow behaviours when dissolved in brine and flooded through porous rocks. At EAGE-ECMOR XV we presented a simulation model for polymer flooding that is capable of modelling all the commonly observed flow regimes in porous media, including mechanical degradation. The model allowed us to match different experiments with most of the input parameters kept fixed, and in particular how HPAM polymers of different molecular weights were mechanically degraded when injected into cores and series of cores with variations in permeability.

The main purpose of this paper was to investigate the mechanical degradation close to an injector. We have performed several hundred simulations, using history matched polymer properties for a single polymer type (HPAM 3630S, SNF Floerger). We found that the estimated mechanical degradation is very sensitive to the grid resolution, and for the simulations presented here we had to use grid cells on the order of millimetres near the well.

For the particular polymer tested, we found that little or no degradation was predicted when the effective shear rate at the sand face was kept below approximately 1000 s^{-1} . This result indicates that in the presence of open fractures near the well, the amount of degradation should be small. Furthermore, the results also suggest that injecting a polymer with the highest possible molecular weight may not always be the most economical option. Instead, if a certain level of degradation is tolerated and expected to occur, injecting a slightly lower molecular weight polymer may lead to more or less the same improved sweep efficiency, while demanding a lower injection pressure. Finally, we see that it is important to include not only shear thinning and shear thickening fluid rheologies, but also degradation, if correct well pressures are to be predicted.

Introduction

Although polymer flooding is regarded as a mature EOR technology, implementations of the method offshore have been relatively rare (Kaminsky et al., 2007; Standnes and Skjevraak, 2014; Sheng et al., 2015). One obvious explanation for this is economic limitations, e.g., periods of declining oil prices. Another explanation is that the proper planning, prediction, and execution of these projects can be very difficult and time-consuming from a technical perspective. The main goal of using polymers is to increase the effective aqueous phase viscosity of the displacing brine, and thereby provide a better sweep of the reservoir. However, the performance of a polymer flood can be very sensitive to properties of both the reservoir, and the fluid under consideration (Thomas et al., 2012). Examples of some important factors to consider are, e.g., formation permeability, oil viscosity, temperature, polymer rheology, and salinity effects.

Two factors that are especially relevant for field performance are the effects of polymer (apparent) shear thickening, and polymer mechanical degradation. The polymers that are typically used for EOR are partially hydrolyzed polyacrylamides (HPAM). These polymers tend to be very large, with a molecular weight on the order of several million Daltons. Moreover, they exhibit a flexible coil conformation in solution, which gives them elastic thickening properties. Specifically, at high flow rates, the flow resistance of these polymer solutions in porous media will tend to rise sharply as a function of flow rate, an effect which is referred to as (apparent) shear thickening in the literature (Chauveteau and Moan, 1981; Chauveteau et al., 1984). Near the wells, this can be problematic, as the additional flow resistance can cause a severe loss in well injectivity. For typical offshore fields on the Norwegian Continental Shelf (NCS), the spacing between wells tend to be large, and it is necessary to inject at high flow rates. As a result, it is crucial that a relatively high injectivity can be sustained throughout the lifetime of the field.

Furthermore, once the polymers enter the shear thickening flow regime they become susceptible to mechanical degradation (Maerker, 1975, 1976; Seright, 1983). Mechanical degradation happens when the polymer molecules experience excessive mechanical stresses in regions of high shear, causing some of the covalent bonds along the polymer chain backbone to break. Polymer mechanical degradation will counteract the decline in injectivity, but at the cost of losing much of the viscosifying power of the added chemicals. In the worst case scenario, the effective viscosity may be reduced down to, more or less, the solvent viscosity. Polymers can also degrade for a variety of other reasons, e.g., as a result of bacterial attacks, thermal hydrolysis at elevated temperatures, or due to rapid redox reactions initiated by certain chemicals, and often in the presence of dissolved oxygen (Ryles, 1988; Levitt et al., 2011; Thomas et al., 2012; Seright et al., 2014).

In a previous paper (Nødland et al., 2016), we introduced a model for the apparent viscosity behaviour of flexible polymer molecules in porous media that included ways to model both shear thinning and shear thickening fluid rheologies, as well as polymer mechanical degradation. The model was originally developed to match resistance factors calculated from laboratory core flooding data. For a given injection experiment where a polymer solution is injected through a core plug at constant flow rate, the resistance factor, or mobility reduction factor, is defined according to

$$RF = \frac{\Delta p_{pol}}{\Delta p_{wat}}, \quad (1)$$

where Δp_{pol} and Δp_{wat} are the steady-state pressure drops over the core for the polymer solution and brine without polymer, respectively (at the given flow rate). A typical example of the match that was obtained between model and experiment is shown in figure 1.

The purpose of this paper is to extend the simulation model to a radial system, in order to explore the issue of polymer mechanical degradation at the field scale. Specifically, we have performed a series of simulations of polymer injection from a single well in radial geometry. For most cases, we have assumed a homogeneous permeability field for the near well region. Then, towards the end of the paper, we show

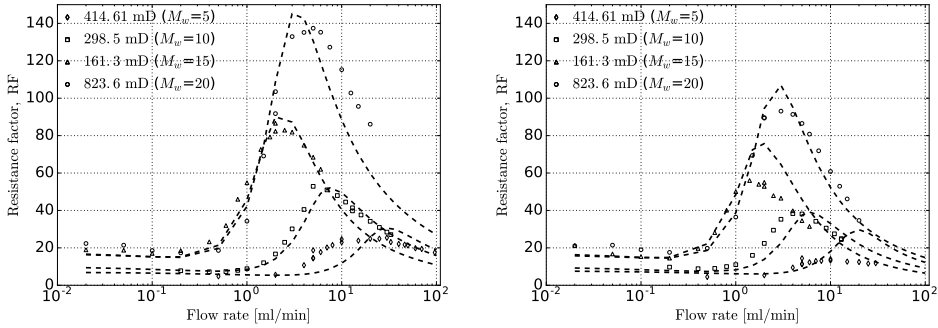


Figure 1 Resistance factors versus flow rate for four different polymer experiments. The RF factors were calculated for two successive (serial) cores, each of length ~ 7 cm. The scatter points are values obtained from the experimental data, whereas the dashed lines are calculated from simulated pressure drops. Note that for the experiments shown here, 4 different HPAM polymers were used, with reported molecular weights varying from $M_w = 5$ MDa to $M_w = 20$ MDa. There were also some variation in rock permeability among the experiments.

an example where we have assumed 2 layers of different RF permeability (no crossflow). Finally, we make some observations concerning the results, and discuss limitations and possibilities for future work.

Numerical model

The mathematical model used to simulate polymer flooding is fairly comprehensive, and we will only give a brief review of the main aspects here. The model includes a description of the effective aqueous phase viscosity, η , that can be both shear thinning and shear thickening, depending on the flow conditions. Each of these flow regimes is governed by the product of a characteristic time scale, and an in-situ, apparent shear rate in porous media. In the apparent viscosity model, the shear thinning viscosity is related to a time scale λ_1 , which is the characteristic relaxation time of the polymer solution. This relaxation time is computed as a function of the fluid properties, and the Carreau-Yasuda equation is used to compute the shear thinning viscosity (Bird et al., 1977). Similarly, the effects of shear thickening are related to a time scale λ_2 , which is a function of both the rock and the fluid properties. For all the details concerning the expressions used to model the apparent viscosity, we refer to our previous paper (Nødland et al., 2016).

The in-situ shear rate is computed as

$$\dot{\gamma} = \frac{4\alpha_c u}{\sqrt{8k\phi(1-IPV_0)}} \cdot \sqrt{R_k}, \quad (2)$$

where R_k is a permeability reduction factor, and IPV_0 represents the polymer inaccessible pore volume (IPV) due to the large molecular size of the polymer macromolecule in solution. Moreover, α_c is a tuning parameter used to correlate the in-situ rheology to bulk data, and u is the Darcy velocity of the water phase. Note that, unlike in (Nødland et al., 2016), we have not attempted to model permeability reduction effects in the present work, that is, we have simply set $R_k = 1$.

Polymer degradation model

In our model, the molecular weight distribution is not explicitly modeled, but instead we use a single, average molecular weight in each grid cell in order to capture how the viscosity changes as a result of

degradation. More specifically, we operate with two different polymer components in the simulator, one volumetric, c_p/ρ_p (e.g., g l^{-1}), and one molar, c_{mol} (e.g., mol l^{-1}). In consistent units, these two concentrations are related by

$$M_v = \frac{c_p}{c_{mol}},$$

where c_p is the mass concentration of polymer, and ρ_p is the polymer density. The polymer molecular weight is recalculated in each grid cell at the end of each transport step. We model the reduction in M_v as a result of mechanical degradation by means of the following differential equation (Nødland et al., 2016):

$$\frac{dM_v}{dt} = -f_{rup} \cdot M_v = -(r_{deg} \cdot \dot{\gamma} \cdot \eta)^{\alpha_d} \cdot \frac{2M_v^{\beta_d+1}}{R_p}, \quad (3)$$

where $f_{rup} = (r_{deg} \cdot \dot{\gamma} \cdot \eta)^{\alpha_d} \cdot 2M_v^{\beta_d}/R_p$ is thought of as the probability of chain fracture, and is related to shear stress, $\tau = \dot{\gamma} \cdot \eta$, effective pore radius for flowing polymer, R_p , and M_v . In equation (3), r_{deg} is a rate constant, η is the effective aqueous phase viscosity, and α_d and β_d are fitting exponents.

The pore radius is calculated from a Kozeny-Carman equation,

$$R_p = \sqrt{\frac{8kC}{\phi}} \cdot \frac{1}{\sqrt{R_k(1-IPV_0)}}, \quad (4)$$

where C is a tortuosity factor. At the end of each transport timestep, equation (3) is discretized implicitly and solved using an iterative algorithm.

Modifications to the numerical model

The full system of equations is solved by means of an operator splitting technique, implemented in an in-house 2-phase simulator at IRIS, IORCoreSim. With the implemented approach, the global pressure and saturation (for 2-phase flow) fields are computed first, for a 'global timestep' Δt . Next, the velocity fields are frozen, and a series of explicit transport steps are performed where at the end of each transport step, the polymer viscosity routine is called and, hence, M_v is updated. During the initial investigations applying the model to 2D and 3D cases, a numerical instability was uncovered, whereby in some cases several variables exhibited oscillatory behaviour. It seems likely that this is due to the strong coupling between the shear rate and some of the variables upon which it depends (e.g., molecular weight). However, these instabilities could be controlled by computing the in-situ shear rate as a weighted average of the values at the current and previous timesteps. Specifically, we have employed the formula

$$\dot{\gamma} = d \cdot \dot{\gamma}_{prev} + (1-d) \cdot \dot{\gamma}_{next}, \quad (5)$$

where d is a 'dampening factor', $0 \leq d < 1$. In equation (5), $\dot{\gamma}_{prev}$ is the shear rate from the previous (global/pressure) timestep, and $\dot{\gamma}_{next}$ is the initially calculated shear rate for the next timestep, using the updated polymer properties after transport and degradation. In this paper, we have set $d = 0.5$, i.e., we have used the arithmetic average of the two shear rates.

Simulation overview, and grid sensitivity

For all simulations discussed in this paper, we have used history matched polymer properties for one of the polymers that were investigated in Nødland et al. (2016). Specifically, we have used the polymer properties for the HPAM polymer with $M_w = 20\text{MDa}$, and with 30 % degree of hydrolysis (see table 2). The commercial name of this polymer is 3630S, and the manufacturer was SNF Floerger.

Radial simulation model - homogeneous case

All simulations have been performed using radial grids with a single, vertical injection well. The well boundary was located at $r = r_w = 0.1\text{ m}$, and the external grid boundary was at $r = r_e = 20\text{ m}$. A constant pressure boundary condition was enforced at the 'producer' (external boundary), with $p_e = p(r = r_e) = 200\text{ bar}$. The total formation thickness was $h = 20\text{ m}$, and the porosity was constant and equal to $\phi = 0.2$. The reservoir and injection fluid temperatures were the same, and equal to $T = 20^\circ\text{C}$. For a summary of the input parameters that were employed, see table 1.

Effects of grid resolution

First, we made some simple investigations of the sensitivity of the model to grid resolution. Since the degradation process occurs at very small spatial and temporal scales, we need a very fine discretization near the injector where the flow rates are highest. Then, as the flow rate rapidly declines with distance away from the injector, we can allow larger grid block sizes. This is illustrated in figure 2, where we plot the amount of degradation (percentage reduction in molecular weight from the initial value) of the polymer that was 'produced' at $r = r_e$, for 10 different simulated cases (left plot). In the right plot of the figure, we show the corresponding steady-state pressures at the injection well.

We emphasize that the only difference among the simulations shown in figure 2 is the choice of grid discretization, see table 3. We observe that for the coarsest grids, virtually no amount of degradation is predicted, whereas for the finest grid the percentage reduction in molecular weight is predicted to be $40 \pm 1\%$. This is a huge difference. We also see that the well pressure at the injector varies by slightly more than an order of magnitude for the most extreme cases, although the total pressure drop across the model varies by less. The main explanation for this behaviour is that as the grid size becomes larger, the shear rate becomes smeared out near the well ($\dot{\gamma} \propto 1/r$). For the largest grid sizes, the polymer is predicted to be in the low shear regime only, and we get minimal amounts of degradation. However, as the grid size decreases, we see that more and more polymer is degraded. Observe also from the right plot of figure 2 that there is a 'peak' in the corresponding plot of well pressures. This is because, as the grid size becomes smaller, the shear rate near the well becomes larger, while at the same time the molecular weight becomes smaller (more degradation). For a polymer in the shear thickening flow regime, these two changes work in opposite direction with respect to the apparent viscosity.

The upshot of figure 2 is that in order to simulate the degradation accurately on realistic field cases, some sort of upscaling and/or grid refinement is needed. Clearly, this is an issue that needs to be addressed in future work. However, herein we have simply chosen to use very fine grids, as the CPU times were not prohibitively long for the kind of issues we wanted to investigate. Based on figure 2, we chose to discretize the first 25 cm of the reservoir into grid blocks of constant size $\Delta r_0 = 5\text{ mm}$ (i.e., corresponding to case 3 in table 3). The length of the remaining set of radial grid blocks were then increased with a constant factor, except for the last block which had a constant size of 0.1 m. The total number of grid blocks was 100. We believe that the selected fine discretization near the injector should provide sufficient numerical accuracy for any of the conclusions drawn in this paper.

A note concerning the quantification of degradation

Before going on, we remark that in this work the amount of degradation is quantified by the percentage reduction in the molecular weight, i.e., we compute

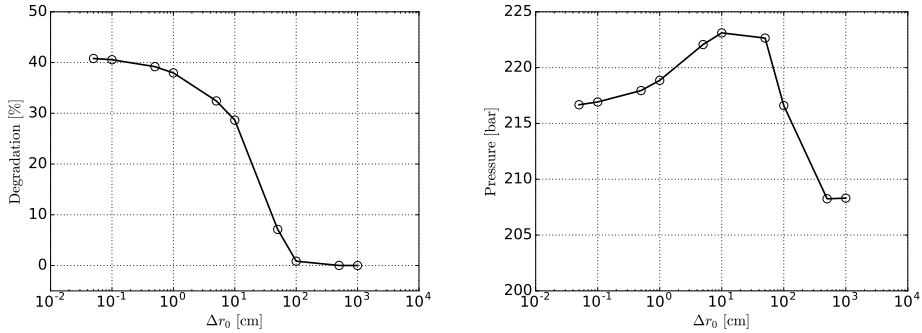


Figure 2 Effect of grid resolution. Left plot: Simulated reduction in the polymer molecular weight plotted versus radial size of the first grid block, Δr_0 . For the finely discretized grids, this cell size was used throughout the first 25 cm of the reservoir (table 3). For the cases shown here, the permeability was $k = 1$ D, and the applied flow rate was $Q = 250 \text{ m}^3 \text{ d}^{-1}$. The formation thickness was $h = 20$ m, and the porosity was $\phi = 0.2$. Right plot: Corresponding injection pressure.

$$P_{degr} = \left(1 - \frac{M_w^{degr}}{M_w^{orig}}\right) \cdot 100,$$

where M_w^{degr} and M_w^{orig} are the produced and original molecular weights, respectively. However, in the experimental petroleum literature it is common to quantify degradation as a percentage reduction in low shear viscosity. For example, in both Morel et al. (2015) and Al Hashmi et al. (2013), the authors calculate the amount of degradation according to

$$P_{degr} = \left(\frac{\eta_0^{orig} - \eta_0^{degr}}{\eta_0^{orig} - \eta_s}\right) \cdot 100 = \left(\frac{\eta_{sp0}^{orig} - \eta_{sp0}^{degr}}{\eta_{sp0}^{orig}}\right) \cdot 100,$$

where η_0^{orig} and η_0^{degr} are the low shear viscosities of, respectively, the original and the degraded polymer. As an example, in Morel et al. (2015), they used the bulk viscosities at $\dot{\gamma} = 17 \text{ s}^{-1}$. In the model, the low shear specific viscosity, η_{sp0} , is calculated from a cubic polynomial in the polymer intrinsic viscosity, $[\eta]$. Here, the intrinsic viscosity scales according to $[\eta] = K \cdot M_w^{0.6}$ (table 2), and so the expression for η_{sp0} contains terms $M_w^{0.6}$, $M_w^{1.2}$, and $M_w^{1.8}$. This should be kept in mind when considering the modelling results.

1-phase simulations in homogeneous permeability fields: $R_k = 1$

For the simulations shown in this section, we kept all input parameters to the model fixed, except the flow rate, Q , and the permeability, k . Both of these parameters were varied over several orders of magnitude, with several hundred combinations of the two parameters investigated. The selected flow rates were in the range $50 \leq Q \leq 2500 \text{ m}^3 \text{ d}^{-1}$, whereas the permeabilities were varied from 10 mD to 50 D. In figure 3 we show two different ways of visualizing the amount of polymer degradation that is predicted near the injector. In both plots, the values on the y-axis show the percentage reduction in the molecular weight of the polymer. Note that, in the left plot we have used the permeability on the x-axis, whereas in the right plot we have used Q/h , where h is the reservoir thickness. We should also remark that although many of the datapoints in the two subfigures overlap, each of the plots contains data that are not shown in the other.

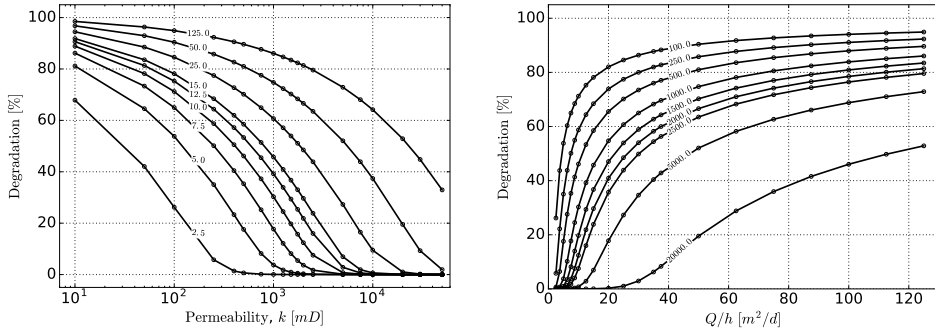


Figure 3 Left plot: Percentage reduction in the molecular weight for various, selected combinations of Q and k . Note that in this plot, each curve corresponds to a particular choice of Q , and the number shown on each curve is the value of Q/h [$\text{m}^3 \text{d}^{-1}$]. Right plot: Percentage reduction in the molecular weight of the polymer plotted versus Q/h on the x-axis. Each curve corresponds to a particular choice of the permeability, k [mD]. The values of the permeabilities are displayed above the individual curves.

Figure 3 shows that for the highest flow rates, a significant amount of degradation can be expected, even for high permeability reservoirs. For example, for $k = 1\text{D}$, both plots reveal that the molecular weight will be more than halved when $Q/h \geq 20 \text{m}^2 \text{d}^{-1}$ ($Q \geq 400 \text{m}^3 \text{d}^{-1}$). And, for $Q \geq 750 \text{m}^3 \text{d}^{-1}$ ($Q/h \geq 37.5 \text{m}^2 \text{d}^{-1}$), the M_w reduction is predicted to be $> 50\%$ for all $k \leq 2500 \text{mD}$. In general, for the cases shown here, the amount of degradation is a function of both Q and k , and the polymer is degraded progressively as it moves radially outward from the injector. However, in the absence of significant heterogeneities, we would expect the amount of degradation to be strongly related to the effective shear rate at the sandface, which scales according to Q/\sqrt{k} . Specifically, when using polymer model parameters $IPV_0 = 0.1$ and $\alpha_c = 2$, equation (2) yields

$$\dot{\gamma}_{sand} = \dot{\gamma}(r = r_w) = \frac{4\alpha_c Q}{2\pi r_w h \sqrt{8k\phi(1-IPV_0)}} = u_f \cdot \frac{Q}{\sqrt{k}}, \quad (6)$$

where $u_f \approx 195.5 \sqrt{\text{mD}} \text{d s}^{-1} \text{m}^{-3}$ is a unit conversion factor to ensure that $\dot{\gamma}$ has units of s^{-1} , and where k and Q are given in units of mD and $\text{m}^3 \text{d}^{-1}$, respectively. If we plot (all of) the degradation data versus $\dot{\gamma}_{sand}$, we get the result shown in left plot of figure 4.

The plot shows a clear trend, but admittedly there is a lot of scatter. Consequently, the simple scaling of Q/\sqrt{k} does not sufficiently describe the degradation for these homogeneous models. Instead, the extent of the degradation is more strongly related to the permeability than just the factor $1/\sqrt{k}$ from the shear rate. This is to be expected from our model, since the amount of degradation depends on the permeability in different ways. For instance, the degradation rate in the model is inversely proportional to the pore radius, see equation (3). And, the effective shear stress term in the equation depends on the depletion layer mechanism, the impact of which will vary depending on the permeability (see discussion further below). In fact, for the particular cases investigated here, plotting the data versus $S = \dot{\gamma}_{sand}/k^{0.1}$ (figure 4, right plot) removes much of the scatter. However, we should remark that this scaling is expected to be different if other parameters are varied besides just Q and k (e.g., if permeability reduction is modeled). Moreover, for injection of polymer into a region with vertical heterogeneities, the highest flow rates will be allocated to the highest permeability layers. Thus, in such cases, more degradation will actually be predicted at higher k . We will later show a simulation example where this happens.

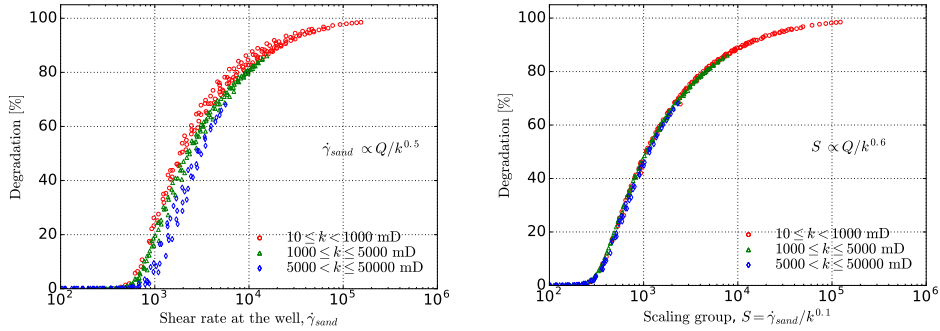


Figure 4 Left plot: Percentage reduction in molecular weight of the polymer that was back-produced at $r = r_e$, plotted versus the effective shear rate at $r = r_w$, $\dot{\gamma}_{sand}$. In the plot, we have split the data into 3 categories depending on the magnitude of the permeability. We see that $\dot{\gamma}_{sand}$ alone does not suffice to predict the degradation, but that for the lower permeabilities (lower effective pore radius), more degradation is predicted at the same $\dot{\gamma}_{sand} \propto 1/\sqrt{k}$. Right plot: The same data plotted versus $\dot{\gamma}_{sand}/k^{0.1}$, i.e., with the values on the x-axis scaled according to $Q/k^{0.6}$.

Examples of radial profiles

To further illustrate the simulation results, we have looked more in-depth at the cases where the permeability was $k = 1$ D, for different Q . In the plots shown here (figure 5 and 6), we have restricted ourselves to flow rates satisfying $Q \leq 400 \text{ m}^3 \text{ d}^{-1}$. However, data for all investigated flow rates are given in table 4. The resulting steady-state profiles for the molecular weight (strictly speaking, molar volume) versus radial distance are shown in the left plot of figure 5. In the right plot, we show how the in-situ shear rate varies with distance. Note that, for the cases investigated here, the shear rates close to the well vary slightly less than one order of magnitude, from $\dot{\gamma} \approx 300 \text{ s}^{-1}$ in the $Q = 50 \text{ m}^3 \text{ d}^{-1}$ case, to $\dot{\gamma} \approx 2400 \text{ s}^{-1}$ when $Q = 400 \text{ m}^3 \text{ d}^{-1}$. For the lowest flow rate, we see that virtually no polymer is degraded (0.06 %, table 4), whereas for $Q = 400 \text{ m}^3 \text{ d}^{-1}$, there is more than 50 % degradation.

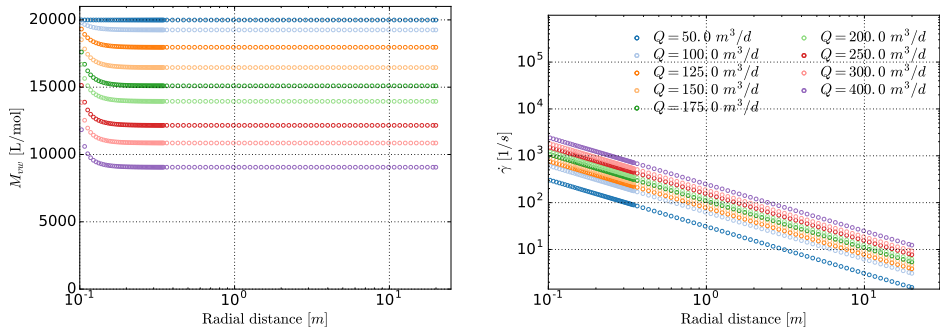


Figure 5 Left plot: Polymer molar volume in the water phase as a function of radial distance, for seven different cases where $k = 1$ D, at steady-state. The formation thickness was $h = 20$ m, and the porosity was $\phi = 0.2$. Note that $r = r_w = 0.1$ m corresponds to the sandface. Right plot: The in-situ shear rate profile.

In figure 6, we have included plots to show how the effective, aqueous phase viscosities (left plot) and water pressures (right plot) change with distance from the injector. Close to the well, we see that the viscosity can be large, on the order of 100 cp for most of the cases. However, the viscosity quickly

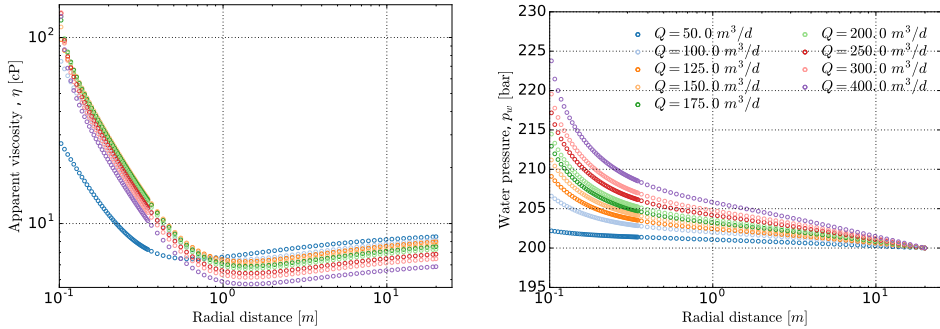


Figure 6 Left plot: Apparent viscosity as a function of radial distance, for seven different cases where $k = 1D$, at steady-state. The formation thickness was $h = 20m$, and the porosity was $\phi = 0.2$. Note that $r = r_w = 0.1m$ corresponds to the sandface. Right plot: Pressure in the water phase.

declines away from the injector, and it reaches values between 4 and 7 cp a metre from the well. Note that as the distance away from the well increases, the effective viscosity starts to increase again. This happens within the first metre of the reservoir in the $Q = 50m^3 d^{-1}$ case, and slightly further out from the well in the remaining cases. In the former case, we see that already at $r \approx 0.7m$ the shear rate is below $50s^{-1}$, which is in the shear thinning region. For the cases with higher flow rate, the polymer displays shear thickening behaviour further out from the well than in the lowest flow rate case. However, due to the rapid degradation that happens near the well, the critical shear rate for the onset of thickening is greatly increased as M_w is decreased (figure 7). For instance, in the case where $Q = 400m^3 d^{-1}$ (54.7 % degradation), the shear rate at $r \approx 1.6m$ is $\dot{\gamma} \approx 153s^{-1}$, which would be in the shear thickening region if the polymer had not been degraded. But, because of the degradation that has already occurred at this stage, the polymer is actually predicted to be shear thinning at this distance. This can clearly be seen from figure 7 (vertical, dashed line), where we have compared the model predicted in-situ rheology for some of the polymers that were produced, assuming $c_p = 1500ppm$.

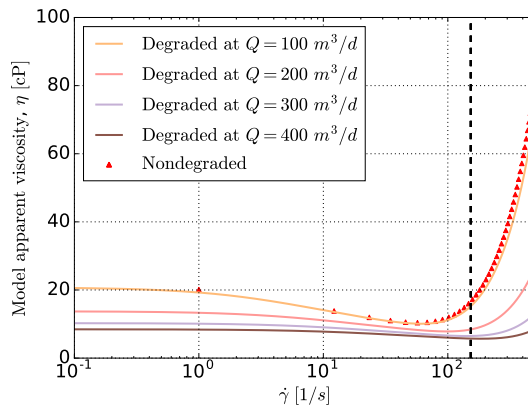


Figure 7 Model predicted apparent viscosity of a 1500 ppm polymer solution as a function of in-situ shear rate, for various values of the molecular weight, M_w . Specifically, we have plotted the model in-situ rheology for the produced polymer for four of the cases reported in table 4. Also shown for reference is the apparent viscosity of the original, nondegraded polymer (red triangles), and the vertical line shows the viscosities at $\dot{\gamma} = 153s^{-1}$ (see discussion in the main text).

Another consequence of figure 7 is that if the same polymer solution were to be reinjected into the reservoir after having been produced, it would experience much less additional degradation. This is in accordance with experimental data (Seright, 1983; Stavland et al., 2010; Zechner et al., 2013). Below, in figure 8, we show an example where we have explicitly simulated this. In the figure, we compare steady-state radial profiles of, respectively, polymer molar volume and pressure drop for two different cases, both using $k = 1 \text{ D}$ and $Q = 300 \text{ m}^3 \text{ d}^{-1}$:

1. The original case, where the nondegraded polymer with $M_w = 20 \text{ MDa}$ was injected
2. A second case, where a polymer with a lower initial M_w was injected. This initial value was chosen to be equal to the molecular weight of the polymer that was 'produced' at $r = r_e$ during the first simulation (approximately 46 % M_w reduction compared with the nondegraded polymer, see table 4)

As can be seen from the left plot of figure 8, during the second run through the system the polymer experienced some additional degradation. The further decrease in the molecular weight was approximately 8 %. And, compared with the original polymer, the polymer that was produced during this second run had a $\sim 50 \%$ reduction in the molecular weight, as opposed to $\sim 46 \%$ after the first injection period. From the right plot of the figure, we see that the pressure drop required to enforce the given flowrate is roughly 30 % higher for the case of the nondegraded polymer. On the other hand, the apparent viscosity far into the reservoir will not very different among the two cases, see figures 9 and 10. A practical implication of this is that, for a given reservoir, it may not always be the best option to select the polymer with the highest possible molecular weight. Instead, by employing a lower molecular weight polymer one may obtain a better injectivity while at the same time keep more or less the same EOR potential.

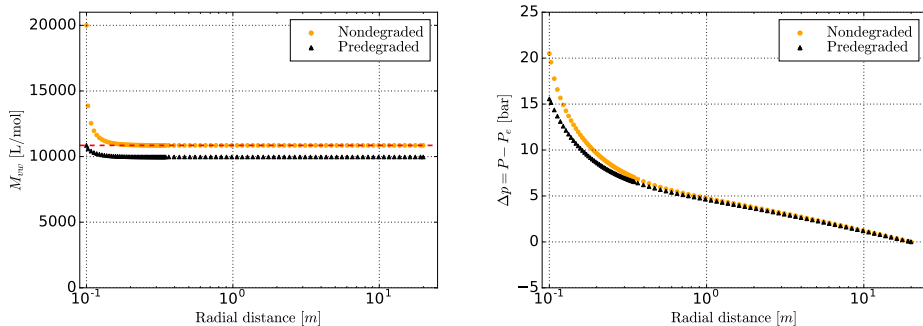


Figure 8 Left plot: Polymer molar volume versus radial distance, for two different injected polymer solutions: 1) the original, nondegraded solution, and 2) the predegraded solution that was produced at the reservoir boundary in the first case. The red, dashed line shows the molar volume of the degraded polymer solution (before reinjection). Right plot: Pressure drops between a given position and the exterior boundary for the two cases. Note that the values at $r = r_w = 0.1 \text{ m}$ correspond to the well pressures.

As a further illustration, in figure 10 we show how the predegraded polymer discussed above performs at all of the flow rates listed in table 4. In the left plot of the figure, we show the relative increase in the pressure drop across the whole model if one uses the nondegraded polymer as opposed to the predegraded one. In the right plot, we show the model predicted apparent viscosity at $r = r_e$ for the two choices of initial polymer. We see from the figure that if we inject the polymer at rates much higher than $Q = 300 \text{ m}^3 \text{ d}^{-1}$, there is not necessarily much difference in injectivity between the two polymer solutions although, at these rates, the viscosity loss will obviously be higher than for the rates close to $300 \text{ m}^3 \text{ d}^{-1}$. Again, the figure shows that for flow rates close to $300 \text{ m}^3 \text{ d}^{-1}$, the lower molecular weight

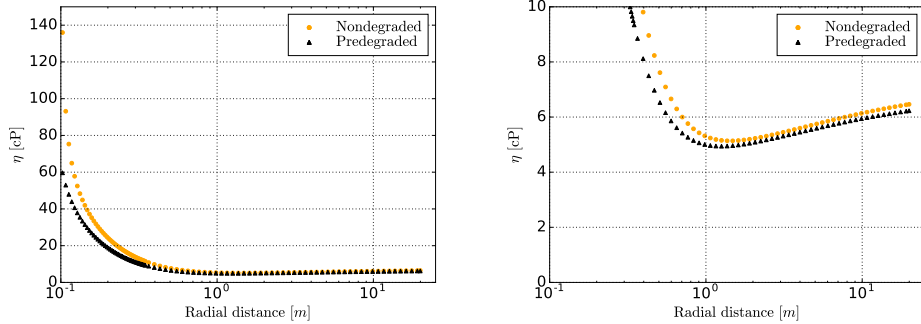


Figure 9 Left plot: Apparent viscosity versus radial distance, for two different injected polymer solutions: 1) the original, nondegraded solution, and 2) the predegraded solution that was produced at the reservoir boundary in the first case, with $\sim 46\%$ reduced molecular weight compared to the original polymer. Right plot: The same data as in the left plot, but zoomed in on the y-axis to see the difference in viscosity as $r \rightarrow r_e$. In this case the viscosities at $r = r_e$ were, respectively, 6.4 cp and 6.2 cp.

polymer has a better injectivity, but more or less the same viscosity as the higher molecular weight polymer at long distances from the well.

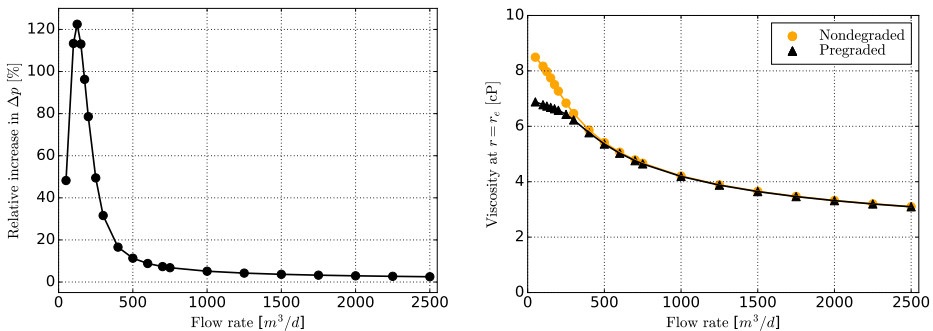


Figure 10 Left plot: The relative increase in $\Delta p = p(r) - p_e$, when using the nondegraded polymer as opposed to the polymer that was previously degraded at $Q = 300 \text{ m}^3 \text{ d}^{-1}$ ($\sim 46\%$ reduced molecular weight). Right plot: The corresponding model predicted apparent viscosities at $r = r_e = 20 \text{ m}$.

Further well injectivity discussion

In general, when it comes to polymer flooding, concerns are often raised about well injectivity (Seright et al., 2008; Seright, 2010; Glasbergen et al., 2015; Sheng et al., 2015). One potential problem is that the polymer may partly plug the reservoir, e.g., if there is debris present in the solution, or if the sizes of the macromolecules (i.e., the effective hydrodynamic radius of the polymer solution) are on the same order of magnitude as the typical pore size in the reservoir. The latter problem may arise when high molecular weight polymers are attempted injected into low permeability reservoirs. It is likely that this might be a problem for the polymer studied in this work ($M_w = 20 \text{ MDa}$) at the lowest permeability investigated ($k = 10 \text{ mD}$). However, we do not consider any plugging effects in the simulations, and we focus most of the discussion on cases where the permeability is large.

Assuming that the above mentioned problems can be avoided, the main issue to investigate is the expected increase in flow resistance near the well when a polymer solution is injected. This is especially

critical for the high molecular weight, viscoelastic polymer types, as they have the potential to induce larger resistance factors than polymer solutions that are primarily shear thinning (e.g., xanthan). Because of this, operators are naturally concerned with whether polymer can be injected at flow rates that are economically feasible. Despite frequent worries, many reports from fields that have been flooded with polymers suggest that well injectivities may be much higher than anticipated. The standard explanation for these observations is that many wells are likely to be fractured. It is known that even for many 'ordinary' waterflooding projects, fractures are likely to be opened during injection (van den Hoek et al., 2008), and when a viscous polymer solution is added to the mix, this opening of fractures is only going to be exacerbated (see, e.g., Seright et al. (2008) for a discussion). Indeed, for several recent field cases, the existence of fractures has been inferred (e.g., at the Daqing oilfield in China (Wang et al., 2008, 2009), at the Tambaredjo field in Suriname (Let et al., 2012; Manichand et al., 2013), and at the Matzen field northeast of Vienna (Gumpenberger et al., 2012; Zechner et al., 2015; Clemens et al., 2016; Lueftenegger et al., 2016)).

Based on the above considerations, it is clear that if fracturing the formation is accepted, and if the extent of the fractures can be controlled so as to not negatively impact the oil recovery, it will be beneficial for the polymer flooding process (Seright et al., 2008). When fractures are present, it is not unrealistic to imagine that the fluid velocity can decrease by as much as two orders of magnitude (Let et al., 2012). This will go a long way to alleviate the problems associated with strong shear thickening behaviour and polymer mechanical degradation in the near well area.

On the other hand, if the opening of fractures is not accepted, well injectivity is necessarily going to be reduced when a polymer solution is injected. However, we have seen that if sufficient amounts of degradation occur, the effective viscosity will rapidly drop as the solution travels through the first few centimetres of the formation. Consequently, the additional flow resistance imparted by the polymer solution will not be as high as one might fear, based on the apparent shear thickening fluid rheology alone. In order to illustrate this more clearly, we have performed some additional simulations where only certain parts of the polymer model were used. Specifically, for the $k = 1$ D model runs shown in table 4, we have run all the simulations again, but this time without the degradation model activated. First, we assumed that the polymer was showing a shear thinning behaviour only, i.e. shear thickening behaviour was also neglected. Next, we assumed that the polymer solution displayed both shear thinning and shear thickening fluid rheologies, but that it was non-degradeable. We then compared, for all simulated rates, the relationship between the steady-state pressures, and the flowrates. The resulting well pressures and pressure drops are shown in figure 11. Note that, in the right plot of this figure, we have computed resistance factors across the whole simulation model. That is, Δp is computed as the difference in the pressure at the well and at the external grid boundary.

For the full model, figure 11 shows that for most investigated cases, the pressure drop is expected to increase by a factor ~ 2 compared to the purely shear thinning polymer. And, for rates in the lower end of the degradation regime (e.g., $Q = 175 \text{ m}^3 \text{ d}^{-1}$, corresponding to a flux of 13.9 m d^{-1} at $r = r_w$), the difference can be even larger, in this case, close to a factor ~ 3 . However, compared to a naive extrapolation of pressure drops measured in the shear thickening regime in the lab, the difference between the two situations is not that large. For a Newtonian fluid with viscosity equal to the low shear viscosity of the polymer, the difference is even smaller.

Indeed, when using the shear thickening model without degradation, extremely high pressures were predicted. For example, at the highest employed flow rate of $Q = 2500 \text{ m}^3 \text{ d}^{-1}$, the well pressure was more than 13 000 bar, corresponding to a resistance factor of ~ 1000 across the simulation grid (figure 11, right plot). This is clearly a nonsensical result, but it illustrates well why it is necessary to include in some way the effects polymer degradation in the simulations. In the polymer modelling literature, previous workers who have implemented shear thickening behaviour, but not degradation, have typically set an upper limit for the apparent viscosity (see, e.g., (Delshad et al., 2008) and (Sharma et al., 2011)).

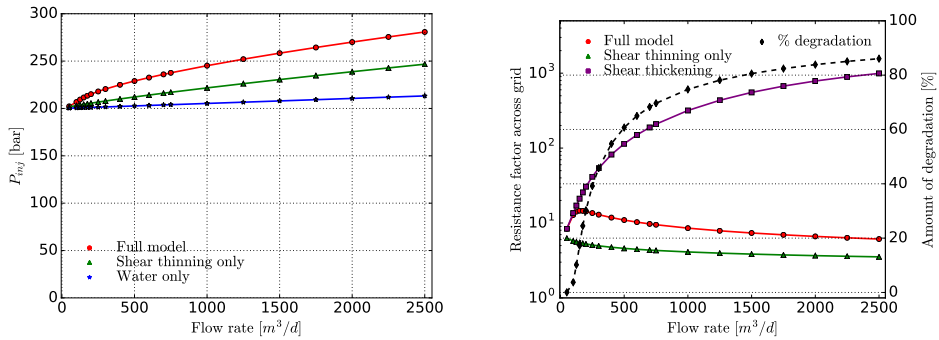


Figure 11 Left plot: Steady-state pressure at the injection well, for the various employed flowrates at $k = 1\text{D}$, and assuming two different polymer rheology models: 1) the full model (with degradation), and 2) a purely shear thinning model. Also shown is the calculated steady-state pressures for pure water injection at the same rates, $p_{\text{wat}} = p_e + \Delta p_{\text{wat}} = p_e + Q\eta_s \ln(r_e/r_w)/2\pi kh$. The formation thickness was $h = 20\text{m}$, and the porosity was $\phi = 0.2$. Right plot, left axis: Resistance factors across the whole simulation model, for three different assumed polymer rheology models. In addition to the two models investigated in the left plot, the purple squares are results obtained when the polymer was assumed to be shear thickening, but not degradable. Right plot, right axis: The percentage reduction in molecular weight of the polymer that was produced at $r = r_e$, for the case when the full model was run, i.e., including both shear thickening and mechanical degradation.

Simulations in layered reservoirs with no crossflow

As a final example, we have performed a simulation in a reservoir with 2 vertical layers of different permeabilities, $k_H = 1462\text{mD}$ ('high' permeability) and $k_L = 537\text{mD}$ ('low' permeability). In order to make the analysis more tractable, we have here only investigated the case with no crossflow. The average permeability is $\bar{k} = (k_1 h_1 + k_2 h_2)/(h_1 + h_2) \approx 1\text{D}$, and the ratio between them is $k_H/k_L = 2.72$. Below, in figures 12 and 13, we show the steady-state simulation results when polymer was injected at the rate $Q = 300\text{m}^3\text{d}^{-1}$. In figure 12, we plot the molecular weights (molar volumes) and shear rates as a function of radial distance in the two layers. Also shown is the corresponding profiles for the homogeneous case with $k = 1\text{D}$. From the figure we observe that the shear rate is higher in the 'high' permeable layer, and that as a consequence more polymer is degraded there. This is because most of the total flow rate is allocated to this layer. In the present example, the flow rates in the two layers were $Q_H = 215.1\text{m}^3\text{d}^{-1}$ and $Q_L = 84.9\text{m}^3\text{d}^{-1}$, respectively. In figure 13 we show the corresponding pressure and apparent viscosity profiles.

Initially, when using the history matched parameters given in table 2, the model apparent viscosity was actually predicted to be higher in the low permeability layer. This is opposite of what one would expect from considerations of the shear thinning rheology of the polymer, as both a higher M_w and a lower γ (figure 12) would lead to a higher viscosity at low shear rates. This behaviour (not shown here) was due to the depletion layer model used in the simulator. The depletion layer effect is caused by the steric exclusion of large polymer molecules from the walls of the pores. As a consequence, the polymer concentration near the walls of the pores is lower than in the middle of the pores, and this results in an apparent slip effect so that the effective viscosity becomes smaller than the corresponding bulk viscosity (the effective polymer concentration used in the viscosity calculations is lower). In the original model, c_p was assumed to be zero in the depleted layer, and the size δ of the depleted layer was set equal to the hydrodynamic radius of the polymer in solution, R_h .

However, as we mentioned in our previous paper Nødland et al. (2016), the experimental bulk viscosity data that were used to tune the model parameters were of rather low quality at the lowest shear rates.

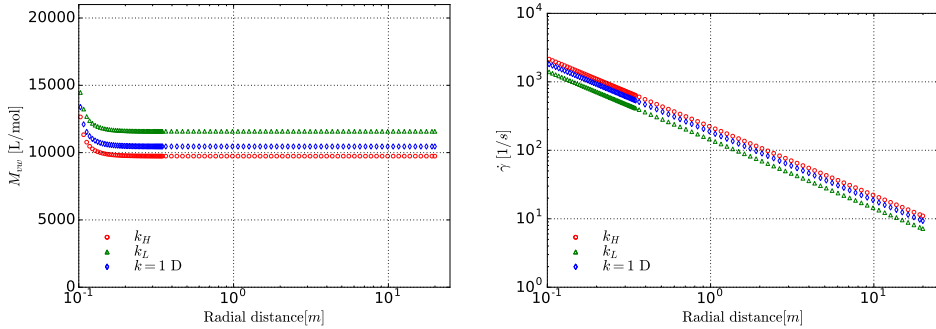


Figure 12 Left plot: Polymer molar volume versus radial distance when polymer was injected at a constant flow rate of $Q = 300 \text{ m}^3 \text{ d}^{-1}$ (at steady-state). In the figure, k_H shows the result in the 'high' permeable layer, and k_L represents the 'low' permeable layer. Both layers have thickness 10m, and there is no communication between them. Also shown is the corresponding profile for the case where the entire thickness of 20m had a permeability of 1 D. Right plot: The in-situ shear rate profiles for the 2 layers, as well as for the homogeneous case. Note that approximately 70 % of the total volumetric injection rate is allocated to the high permeable layer.

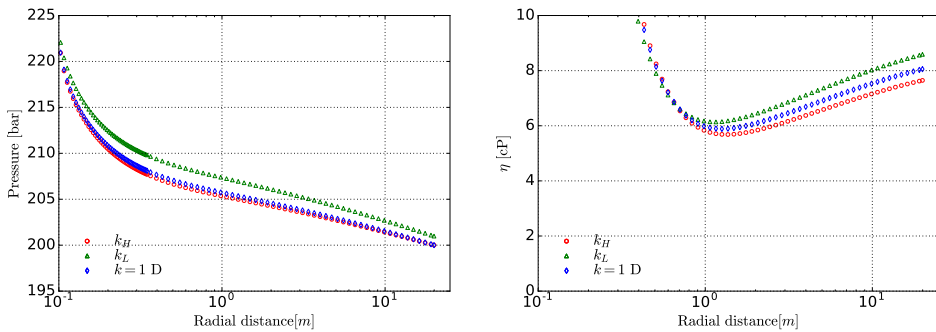


Figure 13 Left plot: Water pressure versus radial distance when polymer was injected at a constant flow rate of $Q = 300 \text{ m}^3 \text{ d}^{-1}$ (at steady-state). In the figure, k_H shows the result in the 'high' permeable layer, and k_L represents the 'low' permeable layer. Both layers have thickness 10m, and there is no communication between them. Also shown is the corresponding profile for the case where the entire thickness of 20m had a permeability of 1 D. Right plot: The corresponding apparent viscosity profiles (zoomed in to see the differences at the distances farthest away from the well).

In the original model, in the formulas for computing corrections in polymer concentration and apparent viscosity due to the presence of layers depleted in polymer, the viscosity ratio $M_v = \eta_p / \eta_{dw}$ between the polymer rich phase (η_p) and the depleted layer (η_{dw}) was used. During subsequent work we have discovered that this gives rise to an overestimation of the depletion layer effect at low permeabilities, and at high polymer concentrations. Therefore, for the heterogeneous case presented here, we introduced a small change to this part of the model, wherein each occurrence of the term M_v in the equations were replaced by $\sqrt{M_v}$. One could also correct the model so that the depleted layer thickness decreases with increasing polymer concentration. (Omari et al., 1989).

For the simulations with the corrected model, shown in figures 12 and 13, the apparent viscosity is highest in the low permeable layer, as expected.

Summary and conclusions

To sum up, we have applied our previously developed polymer flooding simulator to a series of synthetic cases in a radial geometry. The purpose of these simulations was to investigate how the model predicts the in-situ rheology of the polymer in the vicinity of an unfractured, vertical injection well. In particular, we have focused on the amount of mechanical degradation that can be expected near the injector. The model used in this paper has been history matched to lab data, and it is therefore expected that our predictions could be quite realistic.

We should point out some limitations of the current work:

- Permeability reduction due to polymer adsorption has not been taken into account. If this mechanism is significant near the well, additional degradation must be expected
- The brine that was used was the synthetic sea water (SSW) employed in our previous study, and also reported by Stavland et al. (2010). We have not considered how varying the ionic composition of the brine may alter the amount of polymer degradation
- We have only made some preliminary investigations into the effects of near well rock heterogeneity on the polymer behaviour. Moreover, we have only considered the steady-state behaviour of the polymer solutions, and we have ignored the effects of vertical crossflow
- The depletion layer mechanism has not been investigated in detail. However, the amount of degradation that is predicted is not expected to vary greatly depending on the exact model chosen to describe this phenomenon
- We have only performed 1-phase simulations, at isothermal conditions ($T = 20^\circ\text{C}$)
- All simulations conducted in this paper have been based on the history matched properties of a single polymer type: HPAM 3630S, with $M_w = 20\text{MDa}$ (SNF Floerger). However, similar analyses could be made with other polymers as well. The input parameters used in this paper were obtained from matching the model to standard core flooding experiments and bulk rheology measurements

Based on our simulation results, some main observations are:

- A very fine grid is needed in order to accurately simulate the degradation process. This makes it difficult to upscale lab results to realistic field cases
- In the absence of fractures, the amount of polymer mechanical degradation can become significant, even for high permeability reservoirs (e.g., table 4)
- However, the degradation can be greatly reduced by lowering the injection rate. For the polymer investigated here, the degradation is predicted to be relatively low as long as the shear rate close

to the well can be kept on the order of $\mathcal{O}(10^3) \text{ s}^{-1}$, or smaller (figure 4). For a homogeneous reservoir with permeability 1 D, this corresponds to an interstitial velocity at the sandface of at most $\sim 70 \text{ m d}^{-1}$, or a flux of at most $\sim 14 \text{ m d}^{-1}$ ($\sim 46 \text{ ft d}^{-1}$). This value will obviously vary depending on the type of polymer investigated, and on the degree of rock heterogeneity

- The value of resistance factors at the field scale cannot simply be extrapolated from corresponding shear thickening viscosities at the core scale. This is because of the radial geometry that was employed in the near well simulations, as opposed to the linear geometry used in the core floods. Also, if near well degradation is neglected, the predicted well pressures become unrealistically high
- It need not always be the best option to select the polymer with the highest possible M_w (for a given reservoir). Instead, if the polymer is expected to undergo some degradation anyway, a lower molecular weight polymer may provide similar viscosifying ability, but at the benefit of requiring a lower injection pressure

Future work

For future work, it will be interesting to look at situations where both water and oil are present, in order to study the effects of polymer degradation on oil recovery. The model should also be applied using constant pressure boundary conditions on the injector. However, in order to apply the model to realistic field cases, some sort of upscaling procedure or 'effective model' is needed. Otherwise, the simulation times needed to run the model accurately become impractical.

Acknowledgements

The authors acknowledge the Research Council of Norway and the industry partners; ConocoPhillips Skandinavia AS, Aker BP ASA, Eni Norge AS, Maersk Oil Norway AS, DONG Energy A/S, Denmark, Statoil Petroleum AS, ENGIE E&P NORGE AS, Lundin Norway AS, Halliburton AS, Schlumberger Norge AS, Wintershall Norge AS of The National IOR Centre of Norway for support.

Tables

Table 1 Rock and fluid properties used as input parameters for the simulations.

Parameter	Value	Unit	Description
R_{ext}	20.0	m	Exterior radius
h	20.0	m	Reservoir thickness
r_w	0.1	m	Well radius
d_{top}	2200	m	Depth below sea surface of reservoir top
p_{ref}	200	bar	Reference pressure
p_{init}	200	bar	Initial reservoir pressure
T_{ref}	20	°C	Reference temperature
T_{init}	20	°C	Initial reservoir temperature
T_{inj}	20	°C	Temperature of injected water
ϕ	0.2		Porosity
ρ_w	1.0	g ml ⁻¹	Water density at reference conditions
C_r	1.0×10^{-5}	bar ⁻¹	Rock compressibility @ 200 bar
C_w	4×10^{-5}	bar ⁻¹	Water compressibility
μ_w	1.07	cp	Water viscosity at reference conditions
B_w	1.0	m ³ m ⁻³	Water formation volume factor

Table 2 Polymer properties used as input to the simulations.

Parameter	Value	Unit	Description
$[\eta]_{ref}$	3750	ml g ⁻¹	Reference intrinsic viscosity
k'	0.01		First Huggins constant
k''	0.077		Second Huggins constant
M_w	20	MDa	Polymer molecular weight
a_{M_v}	0.6		Mark-Houwink exponent
T	20	°C	Reference temperature
C_p	1500	ppm	Injected polymer concentration
IPV_0	0.1		Inaccessible pore volume (constant part)
f_{dpl}	1.0		Multiplication factor for thickness of depletion layers
C	3.0		Tortuosity used to calculate effective pore radius for polymer
IPV_0	0.1		Inaccessible pore volume (constant part)
α_c	2.0		Parameter used to compute in-situ shear rate
λ_a	0.350	K mol ⁻¹ J ⁻¹	Parameter for determining λ_1 (shear thinning model)
λ_b	1.0		Parameter for determining λ_1 (shear thinning model)
a_n	0.063		Parameter for determining n (shear thinning model)
b_n	0.804		Parameter for determining n (shear thinning model)
x	1.0		Fitting parameter in the Carreau-Yasuda model
m_2	1.5		Slope parameter in the elongational viscosity model
x_2	3.0		Fitting parameter in the elongational viscosity model
r_{deg}	0.0015		Rate parameter for degradation model
α_d	3.0		Exponent used in degradation model
β_d	1.0		Exponent used in degradation model
C_{el}	4.0		Fitting parameter in the elongational viscosity model

Table 3 Information about grid discretization for 10 different investigated cases discussed in the main text. For each case, Δr_0 is the length of the first grid block in the radial direction. This block size was in most cases repeated N_0 times, with the total length of the N_0 grid blocks being equal to 25 cm. For the cases where $\Delta r_0 \geq 25$ cm, only 1 grid block had this size. However, in these cases the following blocks had a lower block size, since it was set as a requirement that the total number of blocks should be equal to $n_{rad} = 100$, if possible (this choice was quite arbitrary). For the cases with the finest discretization, the choice of using N_0 blocks with length Δr_0 naturally led to the use of more than 100 grid cells in the radial direction.

Case id.	n_{rad}	Δr_0 [m]	N_0
1	510	0.0005	500
2	260	0.001	250
3	100	0.005	50
4	100	0.01	25
5	100	0.05	5
6	100	0.1	2
7	100	0.5	1
8	100	1.0	1
9	100	5.0	1
10	100	10.0	1

Table 4 Results for the different simulations performed at $k = 1D$, and at different applied flow rates, Q . The formation thickness was $h = 20m$, and both Q and Q/h are displayed in each row of the table. Also shown is the percentage loss in molecular weight, P_{degr} , the steady-state pressure at the injection well, P_{inj} , as well as the shear rate at $r = r_w$, $\dot{\gamma}_{sand}$.

Q [$m^3 d^{-1}$]	Q/h [$m^2 d^{-1}$]	$\dot{\gamma}_{sand}$ [s^{-1}]	P_{degr} [%]	P_{inj} [bar]
50	2.5	309.0	0.06	202.2
100	5	618.1	3.74	206.8
125	6.25	772.6	10.19	209.4
150	7.5	927.1	17.25	211.6
175	8.75	1081.6	24.51	213.4
200	10	1236.2	30.26	215.1
250	12.5	1545.2	39.19	217.9
300	15	1854.2	45.74	220.5
400	20	2472.3	54.74	225.0
500	25	3090.4	60.70	229.0
600	30	3708.5	65.00	232.6
700	35	4326.5	68.28	236.0
750	37.5	4635.6	69.65	237.6
1000	50	6180.8	74.75	245.2
1250	62.5	7726.0	78.13	252.0
1500	75	9271.2	80.56	258.4
1750	87.5	10816.4	82.41	264.4
2000	100	12361.6	83.87	270.1
2250	112.5	13906.8	85.06	275.5
2500	125	15452.0	86.06	280.8

References

- Al Hashmi, A., Al Maamari, R., Al Shabibi, I., Mansoor, A., Zaitoun, A. and Al Sharji, H. [2013] Rheology and mechanical degradation of high-molecular-weight partially hydrolyzed polyacrylamide during flow through capillaries. *Journal of Petroleum Science and Engineering*, **105**, 100–106.
- Bird, R.B., Armstrong, R.C., Hassager, O. and Curtiss, C.F. [1977] *Dynamics of polymeric liquids*, 1. Wiley, New York.
- Chauveteau, G. and Moan, M. [1981] The onset of dilatant behaviour in non-inertial flow of dilute polymer solutions through channels with varying cross-sections. *Journal de Physique Lettres*, **42**(10), 201–204.
- Chauveteau, G., Moan, M. and Magueur, A. [1984] Thickening behaviour of dilute polymer solutions in non-inertial elongational flows. *Journal of non-newtonian fluid mechanics*, **16**(3), 315–327.
- Clemens, T., Lueftenegger, M., Laoroongroj, A., Kadnar, R., Puls, C. et al. [2016] The Use of Tracer Data To Determine Polymer-Flooding Effects in a Heterogeneous Reservoir, 8 Torton Horizon Reservoir, Matzen Field, Austria. *SPE Reservoir Evaluation & Engineering*.
- Delshad, M., Kim, D.H., Magbagbeola, O.A., Huh, C., Pope, G.A., Tarahhom, F. et al. [2008] Mechanistic interpretation and utilization of viscoelastic behavior of polymer solutions for improved polymer-flood efficiency. In: *SPE Symposium on Improved Oil Recovery*. Society of Petroleum Engineers.
- Glasbergen, G., Wever, D., Keijzer, E. and Farajzadeh, R. [2015] Injectivity loss in polymer floods: causes, preventions and mitigations. In: *SPE Kuwait Oil and Gas Show and Conference*. Society of Petroleum Engineers.
- Gumpenberger, T., Deckers, M., Kornberger, M. and Clemens, T. [2012] Experiments and simulation of the near-wellbore dynamics and displacement efficiencies of polymer injection, Matzen Field, Austria. In: *Abu Dhabi International Petroleum Conference and Exhibition*. Society of Petroleum Engineers.
- van den Hoek, P.J., Al-Masfry, R.A., Zwarts, D., Jansen, J.D., Hustedt, B. and van Schijndel, L. [2008] Waterflooding Under Dynamic Induced Fractures: Reservoir Management and Optimisation of Fractured Waterfloods. In: *SPE Symposium on Improved Oil Recovery*. Society of Petroleum Engineers.
- Kaminsky, R.D., Wattenbarger, R.C., Szafranski, R.C. and Coutee, A. [2007] Guidelines for polymer flooding evaluation and development. In: *International petroleum technology conference*. International Petroleum Technology Conference.
- Let, M.S., Priscilla, K., Manichand, R.N. and Seright, R.S. [2012] Polymer Flooding a ~ 500-cp Oil. In: *SPE Improved Oil Recovery Symposium*. Society of Petroleum Engineers.
- Levitt, D.B., Slaughter, W., Pope, G. and Jouenne, S. [2011] The effect of redox potential and metal solubility on oxidative polymer degradation. *SPE Reservoir Evaluation & Engineering*, **14**(03), 287–298.
- Lueftenegger, M., Kadnar, R., Puls, C., Clemens, T. et al. [2016] Operational Challenges and Monitoring of a Polymer Pilot, Matzen Field, Austria. *SPE Production & Operations*.
- Maerker, J. [1975] Shear degradation of partially hydrolyzed polyacrylamide solutions. *Society of Petroleum Engineers Journal*, **15**(04), 311–322.
- Maerker, J. [1976] Mechanical degradation of partially hydrolyzed polyacrylamide solutions in unconsolidated porous media. *Society of Petroleum Engineers Journal*, **16**(04), 172–174.
- Manichand, R.N., Let, M.S., Kathleen, P., Gil, L., Quillien, B. and Seright, R.S. [2013] Effective propagation of HPAM solutions through the Tambaredjo reservoir during a polymer flood. *SPE Production & Operations*, **28**(04), 358–368.
- Morel, D., Zaugg, E., Jouenne, S., Danquigny, J. and Cordelier, P. [2015] Dalia/Camelia Polymer Injection in Deep Offshore Field Angola Learnings and in Situ Polymer Sampling Results. In: *SPE Asia Pacific Enhanced Oil Recovery Conference*. Society of Petroleum Engineers.
- Nødland, O., Lohne, A., Stavland, A. and Hiorth, A. [2016] A Model for Non-Newtonian Flow in Porous Media at Different Flow Regimes. In: *ECMOR XV-15th European Conference on the Mathematics of Oil Recovery*.
- Omari, A., Moan, M. and Chauveteau, G. [1989] Wall effects in the flow of flexible polymer solutions through small pores. *Rheologica Acta*, **28**(6), 520–526.
- Ryles, R. [1988] Chemical stability limits of water-soluble polymers used in oil recovery processes. *SPE reservoir engineering*, **3**(01), 23–34.
- Seright, R. [2010] Potential for polymer flooding reservoirs with viscous oils. *SPE Reservoir Evaluation & Engineering*, **13**(04), 730–740.

- Seright, R., Skjevraak, I. et al. [2014] Effect of Dissolved Iron and Oxygen on Stability of HPAM Polymers. In: *SPE Improved Oil Recovery Symposium*. Society of Petroleum Engineers.
- Seright, R.S. [1983] The effects of mechanical degradation and viscoelastic behavior on injectivity of polyacrylamide solutions. *Society of Petroleum Engineers Journal*, **23**(03), 475–485.
- Seright, R.S., Seheult, J.M., Talashek, T. et al. [2008] Injectivity characteristics of EOR polymers. In: *SPE annual technical conference and exhibition*. Society of Petroleum Engineers.
- Sharma, A., Delshad, M., Huh, C., Pope, G.A. et al. [2011] A practical method to calculate polymer viscosity accurately in numerical reservoir simulators. In: *SPE Annual Technical Conference and Exhibition*. Society of Petroleum Engineers.
- Sheng, J.J., Leonhardt, B., Azri, N. et al. [2015] Status of polymer-flooding technology. *Journal of Canadian Petroleum Technology*, **54**(02), 116–126.
- Standnes, D.C. and Skjevraak, I. [2014] Literature review of implemented polymer field projects. *Journal of Petroleum Science and Engineering*, **122**, 761–775.
- Stavland, A., Jonsbrotten, H., Lohne, A., Moen, A. and Giske, N. [2010] Polymer Flooding–Flow Properties in Porous Media Versus Rheological Parameters. In: *Presented at the 72nd EAGE Conference and Exhibition incorporating SPE EUROPEC, SPE-131103-MS*.
- Thomas, A., Gaillard, N. and Favero, C. [2012] Some key features to consider when studying acrylamide-based polymers for chemical enhanced oil recovery. *Oil & Gas Science and Technology–Revue d'IFP Energies nouvelles*, **67**(6), 887–902.
- Wang, D., Dong, H., Lv, C., Fu, X. and Nie, J. [2009] Review of practical experience by polymer flooding at Daqing. *SPE Reservoir Evaluation & Engineering*, **12**(03), 470–476.
- Wang, D., Han, P., Shao, Z., Hou, W., Seright, R.S. et al. [2008] Sweep-improvement options for the Daqing oil field. *SPE Reservoir Evaluation & Engineering*, **11**(01), 18–26.
- Zechner, M., Buchgraber, M., Clemens, T., Gumpenberger, T., Castanier, L.M. and Kovscek, A.R. [2013] Flow of polyacrylamide polymers in the near-wellbore-region, rheological behavior within induced fractures and near-wellbore-area. In: *SPE Annual Technical Conference and Exhibition*. Society of Petroleum Engineers.
- Zechner, M., Clemens, T., Suri, A. and Sharma, M.M. [2015] Simulation of Polymer Injection Under Fracturing Conditions–An Injectivity Pilot in the Matzen Field, Austria. *SPE Reservoir Evaluation & Engineering*, **18**(02), 236–249.

Paper IV

A model for non-Newtonian flow in porous media at different flow regimes

By:

Lohne, Arild

Nødland, Oddbjørn

Stavland, Arne

Hiorth, Aksel

Printed in:

Computational Geosciences, 21:5-6: 1289-1312 (2017).

A model for non-Newtonian flow in porous media at different flow regimes

Arild Lohne^{1,2} · Oddbjørn Nødland^{1,2,3}  · Arne Stavland^{1,2} · Aksel Hiorth^{1,2,3}

Received: 30 September 2016 / Accepted: 8 August 2017 / Published online: 18 August 2017
© Springer International Publishing AG 2017

Abstract Polymeric liquids are of great practical importance for porous media flow as they can be used to improve the sweep of water in the reservoir and therefore improve the recovery of oil. Due to the non-Newtonian behavior of these liquids, they are extremely challenging to model. In this paper, we present a model that is capable of describing the most commonly observed flow regimes in porous media: (i) Newtonian, (ii) Shear thinning, (iii) Shear thickening, and (iv) Mechanical degradation. The novel feature of our model is that the time constants for the shear thinning and shear thickening behavior are related to variations in reservoir properties and conditions, thus making it possible to translate lab results to larger scale without introducing new fitting parameters. Furthermore, we present a way to estimate polymer mechanical degradation in porous media. In our model, the polymer degradation rate is linked to the effective pore radius (using a Kozeny-Carman type equation), shear stress, and polymer molecular weight, M_w . The degradation results in a lower M_w , while the polymer volumetric concentration is unaffected. The model is applied to a series of laboratory core flood experiments conducted with partially hydrolyzed polyacrylamide, HPAM, of different initial M_w ranging from 5 to 20 MDa in seawater, and core permeability varied from 137 to 2019 mD. The flow rate is varied approximately three orders of magnitude and

covers the shear thinning, shear thickening, and degradation flow regimes. We show that our model is able to reproduce experimental rate-dependent flow resistance, as well as viscosity of effluent samples. An important aspect supporting the use of the model as a predictive tool is that all the simulations with a given brine have made use of a single set of input parameters to describe the observed shear thickening and degradation behavior. Simulation of a second experimental series using low salinity brine required a separate set of input parameters for the shear thickening and shear degradation. The onset of shear thickening was not affected while shear thickening was reduced and degradation appeared to be slower.

Keywords Polymer flooding · Reservoir simulation · EOR · Shear thickening · Polymer degradation · Porous media

1 Introduction

Polymers added to the injection brine increase the aqueous phase viscosity and can decrease the water permeability. This can result in better sweep and hence, in faster production of oil [60]. However, many factors must be considered for a proper evaluation of a polymer flooding project. Aside from important practical issues, such as economic viability and environmental concerns, there are still many theoretical challenges related to predicting the behavior of polymeric liquids inside the reservoir. In particular, we need to improve our understanding of the different rheological flow regimes of the polymer, and how they depend upon local variations in the reservoir parameters, such as porosity, permeability, temperature, and brine salinity. This is crucial to obtain predictive accuracy for polymer flooding at the field scale.

✉ Oddbjørn Nødland
oddbjorn.m.nodland@uis.no

¹ The National IOR Centre of Norway, Stavanger, Norway

² International Research Institute of Stavanger (IRIS), Stavanger, Norway

³ University of Stavanger, Stavanger, Norway

The main difficulty in modelling polymer flooding lies in the fact that EOR polymers are non-Newtonian fluids. For Newtonian fluids, there is a linear relationship between the shear stress and the rate of strain, $\tau = \eta\dot{\gamma}$, where the slope is the viscosity of the fluid. For non-Newtonian fluids, the dynamical behavior is encoded in the stress tensor, which is determined from constitutive equations [2]. Given a set of such equations, a relationship between flow rate and pressure drop can be found. For porous media flow, this is very challenging as the pore geometry is non-uniform and the shear rate vary from point to point in space. Nevertheless, to describe polymeric flow in porous media it is common to define an apparent shear rate, which is proportional to the Darcy velocity, u , and inversely proportional to the square root of the porosity and permeability, $\dot{\gamma} \propto u/\sqrt{k\phi}$. The apparent viscosity is defined from Darcy's law, $\eta = -k\nabla p/u$. For very low apparent shear rates, the apparent viscosity may be approximately constant (Newtonian flow regime), but at increasing levels of shear it tends to become shear thinning. This is especially the case for biopolymers such as xanthan, which have been consistently observed to display shear thinning behavior in bulk solutions, as well as when flowing through porous rock samples. On the other hand, for synthetic polymers such as HPAM, additional effects are usually observed in porous media as the shear rate increases. For these polymers, experiments have repeatedly revealed dilatant effects at higher shear rates ("apparent shear thickening"), resulting in a dramatic increase in the macroscopic flow resistance [9, 11, 23, 34]. In coreflooding experiments performed at flow rates in this regime, the additional pressure drop can be several orders of magnitude larger than the corresponding pressure drop for a purely shear thinning polymer.

Another critical factor to consider is polymer mechanical degradation in porous media. It is well documented that when sufficient extensional forces are applied, covalent bonds along the polymer chain backbone may rupture [39, 51]. When this happens, the polymer is split up into smaller molecules, and depending on the number of chain scission events, it can lead to a dramatic, permanent decrease in the effective viscosity of the polymer solution. Obviously, the issue of mechanical degradation is especially critical in and around the injection/production facilities, where the molecules are exposed to high shear rates and, possibly, to turbulent flow [67]. Moreover, it has been recognized that the amount of degradation will be a function of the reservoir heterogeneity in the near well region (e.g., [61, 64]). Thus, if proper care is not taken as to minimize the degradation, the EOR potential on the field will be greatly compromised [55]. In one recent field case, polymer degradation was observed to give a 75% reduction in the low shear viscosity, whereas beforehand it had only been expected to be 25% [41].

In order to better quantify the uncertainties surrounding a polymer flooding project, it is therefore important to include all of the relevant physics into the simulation tools used to forecast the performance of the polymer flood. A challenge with models for polymers in a porous medium is that they tend to contain a large number of parameters that needs to be manually tuned for each particular application. However, in a field case there will, in addition to spatial variation in permeability and porosity, be (possibly large) gradients in temperature and salinity, stemming from differences between the injection and formation brines. Temperatures deep within the reservoir are typically much higher than the injected water, and the ion concentrations that are injected are usually lower than those already present in the formation. Variations in all of these parameters will alter the fluid rheology, and this needs to be captured in simulation models. Furthermore, in situations where the elastic contributions to the flow resistance become important, it is necessary to have a suitable model for polymer mechanical degradation, as this process will start to have an impact shortly after the onset of the shear thickening flow regime.

The purpose of this paper is two-fold: (i) to present a new, "unified" simulation model for polymer flooding and, in particular, (ii) to present a model for polymer mechanical degradation in porous media. The model covers all the experimentally observed flow regimes in porous media, and it is compared, successfully, with experimental results over a wide range of flow rates and permeabilities. With our approach, the time constants that define the transition between the various flow regimes are related to reservoir parameters, such as permeability, porosity, temperature etc. As a result, we are able to greatly reduce the amount of free parameters, thus allowing for an easier upscaling of lab results. We demonstrate that we can simulate the behavior of different polymers with mostly the same set of input parameters.

The rest of this article is organized as follows. First, we start by giving a short literature review on existing polymer models. Then, in Section 3, we give a thorough account of the mathematics used to describe the polymer rheology in our proposed model. In Section 3.2 we test the shear thinning part of the model by comparing it to bulk rheology data from Stavland et al. [64]. After this, we summarize the entire viscosity routine with focus on numerical implementation aspects. We apply the simulation model to experimental core flooding data, also from Stavland et al. [64], and we provide a discussion of the results. Finally, we apply the model to a dataset from Howe et al. [28], in which a brine of lower salinity was used compared with the other experiments. Other important elements of the model, such as the computation of in-situ shear rate, inaccessible pore volume effects on polymer transport and reduced apparent viscosity,

as well as a description of the currently implemented temperature and salinity models, are relegated to an [Appendix](#) at the back.

2 Overview of previous polymer simulation models

The commercial simulator that is often used as a reference with which to check other simulators, especially in the industry, is Schlumberger's ECLIPSE [20]. According to the official technical description, ECLIPSE 100 currently has more functionality than ECLIPSE 300 with regard to polymer flooding. In the former simulator, the following modelling options have been included:

- A Todd-Langstaff mixing model for handling dispersion at the front edge of a polymer slug, and viscous fingering at the rear edge
- Polymer (instantaneous) adsorption
- A model for permeability reduction, computed in terms of the adsorbed polymer concentration
- Inaccessible (dead) pore volume
- Various temperature effects
- Various salinity effects, e.g., influence of salinity on polymer adsorption
- Various models for handling non-Newtonian polymer rheology

In ECLIPSE 100, the water viscosity can be modified to account for shear thinning and/or shear thickening flow. This can be done by providing viscosity multiplier tables, where the multipliers are specified at a given set of flow rates or, alternatively, shear rates. In the latter situation, the effect of permeability can be more easily accounted for, since the shear rate satisfies $\dot{\gamma} \propto 1/\sqrt{k}$. In the former situation, a different table needs to be specified for each rock type if permeability effects are to be included. ECLIPSE 100 provides an option to model the polymer solution as a Herschel-Bulkley fluid, in which case yield stress effects can be incorporated. When it comes to polymer degradation, ECLIPSE 100 does provide a model for *thermal* degradation. This effect is modelled as a half-life reduction in the polymer concentration. No model for polymer mechanical degradation has been reported implemented in ECLIPSE.

Another well-known commercial reservoir simulator is CMG STARS [63]. In [24] Hatzignatiou et al. performed simulations using this simulator, in order to test its capabilities with regards to polymer flooding. In [24] no mechanistic models for the polymer viscosity were implemented, and the effects of the different flow regimes were captured by using correlations, in the form of tabular input data, for the effective polymer solution viscosity. The authors concluded that the non-Newtonian behavior of the polymer could be successfully simulated up to certain flow rates, but they

experienced numerical issues at the highest flow rates when shear thickening and degradation effects became significant.

The perhaps most well-known research reservoir simulator is the UTCHEM chemical flood simulator [56]. This simulator was originally launched in the late 1970s in order to simulate EOR processes involving surfactants and polymers. Since its inception, the simulator has included a variety of effects, e.g., effects of temperature, inaccessible pore volume, polymer rock adsorption and permeability reduction, as well as a description of how the ionic composition of the brine may alter the polymer intrinsic viscosity. For a long time, the rheology models that were used only incorporated Newtonian and shear thinning flow. However, during the last decade, a more comprehensive polymer model has been implemented in UTCHEM. In 2008, Delshad et al. [17] proposed a unified viscosity model (UVM), in which Newtonian, shear thinning, and shear thickening flow regimes were accounted for. In their work, Delshad et al. used the model to history match data from an earlier work by Masuda et al. [40]. Since then, the model has been extended by various workers from the same research group. For example, in [54] the authors report that more options have been added to the shear thinning and shear thickening rheology models, such as dependencies of the viscosity on polymer concentration. In addition, a model for polymer hydrolysis in porous media was added. According to Sharma et al. [54], the weight-average degree of hydrolysis, D_h , is represented by an additional component (i.e., a “surrogate tracer”) in UTCHEM. This component is advected through the grid in the same way as the other components, except that a rate equation has also been implemented in order to track how D_h changes with time, and a tentative relation between D_h and the polymer viscosity has been employed. For more details on the hydrolysis model, see [37]. On the other hand, no models for *mechanical* degradation of polymers have been reported implemented in UTCHEM.

In addition to commercial and proprietary research codes, there has recently been much focus on developing open source tools for reservoir simulation. An example of this is the Open Porous Media (OPM) Initiative [46]. In the long run, these frameworks may become very useful for modelling polymer flooding. However, at the present stage, they do not include functionality that is not also available elsewhere. For example, at the time of this writing, the polymer model implemented in OPM basically includes the same functionality as ECLIPSE 100. To the authors knowledge, none of the freely available source codes include models to handle polymer degradation processes.

In general, relatively few models for polymer degradation have been reported in the reservoir simulation literature. As an example, Sorbie and Roberts [59] presented a model for polymer mechanical degradation that was applied to data from Seright et al. [51]. In their simulations, the polymer

was represented by 20 components, a discrete representation of the molecular weight distribution. Kinetic rate equations were introduced to describe how larger molecular weight fractions were split into smaller ones, and random chain scission was assumed. The model assumed that degradation of a given molecular weight species would only occur above a given, critical value of the local fluid shear/elongational stress (correlated with Darcy velocity). However, the method requires detailed knowledge about the molecular weight distribution, and about the statistics of chain scission. In addition, the number of components needed to accurately model the polymer with such an approach will cause a large increase in the computer running time. Sorbie [60] notes that the model presented in [59] was not strictly predictive, but that it gives a good qualitative description of what can happen when polymer mechanical degradation occurs in porous media. A similar approach was recently taken by Brakstad and Rosenkilde [5], although they assumed the polymers to rupture by midpoint scission. In their model, polymer chain rupture starts at a critical value of the Deborah number, defined as the product of a polymer molecular relaxation time and a porous media effective stretch rate. By introducing an appropriate scaling for the relaxation time, their model predicts that large molecular weight species will degrade into smaller pieces, reducing their mole weight by 50%. The effective stretch rate was in their model calculated as $\dot{\epsilon} = K_f \cdot u/D_p$, where u is the Darcy velocity, D_p is a representative grain diameter (computed from the Blake-Kozeny equation), and K_f is a correction factor to account for different experimental conditions.

A different type of approach was taken by Lange and Huh [36], albeit in the context of modelling thermal degradation of biopolymers. Their model was based on a second-order kinetic rate equation for thermal degradation, assuming random chain scission. In their work, the polymer molecular weight distribution was represented by a single component, representing the weight-average molecular weight.

To sum up, many different effects are included in current polymer flooding simulators, but few simulators include all of the relevant effects. In particular, we would argue that the process of mechanical degradation has been given insufficient attention in the petroleum simulation literature. Additionally, there are a variety of other mechanisms that may be important to consider when interpreting laboratory data, but which are currently not available in most simulation codes, e.g., models for depletion layers of polymers, as well as more elaborate models for permeability reduction. Finally, even in cases where most of these effects are possible to represent using existing tools, the application of the models may require a lot of manual labour and fine-tuning. This is especially the case if different sets of input parameters and/or tables are needed for each rock type in a large

field simulation. As such, it is our hope that the model presented herein may lead the way towards better mechanistic models for polymer flooding, and that it can be used to capture the important average flow behavior of polymers in the reservoir.

3 Mathematical model description and preliminary discussion

As mentioned in the introduction, in reservoir simulation, it is common practice to represent the relevant non-Newtonian effects of EOR polymers by means of an apparent aqueous phase viscosity, η , which must in some way be calculated from the velocity obtained from Darcy's law [60]. Moreover, one typically does this by correlating this apparent viscosity to an apparent shear rate in porous media, $\dot{\gamma}$. Then, calculation of η based on the value of the flow rate in a simulation grid block requires the establishment of two mathematical relationships, one between η and $\dot{\gamma}$, and a second one between $\dot{\gamma}$ and the Darcy velocity. We will also adopt this approach. For convenience, we will use interchangeably the terms shear rate and viscosity to denote, respectively, the apparent shear rate and apparent viscosity. In our model, we propose to calculate this viscosity as follows:

$$\eta = \eta_s + (\eta_{sh} - \eta_s) \cdot \eta_{elf} \quad (1)$$

That is, we calculate the total viscosity as consisting of a viscous, shear thinning part, η_{sh} , multiplied with an elongational viscosity factor, η_{elf} . The expression for η_{elf} has been chosen so that, for low shear rates, $\eta \approx \eta_{sh}$, whilst at high shear rates dominated by elongational flow, $\eta \propto \eta_0 \dot{\gamma}^m$, where η_0 is the viscosity at zero shear rate, and m is an empirical parameter determined from experiments. Similar expressions have been used in other simulators reported in the literature, e.g., in [17] they calculate η as the sum of a shear thinning viscosity and an elongational viscosity.

The viscous and elongational contributions to the total viscosity will be further related to the local rock and fluid properties. This will be the topic of the following subsections.

3.1 Shear thinning model: derivation

The shear thinning behavior of EOR polymers can normally be well matched with a Carreau-Yasuda model [2, 71],

$$\frac{\eta_{sh} - \eta_s}{\eta_{sh0} - \eta_s} = (1 + (\lambda_1 \dot{\gamma})^x)^{-n/x}, \quad (2)$$

where η_{sh} is the shear thinning viscosity at a given shear rate, $\dot{\gamma}$, and η_{sh0} is the viscosity at zero shear rate (Newtonian regime). The parameter λ_1 is a relaxation time that

determines the onset of shear thinning, and x and $n > 0$ are dimensionless tuning parameters, with x determining the sharpness of the transition from the Newtonian to the shear thinning regime. In terms of the specific viscosity, $\eta_{sp} = \eta_{sh}/\eta_s - 1$, the Carreau-Yasuda equation can be rewritten as

$$\eta_{sp} = \eta_{sp0} \cdot (1 + (\lambda_1 \dot{\gamma})^x)^{-n/x}, \tag{3}$$

which, in the limit of high shear rates, becomes a power-law model in the specific viscosity with slope equal to $-n$. Equation 3 is an empirical model, and the parameters λ_1 and n obtained from matching it with laboratory data will in general be valid only for a specific polymer-solvent combination at a specific temperature, and at a given polymer concentration. Therefore, to reduce the amount of free parameters, it would be of great interest to be able to relate λ_1 and n to other, known parameters in the model.

The shear thinning index, n , in the Carreau-Yasuda expression has experimentally been found to depend on polymer concentration and the intrinsic viscosity [64]. We have suggested a correlation to capture this dependency,

$$n = 1 - \frac{1}{1 + (a_n[\eta]c_p)^{b_n}} = 1 - \frac{1}{1 + (a_n \cdot X)^{b_n}}, \tag{4}$$

where the symbol X is used to denote the product of polymer mass concentration, c_p , and polymer intrinsic viscosity, $[\eta]$. The correlation has been chosen so as to bind n between its physical limits, $n \in [0, 1)$. In Eq. 4, a_n and b_n are constant input parameters for a given polymer, typically obtained from fitting the Carreau-Yasuda model with at least two different polymer concentrations.

A lot of excellent experimental and theoretical work has been done in polymer science to visualize, and to interpret polymeric molecular motion in shear flow. Microscale behavior of DNA molecules has been studied using video fluorescence microscopy, tumbling configurations such as stretch, align, flip, and collapse have been observed [53, 58] and identified as important for the shear thinning flow regime [66]. During the tumbling motion, the polymeric particles spend on average a longer time oriented in the flow directions, and the resulting frictional losses cause shear thinning. In our description of the shear thinning behavior, all the detailed molecular configurations are averaged out, and we are only interested in the characteristic time that determines the transition from Newtonian to shear thinning flow. This characteristic time can be found by considering when the Brownian motion is overcome by the hydrodynamic forces, and in Eq. 2, it corresponds to when $\dot{\gamma} \cdot \lambda_1 \sim 1$. In the present work, we relate λ_1 to a characteristic time scale of rotational diffusion by

$$\lambda_1 = \frac{1}{2D_{rot}}, \tag{5}$$

which is the rotational relaxation time for a rigid object. Equation 5 is the same expression that was suggested by Chauveteau [8] for rigid rod polymers. The diffusion coefficient is computed from the Einstein relations known from statistical mechanics. For describing both rotational and translational diffusion of a Brownian particle immersed in a Newtonian fluid, we use the Einstein-Smoluchowski relation [18],

$$D = \frac{k_B T}{f}, \tag{6}$$

where D is the diffusion coefficient, $k_B T$ is the thermal energy, and f is an appropriate friction factor. Here, k_B is the Boltzmann constant, which has a numerical value of $k_B = 1.38 \cdot 10^{-23} \text{ J K}^{-1}$ in SI units. For a rotating rigid sphere of radius R immersed in a Newtonian liquid of viscosity η_s , the friction factor in Eq. 6 is $f = 8\pi\eta_s R^3$ [4, p. 95]. By approximating the flexible polymer in solution as a rigid sphere with a given hydrodynamic radius, R_h , we therefore compute the rotational diffusion coefficient according to

$$D_{rot} = \frac{k_B T}{8\pi\eta_s R_h^3}. \tag{7}$$

Inserting (7) into (5) yields

$$\lambda_1 = \frac{4\pi\eta_s R_h^3}{k_B T}. \tag{8}$$

Next, we need an expression for the hydrodynamic radius. Before we give the derivation, we list some basic equations and assumptions that are needed for the derivation.

The polymer viscosity is mainly controlled by the intrinsic viscosity, and polymer concentration. The intrinsic viscosity is defined by [26]

$$[\eta] = \lim_{c_p \rightarrow 0} \frac{\eta_{sh} - \eta_s}{c_p \eta_s}. \tag{9}$$

The relation between $[\eta]$ and the viscosity-averaged polymer molecular weight M_w is given by the Mark-Houwink equation [21]:

$$[\eta] = K \cdot M_w^a. \tag{10}$$

In Eq. 10, K and a are constants, which in general will depend upon the given polymer-solvent pair, and the solution temperature. For random chain polymers in good solvents, typical values of a lie in the range 0.5–0.8 [26].

We use a cubic polynomial to calculate the specific viscosity at zero shear rate, η_{sp0} , in terms of $[\eta]$ and c_p . Specifically, we use

$$\eta_{sp0} = X + k' X^2 + k'' X^3, \tag{11}$$

where k' and k'' are constants and where, as before, $X = [\eta] \cdot c_p$ denotes the product of polymer intrinsic viscosity, and polymer concentration. The intrinsic viscosity in Eq. 11 is a function of M_w , and the equation captures the main

effect of polymer concentration on the effective viscosity. The equation can further account for the viscosity altering effect of changing the ionic concentrations, by making $[\eta]$ salinity dependent (see Appendix A.4).

The hydrodynamic radius is now calculated by combining the following points:

- Calculate the dense spherical radius of the polymer, R_{sph} , as obtained from the polymer molecular weight and polymer density, ρ_p
- Relate R_h to R_{sph} by introducing a “swelling factor,” Φ_{sw} , defined as the ratio between the effective hydrodynamic volume occupied by the polymer and the dense spherical volume, i.e., $\Phi_{sw} = (R_h/R_{sph})^3$
- Obtain an expression for the swelling factor in terms of the polymer intrinsic viscosity

With regards to the latter point, we calculate the swelling factor from the Stokes-Einstein equation for the viscosity of a dilute suspension of solid spheres [49]:

$$\frac{\eta}{\eta_s} = \frac{1 + \Phi_h/2}{(1 - \Phi_h)^2} \approx (1 + 2.5\Phi_h). \tag{12}$$

In Eq. 12, Φ_h is the volume concentration of the spheres. In terms of Φ_{sw} as defined above and the mass concentration of polymer, we get:

$$\Phi_h = \Phi_{sw} \cdot \frac{c_p}{\rho_p}. \tag{13}$$

Then, by using Einstein’s first order approximation, Eq. 12, we get

$$\rho_p \cdot \frac{\eta - \eta_s}{\eta_s c_p} = 2.5 \cdot \Phi_{sw}, \tag{14}$$

from which we deduce, by taking the limit $c_p \rightarrow 0$:

$$\Phi_{sw} = \frac{[\eta] \cdot \rho_p}{2.5}. \tag{15}$$

The dense spherical radius is obtained from the expression

$$\rho_p = \frac{M_w/N_A}{4\pi R_{sph}^3/3}, \tag{16}$$

where N_A is Avogadro’s number. Thus

$$R_h^3 = \frac{3}{4\pi N_A \rho_p} \cdot \Phi_{sw} \cdot M_w, \tag{17}$$

and by combining Eqs. 15 and 17, we finally obtain

$$R_h = \left(\frac{3}{10\pi N_A}\right)^{1/3} \cdot ([\eta] \cdot M_w)^{1/3}. \tag{18}$$

We note that expression (18) is the same as the one given in, e.g., [27], when making the proper unit conversions. It is also commonly seen in various textbooks. Combining Eqs. 8 and 18, the rotational relaxation time can finally be calculated as

$$\lambda_1 = \frac{6}{5R_g} \cdot \frac{\eta_s [\eta] M_w}{T}, \tag{19}$$

where $R_g = k_B \cdot N_A$ is the ideal gas constant. Note that this time constant is equal to the one predicted by the FENE dumbbell model. In the FENE model the factor 6/5 is replaced by $(b + 5)/b$, thus in our model $b = 25$, which fits well with experimental observations where b is reported to be in the range [10, 100] (see e.g. Bird et al. [3, p. 81]). In Eq. 19, to account for the gradual increased relaxation time caused by interaction forces between polymer molecules at higher concentrations, we replace $[\eta]$ with the first order approximation:

$$[\eta] \approx \frac{\eta_{sp0}}{c_p}. \tag{20}$$

Thus, the final expression used in the simulation model becomes

$$\lambda_1 = \lambda_a \cdot \frac{\eta_s \eta_{sp0} M_w}{c_p T}, \tag{21}$$

where the prefactor λ_a , having a theoretical value of $\lambda_a = 0.144 \text{ K mol}^{-1} \text{ J}^{-1}$, is used as a tuning parameter to account for approximations in the derivation by assuming spherical shape, and by ignoring shear deformation of the polymer body. Also, uncertainty in the molecular weight and eventual effects of polydispersity will affect the value of λ_a . Equation 21 provides a scaling of the rotational relaxation time which can be used to generate different shear thinning viscosity curves as a function of the local polymer properties. This scaling group is the same as in the Rouse relaxation time for dilute solutions presented in [8]. The remaining input parameters required to calculate the shear thinning viscosity— k' , k'' , K , and a —may be varied among different polymers, but they should be known from bulk rheology measurements.

3.2 Shear thinning model versus bulk rheology data

The shear thinning model was matched with bulk rheology data for some of the HPAM polymers investigated in Stavland et al. [64]. The polymers are listed in Table 1 using a four-digit name indicating their molecular weight (two first digits) and hydrolysis degree (two last digits), e.g., 2030 indicates an average molecular weight of 20 MDa, with 30% degree of hydrolysis. The commercial names of the polymers have also been provided in the table. For most polymer types the data were recorded at 7 different concentrations in the range from 250 ppm to 5000 ppm, and at shear rates from 0.1 to 500 s^{-1} .

The model parameters were estimated, for one polymer at the time, by minimizing the sum of squared relative error between calculated and measured specific viscosity for all datapoints covering variation in concentration and shear rate. The minimization was first done with a minimum of constraints. The expression for the shear thinning index,

Table 1 Matched parameters for the shear thinning model, as well as calculated zero shear thinning exponents, shear viscosities, and polymer relaxation times for the bulk solution

Polymer	M_w	$[\eta]$	k'	k''	λ_a	a_n	b_n	x	n	η_0	λ_1	ϕ_1	λ_2
530 (3230S)	5	1467	0.01	0.12	0.722	0.063	0.804	1	0.170	4.86	0.031	0.21	0.00103
1030 (3430S)	10	2275	0.22	0.049	0.803	0.063	0.804	2	0.225	9.58	0.155	0.218	0.00335
1530 (3530S)	15	2424	0.247	0.091	0.306	0.078	0.56	1	0.331	13.18	0.126	0.177	0.00413
2030 (3630S)	20	3750	0.01	0.077	0.350	0.063	0.804	1	0.303	22.17	0.336	0.223	0.01138
Howe et al. [28]	3.6–31		0.247	0.178	0.450	0.078	0.505	1.1					

In addition, the critical time scale λ_2 has been calculated, at porosity $\phi = \phi_1$. All the simulated HPAM polymers from SNF Floerger had a reported hydrolysis degree of 30%, and the Mark-Houwink exponent was set to $a = 0.6$ for all four polymers. The injected polymer concentration was 1500 ppm in all of the core experiments from Stavland et al. [64]. Also included is the input parameters used to match bulk viscosity data from Howe et al. [28]. The dimensional quantities listed in the table have the following units: $[M_w] = \text{MDa}$, $[\eta] = \text{ml g}^{-1}$, $[\lambda_a] = \text{K mol}^{-1} \text{J}^{-1}$, $[\eta_0] = \text{mPas}$, $[\lambda_1] = [\lambda_2] = \text{s}$

Eq. 4, was fitted to the result in the left plot of Fig. 1. Then, the minimization was repeated with fixed shear thinning index parameters.

In the right plot of Fig. 1, we see the matched values of λ_1 versus the scaling group $X_c = \eta_s \eta_{sp0} M_w / c_p T$ on a log-log plot, see Eq. 21. The line in the figure indicates a constant λ_a parameter that matches the higher λ_1 -values. However, using λ_a individually matched for each polymer type (see Table 1) resulted in a slightly better match to the simulated coreflood experiments presented later.

3.3 Shear thickening model: background

In straight uniform conduits and steady-state flow, polymers tend to display a shear thinning behavior. In contrast, in a porous medium, the apparent viscosity at high shear rates has frequently been observed to increase with shear rate. Similar behavior has also been seen in capillary tubes with an abrupt contraction, as well as in channels with varying cross-sections [6, 8, 9]. For the case of capillary tubes, it has been argued that the increased flow resistance

is caused mainly by the sharp acceleration at the entry point of the tube, due to the abrupt change in the diameter at the capillary entrance [1, 8].

This effect, which is commonly referred to as (apparent) shear thickening in the petroleum literature, is related to the elastic nature of the polymers. The flow of polymeric liquids is coupled through tensor constitutive equations to the local flow field in the pore space, and time-dependent flow and non-uniform pore geometries give rise to a non-trivial relation between flow rates and pressure drops. It has been common to link shear thickening behavior to the notion of the coil-stretch transition [16], and to explain the increased flow resistance in terms of extensional viscosity, i.e., as an effect due to elongation and contraction of the polymer molecules in the flow field [9, 17]. However, uncovering the exact mechanisms responsible for the increased macroscopic flow resistance is an active area of research. With the development of microfluidic techniques it is now possible to observe directly the response of individual polymer molecules to extensional flow, as well as to visualize the flow field streamlines [25, 29, 50]. Using these techniques,

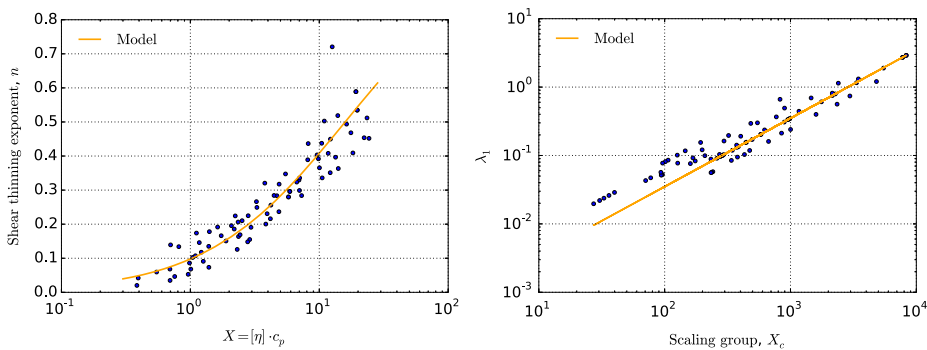


Fig. 1 Left: Shear thinning index n obtained for the dataset fitted with $a_n = 0.063$ and $b_n = 0.804$. Right: λ_1 from the second match, plotted versus the scaling group $X_c = \eta_s \eta_{sp0} M_w / c_p T$. The line represents the model with $\lambda_a = 0.350 \text{ K mol}^{-1} \text{J}^{-1}$

an alternative explanation in terms of time-dependent elastic instabilities has been proposed [28, 33, 38].

In any event, and as we stressed in Section 3.1 when discussing the shear thinning model, we are here mainly concerned with obtaining useful scaling groups that can be implemented to simulate polymer flooding in a standard reservoir simulator. We therefore wish to estimate a critical shear rate at which shear thickening flow is first observed. In our model we calculate this critical rate as the inverse of λ_2 , where λ_2 is a characteristic time scale that depends on both the rock and fluid properties. In the literature, the onset of apparent shear thickening behavior has often been correlated with the dimensionless Deborah number [17, 23, 40], N_{De} . It is defined as

$$N_{De} = \frac{\tau_{el}}{\tau_r}, \tag{22}$$

where τ_{el} is a characteristic time scale for the polymer, and where τ_r is a typical time scale of observation. Herein, we define τ_r as an average residence time of the polymer in the rock. For homogeneous, extensional flow fields the coil-stretch transition has been predicted to occur at a critical value of the Deborah number, $N_{De}^* = 0.5$ [47, 57]. However, in our model for porous media flow, we introduce N_{De}^* as a fitting parameter, to be obtained from a match between modelled and experimental values of λ_2 . The procedure that was used to obtain an expression for λ_2 can be outlined as follows:

- Compute the “elongational relaxation time” for the polymer, τ_{el} , which is the time it takes for the polymer to diffuse a length equal to its effective size in solution
- Compute an average pore residence time for the polymer in the rock, τ_r , using the Kozeny-Carman equation. This residence time is used as the time scale of observation in the calculation of N_{De}
- The onset of shear thickening is assumed to happen when the polymer relaxation time is of the same order of magnitude as the residence time, e.g., when $N_{De} = N_{De}^* \approx 1$ [8, 9]
- Use the previous considerations to derive a critical shear rate for the onset of shear thickening, $\dot{\gamma}_c$, and define $\lambda_2 = 1/\dot{\gamma}_c$

We may note that this use of N_{De} does not describe the actual onset of elongation at pore entrances, but rather the situation where the polymer molecule has insufficient relaxation time to recover from its distortion in the previous pore throat before entering the next. We assume that these events are close in time, and that the shear thickening effect of the initial elongation, if significant, can be accounted for by reducing N_{De}^* with a factor which is fairly independent of permeability.

Details on the derivation of the characteristic time, λ_2 , is provided in Section 3.4. Once it has been obtained, the elongational viscosity factor, η_{elf} , is calculated according to

$$\eta_{elf} = (1 + (\lambda_2 \dot{\gamma})^{x_2})^{\frac{m+n}{x_2}}, \tag{23}$$

where x_2 is a tuning parameter for the transition to the new flow regime, and m is an exponent fitting parameter. The motivation for the model can be seen from Fig. 2.

In this figure, we have plotted the logarithm of the apparent specific viscosity of a polymer solution versus the logarithm of the in-situ porous media shear rate, using data from one of the serial core experiments reported by Stavland et al. [64]. From the figure, the graph looks approximately linear for shear rates following the onset of shear thickening, and it can therefore be described by a power-law scaling. A combination of formulas (1), (2), and (23) yields

$$\eta_{sp} = \eta_{sp0} \cdot \frac{(1 + (\lambda_2 \dot{\gamma})^{x_2})^{(m+n)/x_2}}{(1 + (\lambda_1 \dot{\gamma})^x)^{n/x}}, \tag{24}$$

which for $\lambda_2 \dot{\gamma} \gg 1$ predicts that $\eta_{sp} \propto \dot{\gamma}^m$, i.e., that $\log \eta_{sp}$ is a linear function of $\log \dot{\gamma}$ with slope m . The plot in Fig. 2 was typical for all experiments investigated, and the estimated maximum slope m in the shear thickening region was for all cases determined as $m = 1.5 \pm 0.2$. (11 samples). The maximum slope of the declining part (purple line in Fig. 2) was 0.49 ± 0.09 . The intersection point between the two straight lines in Fig. 2 can be interpreted as the critical point for the onset of polymer degradation in the core experiments. Note that the results in the figure represent average properties integrated over the length of the core plug, and we expect the indicated critical point to depend on the core

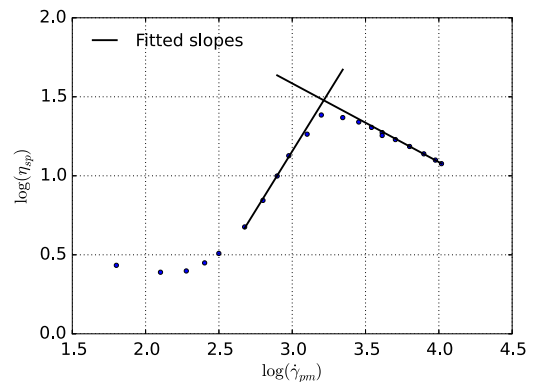


Fig. 2 In-situ rheology of the 1030 polymer in a 0.299 D Berea sandstone core. The slope of the increasing line, which represents the maximum slope in the shear thickening region, was found to be $m = 1.5$. Note that this plot represents averaged parameters, i.e., it is based on measured pressure drops across a full column of length $L \approx 7.0$ cm. The effective shear rate in porous media, $\dot{\gamma}_{pm}$, was calculated according to Eq. 50

length. However, since all investigated core plugs were of the same length (7 cm), some interesting observations can be made by comparing the critical points from all the core tests. The core tests cover variations in permeability from 137 to 2019 mD, and in polymer molecular weight from 5–20 MDa. The average shear rate at the critical point (9 samples, two outliers removed) was $1480 \pm 550 \text{ s}^{-1}$, while average shear stress, calculated as $\tau = \dot{\gamma} \cdot \eta$, was $54 \pm 5 \text{ Pa}$. These correlations with the critical point strongly indicate that shear stress rather than shear rate governs the mechanical degradation. The tests compared here are all from the first core in the dual core experimental setup. Results for the second core essentially overlap the results for the first core in the elongation region, while the declining part shows a parallel shift downwards.

3.4 Shear thickening model: derivation of λ_2

To compute the pore residence time in Eq. 22, we assume a pore length L_p equal to the characteristic grain size D_g of the medium obtained from a Kozeny-Carman equation. The Kozeny-Carman approach consists in converting from a capillary tube representation of the porous medium to a medium of spherical grains by preserving the medium surface area, S_A . The relation between the effective pore radius R_p and effective grain size is $S_A = 2\phi/R_p = 6(1 - \phi)/D_g$ [35]. Then, we can write

$$\frac{L_p}{R_p} = 3 \cdot \frac{1 - \phi}{\phi}, \tag{25}$$

where ϕ is the porosity. The residence time can therefore be computed as

$$\tau_r = \frac{L_p}{v_p} = 12 \cdot \frac{1 - \phi}{\phi \dot{\gamma}}, \tag{26}$$

where $\dot{\gamma} = 4v_p/R_p$ relates the shear rate at the wall to the average pore velocity v_p in the capillary tube representation.

The elongational relaxation time is calculated as a characteristic time scale of diffusion,

$$\tau_{el} = \frac{(2R_h)^2}{D_t} = \frac{4R_h^2}{D_t}, \tag{27}$$

where R_h is the hydrodynamic radius, and D_t is a translational diffusion coefficient determined from the well known Stokes-Einstein equation [8]:

$$D_t = \frac{k_B T}{f} = \frac{k_B T}{6\pi \eta_s R_h}. \tag{28}$$

Combining (18) with (27) and (28), we calculate

$$\tau_{el} = \frac{36}{5} \cdot \frac{\eta_s[\eta]M_w}{R_g T}. \tag{29}$$

We then calculate λ_2 according to $\lambda_2 = 1/\dot{\gamma}_c$, where $\dot{\gamma}_c$ is the shear rate at which $N_{De} = N_{De}^*$. By combining Eqs. 18, 22, 26, and 29, we end up with the following expression for λ_2 :

$$\lambda_2 = \frac{1}{N_{De}^*} \cdot \frac{3}{5R_g} \cdot \frac{\phi}{1 - \phi} \cdot \frac{\eta_s[\eta]M_w}{T}. \tag{30}$$

In the present case, we found that $N_{De}^* = 0.5$ provided a good fit of the model for all the experimental data. Note that the estimated N_{De}^* , representing an average value for the porous medium, will depend on the tuning parameter α_c used for calculating average in situ shear rate (see Table 2). As with λ_1 , the formula for λ_2 can be used to generate different viscosity curves for the shear thickening regime under varying reservoir conditions, and for different polymers. The situation at higher rates ($N_{De} \gg N_{De}^*$), when the polymer chains are already stretched before entering contractions, is represented by the empirical exponent m from experiments, see Eqs. 23 and 24.

3.5 Polymer degradation model: background

As the flow rate is increased further beyond the critical rate for onset of shear thickening, experiments indicate that the viscosity reaches a “maximum level,” after which there is a sharp decline in viscosity at yet higher rates, see Fig. 2. This is because of polymer mechanical degradation in porous media. At sufficiently high stresses, covalent bonds along the polymer chain backbone will break, causing a reduction in the effective molecular weight and apparent viscosity. It has been observed that this chain scission happens more rapidly for polymers with higher molecular weights. Indeed, multiple investigators have reported that for polymers in extensional flow fields, the onset of polymer mechanical degradation seems to occur at a critical strain rate (for a given system), $\dot{\epsilon}_f$, that scales as a power-law with the weight-average polymer molecular weight [6, 19, 34, 42, 44, 69]:

$$\dot{\epsilon}_f \propto M_w^{-\xi}. \tag{31}$$

This power-law scaling has been found for both turbulent and laminar flows, although the numerical value of the scaling exponent can vary depending on the flow geometry, as well on differences in solvent quality [68]. In the literature, there has been considerable debate as to how the obtained scaling exponents can be rationalized from more fundamental physics, i.e., in terms of polymer kinetic theory. One central issue concerns the precise mechanism of polymer chain cleavage. For example, one can ask whether the polymer chains rupture preferentially near the midpoint of the chains, or whether the process is more random?

Table 2 Model input parameters that were kept fixed in all cases

Parameter	Value	Explanation
IPV_0	0.1	Inaccessible pore volume (constant part)
f_{dpl}	1.0	Tuning parameter used in depletion layer model
f_{rkf}	1.0	Tuning parameter for size of adsorbed layer
$C = (L_t/L)^2$	3.0	Tortuosity factor
α_c	2.0	Tuning parameter used in the shear rate calculation
N_{De}^*	0.5	Tuning parameter for calculating λ_2 (critical Deborah number)
m	1.5	Slope parameter for the shear thickening model
x_2	3.0	Governs the sharpness of the transition to the shear thickening regime
r_{deg}	0.0015	Rate constant used in degradation model
α_d	3.0	Degradation dependency on shear stress
β_d	1.0	Degradation dependency on molecular weight
λ_3	$1/8 \cdot \lambda_2$	Determines the onset of reduced swelling of adsorbed polymer
n_3	1.0	Exponent used in the shear dependent permeability reduction model
x_3	4.0	Parameter used in the shear dependent permeability reduction model

Note that the value for the rate constant, r_{deg} , listed here is based on Eq. 33 with τ in units of Pa, R_p in μm , and M_w in MDa

In the polymer science literature, it has been common to distinguish between two types of extensional flow:

- Quasi steady state flow (QSSF), characterized by a flow field that is “purely” elongational in nature, e.g., flow near a stagnation point where the polymer residence time is very large
- Fast transient flow (FTF), characterized by a short residence time (e.g., capillary entrance flows)

A common explanation for the differences in calculated scaling exponents for $\dot{\epsilon}_f$ has been that the mechanism for chain scission is different in the two types of flow [14]. For QSSF flows, it is argued, the polymer molecules stretch to more or less full extension, before breaking near the middle where the tension is greatest [44]. On the other hand, for FTF flows the polymer residence time is too short to obtain full extension, and it has been assumed that the polymer breaks while in a partially stretched state. However, even for such flows midchain scission have been inferred [43], which has been difficult to reconcile with fundamental models for the polymer chain. In general, there seems to be little consensus on this topic, and alternative explanations have been proposed to account for the different chain scission exponents [31]. For example, Islam et al. [31] and Vanapalli et al. [69] have made the argument that the discrepancy may equally well be explained by differences in the Reynolds number at which the experiments were conducted. They claim that many experiments previously thought to having been performed under laminar conditions were, in fact, influenced by turbulence.

Of course, for flows in porous media, the situation is much more complex than in highly idealized experimental

setups investigated in the laboratory. In porous media, the polymer will travel through a complex network of pores, of varying pore sizes, and with rapid variations in the effective, cross-sectional area available to flow. This results in a mixed flow, where both elongational and shearing components contribute to the flow field. Even so, based on coreflooding data such as Fig. 2, it seems that the onset of degradation can be correlated with a critical shear rate in the porous medium. As we discussed in Section 3.3, this shear rate is a system-dependent parameter with a value can vary greatly from case to case. Based on our data, we calculated that the onset of degradation happened at relatively constant values of shear stress, defined as $\tau = \eta \cdot \dot{\gamma}$, where η and $\dot{\gamma}$ are the averaged apparent viscosity and shear rate, respectively, for the core samples investigated. In terms of the capillary tube representation of the porous medium, τ represents the shear stress at the wall of the capillary tube.

Based on these observations, we assume in our model that most of the degradation takes place close to the rock surface, where the shear force is large, and that it decreases away from the surface where τ is lower. While this assumption is dictated by macroscale observations in cores with different permeabilities, a simplified microscale picture could be that while polymer molecules at the flow centre line will be exposed to elongational forces alone, polymer molecules closer to the surface may be exposed to shear forces in addition to elongational forces. To incorporate these mechanisms in the model, the degradation rate is taken to be proportional to the rock specific surface area, which is $S_0 = \text{rock surface/pore volume} = 2/R_p$ for the capillary tube representation of the porous medium. The implication of this term is that at a given shear stress, and for rocks of

different permeability, the polymer will degrade faster in the low permeable rock with smaller effective pore radius, see Eq. 51.

3.6 Polymer degradation model: implementation

We model the mechanical shear degradation by introducing a parameter f_{rup} , which can be considered as the fraction of polymer molecules that rupture per time unit, or as the probability for chain rupture. At the end of a transport timestep in the simulation, the molecular weight is updated according to the differential equation

$$\frac{dM_w}{dt} = -M_w \cdot f_{rup} \tag{32}$$

We calculate f_{rup} according to

$$f_{rup} = (r_{deg} \cdot \tau)^{\alpha_d} \cdot \frac{2M_w^{\beta_d}}{R_p} \tag{33}$$

where r_{deg} is a rate constant. The rationale for using expression (33) can be summarized as follows:

- Intuitively, below a certain threshold of stress, little or no degradation should happen, whereas at and above a certain “critical” level the degradation process should accelerate. This is captured by the term involving τ and the exponent $\alpha_d > 1$
- The term $2/R_p$ is the specific surface area, as discussed above
- Longer polymer chains should have a larger probability of breaking [6, 14, 32]. This is captured by the $M_w^{\beta_d}$ term

To summarize, Eq. 33 predicts more degradation at higher shear stress, at lower permeability, and for larger molecular weight polymers.

A novel feature of the proposed approach is that the polymer is represented by two components in the simulator:

1. A volumetric polymer concentration, c_p/ρ_p (recall that c_p is the mass concentration), and
2. A molar polymer concentration, c_{mol} (e.g. mol l⁻¹).

That is, we do not attempt to explicitly model the molecular weight distribution, but rather use a single component, in addition to the mass concentration of polymer, to keep track of how the molecular weight changes inside the reservoir. It should be noted that the actual target for the model is to keep track of the viscous properties of the degraded polymer, and that the computed molecular weight is related to intrinsic viscosity using the same Mark Houwink exponent α , given as input, throughout the simulation (10).

Equations 32 and 33 establish a mathematical relation between the porous medium effective shear rate, and the molecule rupturing rate. The result is an increased molar

concentration and a corresponding reduction in molecular weight since the volumetric concentration is unchanged. In consistent units:

$$c_{mol} = \frac{c_p}{M_w} \tag{34}$$

Once a new value for M_w has been found, the intrinsic viscosity is updated from the Mark-Houwink Eq. 10. More details concerning the numerical solution of Eq. 32 are provided in Section 4.

3.7 Polymer adsorption and residual resistance factor

Here, we describe the polymer adsorption model used in the simulations. We only use this adsorption model to generate simulated permeability reduction factors, computed from adsorbed polymer, similar to measured values (RRF defined below). No measurements of adsorption were available from the experiments. Although polymer adsorption is reversible, or at least partly reversible, and may change if conditions are changed, processes like desorption or redistribution of already adsorbed polymer due to altered conditions are known to be very slow and may in many cases be neglected (see Zhang and Seright [72]). Therefore, we assume adsorption to be constant and irreversible throughout the experiments. Mathematically, we describe the adsorption by a Langmuir isotherm:

$$A_p = \frac{bc_p Q_m}{1 + bc_p} \tag{35}$$

In Eq. 35, A_p is the polymer concentration adsorbed on the rock and Q_m is the maximum adsorption capacity, both expressed as a fraction of the total pore volume. The parameter b determines how fast the adsorption occurs, i.e., at which polymer concentration the plateau, $A_p = Q_m$, is reached. Polymer adsorption can lead to permeability reduction, which is typically quantified in corefloods by introducing the residual resistance factor, RRF . The latter quantity is defined as

$$RRF = \frac{k_{wi}}{k_{wf}} \tag{36}$$

where k_{wi} is the initial permeability to water before polymer injection, and k_{wf} is the post-flush water permeability. We have tested two models for relating RRF to the adsorbed amount of polymer, which we introduce shortly here (see Appendix A.3 for more details). Let A_{pt} denote the effective volume fraction of the total pore space that is occupied with adsorbed polymer. We then compute RRF according to

$$RRF = \frac{1}{(1 - A_{pt})^2} \tag{37}$$

In model I, which is independent of shear rate, we compute A_{pt} as

$$A_{pt}^I = f_{rkf} \cdot \frac{A_p \Phi_{sw}}{(1 - IPV_0)}, \tag{38}$$

where Φ_{sw} is the swelling factor defined in Eq. 15 computed from the molecular weight of adsorbed polymer, which can differ significantly from M_w in solution. Equation 38 models the extension of adsorbed polymer molecules into the solution. The term IPV_0 is the fraction of the pore volume that is totally inaccessible to the polymer (see Appendix A.1), and f_{rkf} is included as a tuning parameter. The investigated dataset provides no information about adsorbed polymer, so in the simulations we used $f_{rkf} = 1$ and adjusted Q_m to approximate experimental RRF .

Model II should be regarded as a test of one possible method which can improve the match of experimental effluent viscosity (see the section on simulation results). In this model, A_{pt} is made a function of shear rate. We have tested the following expression:

$$A_{pt}^{II} = f_{rkf} \cdot \frac{A_p}{(1 - IPV_0)} \cdot ((\Phi_{sw} - 1)f_{sh} + 1). \tag{39}$$

For simplicity, we relate f_{sh} to a time constant in the same way as for the shear thinning and shear thickening viscosities:

$$f_{sh} = (1 + (\lambda_3 \dot{\gamma})^{x_3})^{-n_3/x_3}. \tag{40}$$

That is, at low flow rates we will have $f_{sh} \approx 1.0$, and polymer molecules adsorbed at the pore wall extend fully into the solution. On the other hand, as the flow rate increases, more and more of the polymer will be forced closer towards the surface, resulting in less pore blocking. In formula (40), x_3 and n_3 are constants, and we take λ_3 to be proportional to λ_2 . Moreover, we assume that the onset of this effect happens at a higher shear rate than the critical shear rate for the onset of shear thickening, i.e., that $\lambda_2 > \lambda_3$. For the simulations presented in this paper, we have used $\lambda_2/\lambda_3 = 8$.

4 Numerical solution of the polymer model

We have implemented the polymer viscosity model in an in-house simulator at IRIS, IORCoreSim. This simulator, which is written in C++, has the capability to simulate a variety of EOR processes for two-phase flow in porous media. The main flow field is obtained from a finite-difference discretization, using a sequential solution method to compute the phase pressures and saturations for the oil and water phases [62, 70]. First, the pressure fields are

calculated using a linear pressure equation, keeping the saturation dependent variables fixed at their values from the previous timestep. Next, the velocities of the water and oil phases that were computed during the first step are updated by solving an additional saturation equation for the water saturation. This saturation equation is formulated in terms of the fractional flow of water, and it is solved implicitly with respect to the saturation dependent variables, k_r (relative permeability) and p_c (capillary pressure), while keeping the total flowrate from the pressure solution fixed.

Once the flow field has been obtained for a global timestep, the transport of the individual species, in this case the brine and polymer components, is performed explicitly using operator splitting. First, the total concentration of polymer is updated in each grid cell. Next, polymer adsorption is computed, followed by an update of the solution viscosity and the RRF factor. The viscosity algorithm used for a grid block during a transport timestep, Δt , can be roughly summarized as follows:

1. Compute in situ shear rate using current flowrate and RRF from the previous timestep
2. Calculate an initial value for the viscosity-averaged polymer molecular weight, M_w^0 , based on the newly updated molar and volumetric concentrations, see Eq. 34
3. Compute the intrinsic viscosity in terms of the updated M_w and the effective salinity of the brine (see Appendix A.4)
4. Find the polymer concentration to be used in the viscosity calculations (correct for inaccessible pore volume, including depletion layer, see Appendix A.1), and calculate polymer apparent viscosity as a function of polymer concentration, shear rate, and depletion layer
5. Add the effect of elongation
6. The degradation is solved implicit in time with respect to M_w , by employing an iterative algorithm where in each iteration the full viscosity model is calculated. The initial value for M_w estimated in step 2 is used as a starting point
7. If adsorption is included, calculate RRF

The crucial step that necessitates an iteration loop is the solution of Eq. 32. This is because most of the parameters in the model are functions of M_w . We discretize (32) as

$$M_w = \frac{M_w^0}{1 + \Delta t \cdot f_{rup}(M_w)}, \tag{41}$$

where M_w^0 is the molecular weight before degradation is included, and M_w represents the unknown value when degradation over the last time step is included. We solve (41) using a modified false position (“regula falsi”) chord method, also known as an “Illinois-type” method [22].

5 Simulation results from experiments in synthetic sea water (SSW)

5.1 Experimental background and simulation procedure

We applied the model to some of the experiments reported by Stavland et al. [64]. The selected experiments cover variations in molecular weight from 5 to 20 MDa, and in permeability from 137 and 2019 mD. The hydrolysis degree was the same, 30%, for all the polymers. The experiments were designed to investigate the apparent shear thickening and degradation flow regimes. Model parameters for the Newtonian and shear thinning regimes were matched to bulk viscosity measurements for each polymer, see Table 1. The adsorption capacities were adjusted to obtain *RRF* factors close to the experimental values, but the values listed (Table 5) are consistent with what would be expected from variation in permeability. The rest of the model parameters describing elongation and degradation were kept fixed among all cases (Table 2). For all simulations, we compared predicted resistance factors, *RF*, to the ones obtained from the experimental data. The resistance factor, or mobility reduction factor, is defined by

$$RF = \frac{\lambda_w}{\lambda_p} = \frac{\Delta p}{\Delta p_w} \tag{42}$$

That is, *RF* is the ratio of the water mobility prior to polymer injection, $\lambda_w = k_{wi} / \eta_s$, to the polymer mobility at the same rate, $\lambda_p = k_p / \eta$. If the residual resistance factor, Eq. 36, can be considered a constant for a given medium, we obtain the following relation between *RRF* and *RF*:

$$RF = \frac{\eta}{\eta_s} \cdot RRF = \eta_{rel} \cdot RRF \tag{43}$$

All the investigated polymers were mixed with synthetic sea water (SSW), with ionic concentrations reported in Table 3. As a result, we could represent the brine by a single component, using a constant viscosity of $\eta_s = 1.07$ mPa s at room temperature, $T = 20$ °C. The polymer-brine solutions were injected into different serial mounted sandstone cores, with properties given in Table 4. All of the cores were

cylindrical, with a length of approximately 7 cm, a diameter of 3.8 cm, and a porosity close to 20%. The solutions were flooded at a variety of rates, and steady state differential pressures were recorded over both cores, which we will denote by Core 1 and Core 2, respectively. The polymer solutions were injected at a polymer concentration of 1500 ppm.

We simulate the experiments starting with the experimental initial rate because, in some of the experiments, the initial rate seemed to be in the lower end of the degradation regime, which affects the molecular weight of adsorbed polymer, and consequently *RRF*. After that, the injection rate was stepwise increased from low to high value, and finally a post-polymer water injection was simulated. Simulated values of in particular *RF*, but also shear rate and *RRF*, showed decreasing trends from the inlet to the outlet end of the core. Therefore, to compare simulation with experiment, these properties are computed in the same way as for the experiments, using the total pressure drop across the core and the flowrate. *RRF* is first calculated based on the simulation of a post-polymer water injection. Then, for each flowrate, *RF* and η are obtained using the Eqs. 42 and 43, while the shear rate is computed from Eq. 50.

In addition to estimating *RF* and *RRF* factors, polymer samples were collected at the effluent, at different injection rates. These samples were subsequently analyzed in a rheometer at a low shear rate, to characterize the extent of degradation.

5.2 Models for permeability reduction

Initially, we matched the experimental *RF* profiles by tuning the degradation model and assuming constant *RRF*, model I (38). Although good reproduction of *RF* values were obtained at all flow rates, computed viscosities using simulated effluent molecular weights were substantially lower than the experimental values, as can be seen from Fig. 3. Since *RF* is a product of viscosity and *RRF*, Eq. 43, the intuitive idea is that if viscosity is higher, *RRF* must be reduced to obtain the same *RF* value. This was the motivation for introducing model II with rate dependent *RRF*, Eq. 39. The difference between the two models is illustrated in Fig. 3, where we have compared the experimentally determined effluent viscosities with values predicted from the simulator for the 1530 polymer.

The shear rate dependent model (model II) is able to reproduce both effluent polymer properties (Fig. 3) and *RF* satisfactory (shown later). We conclude that rate-dependent *RRF* is a good candidate for explaining what goes on inside the core. However, we note that the theory of decreased permeability reduction at higher flow rates seems to contradict experimental data reported in the literature [13, 30]. For example, several authors have reported an increase in

Table 3 Make-up of the synthetic seawater, SSW

Salt	Concentration [g l ⁻¹]
NaCl	23.495
KCl	0.746
MgCl ₂ · 6H ₂ O	9.149
CaCl ₂ · 2H ₂ O	1.911
Na ₂ SO ₄	3.408
NaHCO ₃	0.168

Table 4 Properties for the various dual core systems

System id	Rock type	L_1	L_2	k_1	k_2	ϕ_1	ϕ_2
1	Berea	7.2	7.1	414.61	305.63	0.21	0.22
2	Berea	7.1	7.1	298.5	291	0.218	0.216
3	Berea	7	7	721.7	612.8	0.223	0.213
4	Berea	7.2	7.2	161.3	136.9	0.177	0.176
5	Berea	7.0	7.0	823.6	800.4	0.223	0.213
6	Bentheim	7.1	7.1	2018.8	1998.1	0.235	0.235
Howe et al. [28]	Bentheim	5		3100		0.23	

The diameter was in all cases $d = 3.8$ cm, while the lengths, permeabilities and porosities are denoted by L_i [cm], k_i [mD], and ϕ_i , for cores with indices $i = 1, 2$. Also included is core data from experiments reported by Howe et al. [28]

the permeability reduction at higher flow rates, which they explain as a consequence of more polymer molecules being adsorbed on the surface at the higher flow rates due to an increase in the hydrodynamic forces.

Another possible explanation for the effluent viscosity discrepancy, which remains to be tested, is the choice of the Mark-Houwink exponent, a , from Eq. 10. By decreasing a , the polymer will lose less of its viscosity when degraded. The polymer will be degraded more (to a lower M_w), but may still result in an increased effluent viscosity. Furthermore, an important question to ask is how polymer degradation will alter the molecular weight distribution of the polymer. If the shape of the distribution is heavily altered, it is possible that the relation between $[\eta]$ and M_w which was originally used may no longer be valid after degradation. Another issue is that the rationale for the polymer degradation model, Eqs. 32 and 33, were implicitly

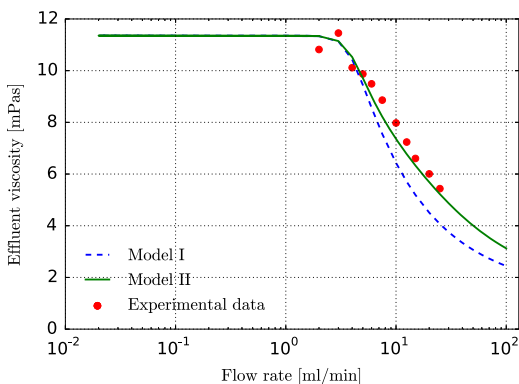


Fig. 3 Effluent viscosities for the 1530 polymer, measured from bulk samples collected at the effluent. The data are taken for the case where Core 1 and Core 2 had permeabilities of 721.7 mD and 612.8 mD, respectively. The red dots are experimental datapoints, whilst the solid line was obtained from the match with the model for shear dependent permeability, model II. The dashed lines represent the shear independent model, model I

based on a conception of M_w as the number average molecular weight, M_n , in that we considered the fraction of polymer molecules expected to rupture. However, the mass and viscosity averages will be quite different from M_n for a polydisperse sample.

It should also be remarked that there are several experimental uncertainties that can make a proper estimation of the residual resistance factor difficult, such as excess pressure drops being measured during the post-polymer phase [52]. Another issue, which may potentially be misleading, is that the RRF factor may not be a constant at all, but may rather depend on the applied flow rate. This is what we have explored with our model II. However, we remark that a predictive simulator needs to take the permeability reduction effect into account, as it would otherwise be impossible to match the observed pressure drops. The same applies to several of the other mechanisms included in the simulator. What is important for us here, in order to properly compare theory with experiment, is that the RRF factors obtained from the final water injections are reasonably close to the experimentally recorded values. A comparison between experimental and simulated RRF factors is given in Table 5.

5.3 Differences between adsorbed and bulk polymer

As remarked previously, the molecular weight of the adsorbed polymer can in the model be very different from the molecular weight of the flowing polymer. Since polymer adsorption is modelled as irreversible, it is the polymer from the first period of injection that sticks to the wall. This means that the RRF factor in our model becomes a function of the initial flow rate. The difference in molecular weight between polymer in the bulk fluid and adsorbed polymer is illustrated in Fig. 4. In the figure, we plot steady-state M_w values versus distance along the core for one of the experiments.

Figure 4 reveals that the polymer in bulk solution is quickly degraded near the inlet of the first core plug,

Table 5 Langmuir adsorption parameters used in the simulations

System id	Rock type	Q_m^1	Q_m^2	Polymer	RRF_1 model	RRF_2 model	RRF_1	RRF_2
1	Berea	0.00044	0.00052	530	1.95	2.28	2	2
2	Berea	0.00034	0.00034	1030	2.28	2.24	2	2
3	Berea	0.00042	0.00045	1530	3.33	3.68	3.4	3.4
4	Berea	0.00058	0.00063	1530	6.26	6.39	6.3	6.3
5	Berea	0.00028	0.00028	2030	3.50	3.38	3.6	3.6
6	Bentheim	0.00027	0.00027	1530	1.99	2.00	2	2

In all cases a value of $b = 1000000$ was used, and the maximum adsorption capacities are denoted by Q_m^1 and Q_m^2 for core 1 and core 2, respectively (pore volume fractions). The last five columns show comparisons between simulated and experimental RRF values

with progressive degradation at increasing flow rates. Furthermore, the degradation continues well into the second core. In contrast, the adsorbed polymer retains a very high molecular weight throughout the whole system, since the adsorption happened at a lower rate when not much polymer was degraded.

5.4 Effects of molecular weight

In Fig. 5, we have compared model versus experimental RF values for 4 different polymer types, all with a hydrolysis degree of 30%, but with varying molecular weight.

We observe that the model is able to capture the main trends of the different experiments, although the result for the 530 polymer is not as good as the others. The resistance factors are slightly over- or underestimated, depending on the case, but overall the match is remarkably good when we take into account that the input parameters used in the shear

thickening and shear degradation models were kept constant for all polymers (Table 2).

If we replot the results from Fig. 5 using shear rate on the x -axis, we get the results in Fig. 6. Compared with Fig. 5, the profiles in Fig. 6 have a more even distribution for the onset of elongation, which is essentially a function of the polymer M_w and $[\eta]$, while the declining parts of the curves come closer together.

5.5 Effects of permeability

In order to look more closely at the effect of permeability, we have studied three of the experiments in more detail. In Fig. 7, we have plotted the simulated and experimental RF values for the 1530 HPAM polymer. We observe that the match is better for Core 1, and that the simulator overpredicts RF in the second core. About half of the decrease in RF , going from Core 1 to Core 2, is accounted for. One may also observe that the increasing part of RF is well matched for both cores in all three experiments, and that the horizontal shift of the curves due to different permeability is very well captured. Overall, considering experimental and model uncertainties, we find the result to be acceptable, as the trends are captured very well for all 3 permeabilities, and for both cores.

If we replot the results from Fig. 7 versus in situ shear rate, rather than applied flow rate, we get the results in Fig. 8. We observe that the curves fall more or less on top of each other, which is to be expected, because the onset of elongation is independent of permeability in the model. There is a difference in RF level at low shear rate, which can be rationalized by permeability dependent effects of a depletion layer, and by differences in RRF , see Table 5 and the further discussion below.

In Fig. 9, we plot predicted steady-state spatial profiles for the molecular weight in two of the simulations shown in Figs. 7 and 8. These plots confirm that more polymer degrades at lower permeability, and at higher applied flow rates.

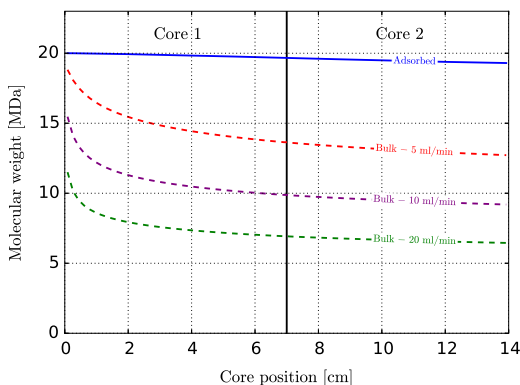


Fig. 4 Molecular weight in the water phase as a function of distance for the case of the 2030 HPAM polymer in the 823.6 mD and 800.4 mD dual core system. The spatial profile for the adsorbed polymer molecular weight is represented by the blue, solid line. The three dashed lines show spatial profiles of M_w at 3 different rates, all higher than the initial rate at which the adsorption occurred

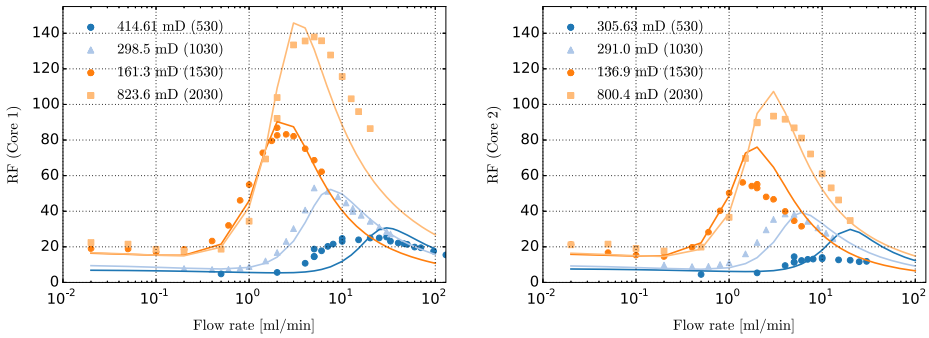


Fig. 5 Resistance factors plotted versus flow rate for 4 different polymer types, with M_w varied from 5 to 20 MDa. Dashed lines are from the simulator, whereas the points are derived from experimentally measured Δp and Q

5.6 Effects at low flow rates

Next, we show some examples of what can happen at low shear rates. In Fig. 10, we clearly see that the predicted RF factors are larger than the bulk viscosity, whereas the predicted apparent viscosity curves lie well below the bulk viscosity curves (Fig. 11). This is especially the case for the low permeable core. The reason for the large difference between RF and η for this core is the high $RRF = 6.3$. We observe that the bulk viscosity is closer to both RF and the apparent viscosity in the high permeability case, as expected due to the lower $RRF = 2$, and since the effect of a depletion layer become smaller at higher permeability. These plots illustrate nicely how the effects of permeability reduction and depletion layers can alter the in-situ rheology of the polymer (for an explanation of the depletion layer phenomenon, we refer to the discussion in Appendix A.1). However, we should point out that the experimental data at the lowest shear rates were of rather poor quality. Therefore, the clear differences between bulk

and in situ rheology, shown in Figs. 10 and 11, may be smaller in reality.

5.7 Parameter discussion

All parameters and equations required for reproducing the simulations presented earlier are provided in the paper. The parameters can be separated into two groups, those representing measured properties directly (e.g., bulk polymer viscosity parameters and core permeability), and the other groups which are history matched to the core flood data.

All the history matched parameters were kept constant in simulations of the first series of core floods with HPAM in synthetic sea water. The history matched property was mainly the mobility reduction factor, RF , measured as a function of shear rate, and effluent viscosity indicating level of degradation. The observed RF is a result of three parts, the rate dependent polymer viscosity, a polymer depleted layer at the rock surface resulting in a reduced effective viscosity, and the permeability reduction factor, RRF . A value

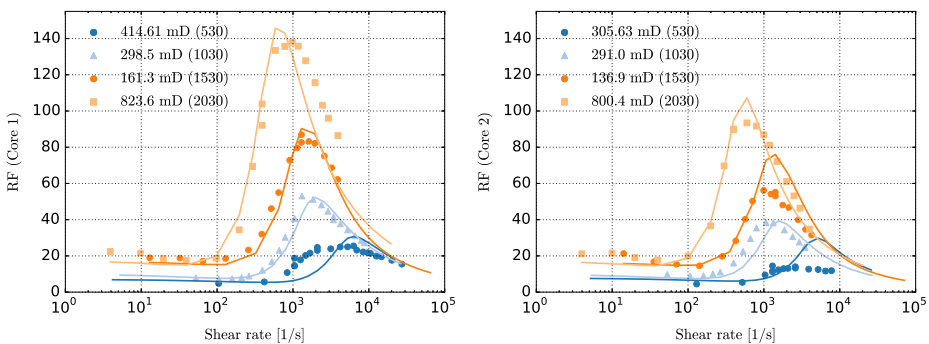


Fig. 6 Resistance factors plotted versus shear rate for 4 different polymer types. Dashed lines are from the simulator, whereas the points are derived from experimentally measured Δp and Q

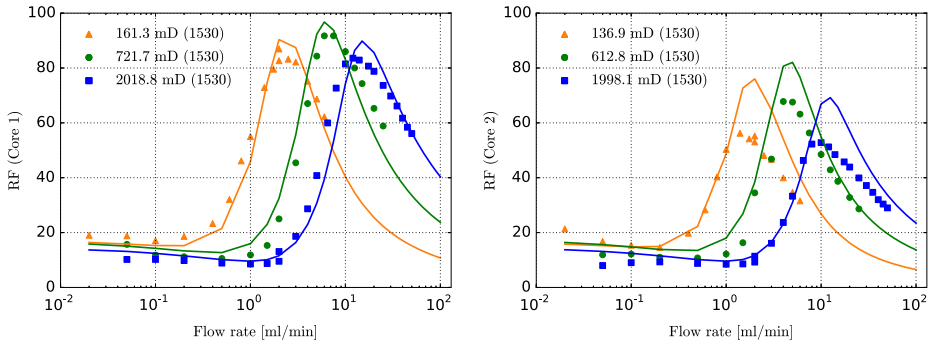


Fig. 7 Resistance factors for experiments performed with the 1530 HPAM polymer in 3 different serial core systems. The permeability varied from 137 mD to 2019 mD

for RRF is obtained at the end of the experiment, and the in situ polymer viscosity is computed from an apparent in situ shear rate.

The relative contributions from RRF and the depletion layer effect during polymer flooding are unknown and must be assumed. The polymer viscosity is based on measurements, however there are uncertainties in the tuning parameter used for in-situ apparent shear rate. Due to this, there will be a non-uniqueness in the parameters related to depletion layer and RRF that mainly affects the solution at lower shear rates. At higher shear rates, the depletion layer effect becomes small, and the relative contribution from elongational viscosity and RRF must be assumed. The effect of changing, e.g., the in-situ shear rate parameter from 2.0 to 1.0 would essentially change the critical Deborah number from 0.5 to 1.0 and result in a slight change in the degradation constant. The shear thickening and degradation would be matched as before, while the effect on the low shear end would be more uncertain.

6 Model test on a high viscosity dataset

The most novel parts of the model, those that deal with shear thickening and mechanical shear degradation, are very much based on experiments conducted with the same salinity (synthetic sea water) and the same polymer concentration (1500 ppm). As a final test, we apply the polymer model on a series of core flood experiments from Howe et al. [28], conducted in Bentheimer cores at very different salt and polymer concentrations. This test includes five core experiments performed with different HPAM polymers with M_w ranging from 3.6 to approximately 30 MDa, in low salinity brine (0.074 M) and viscosity at zero shear rate around 2 Pa s. That is, the effective salinity is roughly one order of magnitude lower than in the previous cases and, because of lower salinity and higher polymer concentrations, the viscosity is two orders of magnitude higher.

The bulk viscosity for the five polymers was matched with a single set of parameters given in Tables 1 and 6.

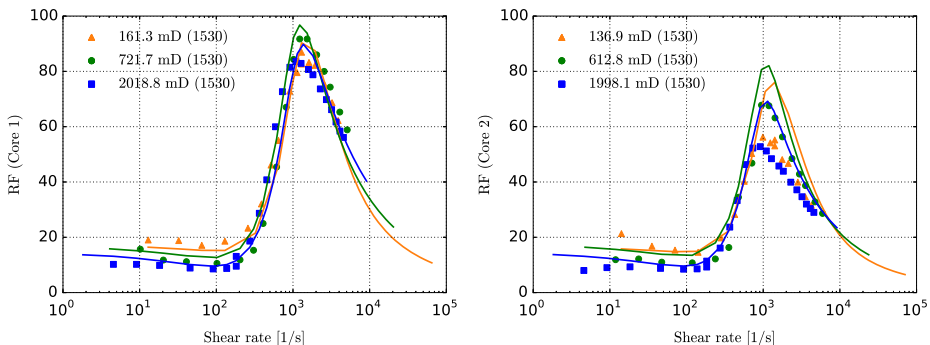


Fig. 8 Resistance factors plotted versus shear rate for experiments performed with the 1530 HPAM polymer in 3 different serial core systems. Dashed lines are from the simulator, whereas the points are derived from experimentally measured Δp and Q

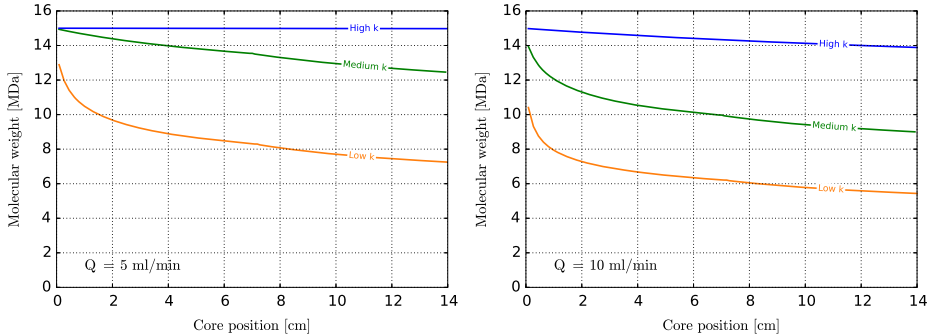


Fig. 9 Molecular weight in the water phase as a function of distance for the case of the 1530 HPAM polymer in cores with different permeability, i.e., for two of the cases shown in Figs. 7 and 8. The figures

show the molecular weight inside the core at applied flow rates of, respectively, $Q = 5.0$ and 10.0 ml min^{-1}

The effective salinity model was activated, and C_s was computed as the sum of the brine strength (assumed to be 0.074 NaCl), and the polymer charge. A list of relevant computed properties is given in Table 6 (C_s , $[\eta]$, η_0 , λ_1), in addition to polymer concentrations used, and the expressions for computing the salinity dependent values.

The matched shear thinning curves are plotted in Fig. 12. Points with increasing viscosity at the high shear rate end due to instabilities are removed. The results demonstrate the capability of the model, Eq. 21, to capture the onset of shear thinning over a large range in polymer concentration, intrinsic viscosity and molecular weight.

The core flood results with the five polymers are shown in Fig. 13. The core is a 3100 mD Bentheimer core with length 5 cm and diameter 3.8 cm. The original reported shear rate is corrected for the difference in expression used for in-situ shear rate with a factor around 3. No information was given about residual resistance factor RRF , so a reasonable salinity dependent adsorption was used to

generate these values. The adsorption capacity, as well as the resulting RRF for each polymer, is given in Table 6.

If we ignore the degradation part of the model, we can compute resistance factors directly without any iteration. The lines in Fig. 13 represent such analytical calculations. From the figure, we see that the model matches the onset of shear thickening for all the polymers using the same critical Deborah number as in the previous cases ($N_{De}^* = 0.5$). Two differences from the previous cases with seawater are that the transition between shear thinning and shear thickening is less sharp, and that the shear thickening increases more slowly. The transition parameter x_2 is reduced from 3 to 1.3 and the slope exponent m is reduced from 1.5 to 0.8, Eq. 23. This is a salinity effect also reported in, e.g., [7].

Another difference from the previous cases is the high viscosity contrast, which makes the computed result very sensitive to the depletion layer model at lower shear rates. In the simulations with much lower viscosity, the depletion layer thickness was assumed constant, and to only contain

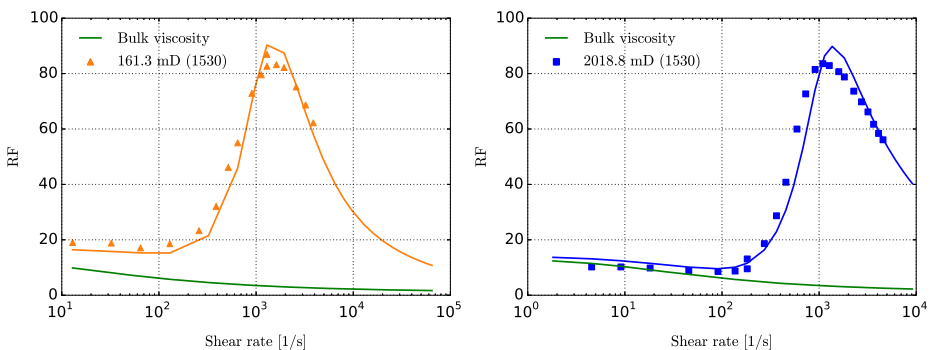


Fig. 10 Resistance factors versus shear rate for experiments performed with the 1530 HPAM polymer in high and low permeability cores. The green solid lines represents the predicted bulk viscosity of nondegraded polymer at the same shear rates

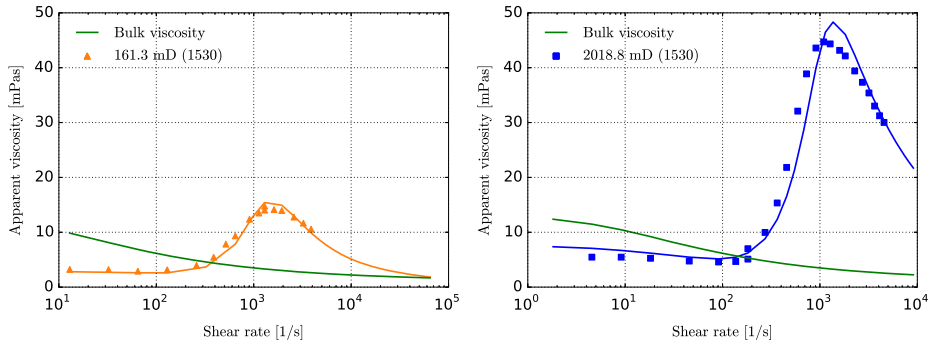


Fig. 11 Polymer apparent viscosity, η , versus shear rate for experiments performed with the 1530 HPAM polymer in high and low permeability cores. The green solid lines represents the predicted bulk viscosity of nondegraded polymer at the same shear rates

water. To capture the experimental flow resistance at lower shear rates, we set the polymer concentration in the depletion layer equal to 40% of that in the bulk solution ($c_{pd}/c_p^* = 0.4$), and we required the depletion layer thickness to decrease with increasing polymer concentration by $\delta = R_h \cdot (c_p/0.001)^{-0.75}$ when $c_p > 0.001$ [45]. This model for the depletion layer captures a significant part of the shear thinning regime, but where the experimental curves level off the computed curves continue to increase with decreasing shear rate. This might indicate that there is a shear rate dependency involved as well, but as pointed out, other unknowns like adsorption and *RRF* may also play a role here.

The analytical solutions for two of the polymers are compared with simulations in Fig. 14. The simulations were run with the same model parameters as before, but now the effect of degradation is also included. The overlap between the analytical and simulated curves verifies the implementation of the model into the simulator. The simulated degradation towards high shear rate is not seen in the experiments. Experimental indication of an onset of degradation can only be seen for polymer 3630S as a levelling off

in the resistance factor curve at high shear rate. This onset of degradation occurs at significantly higher shear rate than in the simulation, see Fig. 14. The simulations are run with the same degradation model parameters as used with polymer in seawater, and the overprediction clearly indicates that also degradation, at a given shear stress $\tau = \eta \cdot \dot{\gamma}$, is slowed down at lower salinity.

The simulations of the two experimental series show that the model handles the effect of molecular weight, permeability and porosity, as well as polymer concentration and salinity in the lower shear rate regime. The implemented polymer salinity model basically computes an effective salinity from the ionic composition of the brine and uses that effective salinity to correct the intrinsic viscosity. The effect of salinity is captured through the functional relationships of η_{sp0} , λ_1 and n on intrinsic viscosity (see Eqs. 4, 11 and 21).

The two data sets examined indicate that the onset of shear thickening, represented by λ_2 in Eq. 30, is captured through its salinity effect on $[\eta]$, while the reduced slope of the shear thickening and slower degradation at low salinity is not captured with the present model. Shear thickening behavior and mechanical degradation of the polymer can be

Table 6 Properties used to interpret experiments by Howe et al. [28]: effective salinity C_s , estimated *RRF*, polymer adsorption capacity Q_m (pore volume fraction), reference intrinsic viscosity used in salinity model $[\eta]_{ref} = 0.00139 \cdot M_w^{1.02}$, and intrinsic viscosity $[\eta] = [\eta]_{ref} \cdot C_s^{-0.4}$

Polymer	M_w	c_p	C_s	$[\eta]_{ref}$	$[\eta]$	<i>RRF</i>	Q_m	n	η_0	λ_1	ϕ	λ_2
6040S	31	0.0012	0.079	6091	16821	2.15	4.7E-5	0.557	1590	63.0	0.23	0.07691
3630S	18	0.00225	0.083	3498	9454	1.52	5.0E-5	0.564	1858	22.8	0.23	0.02517
3430S	11	0.00422	0.092	2117	5509	1.29	5.5E-5	0.575	2419	9.68	0.23	0.00901
3230S	6	0.00728	0.104	1659	2816	1.16	6.3E-5	0.559	1689	2.14	0.23	0.00253
3130S	3.6	0.0146	0.135	678	1508	1.11	8.1E-5	0.568	2118	0.80	0.23	0.00083

Shear thinning exponents, zero shear viscosities, and polymer relaxation times for the bulk solutions are displayed, based on input parameters from Table 1. In addition, values of λ_2 calculated for $\phi = 0.23$ are included. The HPAM hydrolysis degree was reported to be 40% for the 6040S polymer, and 30% for the rest. The dimensional quantities listed in the table have the following units: $[M_w] = \text{MDa}$, $[C_s] = M$, $[\eta]_{ref} = [\eta] = \text{ml g}^{-1}$, $[\eta_0] = \text{mPas}$, $[\lambda_1] = [\lambda_2] = \text{s}$

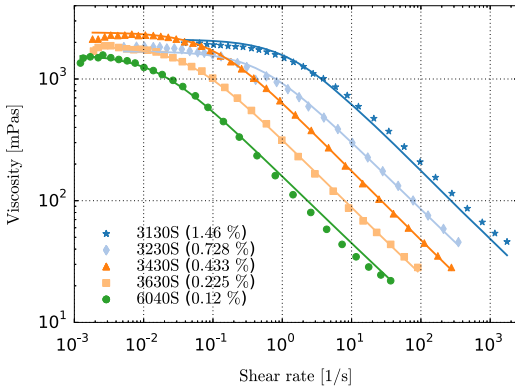


Fig. 12 Shear thinning bulk viscosity for polymers and concentrations given in Table 6

represented by a single set of model parameters for a wide range of experiments if salinity is kept constant. If salinity is changed, then a separate set of model parameters must be used.

To include salinity effects into the shear thickening and shear degradation models, more experimental data with the same polymer at different salinities is needed. Some effects of salinity that may be important can be mentioned. When salinity is reduced, the relaxed size of the HPAM molecule will increase due to reduced electrostatic screening of charged polymer sites. The reduced difference in size between relaxed and stretched state might explain the reduced shear thickening slope and will probably also influence the degradation. Also, distribution of polymer in the shear plane close to mineral surfaces may be affected by, e.g., increased repulsive forces at low salinity. An effect of the latter is a reduction in adsorption.

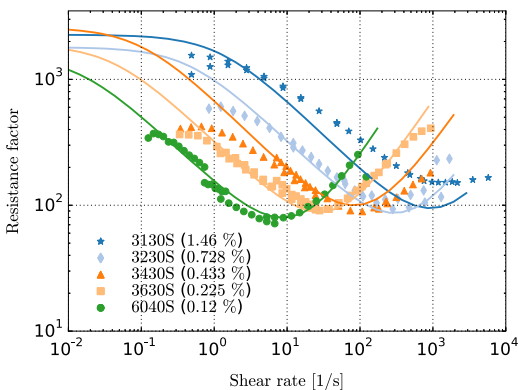


Fig. 13 Resistance factor versus flow rate for Bentheimer core experiments. The solid lines represent the model, whereas the experimental data (points) are adapted from Howe et al. [28]

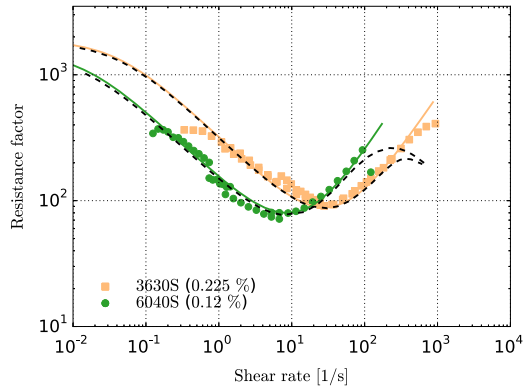


Fig. 14 Comparison of analytical solutions without degradation (solid lines) with simulations including degradation (dashed lines), for two polymers. The experimental data (points) are from Howe et al. [28]

7 Summary and conclusions

We have introduced a new model for simulating transport of polymer in a porous medium. A main focus has been to describe the flow properties of the polymeric fluids so that a correct relationship between flow rate and pressure drop across the core can be predicted. The model was primarily developed and tested in order to match shear thickening and degradation flow regimes inferred from single phase core-flooding experiments. A key aspect has been to relate the rheological parameters to conditions (temperature), properties of the porous media like permeability and porosity, and to fluid and polymer properties. To this end, we have in this work investigated the following factors:

- Effects of polymer concentration, c_p
- Effects of varying polymer molecular weight, M_w
- Effects of varying rock permeability k .

Possible effects of these variables have been included into the models controlling rheological properties, in particular the scaling groups controlling the onset of shear thinning and the onset of shear thickening, and the degradation model. The model has been applied on two series of core floods conducted with HPAM, the first with synthetic sea water and polymer viscosity up to 20 mPas, and the second test in a low salinity brine (0.074 M) with viscosities around 2 Pa s. The first series covers approximately one order of magnitude variation in both M_w and permeability. The second test has a similar variation in M_w and polymer concentration. The two series were matched with two separate input sets due to the difference in salinity.

Several salinity effects are included in the polymer model; however, a more thorough investigation is needed to obtain more precise information on the effect on shear

thickening and degradation parameters. Similarly, the proposed model includes several expressions to account for variations in temperature. The main effect of temperature is included via the solvent viscosity, but we expect that additional effects of temperature on the intrinsic viscosity might be needed. This is also something that needs to be explored in future work.

Acknowledgements The authors acknowledge the Research Council of Norway and the industry partners; ConocoPhillips Skandinavia AS, Aker BP ASA, Eni Norge AS, Maersk Oil Norway AS, DONG Energy A/S, Denmark, Statoil Petroleum AS, ENGIE E&P NORGE AS, Lundin Norway AS, Halliburton AS, Schlumberger Norge AS, Wintershall Norge AS of The National IOR Centre of Norway for support.

The authors would also like to thank two anonymous reviewers for their valuable feedback that helped us improve the quality of the paper.

Appendix

A.1 Excluded volume effects

A common observation in polymer flooding experiments is that the polymer travels at a higher flow rate than its solvent (water). This has been attributed to the large molecular size of the polymer molecules: If a rock contains a significant amount of small pores, not all of them will be available for polymer flow [15]. Furthermore, it has been observed that at low shear rates, effective viscosities estimated from core floods may be lower than corresponding bulk viscosity values [7, 8, 12, 45]. This behavior indicates a parallel flow of water depleted in polymer beside a flow of polymer rich solution. The flow of water may take place inside the micropores and/or in a polymer depleted layer at the pore surface. The idea here is that due to entropic considerations, large polymer molecules will be sterically excluded from layers of fluid close to the rock surface, preferring instead to flow near the centre of the pores.

In our model, we consider both types of inaccessible pore volume, i.e., we calculate

$$IPV = IPV_0 + IPV_d \cdot (1 - IPV_0), \tag{44}$$

where IPV_0 denotes the fraction of pores that are totally inaccessible to the polymer (“micropores”), and IPV_d denotes the volume fraction of the depletion layer in the pores accessible for polymer. We assume negligible flow of water in the micropores, so the handling of IPV_0 is straightforward. The handling of IPV_d is more involved, and we only sketch the method here.

The flow in a capillary tube, representing a fraction $1 - IPV_0$ of the total volume, is divided into a polymer depleted phase and a polymer rich phase, with fractional flows of f_{dw} and f_p respectively. The depletion layer is represented by a layer at the tube surface with thickness δ .

The fractional flows are obtained by integrating the Hagen-Poiseuille equation over the capillary tube, using constant viscosity in each of the two portions of the tube. Next, these results are combined with a single fluid solution for the capillary tube, after which the apparent polymer viscosity in the tube, η_{pa} , is obtained by requiring the same pressure gradient along the tube for the two cases.

Let $M_v = \eta_p/\eta_{dw}$ be the viscosity ratio between the two phases, where η_p is the viscosity in the polymer rich phase, and η_{dw} is the depletion layer viscosity. One can then show that

$$\eta_{pa} = \frac{\eta_p}{M_v - (M_v - 1)E_{PVd}^2}, \tag{45}$$

where

$$E_{PVd} = 1 - IPV_d = ((R - \delta)/R)^2 = (1 - \delta/R)^2, \tag{46}$$

with R being the tube radius. The apparent viscosity correction is applied after shear thinning but before including elongational effects, meaning that η_{sh} in Eq. 1 is used for calculating η_{pa} when the depletion model is activated. The thickness of the depletion layer is assumed to be in the range of the hydrodynamic radius R_h , but may decrease with increasing concentration above some critical concentration, c_{pd0} [45]. It is computed by

$$\delta = \begin{cases} f_{dpl} \cdot R_h & \text{if } c_p \leq c_{pd0} \\ f_{dpl} \cdot R_h \cdot (c_p/c_{pd0})^{\alpha_{dp}} & \text{if } c_p > c_{pd0}, \end{cases} \tag{47}$$

where f_{dpl} and α_{dp} are tuning parameters. For all simulations presented in this paper, $f_{dpl} = 1$. We also need to handle the polymer concentration. The injected concentration is split into a polymer rich phase with concentration c_{pp} , and a water rich depleted layer at the pore surface where the polymer concentration is lower, c_{pd} . The average concentration in the rock is c_p , and c_p^* denotes the concentration after excluding the constant part of the inaccessible pore volume, but before incorporating the depletion layer effect. The relations between the different concentrations are given by

$$c_p^* = \frac{c_p}{E_{PV0}} = c_{pp} \cdot E_{PVd}^* \tag{48}$$

where $E_{PVd}^* = E_{PVd} - (1 - E_{PVd}) \cdot (c_{pd}/c_{pp})$, and where the last term is the relative polymer concentration in the depletion layer. The latter quantity is used to compute the depletion layer viscosity, η_{dw} , that enters the definition of M_v .

The polymer concentration c_{pp} will be higher than the injected concentration when the depletion layer model is activated. Moreover, the polymer rich phase will travel at a higher velocity than the polymer depleted phase close to

the surface. To capture this, we define an effective polymer concentration, c_{pef} , to be used in the transport equation for polymer. Mass balance considerations require the effective concentration to be equal to the injected concentration, c_p^{inj} , at steady state. Applying the mass balance, and combining with Eq. 48 and expressions for f_{dw} and f_p (not shown here), we obtain the following expression for the effective polymer concentration:

$$c_{pef} = c_p \cdot \frac{1}{E_{PV0}} \cdot \frac{2M_v(1 - E_{PVd^*}) + E_{PVd^*}}{M_v - (M_v - 1)E_{PVd^*}}. \tag{49}$$

We remark that, for the low viscosity simulations presented in this paper, we assumed zero polymer concentration in the depleted layer, $c_{pd} = 0$. We also set the thickness δ of the depleted layer equal to the hydrodynamic radius of the polymer, $\delta = R_h$. On the other hand, for the simulations performed to match the dataset from Howe et al. [28], we used the more elaborate model reported herein. The exponent in Eq. 47 was then set to $\alpha_{dp} = -0.75$ [45], and $c_{pd}/c_{pp} = 0.4$.

A.2 Calculation of effective pore radius and in-situ shear rate

The shear rates experienced by the polymer molecules will vary drastically depending on the local conditions in the reservoir. In this paper, we have used the following correlation to calculate an average (effective) shear rate in porous media:

$$\dot{\gamma} = \dot{\gamma}_{pm} = \frac{4\alpha_c u}{\sqrt{8k\phi}} \cdot \sqrt{\frac{RRF}{1 - IPV_0}}. \tag{50}$$

Equation 50 is based on a model of the porous media as a bundle of capillary tubes, and the parameter α_c is a tuning parameter to account for variations in the pore geometry, whereas u is the Darcy velocity, and k is the permeability. We have explicitly included the fraction of pore volume that is totally inaccessible to the polymer, IPV_0 , into the calculation of $\dot{\gamma}_{pm}$, as well as the permeability reduction factor, Eq. 37.

The effective pore radius for the flowing polymer, R_p , is calculated accordingly:

$$R_p = \sqrt{\frac{8kC}{\phi}} \cdot \frac{1}{\sqrt{RRF(1 - IPV_0)}}. \tag{51}$$

We should stress that we have no measurements of the IPV factor in our experiments. For convenience we have simply set it to a value of 0.1, i.e., we assume that 10% of the pores are too small for the polymer to enter. Small variations in α_c and IPV_0 do not greatly affect the results.

A.3 More on polymer adsorption and the permeability reduction model

By looking at the expression for the effective pore radius, Eq. 51, we see that the permeability scales with R_p^2/ϕ . Both of these factors are reduced by a factor $1 - A_{pt}$ when adsorbed polymer is introduced, and this justifies the use of Eq. 37. Moreover, it is not enough to simply take $A_{pt} \approx A_p$, because this does not consider the swelling (volumetric extension) of the adsorbed polymer inside the pores. Had we used $A_{pt} \approx A_p$, we would have to model unrealistically high levels of adsorption in order to match the experimentally determined RRF factors.

A more realistic model might also allow for desorption and re-adsorption of polymer molecules, in line with experimental data from the literature that suggests continuous exchange of lighter molecular weight species at the wall with higher molecular weight species from the solution [10]. However, in this work, we were only able to estimate the adsorption indirectly. We have therefore not considered such an extension to the model, as more data would be needed to properly test it.

We should also mention that in the model the adsorption capacity, Q_m , is scaled with $\sqrt{\phi/k}$, since a smaller effective pore size results in a larger available surface area for adsorption, see Eq. 51. A value of Q_m is specified at reference values k_{ref} and ϕ_{ref} , and Q_m at arbitrary k and ϕ becomes

$$Q_m = Q_m(k, \phi) = Q_m^{ref} \cdot \sqrt{\frac{k_{ref}}{k}} \cdot \sqrt{\frac{\phi}{\phi_{ref}}}. \tag{52}$$

The ability to vary Q_m is important for upscaling to the field, since there are large variations in permeability and porosity in the reservoir.

A.4 Effective salinity model

The effect of solution salinity is included in the simulator by making $[\eta]$ in Eq. 11 salinity dependent. For the present purposes, we calculate $[\eta]$ as a power-law of an effective salinity parameter, C_s :

$$[\eta] = [\eta]_{ref} \cdot C_s^{\alpha_s}. \tag{53}$$

The parameter $[\eta]_{ref}$ is a reference intrinsic viscosity, calculated from the polymer molecular weight, and α_s is a fitting parameter which can be obtained as the slope of the intrinsic viscosity versus effective salinity on a log-log plot. The effective salinity is calculated as a weighted sum of the ionic concentrations in the solution:

$$C_s = \sum_i C_i \beta_i. \tag{54}$$

Here, β_i is a constant that varies according to the valence of ion i , and C_i is the molar concentration. NaCl is used as

a reference salt with $\beta_{Na} = \beta_{Cl} = 0.5$ so that C_s for a pure NaCl electrolyte becomes equal to the molar concentration. Other ions have β_i expressing their relative strength to either Na^+ or Cl^- . A common method is to set C_s equal to the ionic strength,

$$I = \frac{1}{2} \sum_i C_i z_i^2, \quad (55)$$

which would put more weight on divalent ions and in our notation have $\beta_{Ca} = 2$. Investigations on interaction forces between ions and charged surfaces like clay or charged molecules like surfactant have shown that not only the valence, but also the hydrated sizes of the ions are important [48]. The ionic strength expression may severely underestimate the effect of divalent ions, and Stavland et al. [65] used a “modified ionic strength” where the power of the valence term was allowed to be higher than 2 for divalent ions. The presented data indicated an order of magnitude higher effect from Ca^{2+} on the polymer viscosity, i.e., $\beta_{Ca} \approx 20$.

A.5 Temperature effects

In the current model, it is assumed that the main temperature dependence of the effective viscosity is captured by the viscosity of the solvent, which is computed according to an Arrhenius equation. Additionally, we have seen that both relaxation time constants, λ_1 and λ_2 , are inverse functions of temperature, since they are related to diffusion. However, as we have only considered experiments performed at room temperature (20 °C), more experimental data is needed in order to test this part of the model.

References

- Al Hashmi, A., Al Maamari, R., Al Shabibi, I., Mansoor, A., Zaitoun, A., Al Sharji, H.: Rheology and mechanical degradation of high-molecular-weight partially hydrolyzed polyacrylamide during flow through capillaries. *J. Pet. Sci. Eng.* **105**, 100–106 (2013)
- Bird, R.B., Armstrong, R.C., Hassager, O.: Dynamics of Polymeric Liquids, Fluid Mechanics, 2nd edn., vol. 1. Wiley, New York (1987)
- Bird, R.B., Curtiss, C.F., Armstrong, R.C., Hassager, O.: Dynamics of Polymer Liquids, Kinetic, Theory, 2nd edn., vol. 2, p. 2. Wiley, New York (1987)
- Bird, R.B., Stewart, W.E., Lightfoot, E.N.: Transport Phenomena. Wiley, New York (2002)
- Brakstad, K., Rosenkilde, C.: Modelling viscosity and mechanical degradation of polyacrylamide solutions in porous media. In: SPE Improved Oil Recovery Conference. Society of Petroleum Engineers (2016)
- Buchholz, B.A., Zahn, J.M., Kenward, M., Slater, G.W., Barron, A.E.: Flow-induced chain scission as a physical route to narrowly distributed, high molar mass polymers. *Polymer* **45**(4), 1223–1234 (2004)
- Chauveteau, G.: Molecular interpretation of several different properties of flow of coiled polymer solutions through porous media in oil recovery conditions. In: SPE Annual Technical Conference and Exhibition, SPE-10060-MS. Society of Petroleum Engineers (1981)
- Chauveteau, G.: Fundamental criteria in polymer flow through porous media and their relative importance in the performance differences of mobility control buffers. In: Glass, J. (ed.) Water-Soluble Polymers, vol. 213, pp. 227–268. Advances in Chemistry Series of the American Chemical Society (1986)
- Chauveteau, G., Moan, M.: The onset of dilatant behaviour in non-inertial flow of dilute polymer solutions through channels with varying cross-sections. *J. Phys. Lett.* **42**(10), 201–204 (1981)
- Chauveteau, G., Lecourtier, J.: Propagation of polymer slugs through adsorbent porous media. In: Water-Soluble Polymers for Petroleum Recovery, pp. 53–68. Springer (1988)
- Chauveteau, G., Moan, M., Magueur, A.: Thickening behaviour of dilute polymer solutions in non-inertial elongational flows. *J. Non-Newtonian Fluid Mech.* **16**(3), 315–327 (1984)
- Chauveteau, G., Tirrell, M., Omari, A.: Concentration dependence of the effective viscosity of polymer solutions in small pores with repulsive or attractive walls. *J. Colloid Interface Sci.* **100**(1), 41–54 (1984)
- Chauveteau, G., Denys, K., Zaitoun, A.: New insight on polymer adsorption under high flow rates. In: SPE/DOE Improved Oil Recovery Symposium. Society of Petroleum Engineers (2002)
- Clay, J., Koelling, K.: Molecular degradation of concentrated polystyrene solutions in a fast transient extensional flow. *Polym. Eng. Sci.* **37**(5), 789–800 (1997)
- Dawson, R., Lantz, R.B.: Inaccessible pore volume in polymer flooding. *Soc. Pet. Eng. J.* **12**(05), 448–452 (1972)
- De Gennes, P.: Coil-stretch transition of dilute flexible polymers under ultrahigh velocity gradients. *J. Chem. Phys.* **60**(12), 5030–5042 (1974)
- Delshad, M., Kim, D.H., Magbagbeola, O.A., Huh, C., Pope, G.A., Tarahhom, F.: Mechanistic interpretation and utilization of viscoelastic behavior of polymer solutions for improved polymer-flood efficiency. In: SPE Symposium on Improved Oil Recovery. Society of Petroleum Engineers (2008)
- Dill, K., Bromberg, S.: Molecular driving forces: Statistical thermodynamics in biology, chemistry, physics, and nanoscience. Garland Science (2010)
- Dupas, A., Hénaut, I., Argillier, J.F., Aubry, T.: Mechanical degradation onset of polyethylene oxide used as a hydrosoluble model polymer for enhanced oil recovery. *Oil Gas Sci. Technol.—Revue d’IFP Energies nouvelles* **67**(6), 931–940 (2012)
- ECLIPSE, Industry-Reference Reservoir Simulator Technical Description, Schlumberger, 2016 (Version 2016.1)
- Flory, P.J.: Principles of Polymer Chemistry. Cornell University Press (1953)
- Ford, J.: Improved algorithms of Illinois-type for the numerical solution of nonlinear equations. Tech. Rep. CSM-257 University of Essex (1995)
- Haas, R., Durst, F.: Viscoelastic flow of dilute polymer solutions in regularly packed beds. In: Progress and Trends in Rheology, pp. 212–217. Springer (1982)
- Hatzignatiou, D.G., Norris, U.L., Stavland, A.: Core-scale simulation of polymer flow through porous media. *J. Pet. Sci. Eng.* **108**, 137–150 (2013)
- Haward, S.: Microfluidic extensional rheometry using stagnation point flow. *Biomicrofluidics* **10**(4), 043,401 (2016)
- Hiemenz, P.C., Lodge, T.P.: Polymer Chemistry, 2nd edn. CRC Press (2007)
- Hirasaki, G., Pope, G.: Analysis of factors influencing mobility and adsorption in the flow of polymer solution through porous media. *Soc. Pet. Eng. J.* **14**(04), 337–346 (1974)

28. Howe, A.M., Clarke, A., Giernalczyk, D.: Flow of concentrated viscoelastic polymer solutions in porous media: effect of M_w and concentration on elastic turbulence onset in various geometries. *Soft Matter* **11**(32), 6419–6431 (2015)
29. Hu, X., Boukany, P.E., Hemminger, O.L., Lee, L.J.: The use of microfluidics in rheology. *Macromolec. Mater. Eng.* **296**(3–4), 308–320 (2011)
30. Idahosa, P., Oluoyemi, G., Oyenyin, M., Prabhu, R.: Rate-dependent polymer adsorption in porous media. *J. Pet. Sci. Eng.* **143**, 65–71 (2016)
31. Islam, M.T., Vanapalli, S.A., Solomon, M.J.: Inertial effects on polymer chain scission in planar elongational cross-slot flow. *Macromolecules* **37**(3), 1023–1030 (2004)
32. Jouenne, S., Anfray, J., Levitt, D., Souilem, I., Marchal, P., Lemaître, C., Choplin, L., Nesvik, J., Waldman, T.: Degradation (or lack thereof) and drag reduction of HPAM solutions during transport in turbulent flow in pipelines. *Oil Gas Facilit.* **4**(01), 80–92 (2015)
33. Kawale, D., Marques, E., Zitha, P.L., Kreutzer, M.T., Rossen, W.R., Boukany, P.E.: Elastic instabilities during the flow of hydrolyzed polyacrylamide solution in porous media: Effect of pore-shape and salt. *Soft Matter* (2017)
34. Keller, A., Odell, J.: The extensibility of macromolecules in solution; a new focus for macromolecular science. *Colloid. Polym. Sci.* **263**(3), 181–201 (1985)
35. Lake, L.W.: *Enhanced Oil Recovery*. Prentice Hall Inc., Old Tappan (1989)
36. Lange, E., Huh, C.: A polymer thermal decomposition model and its application in chemical EOR process simulation. In: *SPE/DOE Improved Oil Recovery Symposium*. Society of Petroleum Engineers (1994)
37. Lee, A.: *A Polymer Hydrolysis Model and its Application in Chemical EOR Process Simulation*. <http://hdl.handle.net/2152/ETD-UT-2010-12-2579>. Master of Science report, University of Texas, Austin (2010)
38. Machado, A., Bodiguel, H., Beaumont, J., Clisson, G., Colin, A.: Extra dissipation and flow uniformization due to elastic instabilities of shear-thinning polymer solutions in model porous media. *Biomicrofluidics* **10**(4), 043,507 (2016)
39. Maerker, J.: Shear degradation of partially hydrolyzed polyacrylamide solutions. *Soc. Pet. Eng. J.* **15**(04), 311–322 (1975)
40. Masuda, Y., Tang, K.C., Miyazawa, M., Tanaka, S.: 1D simulation of polymer flooding including the viscoelastic effect of polymer solution. *SPE Reservoir Eng.* **7**(02), 247–252 (1992)
41. Morel, D., Zaugg, E., Jouenne, S., Danquigny, J., Cordelier, P.: Dalia/Camelia polymer injection in deep offshore field Angola learnings and in situ polymer sampling results. In: *SPE Asia Pacific Enhanced Oil Recovery Conference*. Society of Petroleum Engineers (2015)
42. Nguyen, T., Kausch, H.H.: Influence of nozzle geometry on polystyrene degradation in convergent flow. *Colloid. Polym. Sci.* **269**(11), 1099–1110 (1991)
43. Nguyen, T.Q., Kausch, H.H.: Chain scission in transient extensional flow kinetics and molecular weight dependence. *J. Non-Newtonian Fluid Mech.* **30**(2–3), 125–140 (1988)
44. Odell, J., Keller, A., Rabin, Y.: Flow-induced scission of isolated macromolecules. *J. Chem. Phys.* **88**(6), 4022–4028 (1988)
45. Omari, A., Moan, M., Chauveteau, G.: Wall effects in the flow of flexible polymer solutions through small pores. *Rheol. Acta* **28**(6), 520–526 (1989)
46. OPM, The Open Porous media Initiative, <http://opm-project.org/>. Accessed 18 March 2017
47. Perkins, T.T., Smith, D.E., Chu, S.: Single polymer dynamics in an elongational flow. *Science* **276**(5321), 2016–2021 (1997)
48. Puerto, M.C., Reed, R.L.: Surfactant selection with the three-parameter diagram. *SPE Reserv. Eng.* **5**(02), 198–204 (1990)
49. Rajagopalan, R., Hiemenz, P.C.: *Principles of Colloid and Surface Chemistry*, 3rd edn. CRC Press (1997)
50. Rems, L., Kawale, D., Lee, L.J., Boukany, P.E.: Flow of DNA in micro/nanofluidics: From fundamentals to applications. *Biomicrofluidics* **10**(4), 043,403 (2016)
51. Seright, R.S.: The effects of mechanical degradation and viscoelastic behavior on injectivity of polyacrylamide solutions. *Soc. Pet. Eng. J.* **23**(03), 475–485 (1983)
52. Seright, R.S., Fan, T., Wavrik, K., Balaban, R.D.C.: New insights into polymer rheology in porous media. *SPE J.* **16**(01), 35–42 (2011)
53. Shaqfeh, E.S.: The dynamics of single-molecule DNA in flow. *J. Non-Newtonian Fluid Mech.* **130**(1), 1–28 (2005)
54. Sharma, A., Delshad, M., Huh, C., Pope, G.A.: A practical method to calculate polymer viscosity accurately in numerical reservoir simulators. In: *SPE Annual Technical Conference and Exhibition*. Society of Petroleum Engineers (2011)
55. Sheng, J.J., Leonhardt, B., Azri, N.: Status of polymer-flooding technology. *J. Can. Pet. Technol.* **54**(02), 116–126 (2015)
56. *Simulators / Computer Resources*, Center for Petroleum and Geosystems Engineering, The University of Texas at Austin, <http://www.cpege.utexas.edu/?q=iap.rs.jsp.simulators/>. Accessed 18 March 2017
57. Smith, D.E., Chu, S.: Response of flexible polymers to a sudden elongational flow. *Science* **281**(5381), 1335–1340 (1998)
58. Smith, D.E., Babcock, H.P., Chu, S.: Single-polymer dynamics in steady shear flow. *Science* **283**(5408), 1724–1727 (1999)
59. Sorbie, K., Roberts, L.: A model for calculating polymer injectivity including the effects of shear degradation. In: *SPE Enhanced Oil Recovery Symposium*. Society of Petroleum Engineers (1984)
60. Sorbie, K.S.: *Polymer-improved Oil Recovery*. Springer Science & Business Media (1991)
61. Southwick, J., Manke, C.: Molecular degradation, injectivity, and elastic properties of polymer solutions. *SPE Reserv. Eng.* **3**(04), 1–193 (1988)
62. Spillette, A., Hillestad, J., Stone, H.: A high-stability sequential solution approach to reservoir simulation. In: *Fall Meeting of the Society of Petroleum Engineers of AIME*. Society of Petroleum Engineers (1973)
63. STARS Resource Library, Computer Modelling Group Ltd., <http://www.cmgl.ca/stars/resource-library/>. Accessed 18 March 2017
64. Stavland, A., Jonsbrøten, H., Lohne, A., Moen, A., Giske, N.: Polymer flooding-flow properties in porous media versus rheological parameters. In: *Presented at the 72nd EAGE Conference and Exhibition incorporating SPE EUROPEC*, SPE-1311103-MS (2010)
65. Stavland, A., Jonsbrøten, H., Strand, D.: When will polymer viscosity be a design criterion for EOR polymer flooding. In: *IEA-EOR 34th Annual Symposium*, pp. 8–11. Stavanger (2013)
66. Teixeira, R.E., Babcock, H.P., Shaqfeh, E.S., Chu, S.: Shear thinning and tumbling dynamics of single polymers in the flow-gradient plane. *Macromolecules* **38**(2), 581–592 (2005)
67. Thomas, A., Gaillard, N., Favero, C.: Some key features to consider when studying acrylamide-based polymers for chemical enhanced oil recovery. *Oil Gas Sci Technol—Revue d'IFP Energies nouvelles* **67**(6), 887–902 (2012)
68. Vanapalli, S.A., Islam, M.T., Solomon, M.J.: Scission-induced bounds on maximum polymer drag reduction in turbulent flow. *Phys. Fluids* **17**(9), 095,108 (2005)
69. Vanapalli, S.A., Ceccio, S.L., Solomon, M.J.: Universal scaling for polymer chain scission in turbulence. *Proc. Nat. Acad. Sci.* **103**(45), 16,660–16,665 (2006)
70. Watts, J.: A compositional formulation of the pressure and saturation equations. *SPE Reserv. Eng.* **1**(03), 243–252 (1986)
71. Yasuda, K., Armstrong, R., Cohen, R.: Shear flow properties of concentrated solutions of linear and star branched polystyrenes. *Rheol. Acta* **20**(2), 163–178 (1981)
72. Zhang, G., Seright, R.: Effect of concentration on HPAM retention in porous media. *SPE J.* **19**(03), 373–380 (2014)

Paper V

Simulation of polymer mechanical degradation in radial well geometry

By:

Nødland, Oddbjørn

Lohne, Arild

Stavland, Arne

Hiorth, Aksel

Submitted to:

Transport in Porous Media (2018).

Simulation of polymer mechanical degradation in radial well geometry

Oddbjørn Nødland^{1,2,3} · Arild Lohne^{1,2} · Arne Stavland^{1,2} · Aksel Hiorth^{1,2,3}

Received: date / Accepted: date

Abstract Polymer flooding is a promising method of enhanced oil recovery (EOR), but for high molecular weight synthetic polymer types it is challenging to estimate field performance. These polymers exhibit a complex non-Newtonian fluid rheology, and they are susceptible to mechanical degradation. In this paper we present a method for how to predict field scale polymer behaviour from core experiments. The model we have developed is capable of describing the relevant flow regimes observed in the laboratory; apparent shear thinning, apparent shear thickening and mechanical degradation. Numerical investigations reveal that a very fine grid resolution, on the order of millimetres to centimetres, is needed near the wellbore to calculate the correct amount of polymer degradation and well pressure. The simulation results are corroborated by numerical, and approximate analytical, integration of the model equations. We study how varying the flow rate Q and permeability k affects the simulated molecular weight far away from the well, M_{wd} . In radial flow the degradation process terminates very close to the wellbore and, for the polymer type investigated, we find the scaling $M_{wd}^{-1} \propto Q^{0.65} \cdot k^{-0.425}$ when in the strong degradation regime. This is in contrast with the case of a linear core displacement, for which there is also a length dependency of degradation. Under certain assumptions, the model predicts an approximate power-law scaling $M_{wL} \propto L^\omega$, with L being the length of the core, and where M_{wL} is the model molecular weight at the core effluent. The power-law exponent depends on input parameters to the polymer model, and in the present study we found $\omega \approx -0.1$ when the initial degradation was substantial. Our findings are broadly consistent with results from the recent polymer pilot at the Dalia field, and with core scale experimental investigations into length effects of degradation.

Keywords Polymer flooding, EOR, Mechanical degradation, Non-Newtonian fluids, Porous media

1 Introduction

Although polymer flooding is regarded as a mature EOR technology, implementations of the method offshore have been relatively rare (Kaminsky et al., 2007; Standnes and Skjjevrak, 2014; Sheng et al., 2015). Contrary to onshore fields, offshore wells are expensive, and the well spacing is usually much larger. Consequently, injection rates tend to be significantly higher offshore, which may be problematic when injecting large molecular weight polymers into the reservoir. The polymers that are most often used for EOR purposes are partially hydrolyzed polyacrylamides (HPAM),

Corresponding author: Oddbjørn Nødland
E-mail: oddbjorn.m.nodland@uis.no

¹ The National IOR Centre of Norway

² International Research Institute of Stavanger (IRIS)

³ University of Stavanger

which typically have a molecular weight on the order of several million Daltons. These polymers exhibit a flexible coil conformation in solution, which gives them elastic thickening properties at high flow rates. This behaviour, referred to as (apparent) shear thickening in the literature (Chauveteau and Moan, 1981; Chauveteau et al., 1984), leads to a sharply increasing flow resistance with increasing rate. Near the wells, it may potentially cause a severe loss in well injectivity.

Polymer molecules are sensitive to the chemical and microbial environment they are exposed to and can degrade as a result of bacterial attacks, thermal hydrolysis at elevated temperatures, or due to rapid redox reactions initiated by certain chemicals, especially in the presence of dissolved oxygen (Ryles, 1988; Levitt et al., 2011; Thomas et al., 2012; Seright and Skjevrak, 2014). In addition, once the polymers enter the shear thickening flow regime they become susceptible to mechanical degradation (Maerker, 1975, 1976; Seright, 1983). Mechanical degradation occurs when the polymer molecules experience excessive mechanical stresses in regions of high shear, causing some of the covalent bonds along the polymer chain backbone to break. If this happens, it will counteract the decline in injectivity, but at the cost of losing much of the viscosifying power of the added chemicals. A recent example of field scale mechanical degradation was reported at the Dalia field in offshore Angola, where a surveillance well dedicated to sampling injected polymer revealed lower viscosity than expected. According to Morel et al. (2015), roughly half of the designed viscosity was lost due to mechanical degradation, and the percentage reduction in low shear viscosity was close to 75 %.

In this paper we demonstrate a method for forecasting field scale polymer flood performance based on core scale experiments. We do this by applying a new mathematical model for polymer flooding, originally developed to simulate linear corefloods, to a radial setting. The polymer behaviour in radial flow is non-trivial, because the flow rate is varying with distance, and thus the shear rates experienced by the polymer molecules will decrease as the polymer travels deeper into the formation. Taking into account the complex character of the in-situ polymer solution rheology, this leads to a different scaling behaviour for the case of radial flow than for a corresponding linear case. Fortunately, in large scale reservoir simulation, effects of apparent shear thickening and mechanical degradation may be safely ignored in the bulk portion of the reservoir. This is because representative reservoir flow rates will be too low to trigger the onset of these flow regimes. On the other hand, the effects are crucial to resolve accurately near the wells.

The model previously used to history match core scale polymer floods is briefly reviewed in section 2. In section 3, we describe the radial sector grid employed in the current work. We illustrate the sensitivity of the simulation results to the chosen grid resolution near the injector. In the main section of the paper, we present a series of simulation cases, conducted to study the effect of injection flow rate and permeability on predicted mechanical degradation. We solve the steady-state degradation problem analytically and semi-analytically in the Appendix. This serves at least three purposes. First of all, it provides a direct validation of the simulator implementation. Secondly, it allows us to derive approximate scaling laws, which gives insight into what controls degradation in the model. Finally, it leaves us with a very good starting point for further development into a full field simulator. This is briefly hinted at towards the end of the article, where we also discuss limitations of our approach.

2 Numerical model

In Lohne et al. (2017) we presented a short review of polymer flooding simulators that have been reported in the literature. Our conclusion was that there is currently a lack of useful models to describe the phenomenon of mechanical degradation of polymers. To remedy this, we suggested a new model to capture the in-situ rheological behaviour of flexible polymer molecules in porous media (Nødland et al., 2016; Lohne et al., 2017). The model was implemented in an in-house simulator, IORCoreSim. Our approach includes ways to model both shear thinning and shear thickening fluid rheologies, as well as mechanical degradation. The model was originally developed to match resistance (mobility reduction) factors calculated from laboratory core flooding data. For a given flow rate, the resistance factor RF is defined as the steady state pressure drop across the core, Δp_{pol} , normalized by the corresponding pressure drop for brine without polymer, Δp_{wat} :

$$RF = \frac{\Delta p_{pol}}{\Delta p_{wat}}. \quad (1)$$

An example of the match that was obtained between model and experiment is shown in figure 1. One of the successes of the model was that it was possible to match experimental data from different labs with mostly the same input. Some differences had to be introduced when matching the low salinity dataset reported by Howe et al. (2015). However, at fixed ionic composition, the impact of varying permeability, molecular weight, and flooding rate was well captured using a single set of parameters.

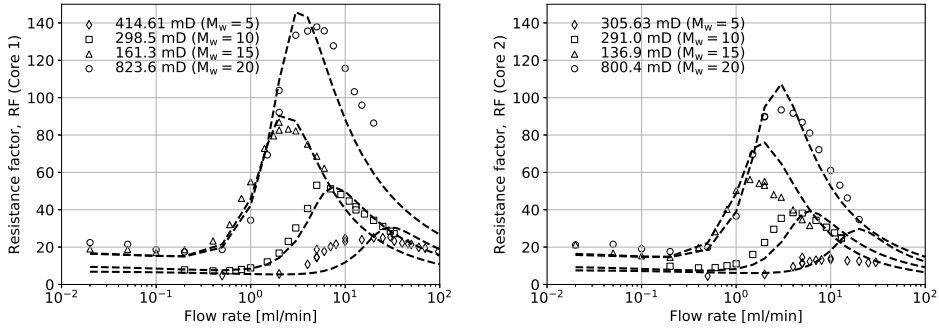


Fig. 1 Resistance factors versus flow rate for four different polymer experiments. The RF factors were calculated for two successive (serial) cores, each of length ~ 7 cm. The scatter points are values obtained experimentally, and the dashed lines are calculated from simulated pressure drops. Note that for the experiments shown here, 4 different HPAM polymers were used, with reported molecular weights varying from $M_w = 5$ MDa to $M_w = 20$ MDa. There were also some variation in rock permeability (and porosity) among the experiments.

The model is fairly comprehensive, and we will only give a brief review of the main aspects here. The model includes a description of the effective aqueous phase viscosity, η , that can be both shear thinning and shear thickening, depending on the flow conditions. Each of these flow regimes is governed by the product of a characteristic time scale and the in-situ, apparent shear rate in porous media. In the apparent viscosity model, the shear thinning viscosity is computed from the Carreau-Yasuda equation (Bird et al., 1977), using as input a polymer characteristic relaxation time λ_1 , which is calculated from properties of the solution. Similarly, the effects of shear thickening are related to a time scale λ_2 , and is made a function of both the rock and the fluid properties. More equations are presented in the Appendix, but for all the details we refer to (Lohne et al., 2017).

For one-phase flow, the in-situ shear rate is computed as

$$\dot{\gamma} = \frac{4\alpha_c u}{\sqrt{8k\phi(1-IPV_0)}} \cdot \sqrt{R_k}, \quad (2)$$

where u is the Darcy velocity of the water phase, R_k is a permeability reduction factor, and IPV_0 represents polymer inaccessible pore volume due to the large molecular size of the polymer macromolecule in solution. Expression (2) is a standard way of defining the shear rate in a porous medium, and the parameter α_c is a tuning parameter used to correlate the in-situ and bulk rheology curves (Cannella et al., 1988; Wreath et al., 1990; Fletcher et al., 1991).

2.1 Polymer degradation model

In principle, a polymer solution should be described by a distribution of components with varying molecular weight, reflecting the polydispersity of the sample. In practice, this is very difficult. Even if the molecular weight distribution

prior to degradation could be known accurately from experiments, it would still pose several challenges for the purposes of modelling. First, it would be computationally demanding to model. Second, specific assumptions about the mechanism of the degradation would be required, such as whether certain components are more prone to chain cleavage, or if the degradation process is random. Because of this, we do not attempt to explicitly model the molecular weight distribution. Instead, we are mainly concerned with matching the correct viscosity behaviour of the degraded solutions. To this end, we represent the polymer by two different polymer components in the simulator, a volumetric component and a molar component. Only the latter component is affected by degradation. In consistent units, the two concentrations are related by

$$M_w = \frac{c_p}{c_{mol}}. \quad (3)$$

where c_{mol} is the molar concentration, c_p is the mass concentration of polymer. The volumetric concentration is the ratio c_p/ρ_p , where ρ_p is the polymer density. The combined transport and reaction (degradation) problem is handled by a standard sequential non-iterative operator splitting approach. First, the polymer components are advected through the grid using a timestep Δt , yielding an intermediate solution M_w^0 . Next, the polymer molecular weight is updated by solving the initial value problem (Lohne et al., 2017)

$$\frac{dM_w}{dt} = -f_{rup} \cdot M_w, M_w(0) = M_w^0, \quad (4)$$

over the same timestep Δt , and where the degradation rate is

$$f_{rup} = (r_{deg} \cdot \dot{\gamma} \cdot \eta)^{\alpha_d} \cdot 2M_w^{\beta_d} / R_p. \quad (5)$$

For completeness, we repeat some of the arguments that were presented in favour of expression (5) in Lohne et al. (2017):

1. Above a certain shear stress inside the porous media there is a probability for chain rupture, and as the shear stress increases the probability for chain rupture increases dramatically. This effect is represented by the term $(r_{deg} \cdot \dot{\gamma} \cdot \eta)^{\alpha_d}$.
2. The velocity gradient inside the pore space is highest closest to the pore surface, and therefore the shear forces are largest there. Letting R_p denote the effective pore radius available to polymer flow, this effect is represented by term $2/R_p$ (i.e., specific surface area)
3. Longer polymer chains will rupture more easily than shorter ones simply because they experience a higher shear force across the molecule, which is represented by the factor $M_w^{\beta_d}$.

The parameters r_{deg} , α_d and β_d are set to constant values, and it was shown in Lohne et al. (2017) that these values matched experimental data when polymer type, permeability, and flooding rate rate was varied. The pore radius is calculated from a Kozeny-Carman type equation,

$$R_p = \sqrt{\frac{8kC}{\phi}} \cdot \frac{1}{\sqrt{R_k(1-IPV_0)}}, \quad (6)$$

where C is a tortuosity factor.

2.2 Simplifying assumptions

To match experimental core flooding data, the inclusion of models for permeability reduction and depletion layer effects was deemed necessary (Lohne et al., 2017). However, by incorporating these mechanisms into the simulator, the mathematical complexity of the resulting equations greatly increase. Therefore, for the analysis presented herein, we have neglected both effects (adsorption was still included, but we set $R_k = 1$). These choices should not alter the results of our analysis in any dramatic way, but it should be kept in mind, particularly when considering the usage of the analytical formulas presented towards the end of the paper. It should also be remarked that only mechanical degradation has been modelled, and not any of the other degradation processes that might be relevant for a given field scenario.

3 Simulation overview, and grid sensitivity

To represent flow near a vertical injector at the field scale, we considered a 360° sector model, with the well boundary located at the inner radius $r = r_w = 0.1$ m, and the outer boundary placed at $r = r_e = 20$ m. The sector model was discretized using 1D cylindrical coordinates, i.e., with a single grid block in the azimuthal and vertical directions. The reservoir thickness was $\Delta z = h = 20$ m, and porosity was $\phi = 0.2$. For the interface between radial grid blocks i and $i + 1$, the numerical flux was calculated by applying a logarithmic transform to the radial coordinate, and by approximating the pressure drop as occurring across pressure equivalent radii R_i^{eq} and R_{i+1}^{eq} . Specifically, the equivalent radius R_i^{eq} for block i is defined as the radius at which the grid block volume-weighted average pressure equals the grid block pressure, at steady-state (assuming radial flow). Another choice involves the radius at which the polymer apparent viscosity is evaluated. In this work, the midpoint radius was selected for each grid block.

For all simulations discussed in this paper, we used history matched input data for the 3630S HPAM polymer, manufactured by SNF Floerger with reported $M_w = 20$ MDa, and 30 % degree of hydrolysis. Shear thinning parameters were obtained from standard bulk viscosity rheometer measurements. For the other parts of the model, the crucial input parameters are the slope and transition parameters for describing apparent shear thickening flow (m and x_2), the critical Deborah number N_{De} that is used to calculate λ_2 (i.e., the onset of thickening), as well as the degradation parameters α_d (exponent for degradation dependence on shear stress) and r_{deg} (degradation rate constant). We refer to Lohne et al. (2017) for details on the history matching procedure.

In the simulations, a constant flow rate boundary condition was enforced at the injector, and a constant pressure was required at the external boundary, $p_e = p(r = r_e) = 200$ bar.

3.1 Effects of grid resolution, and sources of numerical error

Figure 2 illustrates the effect of near well grid resolution on simulated steady-state degradation (left plot), and on injection well pressure (right plot). For the example considered, the permeability was $k = 1$ D, and the applied flow rate was $Q = 250$ m³ d⁻¹. In the left plot, we have included for reference the analytical solution, which was obtained via numerical integration (section 12). We see that for the coarsest grids virtually no degradation is predicted, while for the finest grid the percentage reduction in molecular weight is ~ 45 %. The explanation for this huge difference is that as the grid size becomes larger, the shear rate becomes smeared out near the well. For the largest grid blocks, the calculated shear rate is so low that the polymer is incorrectly predicted to be in the low shear regime, and we get minimal amounts of degradation. As the grid size decreases, more polymer degradation occurs. Observe also that there is a peak in the pressure versus grid size plot. This is because increasing the shear rate induces two simultaneous effects which work in opposite directions with respect to the apparent viscosity. On the one hand, as the grid size becomes smaller, the shear rate near the well becomes larger, which for a polymer in the shear thickening flow regime leads to an increase in the apparent viscosity. At the same time, a higher shear rate leads to more degradation, which reduces M_w and hence leads to a decrease in pressure.

It is well known that the use of operator splitting techniques to decouple transport and reaction leads to an inherent numerical error (Herzer and Kinzelbach, 1989; Hundsdorfer and Verwer, 1996; Carrayrou et al., 2004). This is irrespective of whether each subproblem could be solved exactly, which is usually not the case (e.g., (Lantz, 1971)). The conclusion holds for both linear and radial geometries, but in the radial case there will be additional errors associated with the choice of shear rate at which grid block properties are computed. Moreover, in the current IORCoreSim implementation equation (4) is discretized implicitly in time. The resulting non-linear equation is solved using an iterative chord method, and for large timesteps this solution method is known to incur some error. In several examples that were tested, the algorithm tended to slightly overpredict M_w . As a consequence, simulated results will show some dependence on the timesteps taken in the numerical scheme, even when considering steady-state solutions. Note also that we used an explicit scheme to handle the component transport. However, for the steady-state problems considered in this work, tests performed with a fully implicit scheme revealed no significant differences in the computed solutions.

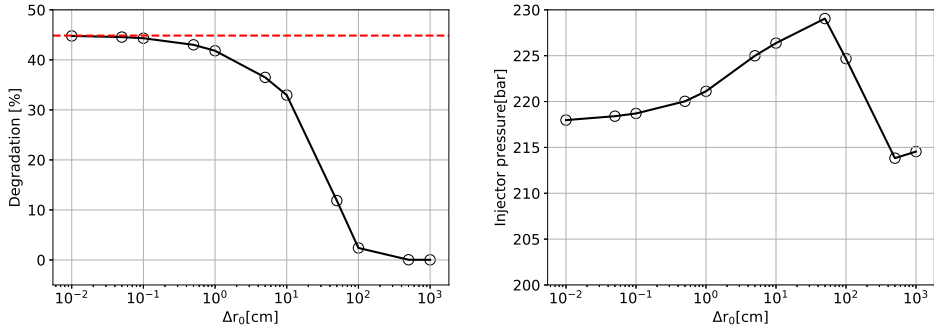


Fig. 2 Effect of grid resolution. Left plot: Simulated reduction in effluent polymer molecular weight (at steady-state) plotted versus radial size of the first grid block, Δr_0 . This cell size was used throughout the first 25 cm of the reservoir, while log spacing was applied thereafter. For cases with $\Delta r_0 \geq 25$ cm, only 1 grid block had this size, and the subsequent blocks had a lower incremental radius, since it was set as a requirement that the total number of blocks should be equal to $n_{rad} = 100$, if possible (this choice is quite arbitrary). For the last grid block, $\Delta r = 0.1$ cm in all cases. Right plot: Corresponding injection pressures.

The slow convergence in the radial grid (figure 2) can be rationalized by considering how the shear rate varies with distance. In radial flow, $\dot{\gamma} \propto 1/r$, which means that the degradation rate declines rapidly with distance away from the injector. If the level of degradation is underestimated in the beginning, it will not be fully compensated for later on with progressive degradation, as would be the case in a corresponding linear case (where the shear rate is constant in space). Indeed, degradation levels at a distance ~ 20 m in linear 1D geometry were found to be quite insensitive to grid resolution, yielding similar results when only a couple of grid blocks were used as when the block size was below 1 mm.

In the rest of the paper we have chosen to discretize the first 25 cm of the reservoir into grid blocks of constant size $\Delta r_0 = 5$ mm. This choice corresponds to case 4 from the left in figure 2.

3.2 Method of quantifying degradation

Unless otherwise is specified, we calculate the amount of mechanical degradation as the reduction in model M_w from its initial value,

$$Degradation[\%] = \frac{M_w^{orig} - M_w^{degr}}{M_w^{orig}} \cdot 100\%, \quad (7)$$

where M_w^{degr} and M_w^{orig} are the produced and original molecular weights, respectively. However, in the experimental petroleum literature it is common to quantify degradation as the percentage reduction in low shear viscosity as measured in a rheometer. Letting η_{sp}^{orig} and η_{sp}^{degr} denote the low shear specific viscosities of, respectively, the original and the degraded polymer solutions, we can then calculate

$$Degradation[\%] = \frac{\eta_{sp}^{orig} - \eta_{sp}^{degr}}{\eta_{sp}^{orig}} \cdot 100\%. \quad (8)$$

The relation between viscosity and molecular weight is given by the Mark-Houwink equation, Eq. (21).

4 1-phase simulations in homogeneous permeability fields

For the simulations shown in this section, all input parameters to the model were kept fixed, except the flow rate Q , and the permeability k . Both of these parameters were varied over several orders of magnitude, with 725 combinations of the two parameters investigated. The selected flow rates were in the range $50 \leq Q \leq 2500 \text{ m}^3 \text{ d}^{-1}$, and permeability was varied from 10 mD to 50 D. In figure 3 we visualize some of the obtained simulation results by plotting the amount of M_w reduction that has occurred at a distance $r = r_e = 20 \text{ m}$ from the injector. In the left plot we have plotted degradation versus permeability, and in the right plot we have used Q/h on the x -axis, where h is the reservoir thickness.

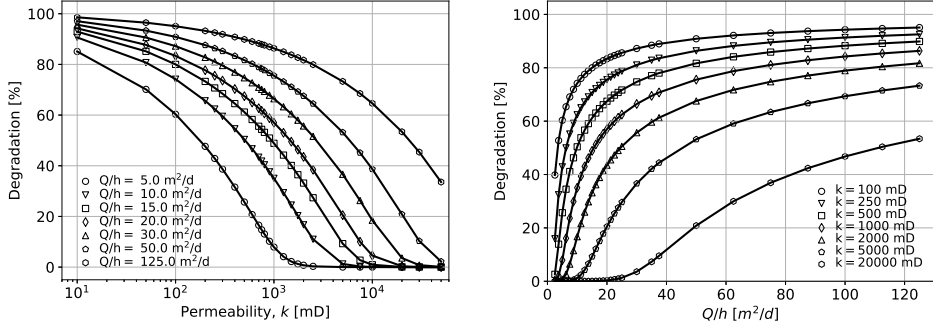


Fig. 3 Percentage reduction in the polymer molecular weight for various, selected combinations of Q and k . Left plot: Versus permeability, for different flow rates. Right plot: Versus flow rate, for different permeabilities.

Figure 3 reveals that for the highest flow rates, a significant amount of degradation can be expected, even when the permeability is high. For example, for $k = 1 \text{ D}$, both plots show that the molecular weight will be approximately halved when $Q/h \geq 15 \text{ m}^2 \text{ d}^{-1}$. From the right plot we observe that for $Q/h \geq 25.0 \text{ m}^2 \text{ d}^{-1}$, the M_w reduction is predicted to be $> 50 \%$ for all $k \leq 2000 \text{ mD}$.

4.1 Analytical and semi-analytical calculations

To validate the simulated results, and to gain a better grasp of what controls mechanical degradation in the model, we have developed several analytical and semi-analytical expressions. The details are presented in the Appendix, but the starting point was the equation

$$\frac{dM_w}{dr} = -\frac{2\pi hr\phi(1-IPV_0)}{Q} \cdot f_{rup} \cdot M_w, \quad (9)$$

and was obtained from mass balance considerations (Appendix A). The use of these methods is illustrated in figure 4. In the figure, we consider three specific flow rates, at different permeabilities. In the left plot, we compare simulated steady-state M_w reduction with results obtained from two explicit formulas of the form (36), derived by assuming that the cubic polynomial used to compute the zero shear specific viscosity, Eq. (20), can be approximated either by 1) the first order term or 2) the third order term (see Appendix B and C, respectively). In both cases, the Carreau-Yasuda exponent n was assumed independent of M_w , and equal to 0.3. It is evident that we underestimate the amount of mechanical degradation when using either formula. We observe that for a given flow rate, there is a permeability at which the two

curves intersect. This is because, as the molecular weight decreases during degradation, the dominant term in Eq. (20) changes. For large M_w , the third order term dominates, but as M_w decreases the first order term becomes most important.

In the right plot of figure 4 we compare the same simulated data with two other approaches: 1) a semi-analytical solution, and 2) an analytical solution, obtained via numerical integration (see section 12). The semi-analytical method is based on the inclusion of both the first *and* the third order term in $\eta_{sp}c_0$ and, as before, it is assumed that n is constant, along with several other simplifications. On the other hand, in the numerical integration routine we do not make any approximations when calculating the apparent viscosity. From the figure, we see that there is still some discrepancy between simulation and calculation, but the match is very close. Moreover, as can be seen from figure 2, an even finer grid discretization would lead to a slightly higher M_w reduction, thus improving the match. As a further test, we conducted a new series of simulations, this time in linear 1D geometry at the core scale. In each case, the simulated M_w reduction was compared with numerical computations akin to the ones already performed for the radial model. The results for the molecular weight at the core effluent revealed a very close agreement between simulation and numerical integration (Appendix E, section 13).

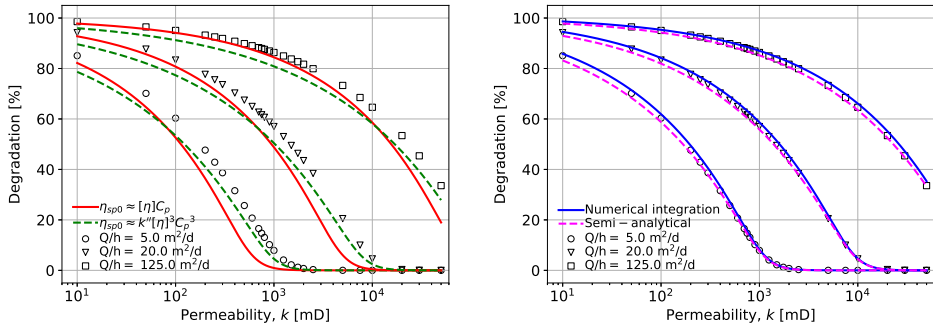


Fig. 4 Percentage reduction in the molecular weight for various, selected combinations of Q and k . Left plot: Comparison between simulated data and two approximate formulas (solid lines). Right plot: Simulated data versus semi-analytical calculations and the analytical solution (numerical integration).

4.2 Scaling relationships

As shown in figures 3 and 4, the amount of degradation is a function of both Q and k , and in the model the polymer is degraded progressively as it moves radially outward from the injector. However, as will be shown later, the molecular weight essentially stabilizes at a constant value within the first tens of centimetres from the well. Thus, in the absence of significant heterogeneities, we would expect the amount of degradation to be strongly linked to the in-situ shear rate at the sandface, $\dot{\gamma}_w$, which scales according to

$$\dot{\gamma}_w \propto Q/\sqrt{k}.$$

In figure 5, we plot all of the degradation data versus $\dot{\gamma}_w$, this time displaying the molecular weight at $r = r_e$ on the y-axis, normalized by the initial value before injection started. Note that we have split the data into 3 categories depending on the magnitude of the permeability. The data in the figure reveal a clear trend, but there is considerable

scatter, and $\dot{\gamma}_w$ alone does not suffice to predict the total amount of degradation occurring in these homogeneous models. For lower permeabilities, more degradation is predicted at the same $\dot{\gamma}_w$.

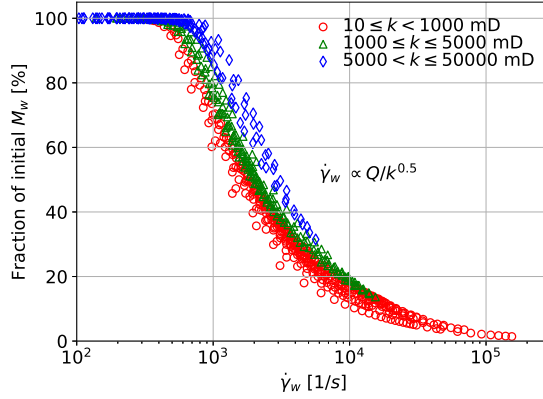


Fig. 5 Molecular weight of the polymer at $r = r_e$, relative to the initial value, plotted versus the in-situ shear rate at the sand face, $\dot{\gamma}_w$.

As mentioned in section 4.1, we can derive an approximate analytical expression to estimate the simulated M_w reduction. By employing that expression, as well as the particular model input parameters used for the simulations, we anticipate the molecular weight to approximately satisfy

$$M_w(r = r_e)^{-1} \propto \dot{\gamma}_w^{0.65} \cdot k^{-0.1} \propto Q^{0.65} \cdot k^{-0.425}, \quad (10)$$

provided there is a substantial amount of degradation. This is verified in figure 6. Compared with figure 5, the amount of scatter is heavily reduced. Also, as predicted by (10), the declining part of the curve is well captured by a straight line when plotted on a log-log plot (right plot). We remark that the approximate scaling behaviour obtained for radial flow, Eq. (10), is markedly different than for the case of flow in linear geometry. In the latter situation, the model predicts an additional length dependency of degradation, typically in the form of a power-law scaling with distance from the injection point (see Eq. (47)). This was recently observed experimentally (Åsen et al., 2018).

4.3 In-situ rheology at $k = 1$ D

To further illustrate the simulation results, we looked more in-depth at the cases with $k = 1$ D, for different Q . In the plots shown here, figure 7 and 8, we have restricted ourselves to flow rates satisfying $Q \leq 400 \text{ m}^3 \text{ d}^{-1}$. However, data for all investigated flow rates are presented in table 3. The resulting steady-state profiles for the molecular weight (strictly speaking, molar volume) versus radial distance are shown in the left plot of figure 7. We see that the steady-state molecular weight effectively stabilizes to a constant value at a distance very close to the injector, in these cases on the order of, at most, 15–20 cm. This is in contrast with the case of linear geometry, where the model predicts progressive degradation with distance from the injection point (see, e.g., Eq.(47)).

In the right plot of figure 7, we show how the in-situ shear rate varies with distance. Note that, for the cases investigated here, the shear rates close to the well vary slightly less than one order of magnitude, from $\dot{\gamma} \approx 300 \text{ s}^{-1}$ in the

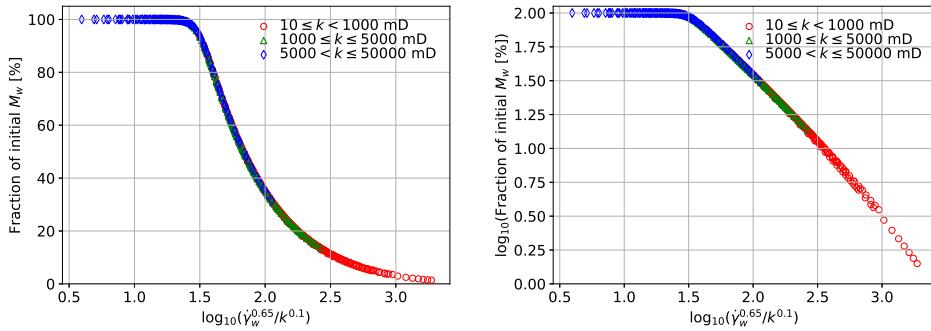


Fig. 6 Left plot: Simulated molecular weight of the polymer at $r = r_e$, relative to the initial value, plotted versus $\log_{10}(\dot{\gamma}_w^{0.65}/k^{0.1})$. The latter quantity was derived from an approximate analytical model, see section 10. Right plot: The same data as in the left plot, but now applying a logarithmic transformation to the values on the y-axis.

$Q = 50 \text{ m}^3 \text{ d}^{-1}$ case, to $\dot{\gamma} \approx 2500 \text{ s}^{-1}$ when $Q = 400 \text{ m}^3 \text{ d}^{-1}$. For the lowest flow rate, we see that virtually no polymer is degraded (0.19 %, table 3), whereas for $Q = 400 \text{ m}^3 \text{ d}^{-1}$, there is more than 50 % M_w reduction.

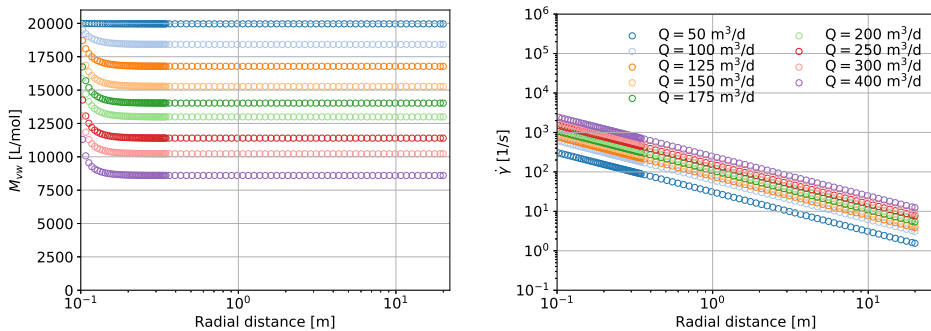


Fig. 7 Left plot: Polymer molar volume in the water phase as a function of radial distance, for seven different cases where $k = 1 \text{ D}$, at steady-state. The formation thickness was $h = 20 \text{ m}$, and the porosity was $\phi = 0.2$. Note that $r = r_w = 0.1 \text{ m}$ corresponds to the sandface. Right plot: The in-situ shear rate profile.

In figure 8, we have included plots to show how the apparent aqueous phase viscosities (left plot) and water pressures (right plot) change with distance from the injector. Close to the well, we see that η can be large, on the order of 100 cp for most cases, but it quickly declines with distance away from the injector, and it reaches values between 4 and 7 cp a metre from the well. After this the apparent viscosity starts to increase again. This happens within the first metre of the reservoir when $Q = 50 \text{ m}^3 \text{ d}^{-1}$ case, and slightly further out from the well in the remaining cases. In the former situation, the shear rate quickly drops below 50 s^{-1} , which is in the shear thinning region. For higher flow rates, the polymer exhibits shear thickening behaviour further out from the well than in the lowest flow rate case. However, due to the rapid

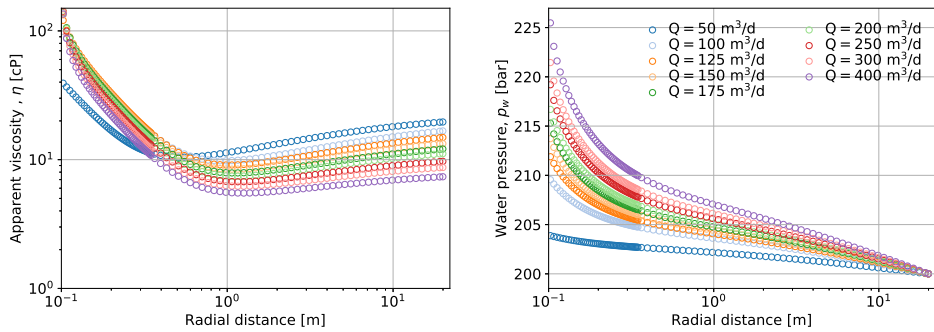


Fig. 8 Left plot: Apparent viscosity as a function of radial distance, for seven different cases where $k = 1D$, at steady-state. The formation thickness was $h = 20$ m, and the porosity was $\phi = 0.2$. Note that $r = r_w = 0.1$ m corresponds to the sandface. Right plot: Pressure in the water phase.

degradation that happens near the well, the critical shear rate for the onset of thickening is greatly increased as M_w is decreased (figure 9). For instance, in the case with $Q = 400 m^3 d^{-1}$ (57.0 % degradation), the shear rate at $r \approx 1.6$ m is $\dot{\gamma} \approx 153 s^{-1}$, which would be in the shear thickening region if the polymer had not been degraded. But, because of the degradation that has already occurred at this stage, the polymer is actually predicted to be shear thinning at this distance. This can clearly be seen from figure 9 (vertical, dashed line), where we have compared the model predicted in-situ rheology for some of the polymers that were produced, assuming $c_p = 1500$ ppm.

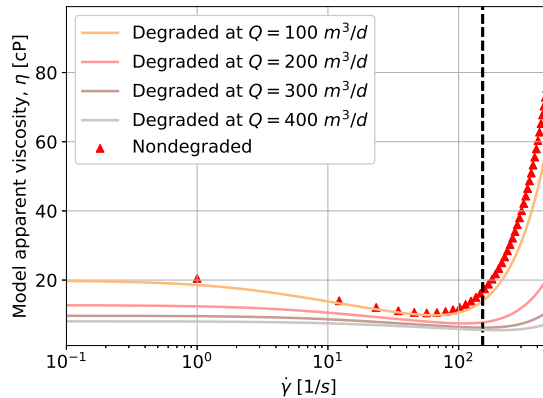


Fig. 9 Model predicted apparent viscosity of a 1500 ppm polymer solution as a function of in-situ shear rate, for various values of the molecular weight M_w . Specifically, we have considered four of the cases reported in table 3. Also shown for reference is the apparent viscosity of the original, nondegraded polymer (red triangles), and the vertical line intersects the viscosities at $\dot{\gamma} = 153 s^{-1}$ (see discussion in the main text).

Another consequence of figure 9 is that if the same polymer solution were to be reinjected into the reservoir after having been produced, it would experience much less additional degradation. This is in accordance with experimental data (Seright, 1983; Stavland et al., 2010; Zechner et al., 2013). This fact is also illustrated by figure 10, where we have plotted the amount of degradation versus applied injection rate for two different polymer solutions ($k = 1D$):

1. The original, nondegraded polymer, with initial $M_w = 20MDa$
2. A polymer with initial $M_w \approx 10.2MDa$, i.e., corresponding to a polymer that was predegraded at $Q = 300m^3 d^{-1}$ (table 3)

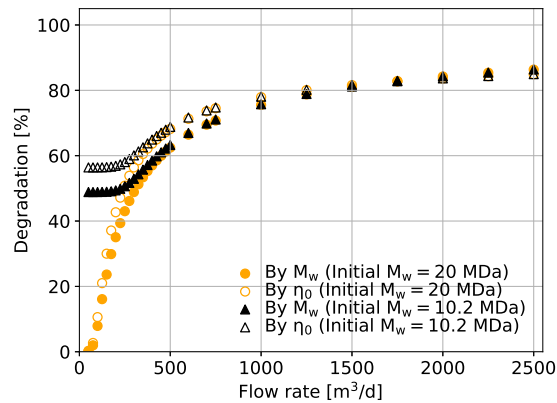


Fig. 10 Degradation at different flow rates for a polymer with initial $M_w = 20MDa$, and a predegraded solution with initial $M_w = 10.2MDa$. The amount of degradation is estimated in two different ways: 1) as a reduction in simulated M_w , and 2) as a reduction in zero shear bulk viscosity, η_0 . In both cases, the amount of degradation is calculated relative to the original, nondegraded polymer with $M_w = 20MDa$.

We observe from figure 10 that if we inject the polymer at rates much higher than $Q = 300m^3 d^{-1}$, there is little difference between the two polymer solutions, although, at these rates, the viscosity loss will obviously be greater than for the rates close to $300m^3 d^{-1}$. For lower injection rates, differences in molecular weight and viscosity become more pronounced, because the polymer solution with initial $M_w = 20MDa$ experienced negligible degradation at these rates. These differences are further illustrated in figure 11. In the left plot, we display the relative increase in $\Delta p = p_w - p_e$ if one uses the nondegraded polymer as opposed to the predegraded one. In the right plot, we show the model predicted apparent viscosity in the last grid block, for the two choices of initial polymer. The figure reveals that, for flow rates close to $300m^3 d^{-1}$, the lower molecular weight polymer has better injectivity, but also that the apparent viscosity at long distances from the well is more or less the same for the two polymers.

A practical implication of this is that, for a given reservoir, it may not always be the best option to select the polymer with the highest possible molecular weight. Instead, by employing a lower molecular weight polymer one may obtain a better injectivity, while at the same time keep a similar EOR potential.

4.4 Further well injectivity discussion

When it comes to potential applications of polymer flooding, concerns are often raised about well injectivity (Seright et al., 2008; Seright, 2010; Glasbergen et al., 2015; Sheng et al., 2015). One worry is that the polymer may partly plug the

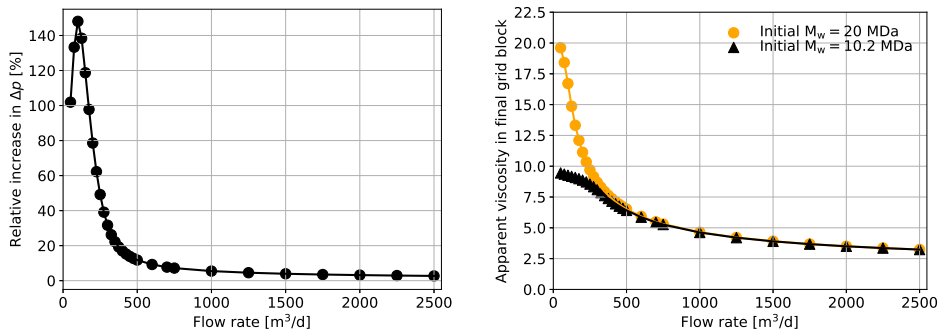


Fig. 11 Left plot: The relative increase in pressure drop across the radial grid, when using the nondegraded polymer as opposed to the polymer that was previously degraded at $Q = 300 \text{ m}^3 \text{ d}^{-1}$. Right plot: The corresponding model predicted apparent viscosities in the last grid block of the radial grid, i.e., at $r \approx r_e$.

reservoir, which may happen if there is debris left in the solution from the manufacturing process, or if the dimensions of the macromolecules are on the same order of magnitude as the typical pore sizes of the rock. For the polymer studied in this work ($M_w = 20 \text{ MDa}$), the latter issue could cause problems at the lowest permeabilities investigated.

The above concerns are usually addressed as part of reservoir screening and pre-injection preparations. As such, the main issue to consider is the expected increase in pressure required to inject a polymer solution into the reservoir, compared with the base case of ordinary waterflooding. This is especially critical for high molecular weight, viscoelastic polymer types, because they have the potential to induce larger resistance factors than polymers which are primarily shear thinning (e.g., xanthan). Operators are naturally concerned with whether polymer can be injected at flow rates that are economically feasible. However, despite frequent worries, practical experience from fields flooded with polymers have often been positive, with reported well injectivities tending to be larger than anticipated. The standard explanation for this is that many wells are likely to be fractured. It is known that even for many ordinary waterflooding projects, fractures are likely to be opened during injection (van den Hoek et al., 2008). For several recent field cases, the existence of fractures has been inferred, e.g., at the Daqing oilfield in China (Wang et al., 2008, 2009), at the Tambaredjo field in Suriname (Let et al., 2012; Manichand et al., 2013), and at the Matzen field northeast of Vienna (Gumpfenberger et al., 2012; Zechner et al., 2015; Clemens et al., 2016; Lueftenecker et al., 2016).

Based on the above considerations, it is clear that if fracturing the formation is accepted, and if the extent of the fractures can be controlled so as to not negatively impact the oil recovery, it will be beneficial for the polymer flooding process (Seright et al., 2008). When fractures are present, it is not unrealistic to imagine that the fluid velocity can decrease by as much as two orders of magnitude (Let et al., 2012). This will go a long way to alleviate the problems associated with strong shear thickening behaviour and polymer mechanical degradation in the near well region. On the other hand, if injectivity is good, care still has to be taken so as to not increase the flow rate by too much.

If the opening of fractures is not accepted, well injectivity is obviously going to be reduced when polymer flooding is performed. However, we have seen that if sufficient amounts of degradation occur, the effective viscosity will rapidly drop as the solution travels through the first few centimetres of the formation. Consequently, the additional flow resistance imparted by the polymer solution will not be as high as one might fear, based on the apparent shear thickening fluid rheology alone. To illustrate this more clearly, we performed additional simulations with only certain parts of the polymer model activated. For the $k = 1 \text{ D}$ cases documented in table 3, we reran all the simulations twice. First, we assumed that the in-situ polymer rheology could be adequately described as purely shear thinning, i.e., shear thickening

and degradation was neglected. Next, we included both flow regimes, but set the degradation rate to zero. The resulting steady-state pressures were plotted versus applied flowrate, and the different approaches were compared, see figure 12.

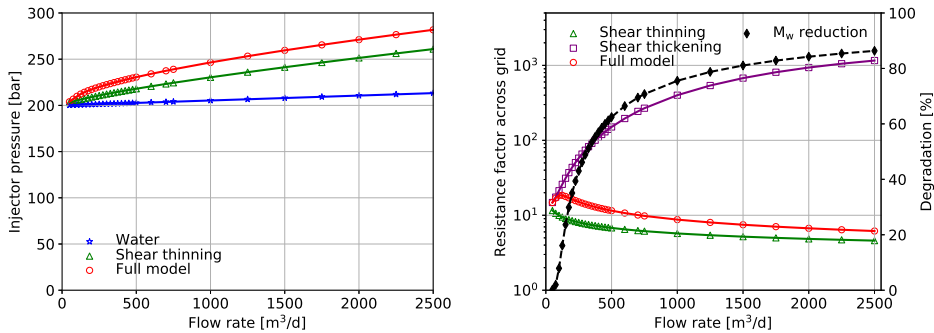


Fig. 12 Left plot: Steady-state pressure at the injection well, for the various employed flowrates at $k = 1$ D, and assuming two different polymer rheology models: 1) the full model (with degradation), and 2) a shear thinning model. Also shown are calculated steady-state pressures for ordinary water injection at the same rates. Right plot, left axis: Resistance factors across the whole simulation model, for three different assumed polymer rheology models. The purple squares represent the case when the shear thickening model is activated, but with the degradation rate set to zero. Right plot, right axis: The percentage reduction in molecular weight of the polymer that was produced at $r = r_e$, for the case when the full model was run, i.e., corresponding to the red circles.

When using the full model, figure 12 shows that, in most considered cases, the pressure drop could be expected to increase by a factor ~ 1.5 compared with the shear thinning polymer model. For rates in the lower end of the degradation regime, the difference was larger (here, close to a factor ~ 2). When using the shear thickening model without degradation, extremely high resistance factors were predicted, and the purple curve in figure 12 (right plot) illustrates well why it is necessary to include in some way the effects of polymer degradation in the simulations. In the polymer modelling literature, previous workers who have implemented shear thickening behaviour, but not degradation, have set an upper limit for the apparent viscosity, see, e.g., (Delsbad et al., 2008) and (Sharma et al., 2011).

5 Summary and conclusions

To sum up, we have applied our previously developed polymer flooding simulator to a series of synthetic cases in a radial geometry. The purpose of these simulations was to investigate how the model predicts the in-situ rheology of the polymer in the vicinity of an unfractured, vertical injection well. In particular, we have focused on the amount of mechanical degradation that can be expected near the injector. The model used in this paper has been history matched to lab data, and it is therefore expected that our predictions could be quite realistic.

Before concluding we should point out some limitations of the current work. First, as mentioned earlier, permeability reduction due to polymer adsorption has not been taken into account. If this mechanism is significant near the well, additional degradation must be expected. Second, the brine that was used was the synthetic sea water (SSW) employed in our previous study, and reported by Stavland et al. (2010). We have not considered how varying the ionic composition of the brine may alter the amount of polymer degradation. Third, we have not considered effects of rock heterogeneity on degradation, and we have only considered steady-state behaviour. The simulations were performed at isothermal conditions ($T = 20^\circ\text{C}$). Finally, we re-iterate that all simulations were conducted using history matched input parameters for a single polymer type. However, similar analyses could be made with other polymers as well.

Based on our simulation results, some main observations are:

- A very fine grid is needed in order to accurately simulate the degradation process. This makes it difficult to upscale results from the lab to the field. However, we have developed several analytical formulas and numerical integration routines which may be used to assess more rapidly the expected amount of degradation
- In the absence of fractures, the amount of polymer mechanical degradation can become significant, even for high permeability reservoirs (e.g., table 3). As a case in point, significant mechanical degradation was reported following the recent polymer injection at the offshore Dalia field (Morel et al., 2015). The observed viscosity reduction was higher than anticipated, and this was attributed to formation damage induced by re-injecting low quality produced water. However, if the model results in this paper are to be believed, the viscosity loss is expected to be large even at a permeability of 1 D, which is close to the reported average permeability of the field
- Mechanical degradation can be greatly reduced by lowering the injection rate. For the polymer investigated here, degradation levels are predicted to be relatively low as long as the shear rate close to the well can be kept on the order of $\mathcal{O}(10^3) \text{ s}^{-1}$, or smaller (figure 5). However, for a specific shear rate there is considerable scatter in the simulated M_w values. The model predicts more degradation at lower permeabilities than what is suggested by a simple scaling with shear rate alone
- The value of resistance factors at the field scale cannot simply be extrapolated from corresponding shear thickening viscosities at the core scale. This is because of the radial geometry that was employed in the near well simulations, as opposed to the linear geometry used in the core floods. Also, if near well degradation is neglected, the predicted well pressures become unrealistically high
- It need not always be the best option to select the polymer with the highest possible M_w (for a given reservoir). Instead, if the polymer is expected to undergo some degradation anyway, a lower molecular weight polymer may provide similar viscosifying ability, but at the benefit of requiring a lower injection pressure

6 Suggested future work

In order for the model to be applied to realistic field cases, some sort of upscaling procedure or effective model is needed. Since mechanical degradation and apparent shear thickening are only important near the wells, on the field scale we only need to take the full model into account for the well blocks. That is, we require to be able to compute accurate well pressures, and to predict the rheological properties of the polymer leaving or entering the well blocks. Though obtaining an analytical model in the form of an explicit formula does not seem likely, one option could be to assume radial flow near the well and to calculate an effective well block viscosity as, e.g.,

$$\bar{\eta} = \frac{\int_{r_w}^{R_1} \frac{\eta}{r} dr}{\ln(R_1/r_w)},$$

with R_1 being an equivalent radius representing the grid block outer boundary, and where the numerical integration approach presented in the manuscript is used to obtain η as a function of distance. Of course, additional complexities will arise if significant permeability anisotropy is present in the near well zone of the reservoir, for 2-phase flow, and if the inclusion of even more physics is desired, e.g., permeability reduction effects. That said, an approach along the lines sketched above seems like a good way to proceed.

For the rest of the reservoir model, the Newtonian and shear thinning rheologies should suffice to describe the polymer behaviour.

7 Acknowledgements

The authors acknowledge the Research Council of Norway and the industry partners; ConocoPhillips Skandinavia AS, Aker BP ASA, Eni Norge AS, Maersk Oil, a company by Total, Statoil Petroleum AS, Neptune Energy Norge AS,

Lundin Norway AS, Halliburton AS, Schlumberger Norge AS, Wintershall Norge AS, and DEA Norge AS, of The National IOR Centre of Norway for support.

8 Tables

Table 1 Rock and fluid properties used as input parameters for the radial simulations.

Parameter	Value	Unit	Description
r_e	20.0	m	Exterior radius
h	20.0	m	Reservoir thickness
r_w	0.1	m	Well radius
d_{top}	2200	m	Depth below sea surface of reservoir top
p_{ref}	200	bar	Reference pressure, and enforced pressure at $r = r_e$
p_{init}	200	bar	Initial reservoir pressure
T_{init}	20	°C	Initial reservoir temperature
T_{inj}	20	°C	Temperature of injected water
ϕ	0.2		Porosity
ρ_w	1.0	g ml ⁻¹	Water density at reference conditions
C_r	1.0×10^{-5}	bar ⁻¹	Rock compressibility at reference conditions
C_w	4×10^{-5}	bar ⁻¹	Water compressibility at reference conditions
η_s	1.07	cp	Water viscosity at reference conditions
B_w	1.0	m ³ m ⁻³	Water formation volume factor

Table 2 Polymer properties used as input to the simulations. The commercial name of the polymer is 3630S (SNF Floerger).

Parameter	Value	Unit	Description
$[\eta]_{ref}$	3750	ml g ⁻¹	Reference intrinsic viscosity
k'	0.01		First Huggins constant
k''	0.077		Second Huggins constant
M_{w0}	20	MDa	Initial polymer molecular weight
a	0.6		Mark-Houwink exponent
C_p	1500	ppm	Injected polymer concentration
IPV_0	0.1		Inaccessible pore volume (constant part)
C	3.0		Tortuosity used to calculate effective pore radius for polymer
IPV_0	0.1		Inaccessible pore volume (constant part)
α_c	2.0		Parameter used to compute in-situ shear rate
λ_a	0.350	K molJ ⁻¹	Parameter for determining λ_1 (shear thinning model)
λ_b	1.0		Parameter for determining λ_1 (shear thinning model)
a_n	0.063		Parameter for determining n (shear thinning model)
b_n	0.804		Parameter for determining n (shear thinning model)
x	1.0		Fitting parameter in the Carreau-Yasuda model
m_2	1.5		Slope parameter in the elongational viscosity model
x_2	3.0		Fitting parameter in the elongational viscosity model
r_{deg}	1.5×10^{-6}		Rate parameter in degradation model (SI units)
α_d	3.0		Exponent used in degradation model
β_d	1.0		Exponent used in degradation model
N_{De}^*	0.5		Critical Deborah number used in shear thickening model

Table 3 Results for the radial simulations performed at $k = 1$ D, for different applied flow rates, Q . The formation thickness was $h = 20$ m, and both Q and Q/h are displayed in each row of the table, as well as the in-situ shear rate at the sand face, $\dot{\gamma}_w$. Also shown is the percentage loss in model M_w , the percentage loss in zero shear bulk viscosity η_0 , and the steady-state pressure at the injection well, P_{inj} .

Q [m ³ d ⁻¹]	Q/h [m ² d ⁻¹]	$\dot{\gamma}_w$ [s ⁻¹]	M_w reduction [%]	η_0 reduction [%]	P_{inj} [bar]
50	2.5	309.0	0.19	0.27	203.9
75	3.75	463.6	1.96	2.82	206.8
100	5.0	618.1	7.9	11.14	209.8
125	6.25	772.6	16.1	22.06	212.2
150	7.5	927.1	23.63	31.54	214.2
175	8.75	1081.6	29.88	38.99	215.9
200	10.0	1236.2	35.05	44.86	217.4
225	11.25	1390.7	39.36	49.56	218.7
250	12.5	1545.2	43.01	53.39	220.0
275	13.75	1699.7	46.14	56.58	221.3
300	15.0	1854.2	48.87	59.28	222.4
325	16.25	2008.8	51.26	61.59	223.6
350	17.5	2163.3	53.39	63.59	224.6
375	18.75	2317.8	55.29	65.34	225.7
400	20.0	2472.3	57.0	66.89	226.7
425	21.25	2626.8	58.55	68.27	227.7
450	22.5	2781.4	59.97	69.51	228.7
475	23.75	2935.9	61.27	70.63	229.6
500	25.0	3090.4	62.46	71.64	230.6
600	30.0	3708.5	66.43	74.91	234.1
700	35.0	4326.5	69.48	77.32	237.4
750	37.5	4635.6	70.75	78.31	239.0
1000	50.0	6180.8	75.55	81.88	246.5
1250	62.5	7726.0	78.74	84.15	253.2
1500	75.0	9271.2	81.06	85.74	259.5
1750	87.5	10816.4	82.83	86.93	265.5
2000	100.0	12361.6	84.23	87.86	271.1
2250	112.5	13906.8	85.38	88.62	276.6
2500	125.0	15452.0	86.34	89.24	281.8

Table 4 Exponents appearing in Eq. (39).

Base	Exponent	Formula	Value in this paper
Q	a_1	$\alpha_d(1+m) - 1$	6.5
k	a_2	$-0.5(\alpha_d(1+m) + 1)$	-4.25
T	a_3	$-m\alpha_d$	-4.5
ϕ	a_4	$1.5 + 0.5\alpha_d(2n+m-1)$	3.15
$1 - \phi$	a_5	$-(m+n)\alpha_d$	-5.4
$1 - IPV_0$	a_6	$1.5 - 0.5\alpha_d(1+m)$	-2.25
R_k	a_7	$0.5 + 0.5\alpha_d(1+m)$	4.25
r_w	a_8	$2 - \alpha_d(1+m)$	-5.5
h	a_9	$1 - \alpha_d(1+m)$	-6.5
M_{w0}	a_{10}	$\beta_d + \alpha_d(a(1+m) + m)$	10.0
C_p	a_{11}	α_d	3.0

9 Appendix A: Derivation of steady-state molecular weight as a function of distance

For the molar polymer concentration, a mass balance applied to a control volume V with boundary A yields

$$\frac{\partial}{\partial t} \int_V \phi C_{mol} dV + \int_A C_{mol} \mathbf{u}_p \cdot \hat{\mathbf{n}} dA = \int_V \phi \mathcal{R}(C_{mol}) dV, \quad (11)$$

where $\hat{\mathbf{n}}$ is the outward-pointing unit normal vector to the surface element dA , \mathbf{u} is the Darcy velocity in vector form, and $\mathbf{u}_p = \mathbf{u}/(1-IPV_0)$. Dividing by IPV_0 ensures that the correct polymer concentration is transported across the boundary. In differential form, the above equation becomes

$$\frac{\partial(\phi C_{mol})}{\partial t} = -\nabla \cdot (\mathbf{u}_p C_{mol}) + \phi \mathcal{R}(C_{mol}). \quad (12)$$

The reaction term, given in units of pore volume concentration per time, is

$$\mathcal{R}(C_{mol}) = f_{rup} \cdot C_{mol}. \quad (13)$$

At steady-state, the volumetric concentration C_{pol} is constant throughout the radial model. For the molar concentration, we obtain

$$\nabla \cdot (\mathbf{u}_p C_{mol}) = \phi \cdot f_{rup} \cdot C_{mol} \quad (14)$$

For radially symmetric flow we get

$$\frac{1}{r} \cdot \frac{d}{dr} (r u_r C_{mol}) = \phi \cdot f_{rup} \cdot C_{mol} \quad (15)$$

Inserting $u_r = Q/(2\pi r h(1-IPV_0))$ yields

$$\frac{Q}{2\pi h r(1-IPV_0)} \cdot \frac{dC_{mol}}{dr} = \phi \cdot f_{rup} \cdot C_{mol}, \quad (16)$$

and using that $M_w = C_{pol}/C_{mol}$ we obtain

$$\frac{dC_{mol}}{dr} = -\frac{C_{pol}}{M_w^2} \cdot \frac{dM_w}{dr} = \frac{2\pi h r \phi (1-IPV_0)}{Q} \cdot f_{rup} \cdot C_{mol}, \quad (17)$$

from which Eq. (9) follows. For the case of linear 1D geometry, we can repeat the above procedure to obtain an identical kind of formula,

$$\frac{dM_w}{dx} = -\frac{A_I \phi (1-IPV_0)}{Q} \cdot f_{rup} \cdot M_w, \quad (18)$$

where A_I is the constant, cross-sectional area of the core.

10 Appendix B: Approximate analytical formulas for degraded M_w

Consider radial flow outwards from an injector at flow rate Q , in a homogeneous reservoir. Based on the derivations in the previous section we see that at steady-state, the molecular weight as a function of radial distance r must satisfy Eq. (9) in the main text, where f_{rup} is given by Eq. (5). The formula used for apparent viscosity in the simulation model is

$$\begin{aligned}\eta &= \eta_s + (\eta_{sh} - \eta_s) \cdot \eta_{elf} \\ &\approx (\eta_{sh} - \eta_s) \cdot \eta_{elf} \\ &= \eta_s \cdot \eta_{sp,sh} \cdot \eta_{elf} \\ &= \eta_s \cdot \eta_{sp0} \cdot (1 + (\lambda_1 \dot{\gamma})^x)^{-\frac{n}{x}} \cdot (1 + (\lambda_2 \dot{\gamma})^{x_2})^{\frac{m+n}{x_2}},\end{aligned}\quad (19)$$

where $\eta_{sp,sh} = \frac{\eta_{sh}}{\eta_s} - 1$ is the specific viscosity for the shear thinning part of the apparent viscosity, and η_{elf} is the elongational viscosity factor. In the second line we have made an approximation by dropping the solvent viscosity term in the expression for η . The zero shear specific viscosity, η_{sp0} , is calculated from a cubic polynomial in the product of intrinsic viscosity and polymer concentration,

$$\eta_{sp0} = [\eta]C_p + k'[\eta]^2C_p^2 + k''[\eta]^3C_p^3, \quad (20)$$

with the intrinsic viscosity obtained from the molecular weight via the Mark-Houwink equation,

$$[\eta] = K \cdot M_w^a, \quad (21)$$

for constants K and a . In terms of the introduced notation and the approximation introduced above, the viscosity term in (4) becomes

$$\eta^{\alpha_d} \approx \eta_s^{\alpha_d} \cdot \eta_{sp0}^{\alpha_d} \cdot (1 + (\lambda_1 \dot{\gamma})^x)^{-\frac{n\alpha_d}{x}} \cdot (1 + (\lambda_2 \dot{\gamma})^{x_2})^{\frac{(m+n)\alpha_d}{x_2}}. \quad (22)$$

Next, since in the degradation regime $\dot{\gamma} \gg 1$, we assume that

$$(1 + (\lambda_1 \dot{\gamma})^x)^{-\frac{n}{x}} \approx (\lambda_1 \dot{\gamma})^{-n}, \quad (23)$$

and

$$(1 + (\lambda_2 \dot{\gamma})^{x_2})^{-\frac{m+n}{x_2}} \approx (\lambda_2 \dot{\gamma})^{m+n}. \quad (24)$$

The expressions for n , λ_1 and λ_2 are given by, respectively, equations 4, 21 and 30 in (Lohne et al., 2017). We reproduce those equations here:

$$n = n(M_w) = 1 - \frac{1}{1 + (a_n K C_p M_w^a)^{b_n}}, \quad (25)$$

and

$$\lambda_1 = \lambda_1(M_w) = \lambda_a \cdot \frac{\eta_s \eta_{sp0}(M_w) M_w}{C_p T}, \quad (26)$$

and

$$\lambda_2 = \lambda_2(M_w) = \frac{1}{N_{De}^*} \cdot \frac{3}{5R_g} \cdot \frac{\phi}{1-\phi} \cdot \frac{\eta_s K M_w^{a+1}}{T}. \quad (27)$$

In the degradation regime, the main contribution to the viscosity is from the shear thickening part. Hence, to make the analysis tractable we assume in the sequel that n is constant, i.e., independent of M_w . With all these approximations, Eq. (22) reduces to

$$\begin{aligned}\eta^{\alpha_d} &\approx \eta_s^{\alpha_d} \cdot \eta_{sp0}^{\alpha_d} \cdot \lambda_1^{-n\alpha_d} \cdot \lambda_2^{(m+n)\alpha_d} \cdot \dot{\gamma}^{m\alpha_d} \\ &= \eta_s^{\alpha_d} \cdot \eta_{sp0}^{\alpha_d(1-n)} \cdot \left(\frac{\lambda_a \eta_s M_w}{C_p T}\right)^{-n\alpha_d} \cdot \left(\frac{3}{5N_{De}^* R_g} \cdot \frac{\phi}{1-\phi} \cdot \frac{\eta_s K M_w^{1+a}}{T}\right)^{(m+n)\alpha_d} \cdot \dot{\gamma}^{m\alpha_d},\end{aligned}\quad (28)$$

Furthermore, we only include the first term in the expression for η_{sp0} ,

$$\eta_{sp0} \approx f_1(M_w) \equiv K C_p M_w^a. \quad (29)$$

The last two approximations are the boldest, especially Eq.(29), however as we shall see, without them it is not possible to integrate the degradation equation in terms of elementary functions. By combining Eqs. (4), (6), (9), (28), and (29), we obtain

$$\begin{aligned}\frac{dM_w}{dr} &\approx -\frac{2\pi h r \phi (1-IPV_0)}{Q} \cdot (r_{deg} \eta_s K C_p)^{\alpha_d} \cdot \sqrt{\frac{\phi}{2kC}} \cdot \sqrt{R_k(1-IPV_0)} \cdot \left(\frac{\lambda_a \eta_s K}{T}\right)^{-n\alpha_d} \\ &\cdot \left(\frac{3}{5N_{De}^* R_g} \cdot \frac{\phi}{1-\phi} \cdot \frac{\eta_s K}{T}\right)^{(m+n)\alpha_d} \cdot M_w^y \cdot \left(\frac{\Omega}{r}\right)^{\alpha_d(1+m)},\end{aligned}\quad (30)$$

with y given by

$$y = 1 + \beta_d + \alpha_d(a(1+m) + m), \quad (31)$$

and where we have defined Ω as the part of $\dot{\gamma}$ that does *not* depend on r . From Eq. (2), using that $u = Q/2\pi r h$, this means that

$$\Omega = \frac{4\alpha_c Q}{2\pi h \sqrt{8k\phi}} \cdot \sqrt{\frac{R_k}{1-IPV_0}}. \quad (32)$$

By collecting all terms other than M_w and r into a factor ζ , it is seen that we approximate the original problem by the separable ordinary differential equation (ODE)

$$\frac{dM_w}{dr} = -\zeta \cdot M_w^y \cdot r^w, \quad (33)$$

with $w = 1 - \alpha_d(1+m)$. Let r_d be the radius beyond which there is no more, or negligible, mechanical degradation. By substituting $\dot{\gamma} = \Omega/r$, and integrating from r_w to r_d , we get

$$\int_{M_{w0}}^{M_{wd}} M_w^{-y} dM_w = \Omega^{1+w} \zeta \cdot \int_{\dot{\gamma}_w}^{\dot{\gamma}_d} \frac{1}{\dot{\gamma}^{2+w}} d\dot{\gamma}, \quad (34)$$

where $M_{wd} = M_w(r_d)$ is the steady-state molecular weight far away from the injection well, and M_{w0} is the initial molecular weight. From this it immediately follows that

$$\frac{1}{1-y} \cdot (M_{wd}^{1-y} - M_{w0}^{1-y}) = \frac{-\Omega^{1+w} \zeta}{1+w} \cdot (\dot{\gamma}_d^{-(1+w)} - \dot{\gamma}_w^{-(1+w)}). \quad (35)$$

By virtue of the definition of r_d , the shear rate $\dot{\gamma}_d$ will be negligible compared with $\dot{\gamma}_w$. Thus, as a final approximation, we will assume $\dot{\gamma}_d^{-(1+w)} \approx 0$. This is justified by comparing with the actual simulation results in the radial grid. Finally, by performing the necessary algebraic manipulations, one can show that

$$\frac{M_{wd}}{M_{w0}} \approx \frac{1}{(1 + (y-1)\chi_r)^{\frac{1}{y-1}}}, \quad (36)$$

where χ_r is the following complicated expression:

$$\chi_r = \chi_0 \cdot (1 - IPV_0) \cdot R_k \cdot \frac{\phi^{1+(m+n)\alpha_d}}{(1-\phi)^{(m+n)\alpha_d}} \cdot C_p^{\alpha_d} \cdot T^{-m\alpha_d} \cdot r_w \cdot M_{w0}^{y-1} \cdot \frac{\gamma_w^{\alpha_d(1+m)-1}}{k}, \quad (37)$$

with

$$\chi_0 = \frac{\alpha_c}{\sqrt{C}} \cdot \frac{1}{\alpha_d(1+m) - 2} \cdot r_{deg}^{\alpha_d} \cdot \lambda_d^{-n\alpha_d} \cdot \left(\frac{3}{5N_{De}^* R_g}\right)^{(m+n)\alpha_d} \cdot (\eta_s K)^{\alpha_d(1+m)}. \quad (38)$$

For the particular choice of model parameters used in this paper (tables 1 and 2), we find that $\chi_r \propto \frac{\gamma_w^{6.5}}{k}$. By inserting the definition of γ_w , and collecting equal terms, one can further reduce (37) to

$$\chi_r = \chi_0 \cdot \left(\frac{\alpha_c}{\sqrt{2\pi}}\right)^{\alpha_d(1+m)-1} \cdot Q^{a_1} \cdot k^{a_2} \cdot T^{a_3} \cdot \phi^{a_4} \cdot (1-\phi)^{a_5} \cdot (1-IPV_0)^{a_6} \cdot R_k^{a_7} \cdot r_w^{a_8} \cdot h^{a_9} \cdot M_{w0}^{a_{10}} \cdot C_p^{a_{11}}, \quad (39)$$

with the exponents given in table 4. We remark that the temperature dependence is not fully captured by the T -term in Eq.(39), as we also have $\eta_s = \eta_s(T)$ and $K = K(T)$ in the term χ_0 . For very large χ_r , Eq. (36) becomes

$$\frac{M_{wd}}{M_{w0}} \approx ((y-1) \cdot \chi_r)^{-\frac{1}{y-1}} \quad (40)$$

11 Appendix C: Alternative approximate equations

Returning to Eq. (28), let us approximate η_{sp0} in a different way than in the development of Eq. (36). Let R denote the ratio between the alternative formula and the original one, i.e.,

$$R \equiv \frac{\eta_{sp0}}{f_1} = \frac{\eta_{sp0}}{KC_p M_w^a}. \quad (41)$$

Then, from Eq. (28) it is clear that the right-hand side of Eq. (33) must be multiplied by a factor $R^{\alpha_d(1-n)}$. Equivalently, when integrating the M_w and r terms, the integrand on the left-hand side of Eq.(34) must be multiplied by a factor $R^{\alpha_d(n-1)}$.

11.1 Power-law

If the factor R is proportional to a power of M_w , the integration can be performed in exactly the same way as before, and we end up with the same kind of formula as (36). The only difference is that the definition of χ_r must be modified with an extra prefactor, in addition to changing the exponent y . For instance, we can assume that $\eta_{sp0} \approx f_3$, where f_3 is the third order term in Eq. (20). An example of using the latter assumption is shown in the left plot of figure 4 (green curve).

11.2 Including both the first *and* the third order term in η_{sp0}

Another possibility is to improve the approximation of the cubic formula by only disregarding the quadratic term (which makes the smallest contribution). In this case, we get

$$R^{\alpha_d(1-n)} = \frac{f_1 + f_3}{f_1} = 1 + \frac{f_3}{f_1} = 1 + k'' K^2 C_p^2 M_w^{2a},$$

resulting in the approximate equation

$$\int_{M_{w0}}^{M_{wd}} (1 + BM_w^{2a})^{\alpha_d(n-1)} \cdot M_w^{-y} dM_w = \Omega^{1+w} \zeta \cdot \int_{\dot{\gamma}_w}^{\dot{\gamma}_d} \frac{1}{\dot{\gamma}^{2+w}} d\dot{\gamma}, \quad (42)$$

with $B = k'' K^2 C_p^2$. Substituting $u = B \cdot M_w^{2a}$, we transform the integral on the left-hand side to

$$\frac{B^{\frac{y-1}{2a}}}{2a} \int_{u_0}^{u_d} (1+u)^C \cdot u^D du$$

with $C = (n-1)\alpha_d$, $D = (1-y-2a)/2a$, $u_0 = B \cdot M_{w0}^{2a}$, and $u_d = B \cdot M_{wd}^{2a}$. This definite integral may be expressed in terms of the Gaussian hypergeometric function ${}_2F_1$,

$$\frac{B^{\frac{y-1}{2a}}}{2a} \cdot \frac{u^{D+1} \cdot {}_2F_1(-C, D+1; D+2; -u)}{D+1} \Bigg|_{u_0}^{u_d},$$

The left-hand side of equation (42) now becomes

$$\frac{M_w^{1-y} \cdot {}_2F_1((1-n)\alpha_d, \frac{1-y}{2a}; (2a-y+1)/2a; -BM_w^{2a})}{1-y} \Bigg|_{M_{w0}}^{M_{wd}}.$$

If we denote the hypergeometric function evaluated at the upper and lower limits by, respectively, \mathcal{F}_d and \mathcal{F}_0 , we obtain the following approximate relationship:

$$M_{wd}^{1-y} \cdot \mathcal{F}_d - M_{w0}^{1-y} \cdot \mathcal{F}_0 \approx \frac{(1-y)\Omega^{1+w}\zeta}{1+w} \cdot \dot{\gamma}_w^{-(1+w)}. \quad (43)$$

To isolate M_{wd} we need to compute the inverse of ${}_2F_1$, which we do by numerically solving the implicit equation (43).

12 Appendix D: Numerical integration

As documented in the main text, the use of Eq. (36) underestimates the amount of degradation. This is in large part due to neglecting the third-order term in Eq. (20). The assumption of a constant Carreau-Yasuda exponent n also explains a part of the discrepancy between simulation and calculation. This can be verified by performing numerical integration of Eq. (9). Tracing through the various definitions, one can show that the integral we need to solve is

$$\frac{dM_w}{dr} = -\frac{2\pi h\phi(1-IPV_0)\Omega^{\alpha_d}}{Q\sqrt{2C}} \cdot \sqrt{\frac{\phi}{k}} \cdot \sqrt{R_k(1-IPV_0)} \cdot (r_{deg}\eta_s)^{\alpha_d} \cdot r^{1-\alpha_d} \cdot \eta_r^{\alpha_d} \cdot M_w^{1+\beta_d}, \quad (44)$$

where the relative apparent viscosity η_r is given by

$$\eta_r = 1 + \eta_{sp0} \cdot (1 + (\lambda_1 \dot{\gamma})^x)^{-n/x} \cdot (1 + (\lambda_2 \dot{\gamma})^{x_2})^{(m+n)/x_2}. \quad (45)$$

Numerical integration was performed using Python's *odeint* function, which is essentially a wrapper to the LSODA solver in the FORTRAN library odepack. According to the online documentation (SciPy.org, 2018), the integrator switches automatically between nonstiff (Adams) and stiff (backwards differentiation formulas, BDF) methods, depending on information available at the end of each integration step. See, e.g., Petzold (1983) for more details regarding this method.

13 Appendix E: Linear geometry, and approximate scaling relationships

The procedure used to derive Eqs.(36) and (44) may also be applied to the case of linear 1D geometry by using Eq. (18). Let M_{wL} denote the steady-state molecular weight at $x = L$. By making the same assumptions as before, one can show that

$$\frac{M_{wL}}{M_{w0}} \approx \frac{1}{(1 + (y-1)\chi_l)^{\frac{1}{y-1}}}, \quad (46)$$

where χ_l is similar to χ_r (not shown here). As a further test of the derived analytical expressions, we conducted a new series of simulations, this time in linear geometry at the core scale. For each simulation, the core permeability was chosen to be the same as in a corresponding radial case, and the flow rate was selected so that $\dot{\gamma}_l = \dot{\gamma}_w$, where $\dot{\gamma}_l$ is the in-situ shear rate in the core. The $L = 7$ cm core was discretized into 100 grid blocks, i.e., with a constant grid spacing $\Delta x = 0.7$ mm. Figure 13 shows a comparison between the numerical integration results, and values obtained from the explicit first order formula and the simulations. As discussed in the main text, the approximate formulas tend to overpredict M_w . For the core scale simulations, very good agreement between simulation and numerical integration was obtained, the maximal relative error being less than 1 %.

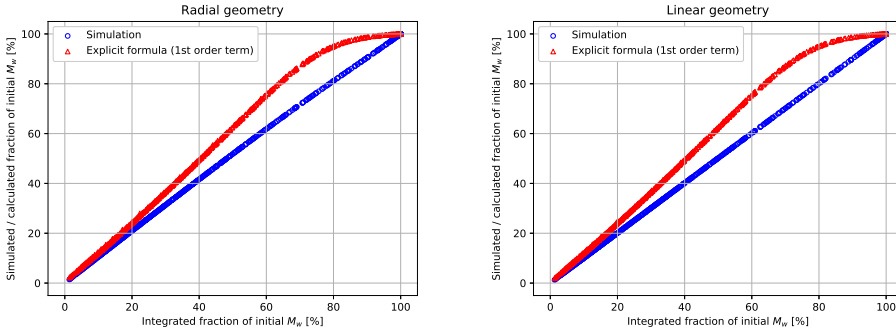


Fig. 13 Left plot: Simulated and calculated molecular weight at the exterior grid boundary, plotted versus the exact solution (numerical integration, Eq.(44)). The red triangles are obtained from the analytical formula, Eq.(36), while the blue circles represent the simulations. Right plot: Simulated and calculated molecular weight at the core effluent for a series of linear simulations, plotted versus the exact solutions.

Note that under the assumptions used to derive Eq. (46), the model predicts an approximate power-law scaling for M_w as a function of distance in linear flow, all else being equal. Specifically, if the constant 1 can be neglected in the denominator, we have

$$\frac{M_{wL}}{M_{w0}} \propto L^\omega, \quad (47)$$

with $\omega = 1 - \gamma = -0.1$ in the present case. If approximating η_{sp0} with the third order term rather than the first order term (section 11.1), a slightly different exponent is obtained, but power-law scaling was seen for all considered cases in which degradation was substantial.

References

- Åsen, S.M., Stavland, A., Strand, D. and Hiorth, A. [2018] An Experimental Investigation of Polymer Mechanical Degradation at cm and m Scale. In: *SPE Improved Oil Recovery Conference*. Society of Petroleum Engineers.
- Bird, R.B., Armstrong, R.C., Hassager, O. and Curtiss, C.F. [1977] *Dynamics of polymeric liquids*, 1. Wiley, New York.
- Cannella, W., Huh, C. and Seright, R. [1988] Prediction of xanthan rheology in porous media. In: *SPE annual technical conference and exhibition*. Society of Petroleum Engineers.
- Carrayrou, J., Mosé, R. and Behra, P. [2004] Operator-splitting procedures for reactive transport and comparison of mass balance errors. *Journal of Contaminant Hydrology*, **68**(3-4), 239–268.
- Chauveteau, G. and Moan, M. [1981] The onset of dilatant behaviour in non-inertial flow of dilute polymer solutions through channels with varying cross-sections. *Journal de Physique Lettres*, **42**(10), 201–204.
- Chauveteau, G., Moan, M. and Magueur, A. [1984] Thickening behaviour of dilute polymer solutions in non-inertial elongational flows. *Journal of non-newtonian fluid mechanics*, **16**(3), 315–327.
- Clemens, T., Lueftenegger, M., Laoroongroj, A., Kadnar, R. and Puls, C. [2016] The Use of Tracer Data To Determine Polymer-Flooding Effects in a Heterogeneous Reservoir, 8 Torton Horizon Reservoir, Matzen Field, Austria. *SPE Reservoir Evaluation & Engineering*.
- Delshad, M., Kim, D.H., Magbagbeola, O.A., Huh, C., Pope, G.A. and Tarahhom, F. [2008] Mechanistic interpretation and utilization of viscoelastic behavior of polymer solutions for improved polymer-flood efficiency. In: *SPE Symposium on Improved Oil Recovery*. Society of Petroleum Engineers.
- Fletcher, A., Flew, S., Lamb, S., Lund, T., Bjornestad, E., Stavland, A. and Gjovikli, N. [1991] Measurements of polysaccharide polymer properties in porous media. In: *SPE International Symposium on Oilfield Chemistry*. Society of Petroleum Engineers.
- Glasbergen, G., Wever, D., Keijzer, E. and Farajzadeh, R. [2015] Injectivity loss in polymer floods: causes, preventions and mitigations. In: *SPE Kuwait Oil and Gas Show and Conference*. Society of Petroleum Engineers.
- Gumpenberger, T., Deckers, M., Kornberger, M. and Clemens, T. [2012] Experiments and simulation of the near-wellbore dynamics and displacement efficiencies of polymer injection, Matzen Field, Austria. In: *Abu Dhabi International Petroleum Conference and Exhibition*. Society of Petroleum Engineers.
- Herzer, J. and Kinzelbach, W. [1989] Coupling of transport and chemical processes in numerical transport models. *Geoderma*, **44**(2-3), 115–127.
- van den Hoek, P.J., Al-Masfry, R.A., Zwarts, D., Jansen, J.D., Hustedt, B. and van Schijndel, L. [2008] Waterflooding Under Dynamic Induced Fractures: Reservoir Management and Optimisation of Fractured Waterfloods. In: *SPE Symposium on Improved Oil Recovery*. Society of Petroleum Engineers.
- Howe, A.M., Clarke, A. and Giernalczyk, D. [2015] Flow of concentrated viscoelastic polymer solutions in porous media: effect of MW and concentration on elastic turbulence onset in various geometries. *Soft Matter*, **11**(32), 6419–6431.
- Hundsdoerfer, W. and Verwer, J. [1996] Numerical solution of advection-diffusion-reaction equations. *CWI Report NMN9603, Centrum voor Wiskunde en Informatica, Amsterdam*, **24**, 30.
- Kaminsky, R.D., Wattenbarger, R.C., Szafranski, R.C. and Coutee, A. [2007] Guidelines for polymer flooding evaluation and development. In: *International petroleum technology conference*. International Petroleum Technology Conference.
- Lantz, R. [1971] Quantitative evaluation of numerical diffusion (truncation error). *Society of Petroleum Engineers Journal*, **11**(03), 315–320.
- Let, M.S., Priscilla, K., Manichand, R.N. and Seright, R.S. [2012] Polymer Flooding a ~ 500-cp Oil. In: *SPE Improved Oil Recovery Symposium*. Society of Petroleum Engineers.
- Levitt, D.B., Slaughter, W., Pope, G. and Jouenne, S. [2011] The effect of redox potential and metal solubility on oxidative polymer degradation. *SPE Reservoir Evaluation & Engineering*, **14**(03), 287–298.
- Lohne, A., Nødland, O., Stavland, A. and Hiorth, A. [2017] A model for non-Newtonian flow in porous media at different flow regimes. *Computational Geosciences*, **21**(5-6), 1289–1312.

- Lueftenegger, M., Kadnar, R., Puls, C. and Clemens, T. [2016] Operational Challenges and Monitoring of a Polymer Pilot, Matzen Field, Austria. *SPE Production & Operations*.
- Maerker, J. [1975] Shear degradation of partially hydrolyzed polyacrylamide solutions. *Society of Petroleum Engineers Journal*, **15**(04), 311–322.
- Maerker, J. [1976] Mechanical degradation of partially hydrolyzed polyacrylamide solutions in unconsolidated porous media. *Society of Petroleum Engineers Journal*, **16**(04), 172–174.
- Manichand, R.N., Let, M.S., Kathleen, P., Gil, L., Quillien, B. and Seright, R.S. [2013] Effective propagation of HPAM solutions through the Tambaredjo reservoir during a polymer flood. *SPE Production & Operations*, **28**(04), 358–368.
- Morel, D., Zaugg, E., Jouenne, S., Danquigny, J. and Cordelier, P. [2015] Dalia/Camelia Polymer Injection in Deep Offshore Field Angola Learnings and in Situ Polymer Sampling Results. In: *SPE Asia Pacific Enhanced Oil Recovery Conference*. Society of Petroleum Engineers.
- Nødland, O.M., Lohne, A., Stavland, A. and Hiorth, A. [2016] A Model for Non-Newtonian Flow in Porous Media at Different Flow Regimes. In: *ECMOR XV-15th European Conference on the Mathematics of Oil Recovery*.
- Petzold, L. [1983] Automatic selection of methods for solving stiff and nonstiff systems of ordinary differential equations. *SIAM journal on scientific and statistical computing*, **4**(1), 136–148.
- Ryles, R. [1988] Chemical stability limits of water-soluble polymers used in oil recovery processes. *SPE reservoir engineering*, **3**(01), 23–34.
- SciPy.org [2018] `scipy.integrate.LSODA`. <https://docs.scipy.org/doc/scipy/reference/generated/scipy.integrate.LSODA.html>. Accessed: 2018-04-09.
- Seright, R. [2010] Potential for polymer flooding reservoirs with viscous oils. *SPE Reservoir Evaluation & Engineering*, **13**(04), 730–740.
- Seright, R. and Skjevrak, I. [2014] Effect of Dissolved Iron and Oxygen on Stability of HPAM Polymers. In: *SPE Improved Oil Recovery Symposium*. Society of Petroleum Engineers.
- Seright, R.S. [1983] The effects of mechanical degradation and viscoelastic behavior on injectivity of polyacrylamide solutions. *Society of Petroleum Engineers Journal*, **23**(03), 475–485.
- Seright, R.S., Seheult, J.M. and Talashek, T. [2008] Injectivity characteristics of EOR polymers. In: *SPE annual technical conference and exhibition*. Society of Petroleum Engineers.
- Sharma, A., Delshad, M., Huh, C. and Pope, G.A. [2011] A practical method to calculate polymer viscosity accurately in numerical reservoir simulators. In: *SPE Annual Technical Conference and Exhibition*. Society of Petroleum Engineers.
- Sheng, J.J., Leonhardt, B. and Azri, N. [2015] Status of polymer-flooding technology. *Journal of Canadian Petroleum Technology*, **54**(02), 116–126.
- Standnes, D.C. and Skjevrak, I. [2014] Literature review of implemented polymer field projects. *Journal of Petroleum Science and Engineering*, **122**, 761–775.
- Stavland, A., Jonsbroten, H., Lohne, A., Moen, A. and Giske, N. [2010] Polymer Flooding–Flow Properties in Porous Media Versus Rheological Parameters. In: *Presented at the 72nd EAGE Conference and Exhibition incorporating SPE EUROPEC, SPE-131103-MS*.
- Thomas, A., Gaillard, N. and Favero, C. [2012] Some key features to consider when studying acrylamide-based polymers for chemical enhanced oil recovery. *Oil & Gas Science and Technology–Revue d'IFP Energies nouvelles*, **67**(6), 887–902.
- Wang, D., Dong, H., Lv, C., Fu, X. and Nie, J. [2009] Review of practical experience by polymer flooding at Daqing. *SPE Reservoir Evaluation & Engineering*, **12**(03), 470–476.
- Wang, D., Han, P., Shao, Z., Hou, W. and Seright, R.S. [2008] Sweep-improvement options for the Daqing oil field. *SPE Reservoir Evaluation & Engineering*, **11**(01), 18–26.
- Wreath, D., Pope, G. and Sepehrnoori, K. [1990] Dependence of polymer apparent viscosity on the permeable media and flow conditions. *In Situ;(USA)*, **14**(3).
- Zechner, M., Buchgraber, M., Clemens, T., Gumpenberger, T., Castanier, L.M. and Kovscek, A.R. [2013] Flow of polyacrylamide polymers in the near-wellbore-region, rheological behavior within induced fractures and near-wellbore-area. In: *SPE Annual Technical Conference and Exhibition*. Society of Petroleum Engineers.

Zechner, M., Clemens, T., Suri, A. and Sharma, M.M. [2015] Simulation of Polymer Injection Under Fracturing Conditions-An Injectivity Pilot in the Matzen Field, Austria. *SPE Reservoir Evaluation & Engineering*, **18**(02), 236–249.

Paper VI

Flow of polymer fluids in a dual porosity sand pack: Experiments and simulations

By:

Nødland, Oddbjørn

Ringen, Irene

Löhne, Arild

Stavland, Arne

Hiorth, Aksel

To be submitted (2018).

Flow of polymer fluids in a dual porosity sand pack: Experiments and simulations

Oddbjørn Nødland^{1,2,3} · Irene Ringen^{1,2,3} · Arild Lohne^{1,2} · Arne Stavland^{1,2} · Aksel Hiorth^{1,2,3}

Received: date / Accepted: date

Corresponding author: Oddbjørn Nødland
E-mail: oddbjorn.m.nodland@uis.no

- ¹ The National IOR Centre of Norway
² Norwegian Research Centre AS (NORCE)
³ University of Stavanger

Abstract

The flow of non-Newtonian fluids in porous media is important in medical science (e.g., for understanding blood flow through organs and tissue), and in engineering applications such as drilling, recovery of hydrocarbons, and soil remediation. In this paper, we investigate the transport properties of polymer molecules in the presence of varying salinities, and involving large pore scale heterogeneities. This has practical implications within the field of petroleum science, because polymer flooding and low salinity water injection have independently been proposed as ways to enhance the oil production. By combining the two methods, less chemicals will be needed to obtain a desired target viscosity within the reservoir, which has both economic and environmental benefits. However, before commencing on such a combined injection scheme, an important question to ask is whether the polymer could be transported differently through the reservoir than co-injected ions?

To investigate this question, we present results from corefloods that were performed in an artificially constructed porous medium with multiple levels of porosity. Two different NaCl concentrations were selected to represent, respectively, a high salinity formation water and a low salinity make up brine for the polymer. A novel laboratory setup was designed, that allowed for bulk electrical resistance to be recorded along six successive sections of the core; this provided a measure of how the salinity front moved through the medium. On the other hand, polymer transport was monitored with differential pressure measurements.

Our results clearly show that, though a substantial part of the pore space was inaccessible to the large polymer molecules, it contributed as a source (and sink) of ions, and thus greatly influenced the rheological behavior of the flowing polymer solution. A numerical simulator, IORCoreSim, was used to interpret the findings. The model is capable of describing different rheological flow regimes of the polymer: (i) apparent shear thinning, (ii) shear thickening, and (iii) mechanical degradation. We were able to match both breakthrough of ions at the effluent, as well as the resistance measurements, by using a Multiple-Rate-Mass-Transfer (MRMT) model. Moreover, by making the polymer solution viscosity salinity dependent, we were able to match transient pressure drops across the core. The simulations revealed that the polymer front moved much faster through the medium than the simultaneously injected ions.

Based on our results we can say that, if a porous medium has a significant volume of micro porosity (i.e., pores not accessible for the polymer to flow in), then a pre-flush with a low salinity brine is needed in order for the polymer slug to keep its designated viscosity.

1 Introduction

Polymer flooding is a promising method of enhanced oil recovery (EOR) that has received a lot of attention during the last decades. The rationale for injecting polymer molecules into the reservoir is well known: it lowers the water phase mobility, which can lead to a better sweep, and hence to a more efficient oil production (Sorbie, 1991). However, despite a long term interest in the method, few offshore polymer floods have been reported (Sheng et al., 2015). A major reason for this is the complicated flow behavior of polymeric liquids inside porous media, such as their non-Newtonian character (Bird et al., 1977; Lohne et al., 2017).

Recently, the suitability of various EOR methods for application on 27 fields on the Norwegian Continental Shelf (NCS) was evaluated by experts from Imperial College, London. Their obtained conclusion was that a combination of low salinity waterflooding and polymer injection holds the greatest technical potential (Norwegian Petroleum Directorate, 2018). To be able to simulate such EOR processes accurately, and thus gain more insight into the *practical* feasibility of the method, it is important to understand how the transport behavior of water molecules and ions may differ from that of the polymer. For instance, the macroscopic velocity of polymer molecules may, under certain circumstances, be significantly larger than that of simultaneously injected molecules of smaller size. This difference can become quite pronounced in certain types of porous media, and it has commonly been explained by invoking the notion of *inaccessible pore volume, IPV* (Sorbie, 1991). One way that the IPV phenomenon can come about is when a subset of pores is practically impenetrable to the macromolecules, at least on the time scale of interest (Dawson and Lantz, 1972). Another fact that needs to be accounted for in reservoir simulators is that the rheological behavior of polymer solutions can be very salt-sensitive. This is especially the case for the large molecular weight flexible polymer types that have received the most scrutiny in the experimental petroleum literature.

The goal of this paper was to study the above-mentioned factors in more detail. To this end, we considered a set of corefloods that were performed in sandpicks made up of synthetic silica gel sand. For the experiments in question, the individual sand grains had an internal porous structure, with a significant fraction of the total pore space occupied by intragranular pores on the nanometer scale. Corefloods both with and without polymer were carried out, and two different concentrations of sodium chloride (NaCl) were employed for the initial and injected brines. A novel laboratory setup was designed that allowed for bulk electric resistance to be measured along successive sections of a core, thus providing information about moving salinity fronts within the medium. Other types of experimental datapoints were also gathered: differential pressure recordings and, in one instance, a chloride breakthrough curve. Some of the experimental results have previously been presented at a conference (Ringen et al., 2016). Here, we report more of them, along with a numerical interpretation. For the theoretical work, we made use of an in-house simulator, IORCoreSim, that has been specifically developed to model core scale transport of IOR chemicals in porous media (Lohne, 2017).

The remainder of the paper is organized as follows. We start by describing the laboratory setup in more detail (section 2). Next, we introduce the mathematical approach taken to model the corefloods (section 3). Selected experimental findings are presented in section 4, along with simulation results, and these form the basis for the ensuing discussion in section 5. We end the paper with a summary, and some concluding remarks.

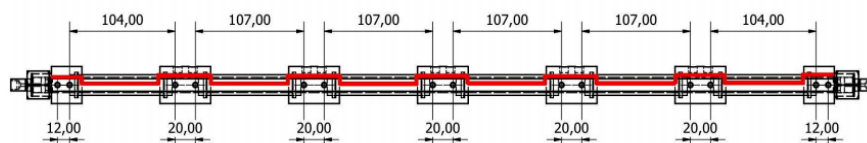


Fig. 1 Resistivity setup. The column consisted of six glass sections connected by metal joints, both of which were in direct contact with the sand and the fluids. The electrical measurements were obtained by using a programmable, automatic RCL meter of type Fluke PM 6304.

2 Experimental design

2.1 Fluids

A synthetic polymer of type Flopaam 5115SH, manufactured by SNF, was used for the experiments. This is an acrylamide-acrylate-ATBS terpolymer with a 15% fraction of ATBS (2-acrylamido-terbutylsulfonic acid). Compared with partially hydrolyzed polyacrylamide (HPAM) polymers, ATBS-based polymers tend to be less sensitive to temperature, as well as more tolerant to salinity effects such as high divalent ion content. They are also less prone to mechanical degradation (Thomas et al., 2012; Stavland et al., 2013).

Table 1 shows the different brines used in this study. The notation introduced in the table will be employed throughout the paper.

2.2 Corefloods

Corefloods were performed in glass columns packed with synthetic mesoporous silica gel sand: Sigma-Aldrich 60741 Fluka, with reported grain particle sizes in the range 63-200 μm , 470-530 m^2g^{-1} surface area, and an internal pore volume of 0.7-0.85 mlg^{-1} sand. The total porosity was estimated from the volume needed to fill the columns with water (after subtracting out the tubing volume). In all cases, it was very high, close to 80%. Based on experimentally determined masses of sand, initial estimates for the column macroporosities were in the range 39-46%, meaning that a substantial fraction of the pore volume was inside the grains.

During any particular coreflood, the column was placed in a vertical position, and brine with or without polymer was injected from the top by employing a Quizix QX-6000 pump (Amatek Chandler Engineering), using a constant flow rate boundary condition. A differential pressure transmitter was set up to record the pressure difference across the column as a function of time. When polymer was injected, an additional pressure transmitter was mounted across a horizontal capillary tube connected to the outlet end, and thus functioned as a rheometer to monitor the effluent polymer viscosity. A backpressure regulator was set up at the end of the system. It was kept at 3 bar.

Resistance measurements were taken across six different portions of the core, and were used for tracking the salinity front. The setup is illustrated in figure 1. Note that in the actual experiments, there were a few variations in the geometry compared to what is indicated by the figure.

Data from two separately packed columns are reported in this paper, hereafter referred to as Column 1 and Column 2, respectively (table 2). The coreflood conducted in Column 1 did not involve polymer. In this experiment, the column was initially filled with a B35 solution, which was subsequently replaced by a lower salinity B10 brine. The flow rate was $Q = 1\text{ ml min}^{-1}$ in the beginning, but was doubled after less than ten minutes. In addition to tracking in-situ electrical resistance, the chloride breakthrough curve was measured by periodically collecting effluent samples, and performing titration with silver nitrate (AgNO_3). More than 2.5 total pore volumes (PVs) of water were injected (i.e., accounting for both inter- and intragranular pores).

Selected experimental results from Column 2 are also provided. Several successive corefloods were performed in this system, both with and without polymer. In the first run through the column, following the initial filling by brine, the

absolute permeability of the medium was estimated. Then followed the injection of a P10 polymer solution to replace a higher salinity B35 solution, at a flow rate of $Q = 0.3 \text{ ml min}^{-1}$. After displacing the B35 brine, polymer injection was continued at a sequence of different flow rates, until more than four PVs had been flooded through the system. For comparison purposes, a second 're-run' polymer injection experiment was also initiated. This second low salinity polymer flood was performed following several periods of flow cessation, and after having flushed out the previously injected polymer for some time. Compared with the first period of P10 injection, the experiment was aborted much more quickly. Only a single flow rate was employed in this case, again 0.3 ml min^{-1} .

3 Mathematical model

IORCoreSim is a standard finite-difference reservoir simulator, implemented using a black-oil type fluid approach, but with extended options to include a variety of EOR mechanisms. Below, we describe aspects of the numerical implementation that were especially relevant for this study.

3.1 Mass transfer model

Fluid transport was modelled in 1D. In the standard IORCoreSim implementation, component transport is described by the classical Advection-Dispersion-Equation (ADE). However, for this work a modification was made to the code by introducing the Multiple-Rate-Mass-Transfer (MRMT) model as an option to describe solute transport. The transport equations used in this approach are (Haggerty and Gorelick, 1995)

$$\frac{\partial(\phi_m C_m)}{\partial t} = \mathcal{L}(C_m) + \sum_{j=1}^{N_{im}} \alpha_j (C_{im}^j - C_m) \quad (1)$$

$$\frac{\partial(\phi_{im}^j C_{im}^j)}{\partial t} = \alpha_j (C_m - C_{im}^j), \quad j = 1, \dots, N_{im}, \quad (2)$$

with the advection-dispersion operator for the mobile domain given by

$$\mathcal{L}(C_m) = \frac{\partial}{\partial z} (\phi_m D_m^* \frac{\partial C_m}{\partial z}) - u \frac{\partial C_m}{\partial z}, \quad (3)$$

and where the meaning of the different terms is provided in table 3. The effective diffusion coefficient D_m^* is a sum of molecular diffusion, and a hydrodynamical dispersion term. Generally, the latter term is a tensor, but for 1D flow it is usually assumed a scalar proportional to the mean advective velocity (Perkins and Johnston, 1963):

$$D_m^* = \frac{D_{mol}}{\tau} + \lambda_{ed} \cdot v. \quad (4)$$

The MRMT model was implemented numerically using operator splitting. At a given transport timestep Δt , first advection and dispersion were handled in the macropores, while ignoring mass exchange with the immobile zones. Then, we set $\mathcal{L}(C_m) = 0$, and Eqs. (1) and (2) were discretized and solved for a set of subtimesteps adding up to Δt .

3.2 Polymer model

A comprehensive model for polymer flooding is available in IORCoreSim, and was used for the theoretical work presented in this paper. A thorough presentation of the polymer model can be found in Lohne et al. (2017). However, we repeat here that in the simulator, the intrinsic viscosity $[\eta]$ of a polymer solution is assumed to scale as

$$[\eta] = [\eta]_{ref} \cdot C_S^{-\alpha_s}, \quad (5)$$

where $[\eta]_{ref} = K \cdot M_w^a$ is a reference value, $C_S = C_m$ is the NaCl concentration (effective salinity), and α_s is a fitting exponent.

Both the depletion layer mechanism and polymer adsorption was neglected in the presented simulations. To represent the polymer size exclusion effect due to microporosity, a different approach was taken than previously (Lohne et al., 2017). Herein, the MRMT model was employed to describe transport of salt, while polymer transport was described by the classical ADE equation, using the porosity ϕ_m of the macropores. Then, the (constant) *IPV* factor becomes

$$IPV = 1 - \frac{\phi_m}{\phi_t}. \quad (6)$$

It is remarked that when the effect of inaccessible pore volume is captured in this way, the apparent shear thickening viscosity predicted by the simulator becomes dependent on IPV . This is because the time constant λ_2 used to compute the elongational viscosity factor becomes a function of the macroporosity. According to Eq. 30 of Lohne et al. (2017):

$$\lambda_2 = \frac{1}{N_{De}^*} \cdot \frac{3}{5R_g} \cdot \frac{\phi_m}{1 - \phi_m} \cdot \frac{\eta_s[\eta]M_w}{T} \propto \frac{\phi_t(1 - IPV)}{1 - \phi_t(1 - IPV)}. \quad (7)$$

It makes intuitive sense that λ_2 should also depend on IPV , because a lower available pore space for polymer will reduce the average residence time of the polymer in the flow field, and thus alter the balance between the polymer relaxation time and residence time.

3.3 Petrophysical model

Bulk electrical conductivity σ_b , and hence resistivity ρ_b , is linked not only to the ionic composition of the pore fluid, but also depends on the structure of the porous medium, such as the degree of pore connectivity, and the sizes and shapes of the grains (Sen et al., 1981; Mendelson and Cohen, 1982). In some situations, flow of electricity at the solid-fluid interface may also play an important role (Revil and Glover, 1997). Here, we will assume that surface conduction can be neglected, and thus we calculate σ_b from Archie's law

$$\sigma_b = \frac{1}{F} \cdot \sigma_f, \quad (8)$$

where σ_f is the fluid conductivity, and F is known as the *formation factor*. In Archie's original empirical work (Archie, 1942), the formation factor was taken as a power-law in porosity, $F = \phi^{-q}$. Fitted exponents are typically found to be in a relatively narrow range close to $q = 2.0$, but higher values have also been reported, particularly for carbonates, which tend to have a less well-connected pore network (Dullien, 1992; Glover, 2009).

For rocks with widely varying pore sizes, such as the presently studied case, the simple form of Archie's law may prove inadequate to describe the effective conductivity of the system. Still, as a first approximation, we have applied Eq. (8), but with the proviso that only the fluid in equilibrium with the macropores conduct electricity.

As a simple way to model the electrical resistance across a section, we assumed the individual grid blocks to contribute in a series resistor fashion. Letting Z_i denote the resistance of section i ($i = 1, 2, \dots, 6$), we then compute

$$Z_i = \sum_{k=n_1^i}^{n_2^i} Z_k = \sum_{k=n_1^i}^{n_2^i} \frac{1}{\sigma_b^k} \cdot \frac{L_k}{A_k}, \quad (9)$$

in which n_1^i and n_2^i are the cell indices of the first and last grid block representing section i , σ_b^k is the bulk conductivity of cell number k , and $L_k = \Delta z$ and $A_k = \Delta x \cdot \Delta y$ are the geometric dimensions of the relevant grid blocks.

Fluid conductivities were computed using an empirical correlation found in the literature (Tiab and Donaldson, 2012). In the concentration range of interest, the formula predicts a linear relationship between σ_f and the NaCl concentration, which is in accordance with experimentally determined fluid conductivities (table 4).

4 Results

This section mainly contains experimental and simulation results; the main discussion of the results will be postponed until section 5.

4.1 Column 1: Low salinity water replacing high salinity water (B35 → B10)

Experimental findings for Column 1 are provided in figures 2 and 3, and are compared with simulations: Figure 2 plots effluent concentrations versus time, while bulk electrical resistance measurements are plotted in figure 3. Both types of data have been normalized, in a way that indicates whether the absolute values increased or decreased during the experiment. This will be the convention throughout the paper, unless otherwise is specifically noted.

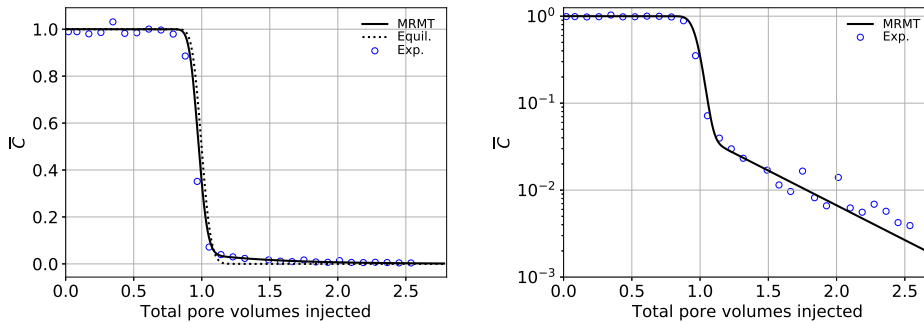


Fig. 2 Normalized effluent NaCl concentration, $\bar{C} = (C_{\text{NaCl}} - C_{\text{inj}})/(C_{\text{init}} - C_{\text{inj}})$, for an experiment without polymer (blue circles). In the left plot, simulation results from both an equilibrium model (dotted lines) and an MRMT model (solid lines) are displayed. In the right plot, the data have been replotted on a logarithmic y-axis, and only the latter simulation profile is shown.

Assuming a macroscopically homogeneous medium, the ionic transport through Column 1 cannot be explained by a single continuum model that accounts for advection and Fickian dispersion (figure 2, dotted line). This is because of the lack of an observed *S*-shape in the effluent concentration profile, which is a defining characteristic of such dispersion processes (Dullien, 1992). For comparison purposes, the NaCl transport was therefore additionally simulated using an MRMT model, in which it was assumed that a small fraction of the intragranular pore volume exchanged mass at a much slower time scale (table 7).

This was also done for the experiments in Column 2. For all simulated curves plotted in this section, the single continuum (equilibrium) model is represented by dotted lines, while MRMT model results are shown as solid lines.

4.2 Polymer rheology

Polymer solutions are non-Newtonian fluids, i.e., with a flow resistance that depends on the local shear rate. When characterized in a rheometer, shear thinning is commonly observed. In IORCoreSim, this behavior is modelled by the Carreau-Yasuda equation (Bird et al., 1977),

$$\eta = \eta_s + (\eta_0 - \eta_s) \cdot (1 + (\lambda_1 \dot{\gamma})^x)^{-n/x}, \quad (10)$$

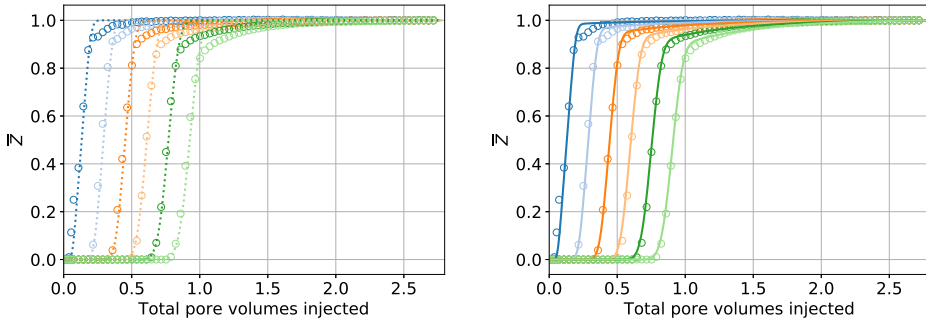


Fig. 3 Normalized bulk resistance, $\bar{Z} = (Z - Z_{init}) / (Z_{inj} - Z_{init})$, for an experiment without polymer (circular scatter points). Left plot: Comparison between experiment and simulation when using the equilibrium model for mass transport (dotted lines). Right plot: Comparison between experiment and simulation when using the MRMT model for mass transport (solid lines).

with η_0 , λ_1 and n further described by the equations presented in Lohne et al. (2017). Moreover, for the polymer employed in this study, the viscosity was clearly sensitive to the ion content of the brine: a lower viscosity was measured when the NaCl concentration increased, which can be understood as due to electrostatic screening of charges distributed along the polymer chain backbone. The shear thinning model was fitted to bulk viscosity data for the end point P10 and P35 brines (figure 4). A single set of input parameters was used to generate both curves; as described previously, the salinity-dependence was captured by computing intrinsic viscosities of the solutions from the respective NaCl concentrations (table 1). The experimental curves show some deviations from the model, especially at low and high shear rates. However, it is often the case that these values are less reliable, due to several experimental artifacts that may occur at such rates (Ewoldt et al., 2015).

Input parameters to the shear thickening part of the IORCoreSim model were selected based on recorded steady-state values of the potential pressure drop across the column, $\Delta P + \rho g L$. These parameters were somewhat more uncertain (see section 5.5).

4.3 Column 2, Experiments 1 and 4: Low salinity polymer replacing high salinity water (B35 \rightarrow P10)

For the two P10 injection experiments, measured pressure drops are shown in figure 5. The left plot only shows ΔP across the column, while the right plot additionally displays the pressure drop ΔP_{cap} across the capillary tube (on a separate y-axis). Resistance data for the initial part of the first polymer flood are exhibited in figure 6. In both figures, simulated profiles are shown as well.

For the polymer floods, the match between model and data was not as good as for ordinary waterflooding. It is noted that the simulated resistance curves started to deflect earlier than the experimental ones. The same kind of behavior was also visible from the ΔP_{cap} signal, in that the calculated pressure drop curve was more spread out at $\sim 1 PV$ than what was observed (figure 5, right plot).

4.4 Column 2, Experiment 3: High salinity water replacing low salinity water (B10 \rightarrow B35)

Subsequent to the first polymer flood, a duration of B10 injection followed, after which the core was again filled with B35 brine. This was done to prepare for the second polymer flood (i.e., the orange curves in figure 5). Figure 7 shows

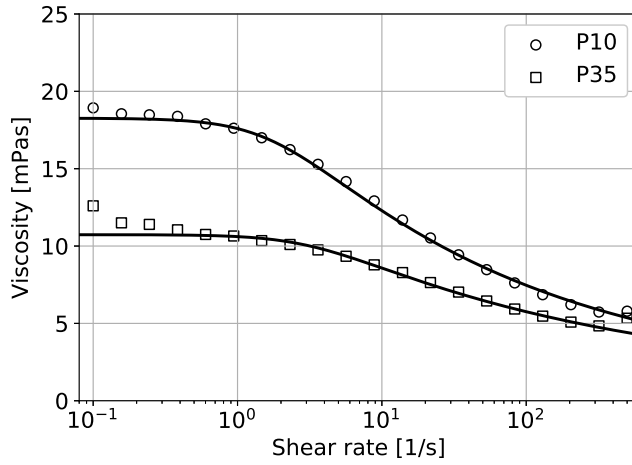


Fig. 4 Polymer bulk viscosity measured in a rotational cone-and-plate rheometer (Anton Paar Physica MCR301). The solid lines represent the IORCoreSim simulation model (shear thinning apparent viscosity).

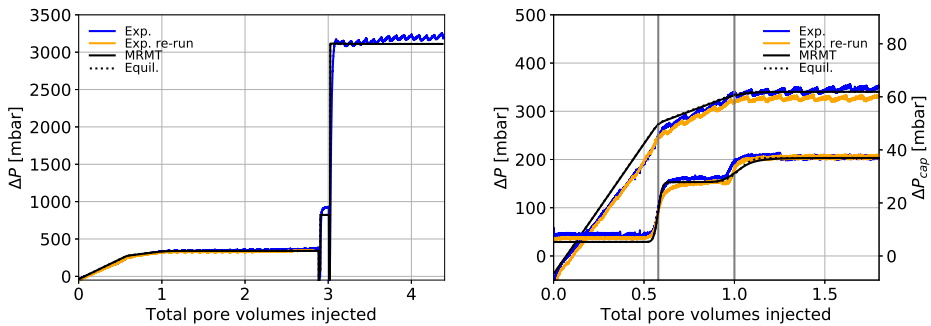


Fig. 5 Measured and simulated differential pressures, $\Delta P = P_{out} - P_{in}$ (corrected for gravity), when a P10 solution was injected to displace a B35 solution. Left plot: Simulated (black lines) versus experimental (blue and orange lines) ΔP . Right plot: A zoomed in version of the left plot, highlighting the initial period when the flow rate was $Q = 0.3 \text{ ml min}^{-1}$. Also shown are registered pressure drops ΔP_{cap} across the capillary tube that was connected to the effluent (secondary axis). The solid line in this plot was obtained by combining the IORCoreSim shear thinning model with the Hagen-Poiseuille law for the tube, using simulated effluent concentrations.

resistance profiles for this period, during which the direction of salinity change was the opposite of previously. It is seen that both transport models provided acceptable fits to the data in this case, the differences between the two predictions being very small.

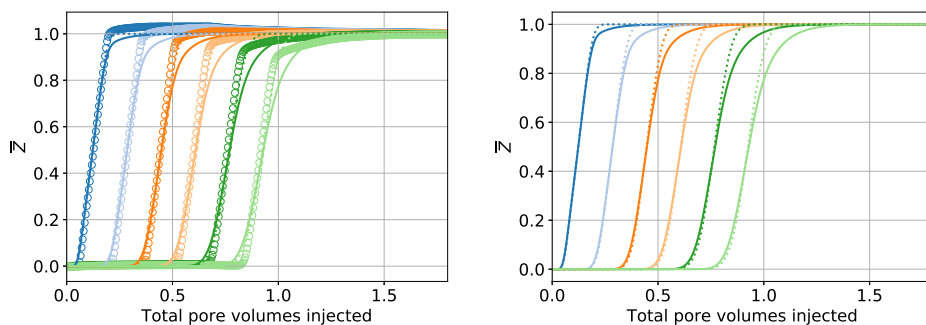


Fig. 6 Normalized bulk resistance, $\bar{Z} = (Z - Z_{init}) / (Z_{inj} - Z_{init})$, when a P10 solution was injected to displace a B35 solution. The flow rate for this part of the experiment was $Q = 0.3 \text{ ml min}^{-1}$. Left plot: Comparison between experimental data (circles) and the two different simulations. Right plot: Only the simulation results.

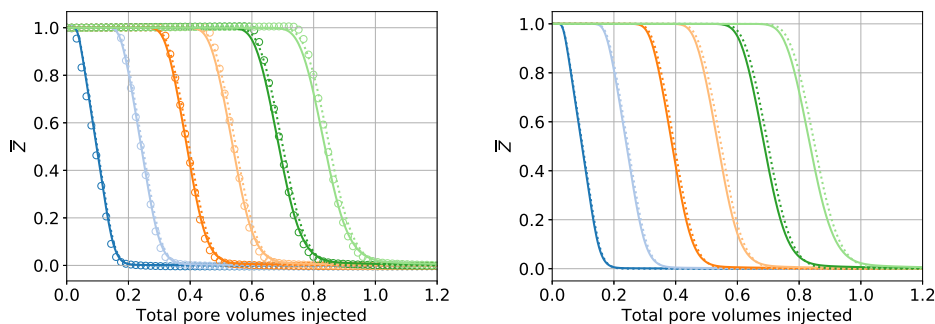


Fig. 7 Normalized bulk resistance, $\bar{Z} = (Z - Z_{inj}) / (Z_{init} - Z_{inj})$, when a B35 solution was injected to displace a B10 solution, in-between successive polymer floods. The left plot shows comparison between experiment and simulations, while the right plot only displays the modelled resistance curves. The flow rate was in this case $Q = 1 \text{ ml min}^{-1}$.

4.5 Column 2, Experiment 5: High salinity water replacing low salinity polymer (P10 \rightarrow B35)

Figure 8 exhibits another case in which the injected solution had the highest salinity. However, in this case, polymer was also present initially, meaning that a low viscosity solution was injected to displace a high viscosity one. The viscosity contrast resulted in an unstable flow situation, as clearly evidenced by the shapes of the resistance profiles, especially for sections 5 and 6.

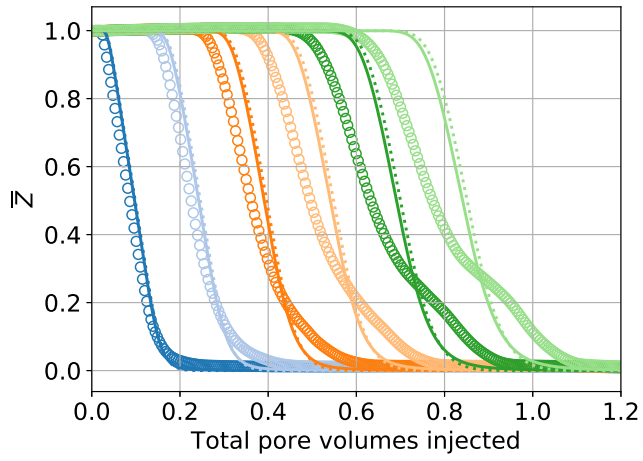


Fig. 8 Normalized bulk resistance when an initial P10 polymer solution was replaced by a higher salinity B35 brine. Comparison between experimental data (circles) and the two different simulations. The employed flow rate was $Q = 0.3 \text{ ml min}^{-1}$.

5 Discussion

As already mentioned, to rationalize the experimental findings, the NaCl transport was simulated using a MRMT model, i.e., by combining Eqs. (1), (2), (3), and (4), with the sum of the immobile porosities representing the fraction of the total pore volume that resided inside the grains. Two compartments were used to represent the intragranular pore volume ($N_{im} = 2$), but most of it was assumed to be in equilibrium with the fluid in the macropores at all times, which was ensured by using a large value for the mass transfer rate, $\alpha_1 > 1$. Only a very small fraction was assumed to exchange mass at a much slower time scale (table 7). Effectively therefore, the transport of ions was modelled by a single-rate mobile-immobile model (MIM) (Van Genuchten and Wierenga, 1976), but with a very small immobile porosity.

As is clear from the solid line in figure 2, the addition of non-equilibrium behavior improved the match between the simulated and measured breakthrough curve. Thus, one way to understand the observations is that there was a slow release of high saline water from a small fraction of the pores into the more rapidly flowing stream. The exact reason for why this assumption was needed is unclear. It is speculated whether the behavior could have been caused by restricted diffusion into and out of the very smallest pores inside the grains. Another contributing factor might be adsorption and desorption of ions.

Alternatively, there could have been significant macroscopic heterogeneities present in the sand packs. To investigate this possibility, preliminary 2D (radial) simulations were conducted, in which it was assumed that a thin layer close to the column walls had a $\sim 20\%$ lower permeability than the middle part. If diffusion was ignored in the simulations, it was indicated that such an assumption might be able to explain the observations. However, when diffusion was included, the concentrations in the two layers were rapidly equalized, yielding only small differences from the simulations assuming a homogeneous core. Thus, while heterogeneity should still be considered a plausible hypothesis, it was not found straightforward to reproduce the experimental data with such an approach.

5.1 Calibrating the transport model based on the Column 1 low salinity waterflood

Input parameters to the transport model for Column 1 were selected based on obtaining a satisfactory visual match with the effluent chloride breakthrough curve. The values thus selected for the mass transfer coefficient α_2 and the dispersivity coefficient λ_d were subsequently used as input to simulate the Column 2 corefloods (table 7).

Note that, in IORCoreSim, some smearing of the salinity front will occur purely as a consequence of numerical diffusion (Lantz, 1971). To fit the model to the data, it is important that the contribution due to numerical dispersivity is lower than the observed amount of dispersion. With the chosen grid resolution ($\Delta z = 1$ mm, for the vast majority of grid blocks), roughly one third of the effective longitudinal dispersivity could be accounted for by errors in the numerical approximation (table 7).

5.2 Interpreting the electrical resistance data during waterflooding

For the corefloods not involving polymer, the MRMT model also provided decent fits to the electrical resistance data. This was true both when a low salinity B10 solution was injected to displace a higher salinity B35 solution (figure 3), and when the direction of salinity change was reversed (figure 7). It was conjectured that the shapes of the resistance curves could be have been influenced by the dimensions and/or placement of electrodes used to measure the resistance. However, direct numerical simulation of the steady-state electrical transport problem revealed a negligible impact of such factors (not shown here).

It is worth pointing out some noticeable differences between the two cases without polymer (figure 9, left plot). First, the late-time tails that were seen in the low salinity injection case more or less disappeared when the salinities were switched. Second, and more importantly, the electrical signal showed an earlier response in the high salinity injection experiment. It is noted that the time shift between the two sets of curves increased with distance from the inlet, meaning that it was largest for section 6, and smallest for section 1. The latter observation can be understood as a consequence of

salinity mixing within the porous medium. For the idealized case of a piston displacement, both sets of resistance curves should look the same, if plotted versus injected volume on the time axis. However, the introduction of dispersion in the macropores creates a mixing zone, the length of which increases with the square root of time (Lake, 1989). For 1D flow, the effective conductivity across a spatial interval is essentially the harmonic average of local conductivities. Therefore, since the relation between fluid resistivity (inverse of conductivity) and salinity is non-linear, the electrical resistance of a section will be sensitive to the direction of salinity change. Locally, we have a mathematical relationship of the form

$$\rho_f = 1/\sigma_f = \frac{1}{k_1 \cdot C_S + k_2}, \quad (11)$$

where C_S is the NaCl concentration, ρ_f is the corresponding fluid resistivity, and k_1 and k_2 are constants. The fluid resistivity changes more slowly when going from a high salinity to a low salinity, than when the fluid transport occurs in the opposite order (figure 9, right plot). These observations show that, though performing electrical resistance measurements can be a useful way to track salinity fronts within the porous medium, numerical simulation studies may be needed to fully understand the relation between concentration and resistance.

Similarly, in the model, the impact of non-equilibrium mass exchange will also depend on which brine was present in the column initially. From figure 9, it is seen that the MRMT model predicts pronounced late-time tails in the resistivity curves in the low salinity injection case, but that they virtually disappear for the high salinity injection experiment.

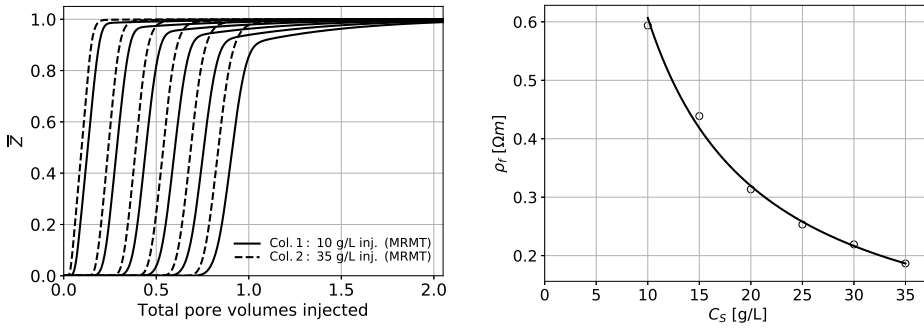


Fig. 9 Left plot: Normalized bulk resistance for two different simulated scenarios: 1) B10 replacing B35 (solid lines), and 2) B35 replacing B10 (dashed lines). Both sets of curves have been normalized to go from zero to unity, regardless of the actual direction of salinity change. Right plot: Measured fluid resistivities (circles)

5.3 Interpreting the transient pressure data during low salinity polymer injection (Column 2)

For the first pore volume of P10 injection, the transient pressure drop response across the core could be divided into two distinct periods, after which a stable plateau value in ΔP was reached (figure 5):

1. An initial period of linear increase in ΔP starting from $t = 0$ and continuing until a dimensionless time T_1
2. A second period of linear increase, but with a different slope than before, lasting until a time $T_2 \approx 1 PV$

The critical times T_1 and T_2 are marked by vertical grey lines in the right plot of figure 5. The observations are interpreted as a combined effect of a) polymer inaccessible pore volume, and b) salinity-dependent polymer solution

viscosity. Specifically, during the initial transient period the polymer was predominantly transported through the macropores, while the co-injected ions were small enough to enter the pore volume internal to the silica grains. In other words, the injected polymer mixed with the already present B35 brine, while the injected salinity front lagged behind. This resulted in the establishment of two separate fronts moving through the medium, with a marked time separation between them: the P35 solution reached the column effluent first, and then the P10 solution arrived at the outlet some time later. The conclusion is corroborated by looking at the pressure drop ΔP_{cap} measured across the capillary tube, which exhibited two sharp increases in pressure at the relevant times. At time T_1 , ΔP_{cap} rose to a value slightly below ~ 30 mbar, which corresponds to the shear thinning viscosity of the P35 solution at the given apparent shear-rate in the tube (corrected for the non-Newtonian velocity profile by applying the Weissenberg-Rabinowitsch correction (Bird et al., 1977)). Similarly, around $T = 1 PV$, ΔP_{cap} increased again, to a value which is representative of the P10 polymer solution. That the salinity front lagged behind the polymer front was also clear from studying the electrical resistance measurements. For instance, at the time of polymer breakthrough, the salinity front had still not reached the last two resistance sections, as can be seen by comparing the left plot of figure 6 with the right plot of figure 5.

The experimentally observed trend is well reproduced by the IORCoreSim model. Moreover, based on the simulations, analytical expressions can easily be derived for the slopes of the ΔP versus T curve, as long as the diffusion and dispersion part of the transport model can be neglected, and assuming no mechanical degradation of polymer (this was not observed experimentally). By treating the experiment as a sequence of piston displacements, in which ions are advected through the whole pore volume while polymer only has access to the macropores, the 1D Darcy Law may be integrated, and subsequently differentiated with respect to time, to yield

$$\frac{d\Delta P}{dT} = \frac{QL}{kA} \cdot (\eta_{10} - \eta_{35} + \frac{\eta_{35} - \eta_s}{1 - IPV}) \quad (12)$$

for times $T \leq T_1$, and

$$\frac{d\Delta P}{dT} = \frac{QL}{kA} \cdot (\eta_{10} - \eta_{35}) \quad (13)$$

for $T_1 < T \leq T_2$. In the above equations, η_{10} is the apparent viscosity of the P10 polymer solution at the given flow rate of $Q = 0.3 \text{ ml min}^{-1}$, η_{35} is the apparent viscosity of the P35 solution, while η_s denotes the viscosity of the brine that was initially residing in the core. Equations (12) and (13) describe how the slope of the modelled ΔP versus T curve is a function of gradients in apparent viscosity inside the medium. Before polymer breakthrough, the slope is a sum of two different terms, one representing the viscosity difference between the low and high salinity polymer solutions, and one that accounts for the difference between the P35 solution and the pure NaCl brine. After polymer reaches the outlet at $T_1 = \phi_m / \phi_t$, only the former term contributes, thus lowering the slope. Eventually, all of the core will be filled with the P10 solution, whereby the pressure drop stabilizes until the flow rate is changed.

5.4 Interpreting the electrical resistance data during polymer flooding

When polymer was injected alongside low salinity water, the theoretically calculated resistance curves gave a poorer match with the data than before. As already commented, the simulations showed clear deviations from the experimental curves, which appeared to be steeper than for ordinary waterflooding (figure 6, left plot). Obviously, the presence of polymer in the macropores should enhance flow of ions in the grains. It was first speculated whether this mechanism could be responsible for the noted discrepancy between theory and data. However, as the very small pore sizes involved yield extremely low permeabilities inside these pores, this does not seem realistic.

Instead, perhaps the behavior can be related to a reduction in macroscopic dispersion? As already noted in section 5.3, breakthrough of the injected low salinity polymer solution did not occur until $T \sim 1 PV$, because the salt front lagged behind the polymer front. Since the trailing P10 solution had a higher viscosity than the leading P35 solution, it is possible that the amount of dispersion associated with the arrival of the second front was reduced as a consequence

of suppressing macroscopic viscous fingering (Homsy, 1987). Such an explanation was also suggested by Nilsson et al. (1997).

When a B35 solution was injected to displace a P10 brine, clear evidence of viscous fingering was detected (figure 8). Because of the *IPV* effect, the polymer would not be expected to see the injected salt solution, instead being pushed out of the core by a B10 brine. Again, two fronts would be moving through the medium. In this case, the observations are clearly linked to the unfavourable viscosity gradient that existed near the leading front, i.e., the difference between the B10 and P10 brines. However, in theory the lagging front should show signs of a stable displacement, because the displacing NaCl solution had the highest salinity. The irregularity of the displayed resistance curves even at late times suggests that the initially developing fingers must have propagated backwards towards the core entrance during the experiment.

As is clear from figure 8, the effects of viscous fingering cannot be described with the 1D modelling approach taken in this work.

5.5 Challenges when modelling the polymer experiments

When attempting to history match the Column 2 experiments, the registered pressure drop before initiation of polymer flooding did not accord with the theoretically expected value at $t = 0$ (based on the estimated water permeability). The raw data was therefore adjusted downwards with a constant factor, $\Delta P_{corr} = 64.6$ mbar. However, when this was done for all times $t > 0$ during the long term polymer injection experiment, the values of $\Delta P + \rho g L$ became negative, a physical impossibility. As a consequence of these and other uncertainties, both in terms of accuracy and availability of data, the selected input parameters to the polymer model must be regarded as uncertain. In particular, there was insufficient data to determine the shear thickening parameters with a high degree of confidence. There is also the question as to whether an additional salinity-dependence should be incorporated into this part of the model. In Lohne et al. (2017) it was indicated that a less pronounced shear thickening effect can be expected at lower salinities. However, no explicit model for this salinity dependence has so far been thought of, and in the present work a set of constant input parameters were used, regardless of the value of the NaCl concentration.

6 Summary and conclusions

Sodium chloride brines with and without dissolved polymer molecules were injected into columns packed with porous silica gel sand. For the system under consideration, the total porosity was exceptionally high, approximately 80 %, but with a large portion of the pore volume residing inside the grains. It was observed that the polymer moved much faster through the sand packs than co-currently injected ions, which was shown to be a consequence of size exclusion, meaning that a substantial number of pores were simply too small to allow any macromolecules to enter. The polymer transport could therefore be well described by the notion of inaccessible pore volume, *IPV* (Dawson and Lantz, 1972; Lotsch et al., 1985). While ions were transported through most areas of the pore space, including the pores inside the individual silica grains, polymer flow took place primarily in the macropores in-between the grains. However, it is important to note that the *IPV* acted as a source and sink of ions, and thus had a considerable impact on the rheological behavior of the flowing polymer solution.

The above conclusions were reached by combining multiple sources of information: a chloride breakthrough curve, in-situ electrical resistivities, as well as differential pressure recordings. The latter were taken across the column itself, and across a capillary rheometer connected to the outlet end. Since the flow resistance of the employed polymer solutions were salt-sensitive, the arrival of polymer at the effluent could be deduced from the ΔP measurements. The IORCoreSim polymer model (Lohne et al., 2017) was applied to interpret the experimental data. The model includes correlations to describe the non-Newtonian flow rheology, as well as salinity-dependent intrinsic viscosities. The simulations explained the main trends in the data very well, though it was found difficult to obtain a completely satisfactory history match. Some possible reasons for this were suggested.

A simplified mathematical model was proposed to interpret the resistance data. When comparing low salinity injection with high salinity injection, the inclusion of dispersion proved important to capture the timing of the observed electrical response. This highlights the fact that, while the section resistances provide useful information about in-situ ionic concentrations, differences between the two measures should be kept clearly in mind. It was further observed that the presence of polymer affected the electrical signal. In particular, for injection of water to displace polymer, the electrical resistance measurements revealed premature breakthrough of ions, and the profiles showed distortions at late times, which indicated an unstable flow situation (i.e., viscous fingering).

Although the reported experiments were conducted in an artificially manufactured medium, a similar kind of transport behaviour might be expected in more realistic settings as well, e.g., in fractured reservoirs; or more generally, in reservoirs with a wide pore size distribution. If large polymer molecules are injected into such a formation, it can result in a situation where the polymer front moves rapidly from the injector to the producer, bypassing most of the oil stored in low permeable zones in the matrix, and leaving the co-injected water behind. This could be problematic, especially if the desired goal is to combine polymer flooding with other EOR methods that involve modifying the brine composition, such as low salinity waterflooding. Indeed, since the reservoir formation water typically has a high salinity, the size exclusion effect would then negatively limit the possibility of a synergy effect between the two methods. One remedy for this would be to perform a low-salinity pre-flush for a sufficient duration of time before the start-up of polymer injection.

7 Acknowledgements

The authors acknowledge the Research Council of Norway and the industry partners, ConocoPhillips Skandinavia AS, Aker BP ASA, Eni Norge AS, Total E&P Norge AS, Equinor ASA, Neptune Energy Norge AS, Lundin Norway AS, Halliburton AS, Schlumberger Norge AS, Wintershall Norge AS, and DEA Norge AS, of The National IOR Centre of Norway for support.

8 Tables

Table 1 Aqueous solutions used in the reported experiments.

Brine	NaCl concentration [g l^{-1}]	Polymer concentration [ppm]
B10	10	0
B35	35	0
P10	10	1000
P35	35	1000

Table 2 Estimated column properties, for the two columns considered in this paper. The value for macroporosity ϕ_m used in the polymer simulations was based on matching the experimental breakthrough time of polymer, as determined from the effluent capillary tube rheometer. For more precision, an additional correction should be made for the volume in-between the column and the capillary tube, but this was not recorded.

Quantity	Column 1	Column 2
Length, L	81.474 cm	80.708 cm
Average diameter, d	1.511 cm	1.577 cm
Average permeability, k	6.2 D	4.9 D
Pore volume, V_p	111.912 ml	125.104 ml
Total porosity, ϕ_t	76.6 %	79.4 %
Estimate for macroporosity, ϕ_m		45.5 %

Table 3 Explanation for parameters used in the implemented MRMT framework (Haggerty and Gorelick, 1995). The total pore space is assumed to consist of a single 'mobile domain' (macropores), as well as N_{im} immobile (stagnant) zones. The latter fluid continua are indexed by the letter j . In the present work, $N_{im} = 2$.

Parameter	Description
ϕ_m	Porosity of the mobile domain
ϕ_{im}^j	Porosity of immobile domain j
ϕ_{im}	Total porosity of immobile domain, i.e., the sum of all ϕ_{im}^j
ϕ_t	Total porosity, i.e., the sum of ϕ_m and ϕ_{im}
C_m	Solute concentration in the mobile domain
C_{im}^j	Solute concentration in immobile domain j
α_j	The j -th mass transfer coefficient
D_m^*	Effective diffusion coefficient for the mobile domain
u	Darcy velocity
$v = u/\phi_m$	Mean advective velocity in the mobile domain
D_{mol}	Molecular diffusion coefficient
τ	Dimensionless tortuosity factor, to account for restricted diffusion in porous media
λ_d	Longitudinal dispersivity coefficient

Table 4 Measured NaCl conductivities at $T = 22.5^\circ\text{C}$.

Concentration, C_S [g l^{-1}]	Conductivity, σ_f [mS cm^{-1}]
10	16.84
15	22.79
20	31.9
25	39.5
30	45.6
35	53.6

Table 5 Polymer input parameters for the IORCoreSim simulations. The dimensional quantities listed in the table are based on using the following units: $[M_w] = \text{MDa}$, $[\eta] = \text{ml g}^{-1}$, $[\lambda_a] = \text{K mol J}^{-1}$.

Parameter	Value
Molecular weight, M_w	15
Mark-Houwink prefactor, K	345.6
Mark-Houwink exponent, a	0.68
Salinity dependence exponent, α_s	0.239
Huggins constant, k_1	0.720
Huggins constant, k_2	0.153
Shear thinning slope parameter, a_n	0.055
Shear thinning slope parameter, b_n	0.661
Relaxation time prefactor, λ_a	0.635
Shear thinning transition parameter, x	1.82
Critical Deborah number, N_{De}^*	3.76
Shear thickening slope, m	0.93
Shear thickening transition parameter, x_2	4.0

Table 6 Fitted Carreau-Yasuda parameters for the P10 and P35 polymer solutions, when using the input parameters from table 5. Note that the solvent viscosity was treated as independent of salinity. In reality, the viscosity of a B35 solution is approximately 4 % larger than that of a B10 solution (at room temperature).

Parameter	Value for P10 brine	Value for P35 brine
Solvent viscosity, η_s	1 mPas	1 mPas
Zero shear rate viscosity, η_0	18.3 mPas	10.7 mPas
Relaxation time, λ_1	0.56 s	0.31 s
Shear thinning transition parameter, x	1.82	1.82
Shear thinning slope parameter, n	0.25	0.21

Table 7 Input parameters for the IORCoreSim MRMT model simulations. For both Column 1 and Column 2, the intragranular pore space was divided into two compartments, most of which was assumed to be in equilibrium with the fluid in the macropores.

Parameter	Value
Fraction of slowly exchanging intragranular pore space, ϕ_2/ϕ_m	0.05
Mass transfer coefficient, α_2	$1.019 \times 10^{-5} \text{ s}^{-1}$
Input dispersivity coefficient, λ_d	0.081 cm
Estimated numerical dispersivity coefficient when $\Delta z = 1 \text{ mm}$	0.047 cm
Effective dispersivity coefficient	0.128 cm

References

- Archie, G. [1942] The electrical resistivity log as an aid in determining some reservoir characteristics. *Trans., AIME*, **146**, 54–67.
- Bird, R.B., Armstrong, R.C., Hassager, O. and Curtiss, C.F. [1977] *Dynamics of polymeric liquids*, 1. Wiley, New York.
- Dawson, R. and Lantz, R.B. [1972] Inaccessible pore volume in polymer flooding. *Society of Petroleum Engineers Journal*, **12**(05), 448–452.
- Dullien, F.A. [1992] *Porous media: fluid transport and pore structure*. Academic press, 2nd edn.
- Ewoldt, R.H., Johnston, M.T. and Caretta, L.M. [2015] Experimental challenges of shear rheology: how to avoid bad data. In: *Complex fluids in biological systems*, Springer, 207–241.
- Glover, P.W. [2009] What is the cementation exponent? A new interpretation. *The Leading Edge*, **28**(1), 82–85.
- Haggerty, R. and Gorelick, S.M. [1995] Multiple-Rate Mass Transfer for Modeling Diffusion and Surface Reactions in Media with Pore-Scale Heterogeneity. *Water Resources Research*, **31**(10), 2383–2400.
- Homsy, G.M. [1987] Viscous fingering in porous media. *Annual review of fluid mechanics*, **19**(1), 271–311.
- Lake, L.W. [1989] *Enhanced oil recovery*. Prentice Hall Inc., Old Tappan, NJ.
- Lantz, R. [1971] Quantitative evaluation of numerical diffusion (truncation error). *Society of Petroleum Engineers Journal*, **11**(03), 315–320.
- Lohne, A. [2017] User's manual for IORCoreSim - combined EOR and SCAL simulator.
- Lohne, A., Nødland, O., Stavland, A. and Hiorth, A. [2017] A model for non-Newtonian flow in porous media at different flow regimes. *Computational Geosciences*, 1–24.
- Lotsch, T., Muller, T. and Pusch, G. [1985] The effect of inaccessible pore volume on polymer coreflood experiments. In: *SPE Oilfield and Geothermal Chemistry Symposium*. Society of Petroleum Engineers.
- Mendelson, K.S. and Cohen, M.H. [1982] The effect of grain anisotropy on the electrical properties of sedimentary rocks. *Geophysics*, **47**(2), 257–263.
- Nilsson, S., Lohne, A. and Veggeland, K. [1997] Effect of polymer on surfactant floodings of oil reservoirs. *Colloids and Surfaces A: Physicochemical and Engineering Aspects*, **127**(1-3), 241–247.
- Norwegian Petroleum Directorate [2018] Positive prospects for producing more. <http://www.npd.no/en/Topics/Improved-Recovery/Temaartikler/Positive-prospects-for-producing-more/>. Accessed: 2018-08-29.
- Perkins, T. and Johnston, O. [1963] A review of diffusion and dispersion in porous media. *Society of Petroleum Engineers Journal*, **3**(01), 70–84.
- Revil, A. and Glover, P. [1997] Theory of ionic-surface electrical conduction in porous media. *Physical Review B*, **55**(3), 1757.
- Ringen, I., Stiegler, H., Nødland, O., Hiorth, A. and Stavland, A. [2016] Polymer Flooding In Sandpicks with a Dual-Porosity. In: *Paper prepared for presentation at the International Symposium of the Society of Core Analysts held in Snowmass, Colorado, USA, 21-26 August 2016*.
- Sen, P., Scala, C. and Cohen, M. [1981] A self-similar model for sedimentary rocks with application to the dielectric constant of fused glass beads. *Geophysics*, **46**(5), 781–795.
- Sheng, J.J., Leonhardt, B. and Azri, N. [2015] Status of polymer-flooding technology. *Journal of Canadian Petroleum Technology*, **54**(02), 116–126.
- Sorbie, K.S. [1991] *Polymer-improved oil recovery*. Springer Science & Business Media.
- Stavland, A., Jonsbrotten, H. and Strand, D. [2013] When will polymer viscosity be a design criterion for EOR polymer flooding? In: *IEA-EOR 34th Annual Symposium, Stavanger, Norway*.
- Thomas, A., Gaillard, N. and Favero, C. [2012] Some key features to consider when studying acrylamide-based polymers for chemical enhanced oil recovery. *Oil & Gas Science and Technology—Revue d'IFP Energies nouvelles*, **67**(6), 887–902.
- Tiab, D. and Donaldson, E.C. [2012] *Petrophysics: theory and practice of measuring reservoir rock and fluid transport properties*. Elsevier/Gulf Professional.

Van Genuchten, M.T. and Wierenga, P. [1976] Mass transfer studies in sorbing porous media I. Analytical solutions. *Soil Science Society of America Journal*, **40**(4), 473–480.